SKB

Testing of fracture-matrix transport models using in-situ data and benchmark problems

Task 9 of SKB Task Force GWFTS – Increasing the realism in solute transport modelling based on the field experiments REPRO and LTDE-SD

M Hokr

V Havlová

A Vetešník

L Gvoždík

M Milický

M Polák

D Reimitz

J Říha

D Trpkošová

J Višňák

D Vopálka

SVENSK KÄRNBRÄNSLEHANTERING

Testing of fracture-matrix transport models using in-situ data and benchmark problems

Task 9 of SKB Task Force GWFTS – Increasing the realism in solute transport modelling based on the field experiments REPRO and LTDE-SD

M Hokr[1], V Havlová[2], A Vetešník[3], L Gvoždík[4], M Milický[4], M Polák[4], D Reimitz[3], J Říha[1], D Trpkošová[2], J Višňák[3], D Vopálka[3]

1 Technical University of Liberec
2 ÚJV Řež
3 Czech Technical University in Prague, Faculty of Nuclear Sciences and Physical Engineering
4 PROGEO s.r.o.

Abstract

This report compiles the work performed by the Czech teams within Task 9 of SKB Task Force on Modelling of Groundwater Flow and Transport of Solutes (TF GWFTS). The overall goal of Task 9 is to improve transport models so more realistic modelling can be performed. This is mainly done by conducting predictive and back-analysing modelling using in-situ data from the underground laboratories Äspö Hard Rock Laboratory in Sweden and ONKALO in Finland. The modelling work is based on the specification of the international project Task 9 of TF GWFTS.

The modelling task includes three experiments (WPDE, LTDE-SD and TDE) and one synthetic transport task of the safety-assessment scale. The result was mutual verification of several simulation software (GoldSim, Flow123d, MT3D) on selected tasks and data. Cases were defined where inaccuracy may occur due to discretisation for strongly sorbing radionuclides. Other results were inverse analyses of experimental data. In various cases, it has been shown that the measured diffusion profiles as well as the breakthrough curves, etc. can be more accurately represented by models with inhomogeneous rock matrix (typically porosity and distribution coefficient), which is physically interpreted as a zone affected by drilling or sample processing. The second procedure to explain the measured data was the micro-DFN model based on autoradiographic images of the samples and a model inhomogeneous on a microscopic scale.

Sammanfattning

Denna rapport sammanställer det arbete som utförts av de tjeckiska teamen i modelleringsuppgift 9 inom SKB Task Force om modellering av grundvattenflöde och transport av lösta ämnen (TF GWFTS). Det övergripande målet med Task 9 är att förbättra transportmodeller så att mer realistisk modellering kan utföras. Detta görs främst genom att genomföra predikterande och efteranalyserande modellering med hjälp av in-situ-data från de underjordiska laboratorierna Äspö Hard Rock Laboratory i Sverige och ONKALO i Finland. Modellarbetet baseras på distribuerade specifikationer för det internationella projektet Task 9 inom TF GWFTS.

Modelleringsuppgiften inkluderar tre experiment (WPDE, LTDE-SD och TDE) och en syntetisk transportuppgift relaterat till säkerhetsanalys. Resultatet blev en ömsesidig verifiering av flera simuleringsprogram (GoldSim, Flow123d, MT3D) för utvalda uppgifter och data. Fall definierades där felaktigheter kan uppstå på grund av diskretisering när transport av starkt sorberande radionuklider modelleras. Andra resultat var inversanalyser av experimentella data. I olika fall har det visat sig att de uppmätta diffusionsprofilerna såväl som genombrottskurvorna kan representeras bättre av modeller med inhomogen bergmatris (porositet och distributionskoefficient), vilket fysiskt kan tolkas som en zon som påverkats av borrning eller provbearbetning. Ett annat förfarande för att förklara de uppmätta data var användande av en mikro-DFN-modell baserad på autoradiografiska bilder av proverna och en modell som är inhomogen i mikroskopisk skala.

Contents

1   Introduction

Task 9 is part of the SKB Task Force on Modelling of Groundwater Flow and Transport of Solutes (TF GWFTS), which focuses on the fractured crystalline host rock surrounding present and future repositories for spent fuel and other radioactive waste. Special interest is taken in work on fracture flow and solute transport made by the Äspö Hard Rock Laboratory (HRL), Sweden.

The title of Task 9 is "Increasing the realism in solute transport modelling – Modelling the field experiments of REPRO and LTDE-SD". The task focuses on the realistic modelling of coupled matrix diffusion and sorption in the heterogeneous crystalline rock matrix at depth. This is done in the context of inverse and predictive modelling of tracer concentrations of the in-situ experiments performed within LTDE-SD at the Äspö HRL in Sweden, as well as within the REPRO project at ONKALO in Finland, focusing on sorption and diffusion. The aim is to develop models that in a more realistic way represent retardation in the natural rock matrix at depth.

In this report, the studied experiments and models focus on the issues of retention phenomena in the rock matrix affecting the migration of radionuclides by advection in fractures. The solved question involves deviations of experimental data from linear diffusion and sorption models in a homogeneous environment, which is often also associated with discrepancy of diffusion and sorption behaviour between laboratory and in-situ conditions, depending on the scale, etc.

The specified model task description and aims of the solution were based on documents issued by the international project of TF GWFTS, which is explained in the next part of the introduction.

1.1   Context of the work – Project GWFTS, Task 9

The participation of authors in the Task Force on Modelling of Groundwater Flow and Transport of Solutes was under contract from Czech Radioactive Waste Repository Authority (SÚRAO). The programme started as early as 2003, with gradually changing tasks/themes and serial numbers. SÚRAO has been a participant since 2015 in connection with the solution of the sub-project in this report, "Task 9". The task is actually meant to be a broader theme with more specific tasks and data. The website of the programme is https://www.skb.se/taskforce/, in which the non-public part contains all of the data from the whole history.

The projects of the Task Force (TF) led by SKB focus on the collaboration of numerical modelling experts in various areas relevant to deep geological repositories across participating countries. Tasks are focussed on comparing models among themselves and common interpretation of the provided experimental data, which are currently mainly in-situ. The aim of the participation is to improve the verification of software used for the simulation of phenomena essential for safety analysis – in this case Flow123d and GoldSim, or others, for the simulation of flow and transport phenomena in the rock environment.

According to the task description, Task 9 for the period 2015–2019 involves the verification of models of the transport of radionuclides, specifically a combination of phenomena of advection, diffusion and sorption on a small scale, based on experimental data from the underground laboratories Äspö Hard Rock Laboratory in Sweden and ONKALO (Olkiluoto, Finland) and their experiments. The sub-themes and their factual and temporal sequence according to the original task description are shown in Figure 1-1. During the solution, the specifications and continuity of Tasks 9C and 9D were modified by the GWFTS Steering Committee. Sub-tasks 9A–9D have their coordinators designated.

Project work covers a wide and interdisciplinary scope. For the evaluation it is necessary to inter-connect the facts of the details of the behaviour of radionuclides in the rock through understanding various conceptual transport models and their connections, and the properties of numerical algorithms, which can influence the results (method variants, discretisation, non-linearities). In the modelling of experimental data, the different contexts of the models use are distinguished – as a direct problem we may design a calculation with specific given inputs, while in the inverse problem we look for parameter values (or choose from several model descriptions) in order to agree with the results of

the experiment. In the first case, in addition to verification (the correctness of the models in terms of the accuracy of the solution of equations), so-called blind predictions have a specific meaning, when the author does not know the (experimental) data with which the model results are to be compared. The concept of the project also allows for validation, where models created by the inverse analysis of one experiment are verified against another experiment under comparable conditions using a blind prediction.

The model task descriptions are based on experiment configurations and are specified in detail in the documents of GWFTS for each sub-task (9A–9D) – for each sub-task the coordinator responsible for the formulation and provision of data was appointed by the Steering Committee as well as the evaluator of the whole project was Josep Soler, whose responsibility was to evaluate the outputs of the models. The individual documents of the task description are referred to in the relevant sections. Along with the primary task description, other supporting data – tables with experimental data, templates for processing the results, clarifying commentaries, photo documentation, etc. – were also distributed. A complete list of the deliverables is included in a tabular form in Appendix 1.

The management of GWFTS (in which SÚRAO representatives also participated) developed the time schedule of the investigators' work, and the sub-project task description was updated accordingly. The form and scope of the involvement of the individual co-investigators in selected tasks of the GWFTS-Task 9 project were continuously discussed during executive meetings with the participation of SÚRAO.

1.2   Project structure and content of reports

The sections of the report are arranged according to the tasks specified by GWFTS – 9A to 9D. To this is added the first section describing the mathematical formulations of the models used and software characteristics related to the tasks. In a separate section, a specific application of the micro-DFN method is elaborated, which was one of the stimuli for the solution in the framework of GWFTS and at the same time the subject of the sub-project of SÚRAO for the co-investigator PROGEO. The section is after the section of Task 9B, to which it is linked, but also refers to data from other sources. The first part of each section includes a summary of the task description and the provided data with references to the source documents from GWFTS made available to SÚRAO.

In addition to the presentation of results directly linked to GWFTS tasks, the subject of the solution is also a comparison of Czech research teams with each other. In the structure of the report, this is usually the first section following the task description and data. In the case of Tasks 9A, 9C, 9D, a predictive analysis was used to compare the results according to the GWFTS specification, under the assumption that the model parameters were unified. In the case of Task 9B, this was an inverse analysis, where the subject of the task description is to look for an optimal assumption for the model type and parameters. Therefore, for the purpose of the comparison, a preparatory task with fixed data was also specified.

In addition to the GWFTS specification, and in accordance with the opinion of SÚRAO at the executive meetings, an inverse model was also solved in relation to Task 9A and 9C after the publication of the experiment data (after the predictive models were processed by the individual investigators). Similarly, this is the subject of other sections following on from the predictive model in the section of the relevant Task.

The presented procedures of the solution and the model results are indicated based on the software used (in the section titles, graphic descriptions, etc.), or together with abbreviations of the institutions implementing the given solution. References to the institutions are essential for distinguishing between the use of GoldSim in the two different workplaces. Other cases are various complementary evaluations in relation to the inverse models, where there is no specific link to the software, and abbreviations of the institutions are also used to indicate the specific part of the work or the data of the results.
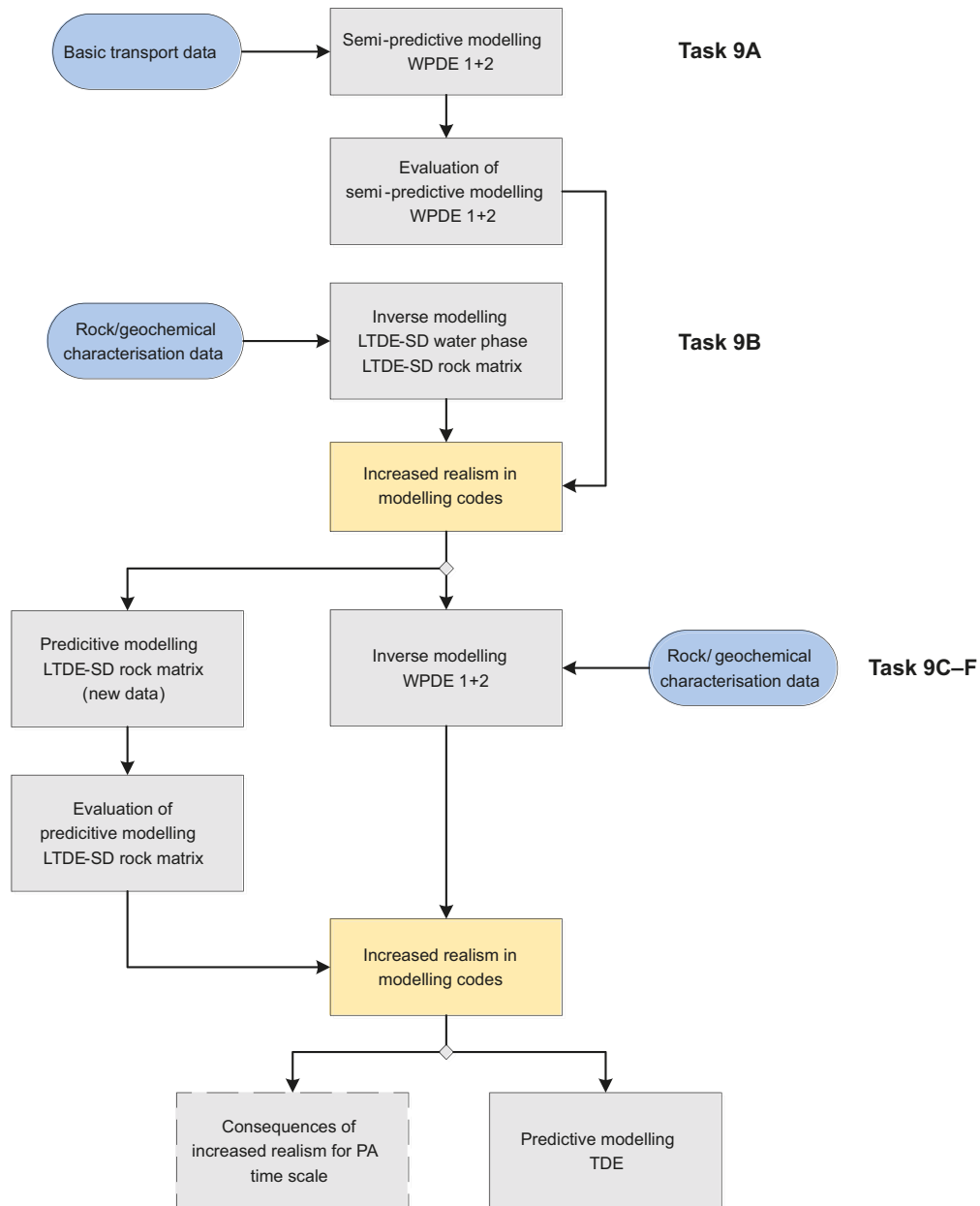
Figure 1-1. *Roadmap of the individual steps of Task 9 in the TF GWFTS program (Löfgren and Nilsson 2019).*

1.3   The Task 9 report by the Czech teams

This report was originally prepared by Hokr et al. (2020) within the framework of the SÚRAO project entitled "Research Support for the Safety Assessment of a Deep Geological Repository", which is part of the preparation of a deep geological repository of radioactive waste (hereinafter referred to as "DGR"). The aim of the project is to obtain selected data, models, arguments and other information needed to evaluate potential sites for the location of a DGR from the point of view of long-term safety. Following a public tender, a four-year contract was concluded in July 2014 with ÚJV Řež, a.s. and its subcontractors: the Czech Geological Survey; Czech Technical University in Prague (FJFI ČVUT); Technical University of Liberec; Institute of Geonics AS CR, v.v.i; and Arcadis CZ a.s.; PROGEO, s.r.o.; Chemcomex Praha, a.s. and Research Centre Řež s.r.o. for the provision of research support for the long-term safety assessment in the following areas:

i.   Behaviour of spent nuclear fuel (SNF) and forms of radioactive waste (RAW) not acceptable for surface repositories in deep geological repository environments.

ii. Behaviour of waste packages (WP) of SNF and RAW in deep geological repository environments.

iii. Behaviour of buffer, backfill, and other structural materials in deep geological repository environments.

iv. Configuration and construction of repository boreholes and their influence on the properties of the surrounding rock environment.

v. Behaviour of the rock environment.

vi. Transport of radionuclides from the repository.

vii. Other characteristics of sites potentially affecting storage safety.

The aim of the sub-project entitled "Testing of transport models using foreign in-situ experiments" is to validate conceptual and computer models of the transport of radionuclides, created in GoldSim and Flow123d, or others, using data provided from foreign underground laboratories, in particular those available for "Task 9" in the GWFTS project.

The aim of this report is to summarise the results for the whole solution period and to evaluate the benefits for the Czech DGR programme and the applicability of models and experimental experience in future SÚRAO projects.

1.4 List of abbreviations

These abbreviations are used in this report:

BDZ	Borehole disturbed zone
CTU	Czech Technical University
DFN	Discrete fracture network
EDZ	Excavation disturbed zone
F123	Flow123d
GS	GoldSim
GWFTS	Groundwater Flow and Transport of Solutes
DGR	Deep geological repository
IB	Injection borehole
LTDE-SD	Long Term Sorption Diffusion Experiment
MB	Monitoring borehole
BC	Boundary conditions
PEEK	Polyetheretherketone
RAW	Radioactive waste
REPRO	REtention PROperties
SKB	Swedish Nuclear Fuel and Waste Management (Svensk kärnbränslehantering)
SA	Safety assessment
SNF	Spent nuclear fuel
SÚRAO	Radioactive Waste Repository Authority (Správa úložišť radioaktivních odpadů)
TF	Task Force
TDE	Through Diffusion Experiment
TUL	Technical University of Liberec
WPDE	Water Phase Diffusion Experiment

2 Simulation software and calculation methods

2.1 Flow123d

Investigators from TUL used their own software Flow123d (TUL 2015). Flow123d is used to simulate groundwater flow and transport of solutes and heat in a fractured and porous media. The originality of this software lies in the support of computations on complex networks consisting of simplex elements of various dimensions. This makes it possible to combine equivalent continuum models with discrete fracture network models (Figure 2-1).

The current version includes a mixed-hybrid solver for steady and unsteady Darcy flow, a finite-volume model and a model implementing the discontinuous Galerkin method for the transport of mass and heat (advection, diffusion/conduction, dispersion). Using the operator splitting, the software supports models of various local processes including dual porosity, sorption, decay and simple chemical reactions.

Calculations may be run in parallel using an MPI (message parsing interface) with scalability up to hundreds of processors. The input interface based on the JSON file format allows the specification of general spatial and temporal data for any physical parameter. The program supports outputs in GMSH and VTK formats.

The project development website is http://flow123d.github.io/. The simulations described in this report were implemented sequentially in versions 1.8.3. (Tasks 9A, 9B, 9C), 2.2.0 (9D-1), 3.0.1. (9D-2).

The most important parts of the model (relevant to the simulations of the experiments in this report) will be briefly described in the next few paragraphs.

Calculations of steady and unsteady flow in porous and fracture environments are described by Darcy's equation and a continuity equation. Currently, three types of boundary conditions (Dirichlet, Neuman and Robin) are supported as a tool for obtaining a unique solution. The principle unknowns are pressure head and flow.
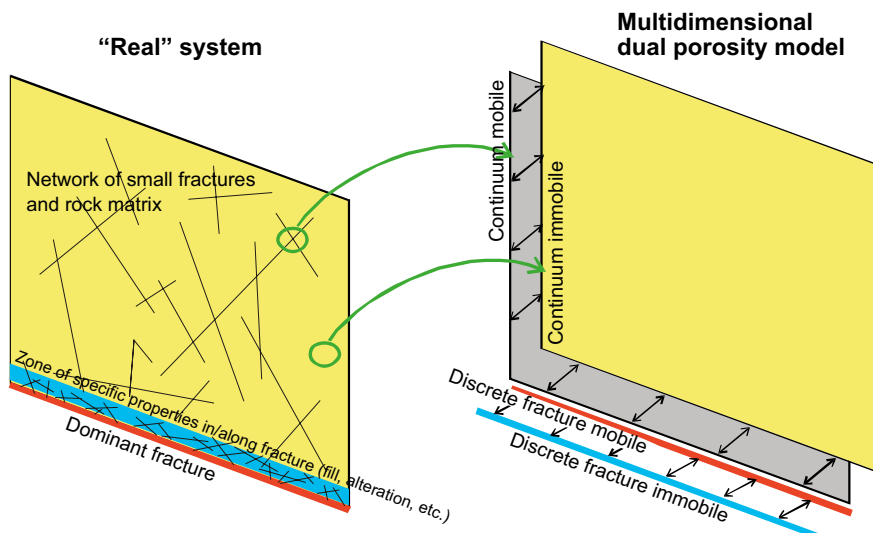
Figure 2-1. *Illustration of the importance of connecting sub-regions of different dimensions in the transport model used in Flow123d.*

The movement of solutes is controlled by advection and hydrodynamic dispersion. The process is described by the following system of mass balance equations:

$$\partial_t(\delta_d \vartheta c^i) + div(\boldsymbol{q} c^i) - div(\vartheta \delta_d \boldsymbol{D}^i \nabla c^i) = F_S^i + F_C^c + F_R(c^1, \ldots, c^s). \tag{2-1}$$

The principal unknown is the concentration c^i [kgm^{-3}] of the substance $i \in \{1, \ldots, s\}$, which is the mass of the substance in a unit volume of water. Other variables are:

- Porosity ϑ [-], i.e. the ratio of the volume filled with water to the total volume.

- The hydrodynamic dispersion tensor $\boldsymbol{D}^i$ [m^{2}s^{-1}] has the form:

$$\boldsymbol{D}^i = D_m^i \tau \boldsymbol{I} + |\boldsymbol{v}| \left(\alpha_T^i \boldsymbol{I} + \left(\alpha_L^i - \alpha_T^i \right) \frac{\boldsymbol{v} \otimes \boldsymbol{v}}{|\boldsymbol{v}|^2} \right), \tag{2-2}$$

  which represents (isotropic) molecular diffusion and mechanical dispersion in the longitudinal and transverse directions in relation to the flow direction. Here, D_m^i [m^{2}s^{-1}] is the molecular diffusion coefficient of the i-th substance, t $= \vartheta^{1/3}$ is a geometric factor (referred to as tortuosity in the documentation and certain literature), α_L^i [m] and α_T^i [m] they are longitudinal or transverse dispersivity. Finally, $\boldsymbol{v}$ [ms^{-1}] is the microscopic velocity of water whose relationship to Darcy's flow $\boldsymbol{q}$ It is determined by $q = \vartheta \delta \boldsymbol{v}$, where δ_d [m^{3-d}] is the cross-section coefficient (fracture aperture or cross-sectional area of a channel according to the domain dimension d).

- F_S^i [kgm^{-d}s^{-1}] represents the density of the concentration sources in the porous media.

- F_C^c [kgm^{-d}s^{-1}] represents the density of the concentration sources given by the exchange between regions of different dimensions.

- $F_R(\ldots)$ [kgm^{-d}s^{-1}] is the reaction term (double porosity, sorption, radioactive decay).

The Flow123d model described above allows two different approaches to the solution of the transport task:

- To simulate pure advection ($\boldsymbol{D} = 0$), it is advisable to choose a transport model using an operator splitting method that represents a finite-volume solver explicit in time. The solution is faster for one calculation step, but the maximum time step is limited. The resulting concentration is constant in parts on the mesh elements. This solver supports the reaction term (including simple chemical reactions, double porosity and sorption).

- The full model containing diffusion (dispersion) is solved by the discontinuous Galerkin method (implicit in time). The method does not impose any restrictions on the time step calculation. Approximation in space is polynomial in parts, currently up to the third order. The reaction term is implemented only for linear sorption:

$$F_R^i = -\partial_t \left((1 - \vartheta) \delta M^i \rho_s c_s^i \right), \ c_s^i = \frac{k_l^i}{\rho_l} c, \tag{2-3}$$

where c_s^i [mol kg^{-1}] is the concentration of the sorbed substance, k_l^i [mol kg^{-1}] is the sorption coefficient, ρ_s and ρ_l [kgm^{-3}] are the densities of the solid phase (rock) or the liquid phase (solvent). M^i [kg mol^{-1}] represents the molar mass of the i-th substance. The initial solid phase concentration is considered to be in equilibrium with the liquid phase concentration.

A more detailed description of the mathematical model used in Flow123d can be found on the project development website mentioned above.

2.2 GoldSim

Two approaches can be used in GoldSim (GoldSim 2014) to solve radionuclide migration tasks. The first approach is based on modelling the transport area using finite volumes represented by the Cell Pathway component in GoldSim. An overview of the methodology is given in Section 2.2.1. The second approach is based on discrete fracture modelling of the area, which is represented in GoldSim by the Pipe Pathway component, an overview of the methodology is given in Section 2.2.2. One or both procedures were applied to the individual tasks by investigators from ÚJV and CTU.

2.2.1 Methodology of the solution using Cell Pathway with regard to possibilities of interconnection of objects of this type within Cell Net

The volumetric approach divides the area of interest into elementary volumes, which are called Cell Pathway in GoldSim. The whole area is then represented by a network of interconnected cells (Cell Net). The mass of the radionuclide in one cell can be varied both by diffusion and/or advection transport between adjacent cells and by radioactive decay of the radionuclide itself, or the parent radionuclide present in the cell. The basic mass balance equation of the i-th cell can be written in the following form (GoldSim 2014):

$$\frac{dm_k^i}{dt} = -m_k^i \lambda_k + m_p^i \lambda_p \frac{A_k}{A_p} + \sum_{c=1}^{NF^i} f_k^c , \qquad (2\text{-}4)$$

where index k indicates the daughter and index p the parent radionuclide, m_k^i [M] is the mass of radionuclide in the i-th cell, t [T] is time, $\lambda_{k,p}$ [T^{-1}] are decay constants and $A_{k,p}$ [M/mol] are the atomic mass, f_k^c [M/T] indicates the inlet speed with c-th transport connection to the i-th cell and NF^i is the number of transport pathways to/from the i-th cell. In the case of advective transport connection from the i-th to j-th cell it is defined as

$$f_{i \to j}^A = q_{i \to j} c_k^i , \qquad (2\text{-}5)$$

where $q_{i \to j}$ [L^3/T] is the volume velocity of the liquid phase and c_k^i [M/ L^3] is the concentration of the k-th radionuclide in the liquid phase of the i-th cell. The rate of diffusion flow from the i-th to j-th cell is defined as

$$f_{i \to j}^D = D_k^{i,j} \left(c_k^i - c_k^j \right) , \qquad (2\text{-}6)$$

where $D_k^{i,j}$ [L^3/T] is the diffusion conductivity between the i-th and j-th cell, which is calculated as

$$D_k^{i,j} = \frac{A^{i,j}}{\frac{\Delta x_i}{D_e{}^i} + \frac{\Delta x_j}{D_e{}^j}} , \qquad (2\text{-}7)$$

where $A^{i,j}$ [L^2] is the diffusion surface, $\Delta x_{i,j}$ [L] is the diffusion length in the i-th or j-th cell. $D_e{}^{i,j}$ [L^2/T] indicates the effective diffusion coefficient of a porous material in a cell that is equal to $D_e = \varepsilon G D_f$, where ε is the porosity of the material and G is a geometric factor (Note: GoldSim incorrectly indicates G as tortuosity τ, whereas the known relationship $G = \delta/\tau^2$ applies, were δ is constrictivity).

The cell acts as an ideal mixing reactor in which an instantaneous equilibrium between the liquid and solid phases occurs. If the solubility limits are neglected, the concentration c_k^i in the liquid phase is calculated as

$$c_k^i = \frac{m_k^i}{K_{d,k}^i M^i + V^i} , \qquad (2\text{-}8)$$

where $K_{d,k}^i$ [L^3/M] is the distribution coefficient if the k-th radionuclide in the i-th cell, whose mass is M^i [M], V^i [L^3] indicates the volume of the liquid phase in the i-th cell.

In order to solve Equation (2-4) for the whole network of cells, GoldSim first identifies the subnets of cells interconnected by transport, and solves the evolution of these subnets separately. The radionuclides that are part of the decay series are also interconnected. Therefore, GoldSim constructs a separate set of differential equations from Equation (2-4) for each decay series of cell subnets, which can be written in matrix form as

$$\mathbf{m}' = [\mathbf{D} + \mathbf{T}]\mathbf{m}, \qquad (2\text{-}9)$$

where $\mathbf{m}$ [M] is vector of the radionuclide mass of the decay series, $\mathbf{m}'$ [M/T] is the velocity vector of the change in the radionuclide mass of the decay series, $\mathbf{D}$ [1/T] is a matrix containing decay and incremental coefficients, $\mathbf{T}$ [1/T] is a matrix containing transport coefficients. GoldSim uses the Euler implicit method (Press et al. 2007) for the system of differential equations, see Equation (2-9), which is solved for the time step Δt as

$$\mathbf{m}(t + \Delta t) = [\mathbf{I}\text{-}\mathbf{D}\Delta t - \mathbf{T}\Delta t]^{-1}\mathbf{m}(t), \qquad (2\text{-}10)$$

where $\mathbf{I}$ indicates the unit matrix and the operation^{-1} with matrix inversion. If the solubility limits are not considered, the matrix Equation (2-10) is linear. GoldSim uses a modified version of the Iterative Methods Library IML++, version 1.2a, available on the National Institute of Standards website at http://math.nist.gov/iml++/ (GoldSim 2014).

To increase the precision of the implicit Euler method, GoldSim automatically divides the time step depending on the precision of the calculation selected by the user. Calculation accuracy (high, medium, low) can be set in the Contaminant Transport tab of the dialogue box Model | Options. However, it should be noted that the implicit Euler method is stable, the division of time steps only provides a more accurate solution (Press et al. 2007).

GoldSim provides a special element, called CellNet Generator, to automate the creation of the cell net. CellNet Generator allows you to create a two-dimensional grid of cells representing a rectangular or cylindrical region including advective or diffuse transport connections (Figure 2-2). The number of cells in a rectangular net of cells is defined by the X, Y coordinates and thickness. The X and Y coordinates can either equidistantly divide the total length and width of the area or can be entered by the user. The number of the cells in the cylindrical net is defined by the axial Z and radial R coordinates, and the angle which may be from the interval (0°, 360°) (a 360° angle belongs to the whole cylinder). As in the case of the rectangular grid, the Z and R coordinates can either equidistantly divide the total length and radius of the cylindrical region, or they can be entered by the user.

It is possible to model zones with different characteristics within one network of cells. To do this, it is first necessary to define the properties of the individual zones (e.g. liquid and solid phase, Darcy's velocity, etc.) and then use the graphical interface to specify the subnet of the cell network where the zone is located. When all of the properties of the modelled region are specified, CellNet Generator generates a cell network. CellNet Generator allows you to create a network of cells with a maximum of 9 801 cells (99 × 99). For a larger number of cells, it is necessary to increase the maximum limit for GDI objects (at least 50 000, the maximum possible value is 65 536) in the Windows operating system.

2.2.2 Methodology of the solution using Pipe Pathway

The default option for modelling transport tasks combining advection with matrix diffusion is the Pipe Pathway component, which is a "chromatographic column" where liquid along with the studied substances (contaminants, radionuclides) flows in on one side of the component, flows through the component and flows out at its end. The temporal change in concentration in the mobile zone of the i-th component of the Pipe Pathway, $^F C_k^i$ [M/L³], is described by a second order partial differential equation, which can be expressed as:

$$\frac{\partial ^F C_k^i}{\partial t} = -\frac{Q_k^i}{^F S^i \, ^F R_k^i} \frac{\partial ^F C_k^i}{\partial z} + \frac{\alpha^i Q_k^i}{^F S^i \, ^F R_k^i} \frac{\partial^2 \, ^F C_k^i}{\partial z^2} - \lambda_k \, ^F C_k^i + \frac{P^i \, ^G D_{w,k} \, ^G \delta \, ^G \varepsilon}{^F S^i \, ^F R_k^i} \frac{\partial ^G C_k^i}{\partial x}, \qquad (2\text{-}11)$$

where the members in the sum on the right side represent, sequentially, advection and dispersion (in the direction of the z axis), radioactive decay, and diffusion and sorption perpendicular to the fracture wall in the rock mass (indicated as direction x). Q_k^i [L³/T] is the volume flow of water in the mobile zone of the i-th component of Pipe Pathway, $^F S^i$ [L²] indicates the transverse surface (relative to the flow direction) of the mobile zone of Pipe Pathway and $^F R_k^i$ is the radionuclide retardation factor of the k-th radionuclide, α^i [L] indicates the dispersion, P^i [L] is the wetted circumference of Pipe Pathway, $^G D_{w,k}$ [L²/T] is the diffusion coefficient of the k-th radionuclide in free water, $^G \delta$ is a geometric factor and $^G \varepsilon$ is the porosity of the rock, and finally $^G C_k^i$ [M/L³] indicates the concentration of the k-th radionuclide in the rock mass, whose evolution is governed by the equation

$$\frac{\partial ^G C_k^i}{\partial t} = \frac{^G D_{w,k} \, ^G \delta}{^G R_k^i} \frac{\partial^2 \, ^G C_k^i}{\partial x^2} + \frac{^G D_{w,k} \, ^G \delta}{^G S^i \, ^G R_k^i} \frac{\partial ^G S^i}{\partial x} \frac{\partial ^G C_k^i}{\partial x} - \lambda_k \, ^G C_k^i, \qquad (2\text{-}12)$$

where the first two members on the right correspond to diffusion with sorption, and the third member describes the radioactive decay. $^G S^i$ [L] is the diffusion surface per unit length and $^G R_k^i$ is the retardation factor whose value is defined as

$$^G R_k^i = 1 + \frac{^G \rho \, ^G K_{d,k}}{^G \varepsilon}, \qquad (2\text{-}13)$$

where $^G \rho$ [M/L³] is the density of the rock in the dry state, and $^G K_{d,k}$ [L³/M] is the partition coefficient of the k-th radionuclide in the rock. Pipe Pathway uses a numerical Laplace transform to solve Equations (2-11 and 2-12).
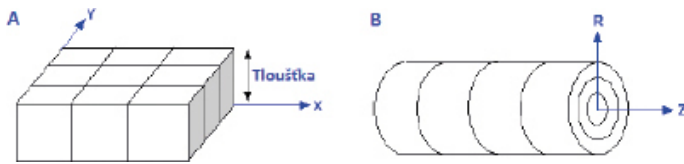
Figure 2-2. *Schematic representation of the rectangular (A) and cylindrical (B) geometry of the cellular network. Taken and modified from GoldSim (2014).*

The following processes may occur inside a component:

- 1D advective flow,
- longitudinal dispersion,
- longitudinal diffusion,
- retardation,
- conversion of radionuclides,
- exchange between mobile and immobile zones (diffusion into the rock matrix).

The component is defined by the following parameters:

- length,
- flow area,
- wetted circumference,
- dispersion,
- presence of a layer where diffusion into the rock matrix takes place.

2.2.3 Importance of the porosity fraction in GoldSim

The GoldSim program also uses the porosity fraction parameter. This expresses the limited availability of pores for the contaminant studied and is calculated from the porosity of the material and the effective porosity. The fraction of porosity is given by:

$$f_{m,s} = \frac{D_{f,m,s}}{n_m \cdot t_m \cdot d_f \cdot d_{f,s}} = \frac{D_{f,m,s}}{n_m \cdot t_m \cdot d_f \cdot \dfrac{D_{f,s}}{d_f}} = \frac{D_{f,m,s}}{n_m \cdot t_m \cdot D_{f,s}} , \qquad (2\text{-}14)$$

where:

d_f reference diffusion coefficient of contaminant s and carrier medium f, [$L^2 \cdot T^{-1}$],

$D_{f,m,s}$ effective diffusion coefficient of contaminant s in the mobile zone (D_e),

$D_{f,s}$ diffusion coefficient of contaminant s, in carrier medium f, at an infinite dilution, (for water also $D_{w,s}$), [$L^2 \cdot T^{-1}$],

$d_{f,s}$ relative diffusion coefficient of contaminant s, in carrier medium f, at an infinite dilution, [-],

$f_{m,s}$ porosity fraction of material m available for contaminant s [-],

n_m porosity of material m [-],

t_m geometric factor of material m [-], t_m lies in the half-open interval (0, 1] (GoldSim 2014) and is given as the cube root of the porosity.

2.3   ConnectFlow/NAPSAC

The NAPSAC program for mathematical modelling of flow and transport in a discrete fracture network (DFN concept) is part of the ConnectFlow software package (Hartley 1998, Wood 2018). ConnectFlow includes two modelling programs, NAMMU and NAPSAC. NAMMU is an equivalent continuum concept (ECPM) application and NAPSAC works with the concept of a discrete fracture network (DFN). ConnectFlow also allows you to combine simulations made by NAMMU and NAPSAC to create a very flexible application that allows for modelling in fracture and porous environments at different scales. The modelling is based on the mathematical formulation of the problem by the numerical finite element method. For the mathematical modelling of the solved task, PROGEO used the NAPSAC program for generating micro-fracture DFNs and the NAMMU program for their upscaling and transfer to a continuous rock matrix environment in CPM.

The NAPSAC/NAMMU programs have been developed over the last 30 years (formerly AEA Technology, Serco Assurance, AMEC and currently WOOD) and verified internationally (e.g. SKB, STRIPA mine, TRUE site, etc.). They also meet international quality standards ISO 9001 and TickIT.

NAPSAC allows modelling of the following geological aspects of the rock environment:

- Modelling of fractures over a wide range of scales, from heterogeneous single fracture modelling to modelling of millions of fractures on a regional scale.

- Generation of regular and irregular networks and structural grids to characterise geological characteristics.

- Generation of individual stochastic fractures and fracture sets based on various geostatistical probabilistic distribution functions.

- Insertion of a deterministic fracture or fractures into a stochastic fracture set.

- Use of deterministic fractures for controlled generation of stochastic fractures populations.

- Determination of mutual correlation of parameter pairs, combining some parameters into one property, e.g. length-aperture relationship.

- Import the areal or spatial distribution of fractures from external sources and data grids based on parameters such as lithology, deformation or thickness.

- Formation of dynamic fractures and analysis of current stress.

- Simulation of any scale range, from values obtained from the drill core to continental scale observations.

The NAPSAC program allows you to:

- Simulate stationary or transient flow in the fracture network.

- Perform stationary simulations in a very large fracture network due to an effective computational numerical method.

- Calculate a fully continuous permeability tensor, including the main values and directions, which allows changes in scale, analysis of the dependence on scale and representative elementary volume determination.

- Calculate porosity and size of rock matrix blocks between fractures.

- Calculate stationary and transient inlets into tunnels and mine workings.

- Calculate the effect of hydromechanical coupling (mutual dependence of parameters). The hydraulic expansion is dependent on the pressure distribution based on the analytical description of the pressure field resulting from the overburden or radial stress around the tunnel.

- Simulate the transport of the tracer through the fracture network using the stochastic particle tracking method, which can be used to calculate the dispersion of solutes transported by groundwater.

- Simulate mass transport for variable density fluid.

- Simulate unsaturated flow in a fracture environment.

2.4   MT3DMS

MT3DMS (Zheng and Wang 1999, Zheng 2010) or MT3D USGS (Bedekar et al. 2016a, b) is a modular three-dimensional transport model developed in 1990 to simulate the movement of a solute under the hydrogeological conditions of a continuous porous environment – CPM concept. Originally referred to as MT3D (modular 3-D transport model), it has been expanded to include a number of reaction packages to simulate multi-component mixtures. The current version MT3DMS (MS designates multi-species and can also simulate the transport of multi-component solutions and mixtures of substances) is able to simulate the movement of substances in groundwater caused by advection, dispersion, diffusion and various chemical reactions. The program was used by investigators from PROGEO.

MT3DMS was developed for use with any groundwater flow model using a finite difference method with a block centralised grid (e.g. MODFLOW model). The MT3DMS program is based on the assumption that changes in the concentration field do not have a significant effect on the calculation of the flow field (i.e. this program is not designed for multi-phase flow of substances with different densities). After assembling and calibrating the hydraulic model (after calculating the flow field), it is necessary to prepare the input data of the transport model, which are then read during the transport simulation. Transport is therefore solved by MT3DMS independently of the calculation and calibration of the flow model.

MT3DMS contains three computational mechanisms of transport solution in one code:

*   Standard finite difference method.

*   Particle-tracking method based on the Euler-Lagrange method.

*   TVD (total-variation-diminishing) method of finite differences of higher order.

MT3DMS can be used to simulate changes in solute concentrations in groundwater with different types of boundary conditions and external sources or sinks. MT3DMS can help solve the spread of dissolved pollution (solutions) by including all basic transport processes in the solved equations:

*   Advection – transport of the solute at the same speed as the flowing groundwater described by the advection element of the transport equation.

*   Dispersion (hydrodynamic dispersion) as the sum of mechanical dispersion and molecular diffusion.

*   Basic chemical reactions – linear or non-linear equilibrium sorption, rate-limited sorption, first-order reactions representing radioactive decay or biodegradation (more sophisticated chemical reactions can be simulated using special packages, e.g. RT3D).

*   Point or area source and sink elements (inlet/outlet of water of defined concentration, dissolution of substances, etc.).

MT3DMS allows the conceptualisation of solute transport in a fractured or highly heterogeneous environment using a system consisting of two different environments (dual-domain). The dual-domain concept replaces the effective porosity value that characterises the inhomogeneous porous environment in the computational cell, with two porosity values separately for the mobile (preference zone with dominant advection flow) and immobile domain (low permeability matrix with dominant diffusion). The transfer of substances between the mobile and immobile domains is made possible by the mass transfer coefficient. The dual-domain advection-diffusion model may be more suitable for modelling transport in a fractured environment or a strongly heterogeneous porous environment than the classical advection-dispersion model. Of course, assuming that both the porosity values and the mass transfer coefficient in the computational cells can be appropriately characterised.

3 Solution of task WPDE (Task 9A)

3.1 Summary of the task description and input data

The subject of the WPDE experiment at the ONKALO underground laboratory in Finland is to monitor the diffusion of radionuclides into the rock matrix with transport by advection in the fracture, which is imitated by a slot between the wall of a borehole and an inserted cylinder (Figure 3-1, Löfgren and Nilsson 2019). Only the concentration in the drainage outlet pipe (breakthrough curve) is measured, without analysis of rock samples.

The model task proposed in the task description conceptually simplifies the experiment as follows (Figure 3-2):

- Uniform flow through the cylindrical slot with the assumption of ideal mixing in the radial direction, which leads to the axially symmetrical role of diffusion into the rock.

- The rock is homogeneous within differentiated PGR and VGN blocks (with different parameters).

- Inlet and outlet pipes are included as time delay or with a dispersion effect.

The main input parameters of the model are rock porosity, effective diffusion coefficient in the rock, free water diffusion coefficient of each radionuclide, a distribution coefficient of linear sorption of each radionuclide, and longitudinal dispersivity in the fracture. The capacity factor for chlorine Cl-36 was determined experimentally, and expresses the assumed anion exclusion (which implies a different method of data input for the individual software programs and investigators). The data compiled from the task description (Löfgren and Nilsson 2019) and other literature are shown in Table 3-1 and are also included in Table 3-7 below extended by uncertainty intervals in Section 3.4. The porosity was derived on the basis of Table 2-8 in the task description (as the arithmetic mean for each rock type). Effective diffusivity for both rock types was partly taken from Table 2-9 of the task description (Löfgren and Nilsson 2019). Values for Na-22, Sr-85 and Ba-133 were not included in the task description. Their sources are also shown in Table 3-1. Linear sorption coefficients were taken from Table 2-11 of the task description (Löfgren and Nilsson 2019).
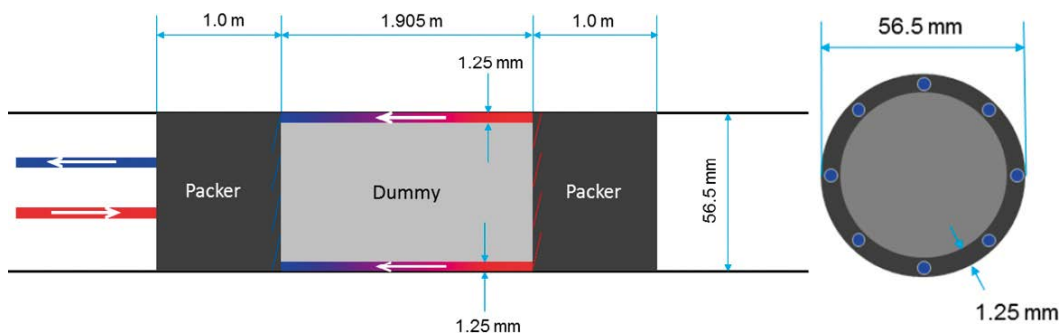
Figure 3-1. Configuration diagram of the WPDE experiment, which is modelled in step 9A (the solution is described below in this report) (Löfgren and Nilsson 2019).
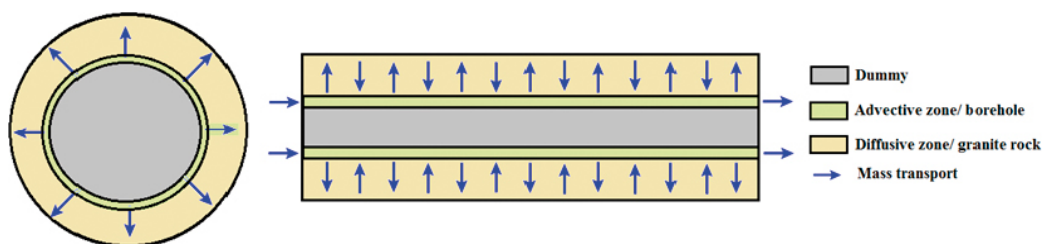
Figure 3-2. Conceptual model of radionuclide transport in the WPDE experiment for Task 9A.

Table 3-1. **Transport parameters considered in the mathematical model that are common to all three models (calculations in Section 3.3). The free water diffusion coefficient (reference) differs in other models and is given in the relevant sections. The source is given for the values not specified in the task description.**

Nuclide	K_d VGN [m³/kg]	K_d PGR [m³/kg]	D_e VGN [m²/s]	D_e PGR [m²/s]	D_w [m²/s]		Porosity VGN [-]	Porosity PGR [-]	Bulk density [kg/m³]	Half-life [a]
H-3	0	0	1.83E−13	5.70E−13	2.30E−09		8.20E−03	5.00E−03	2.70E+03	1.23E+01
Na-22	1.30E−03	8.00E−04	4.65E−13 (POSIVA-97-07)		1.33E−09	Vanýsek (2009)	8.20E−03	5.00E−03	2.70E+03	2.60E+00
Cl-36	0	0	5.00E−15	5.00E−13	2.03E−09		8.20E−03	5.00E−03	2.70E+03	3.01E+05
Sr-85	1.10E−03	1.10E−03	3.30E−13 (Skagius et al. 1999)		7.91E−09		8.20E−03	5.00E−03	2.70E+03	1.78E−01
Ba-133	6.00E−02	8.00E−02	1.47E−13 (Widestrand et al. 2007)		5.41E−10		8.20E−03	5.00E−03	2.70E+03	1.05E+01
Note	In the Cell model under the Solid element		In the Cell model under the Fluid element		RN resolution only for Goldsim-Pipe		In the Goldsim Cell model under the Solid element			Flow123d not used

Other parameters are the spatial and temporal data of the experiment, summarised in Table 3-2 and Table 3-3. The specific geometry in relation to the conceptual model differs according to the type of numerical solution. In fact, it differs in size in the radial direction, i.e. the affected rock volume.

The experiment was performed in two variants ((Table 3-2), WPDE-1 with faster flow and a shorter execution time, with three radionuclides, and WPDE-2 with slower flow and a longer time, with five radionuclides. A list of radionuclides with their injected amount is included in Table 3-4.

Table 3-2. Time constants of the experiments and transport model.

	WPDE-1	WPDE-2
Duration of the experiment (and simulation)	8 760 h (1 year)	17 520 h (2 years)
Length of injection	50 min	5 h
Flow of liquid	20 µl/min	10 µl/min
Delay in the inlet pipe	16 h	32 h
Delay in the outlet pipe	17 h	34 h

Table 3-3. Geometry of the individual parts of the transport pathway (rock sections VGN2, PGR1, VGN1 are given in the direction of transport, i.e. from the furthest end of the borehole to the mouth).

	Inlet pipe	VGN2	PGR1	VGN1	Outlet pipe to the detector	Outlet pipe to collection device
Length [m]	24.2	1.41	0.15	0.35	25.7	4.6
Flow area [m^2]	7.85E−07	2.17E−04	2.17E−04	2.17E−04	7.85E−07	7.85E−07

Table 3-4. Injected activity of radionuclides in experiments WPDE_1 and WPDE_2.

Radionuclide	Activity of WPDE_1 [Bq]	Activity of WPDE_2 [Bq]
H-3	1.71E+07	3.11E+07
Na-22	1.38E+06	2.04E+06
Cl-36	1.25E+06	5.09E+06
Sr-85		4.12E+06
Ba-133		2.46E+06

The required output of the calculations are breakthrough curves, i.e. time courses of concentrations of radioactive tracers. These are expressed for ease of comparison as activity flow normalised by total injected activity (dimension 1/time). In addition, dimensional parameters of the breakthrough curve graph (height and position of selected points) are determined. Radioactive decay was not part of the simulation – results are supposed to be compared with experimental results corrected for decay back to the start of the experiment according to the task description.

The task description (Löfgren and Nilsson 2019) and the templates provided for the results tables included a calculation of sensitivity and uncertainty. However, the specific meaning of the terms was not given and was left to the investigators' discretion. Therefore, a largely unified approach was also agreed upon among the Czech investigators (Section 3.4).

Sections 3.2 and 3.4 describe in detail the methodology of the solution and a comparison of the results between Czech institutions for uniformly of the entered inputs.

3.2 Implementation of the model solution

The common parameters for the models were presented in the previous section. The specific ways of using this data for specific software programs, as well as deviations from the conceptual models on which the software is based, are described below. Use by individual investigators was as follows: ÚJV – GS Pipe pathway, CTU – GS Cell Net, TUL – Flow123d and PROGEO – MT3D.

3.2.1 Solution using GoldSim Pipe pathway

The Pipe Pathway component was used in all of the monitored parts of the system for the solution of the task, i.e. both for the simulation of processes in the rock environment and for the inlet the tracer from its source to the part defined by the obturator and subsequent outlet of the tracer to the collection device. Only the collection device itself is simulated by the Cell Pathway component.

The transport pathway of the tracer was divided into several parts, where the individual parts differ in the considered transport processes (Figure 3-3):

- Inlet pipe.
- Rock environment formed by rock type VGN (divided into two parts).
- Rock environment formed by rock type PGR.
- Detector outlet pipe.
- Outlet pipe to the collection device.

Advective flow was considered in all parts of the transport pathway. In addition, the transport processes of dispersion and matrix diffusion were considered in the parts formed by the rock environment (parts VGN1, VGN2 and PGR1) (Table 3-5). The dispersion process can also occur in the inlet and outlet pipes, but in the first calculations these processes were not considered for the purpose of comparing the results of the individual investigators. Therefore, the radionuclides are propagated through the advection pipe, their transport in the part defined by the obturator proceeds further due to advection and partly due to dispersion and molecular diffusion. Due to the dispersion, the radionuclide concentration disperses in the flow direction, and due to molecular diffusion, diffusion into the rock matrix occurs where the radionuclide is captured and subsequently released back to the liquid flow field in the slot between the borehole wall and the obturator based on the concentration gradient (Figure 3-2). Thereafter, the radionuclides are discharged through an outlet pipe into a pipe directed towards the collection device, and the transport process in these pipes is again advection. The longitudinal dispersion was considered to be 1/10 of the scale of the problem (length of the transport pathway), a diffusion zone thickness of 1 m was prescribed. The geometry of the individual parts is given in Table 3-3.

Table 3-5. Representation of the transport processes considered in individual parts of the transport pathway.

Part of the system	Inlet pipe	VGN2	PGR1	VGN1	Outlet pipe to the detector	Outlet pipe to collection device	Collection device
Considered processes	Advection	Advection	Advection	Advection	Advection	Advection	Balancing concentration
		Dispersion	Dispersion	Dispersion			
		Matrix Diffusion	Matrix Diffusion	Matrix Diffusion			
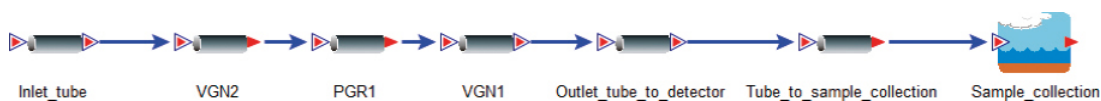
Figure 3-3. *Division of the transport pathways into individual parts according to their geometry and the processes considered within them.*

The following parameters of transport processes were considered in the mathematical model (Table 3-1):

- K_d as a sorption parameter, a linear sorption isotherm was considered.
- D_e and D_w as parameters of matrix diffusion, they are essential for calculating the porosity fraction, i.e. the porosity that actually participates in the transport of radionuclides (Section 2.2.3).
- Porosity as a parameter necessary to calculate the porosity fraction and geometric factor/tortuosity.
- Bulk density.
- Half-life.

The flow in the inlet pipe and the activity of the monitored radionuclides, whose value differed according to the simulated experiment, were prescribed as boundary conditions. (Table 3-2, Table 3-4).

3.2.2 Solution using GoldSim Cell Net

Migration of the tracer in the WPDE1-2 experiments may be divided into a section where only dispersion advection (transport through the inlet and outlet PEEK pipes) took place, and a section where the dispersion advection was accompanied by diffusion with sorption into the rock environment (transport through the slot in the surrounding rock environment and into the rock). This transport may also be modelled in GoldSim using Pipe Pathway. The rock environment, however, exhibits heterogeneity, which can affect the course of the transport, and Pipe Pathway is intended more for modelling transport in a homogeneous environment. Therefore, it was proposed to test the model of the slot and the rock environment using a network of cells, which makes it possible to model the heterogeneity of rock environment properties using a relatively simple procedure. One of the aims of this work was to test whether a simplified model of the WPDE1-2 experiments, equivalent to one Pipe Pathway element, could be represented using a network of cells.

Figure 3-4 schematically depicts a conceptual model of the WPDE1-2 experiments (full description in the previous Section 3.1 and report Löfgren and Nilsson 2019). The inlet and outlet PEEK pipes modelled using two Pipe Pathways are identified as PipeInlet and PipeOutlet in the model. Their basic parameters are shown in Table 3-3. The axial dispersion in these first pipes is 1/10 in length, i.e. 2.42 m. The slot and the surrounding rock were modelled using a network of cells with cylindrical geometry. The Cell Net network was divided into three zones, two zones modelling VGN and PGR rocks and a third zone the slot with a flow of synthetic groundwater. In PipeInlet and PipeOutlet and in the cells representing the slot, only transport by advection with dispersion was considered. In the cells with rock only the diffuse transport in the pore water of the rock with sorption to the rock environment was implemented. The results of the simulations, the so-called breakthrough curves, were saved and are presented in the report for the output from PipeOutlet.
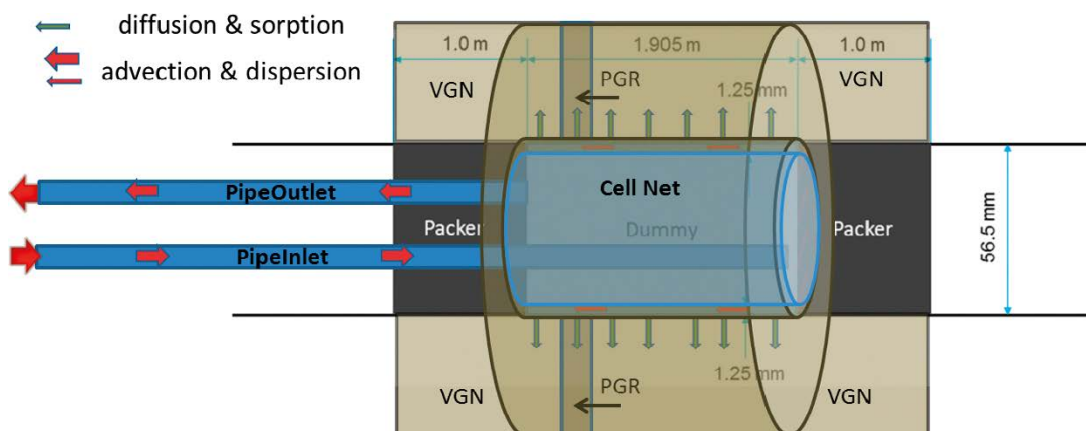
Figure 3-4. *Schematic representation of the conceptual model of the WPDE1-2 experiments in GoldSim – using a cell network for the rock and slot and two Pipe pathway elements (PipeInlet and PipeOutlet) for the inlet and outlet pipes.*

Injection of the tracer into the PEEK pipes was modelled using the Selector element. If the simulation time, marked as *ETime* in GoldSim, from [0;48.7] min (WPDE1) or [0;300] min (WPDE2), the input rate in PipeInlet (marked as Input Rate in GoldSim) was non-zero, calculated as: (total density of the tracer × liquid flow rate in the experiment) / injection loop volume. At other times of the simulation, the input rate to the PipeInlet element was zero, which corresponds to a constant flow rate of the synthetic groundwater without the tracer.

The slot between the rock and the inert material (marked as dummy in Figure 3-4), as well as the surrounding rock, was modelled using a network of cells. A cell network with a cylindrical geometry and an angle of 360° was selected. Three zones were defined, two zones represented two different types of rock, and the third zone represented a slot through which the synthetic groundwater with the tracer flowed. Both rocks were modelled using the *Solid* element whose parameters are included in the table common to all of the models (Table 3-1). In addition, a geometric factor corresponding to the GS parameter "Tortuosity" is specified and its value was set to 1 because it is only used in GS to convert effective diffusivity to relative diffusivity. In order to define different effective diffusion coefficients of both types of rock material, it was necessary to create two *Fluid* elements, whose parameters are also given in Table 3-1. The axial dispersion of the water flow in the slot was taken into account by increasing the reference diffusion coefficient of the *Fluid* element belonging to the whole of the slot, according to the relation $D_L = D_w + \alpha_L v_L$, where D_w [L2/T] is the reference diffusion coefficient, α_L [L] the axial flow dispersion and v_L [L/T] the flow rate. For D_w, a value of 2.3×10^{-9} m²/s was used for all of the radionuclides (corresponding to the value in the Pipe model for HTO). All of the important input parameters of the model were entered using the *Spreadsheet* element, which enables dynamic data exchange with a Microsoft Excel file.

When implementing the model in GoldSim using a cell network, it was necessary to optimise the stratification and the number of Z and R coordinates of the cell network so that the discretisation of the slot and the rock does not produce a significant numerical error in the results. The first calculations showed that a too-coarse network of cells around the slot leads to incorrect results for sorbing radionuclides (e.g. Na-22). Initial evaluation and comparison, among other things, with the analytical solution was part of the interim report (Hokr et al. 2015). This report presents the results with an optimised network.

3.2.3 Solution in Flow123d

The geometry consists of a 2D fracture and a 3D rock (divided into three parts according to the specifications in Section 3.1. According to the task description, a greater degree of heterogeneity of the rock matrix was not permitted in the blind prediction. The geometry is shown in Figure 3-5. The thickness of the rock in the default version is 0.1 m (in other variants it was increased). The discretisation of the geometry is shown in Figure 3-6 and Figure 3-7. The mesh has 720 2D elements representing the fracture and 12 096 3D elements representing the rock. The fracture is surrounded by two thin layers of matrix elements. Their presence makes the model results for the sorbent tracers significantly more accurate (see below).
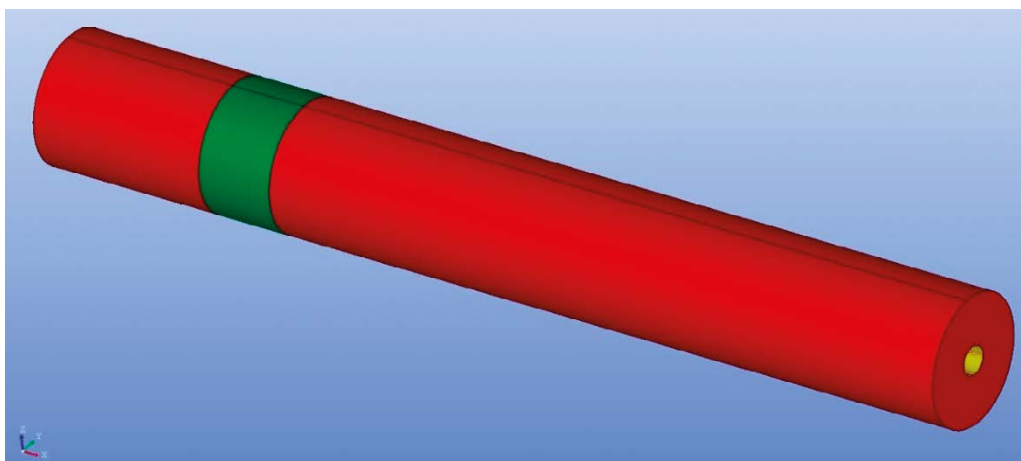
Figure 3-5. *Geometry of the WPDE model for the blind prediction. The red part represents the veined gneiss (VGN) and the green part represents the pegmatite granite (PGR).*
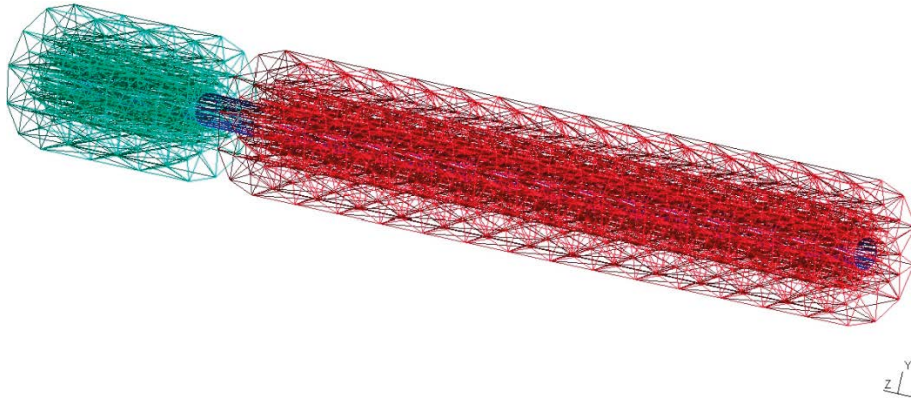
Figure 3-6. *Computational mesh of WPDE for the blind prediction (the PGR part is hidden in order to show the discretisation of the fracture).*
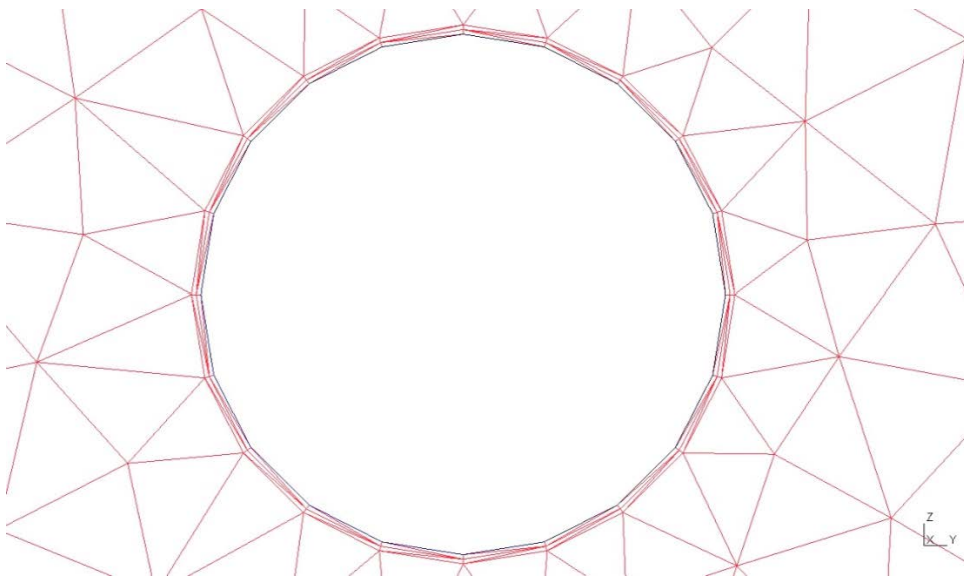
Figure 3-7. *Computational mesh of WPDE for the blind prediction – cross-section. Two thin layers of matrix elements around the fracture.*

The parameters of the flow model were calculated (or selected) so that the resulting flow rates corresponded to the flow rates in the experiment (20 µl/min for WPDE-1 and 10 µl/min for WPDE-2) and to comply with the task description (rock matrix permeability of about 10^{-19} m^2). They are shown in Table 3-6.

Table 3-6. Flow model parameters.

	WPDE-1	**WPDE-2**
Hydraulic conductivity of the fracture	1.28 m/s	1.28 m/s
Hydraulic conductivity of the rock	9.81e−13 m/s	9.81e−13 m/s
Boundary condition at x=0 m	Dirichlet Φ = 0 m	Dirichlet Φ = 0 m
Boundary condition at x=1.905 m (corresponds to the flow rate as specified by the experiment)	Neumann q = −1.536e−6 m/s	Neumann q = −0.768e−6 m/s
Remaining boundary conditions	Neumann zero flow	Neumann zero flow

The hydraulic conductivity of the fracture was calculated from its aperture by the cubic law:

$$K = \frac{\rho \cdot g}{12\mu} \cdot b^2,$$

where b is the aperture of the fracture [m], ρ is the density of water [kg/m^3], g is the acceleration of gravity [m/s^2] and μ is the dynamic viscosity of water [N·s·m^{-2}].

The hydraulic conductivity of the rock matrix was calculated from a known value of permeability κ [m^2] as:

$$K = \kappa \cdot \frac{\rho \cdot g}{\mu}.$$

The value of the Neumann boundary condition at the inlet part of the boundary was calculated as the ratio of the required flow through the fracture and the area of its cross-section (calculated as the area of the annulus). In the used version of Flow123d, the flow is always considered in the direction of the unit external norm, so there is a negative sign for the inlet value.

Three (WPDE-1) and five (WPDE-2) tracers were simulated. In the task description, injected activity [Bq] is given for each of the experiments and for each tracer. Furthermore, the volume of solution in which the tracers were dissolved (1 ml for WPDE-1, 3 ml for WPDE-2) was known. Since in Flow123d, the transported quantity is not activity but mass, it was first necessary to recalculate activity to mass [g] by dividing it by the specific activity a [Bq/g]:

$$a = \frac{\ln(2) \cdot N_A}{T_{1/2} \cdot M},$$

where N_A is the Avogadro constant, $T_{1/2}$ is the half-life [s] (tabulated in the task description) and M is the molar mass [g/mol].

Boundary conditions for the transport were prescribed on the inlet part of the fracture so that the injected amounts correspond to the task description.

The duration of injection was calculated from known quantities (tracer solution volume and flow rate). The zero time of the simulation period is when the injection of the tracer begins. Before entering the experimental section (fractures), the solution had to pass through a PEEK pipeline of known length and internal diameter from which the delay time was calculated. Therefore, in a model that includes only the experimental section, the boundary condition is only switched on at the time corresponding to this delay. An analogous delay also occurs at the outlet of the experimental section, in which case its timeline of the model outputs (breakthrough curves) is shifted by its value to be comparable with the experimentally measured data. Since neither the inlet nor the outlet piping is explicitly modelled, any dispersion therein is neglected in the simulation.

At the end of the injection, the boundary condition of the transport was switched to Dirichlet BC of a zero concentration. The simulation time constants are given in Table 3-2.

The material parameters of the model (coefficients in equations) are given in the common table with GoldSim models Table 3-1. In addition, a porosity value of 1 is specified for the elements of the fracture (free space) and lower values for Cl-36 as the equivalent of anion exclusion based on measured capacity factor data (Löfgren and Nilsson 2019), 1.75×10^{-4} for VGN and 0.013 for PGR.

Since the flow rate of the groundwater in the rock matrix is negligible, the hydrodynamic dispersion is considered only in the fracture. The longitudinal dispersion coefficient is considered to be 10 % of the characteristic length ($\alpha_L = 0.19$ m), and the transverse dispersivity coefficient is considered to be one tenth of the longitudinal ($\alpha_T = 0.019$ m). This is the only parameter of the model whose value is not supported by the measured data, hence the uncertainty of its input is large. In the fracture, an effective diffusivity of 10^{-9} m^2/s was considered, the same for all tracers (it was not entered, the chosen value is different from the GoldSim models, it has no effect on the dispersion).

The linear sorption coefficients used in the simulation are given in Table 3-1. Sorption is not considered in the fracture. The rock density was set at 2 700 kg/m^3 and the water density at 1 000 kg/m^3.

All of the described simulations of Task 9A were performed using SW Flow123d version 1.8.3.

The results of all three sorbent tracers looked significantly different in the first simulations than presented below, the breakthrough curves showed much higher retardation. By comparing the results of the simulations with the results of other teams involved in GWFTS, this discrepancy was detected and, after verifying the correctness of the mathematical and physical model and its inputs, was explained by the discretisation of the computational domain near the fracture. The discretisation was subsequently adjusted by adding two thin layers of elements in the rock matrix immediately adjacent to the fracture. This modification dramatically improved the consistency of the Flow123d's output with that of other investigators, with results still slightly different for the strongest sorbing tracer (barium). Even in the case of barium, it would be possible to improve the consistency with others by further modification of the computational mesh, but in the blind prediction phase it was not beneficial. The effect of fineness of the mesh on the barium results is discussed in the section dealing with the measured breakthrough curves.

3.2.4   Solution in MODFLOW/MT3D

The simulation of task WPDE in MODFLOW2000 and MT3DMS (v5.3) was performed by PROGEO for selected variants above and beyond the originally planned solution. The basic model configurations, i.e. the division of the model domain into fractures and rock types, the entered hydraulic and transport parameters, and boundary conditions, etc., were taken from the joint task description. The effect of dispersion, fracture aperture variability and discretisation (computational cell size) on the results of the model was solved as a variant.

The task was solved analogously as 2D axially symmetric problem. The model domain consists of a rectangular grid of computational cells and has a size of 1.9 m × 0.2 m (1.9 m corresponds to the length of the open section of the borehole and 0.2 m is the specified thickness of the rock matrix). The length of the calculation cells in the direction of the borehole axis is constant 10 mm (190 columns in total). The width of the first row of computing cells representing the fracture is 1.25 mm. The width of the computational cells representing the rock matrix gradually increases from 1 mm to 20 mm (42 rows in total) in the direction from the fracture to the rock. The geometry of the model and the size of the computational cells are shown in Figure 3-8.
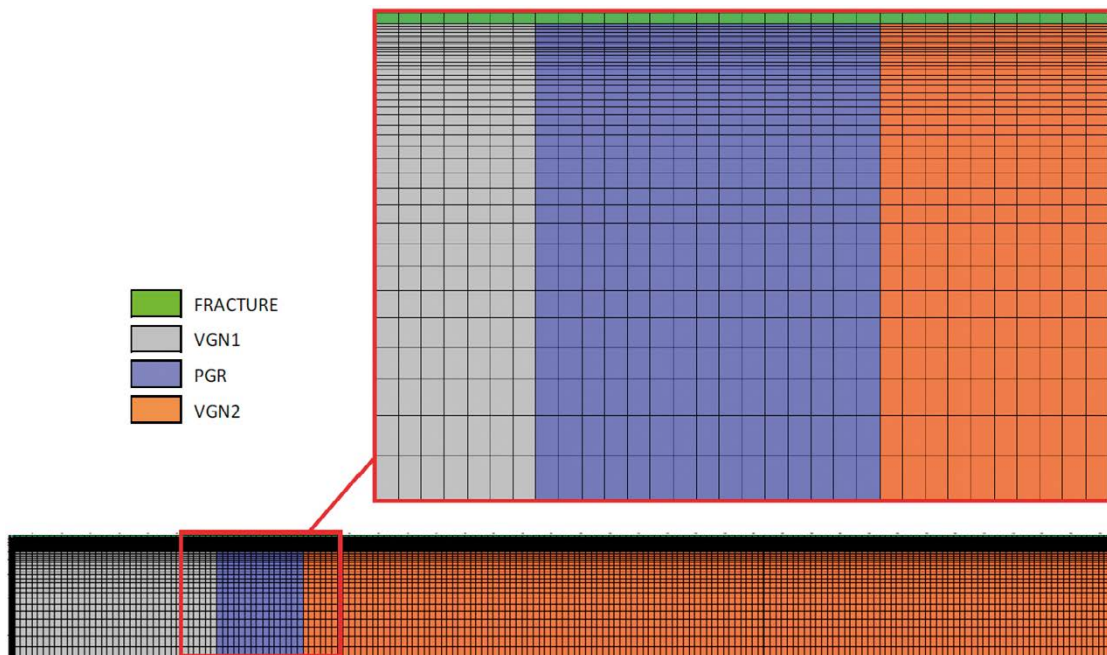
Figure 3-8. *Geometry and discretisation of the model.*

The MODFLOW/MT3DMS programs allow only 3D tasks in Cartesian coordinates to be solved, i.e. it is also necessary to specify the thickness of the model layer. The axial symmetry of the task is therefore entered in such a way that the thickness of the computational cells (in the direction of the z-axis) increases from the fracture to the rock, so that it corresponds to the circumference of the circle at a given distance from the borehole axis.

The simulation of the task was performed in two steps – first, the MODFLOW program calculates a steady flow model and stores the velocity field (volume flows between computational cells). In the next step, the MT3DMS program calculates a transient transport model with a constant time step of 100 s.

Input model values for the hydraulic and transport parameters for individual tracers HTO, Cl-36 and Na-22, for the fracture and for rock types VGN1, PGR and VGN2 entered in the basic comparison variants (var0) correspond to the common task description to allow direct comparison of model results implemented in various software programs. In the case of other variant simulations, certain input parameter values were modified in order to verify the sensitivity of the model solution to the change in the entered parameters (Section 3.6.3).

The mathematical model included the movement of tracers through the inlet and outlet piping. Therefore, for the WPDE 1 experiment, the piping time of 32 hours was added to the presented results (graphs and tables).

3.3   Comparison of the breakthrough curves

The comparison presented in this section is for the updated calculations after the first comparison and discussions at the executive meetings to clarify some minor differences in the input parameters. It contains data sent to the coordinator as final data for Task 9A in the prescribed templates in June 2016.

Breakthrough curves are plotted for each radionuclide in both experiments, always in pairs in log-log axes and in linear axes. In the first case, the slope part of the curve is easily comparable, where the properties of the rock matrix appear. In the second case, the shape and value of the peak maximum are more accurately seen (in addition to the secondary effect of sorption, the dispersion in the fracture is controlled). Figure 3-9 to Figure 3-16 are HTO, Na-22 and Cl-36 for WPDE-1 and HTO, Na-22, Cl-36, Sr-85 and Ba-133 for WPDE-2. The models are marked with abbreviations: F123 is Flow123d (performed by TUL), GS is GoldSim, Pipe (Pipe Pathway element, performed by ÚJV), Cell (network of Cell elements, performed by CTU) and MT3D (performed by PROGEO).

The difference in peak size of F123 compared to both GS variants of Na-22 and Sr-85 for WPDE-2 is viable (but in the case of WPDE-1, it is negligible for the similar Na-22), which may be a remnant of the discretisation effect observed in sorbing radionuclides, where without mesh refinement the results were significantly different. A similar effect may be observed in the case of the Na-22 (WPDE-1) curve calculated by MT3D, which is different despite the performed refinement. Also, the disparity of the Ba-133 curve calculated by F123 remained. The effects of discretisation for MT3D are discussed in more detail in Section 3.6.3 and were analysed in more detail in the interim report (Hokr et al. 2015). It can be said that this is a general phenomenon, not related to a particular software or numerical method, because even in the case of GS-cell it was necessary to make network modifications in the case of Ba-133; moreover, this gives us an indication of "convergence", based on which the GS curve can be considered the right one. In the case of GS-Pipe, the decrease in the HTO and Cl-36 curves (non-sorbing) is different, which is due to the interpretation of the fraction of porosity and geometric factor (tortuosity) – Section 2.2.3.
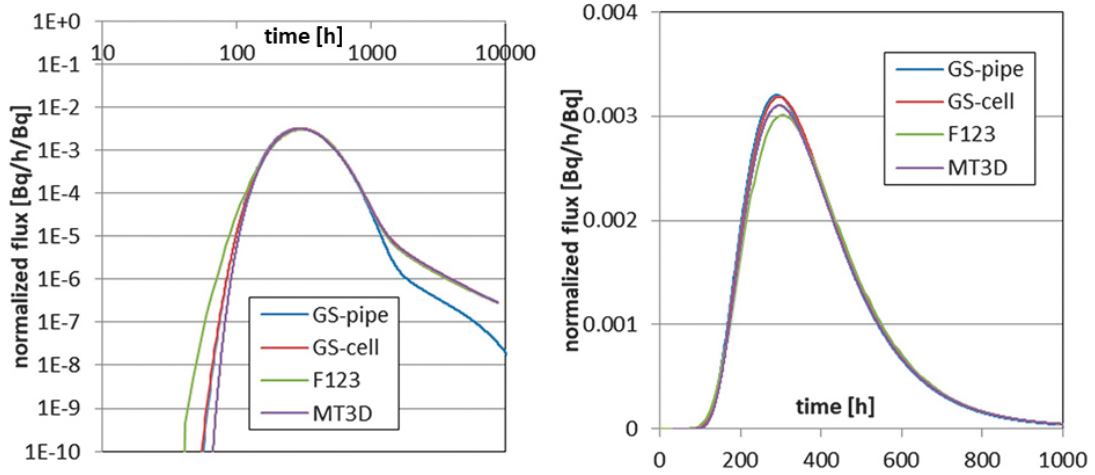
Figure 3-9. *Comparison of the calculated breakthrough curves of WPDE-1 by individual models for HTO.*
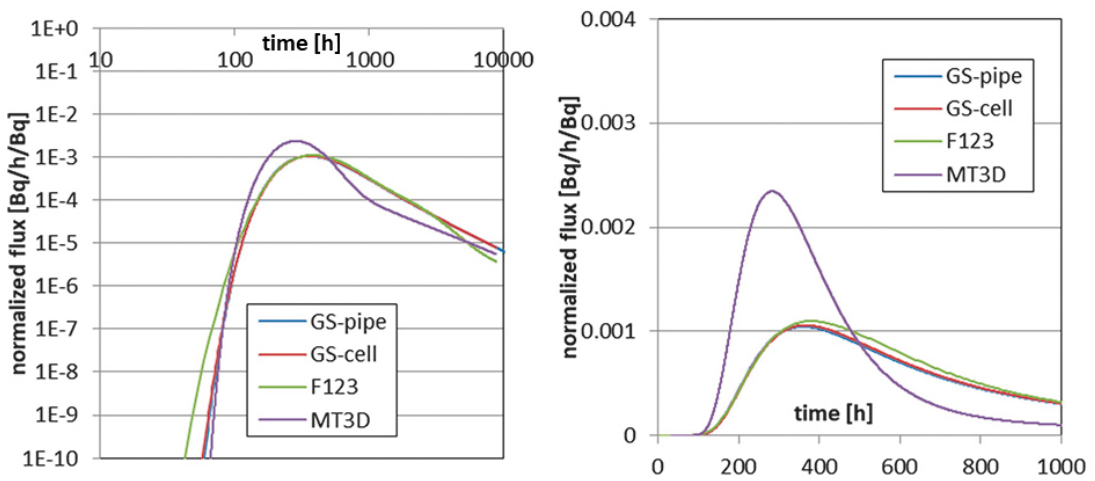
Figure 3-10. *Comparison of the calculated breakthrough curves of WPDE-1 by individual models for Na-22.*
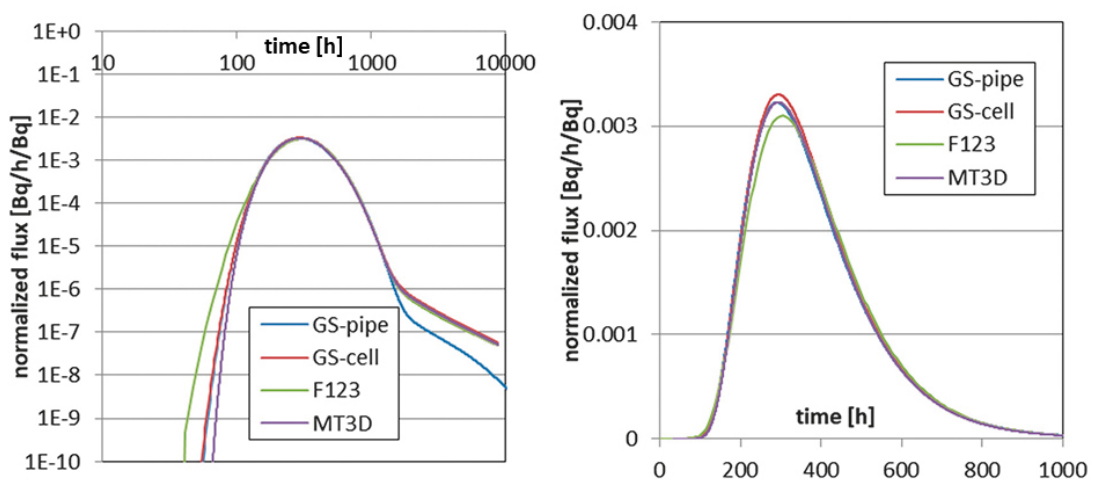
Figure 3-11. *Comparison of the calculated breakthrough curves of WPDE-1 by individual models for Cl-36.*
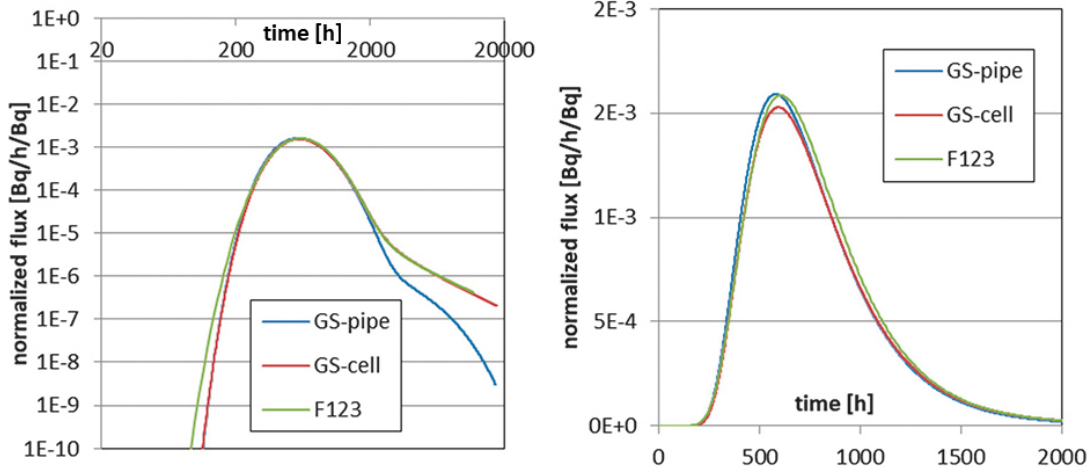
Figure 3-12. *Comparison of the calculated breakthrough curves of WPDE-2 by individual models for HTO.*
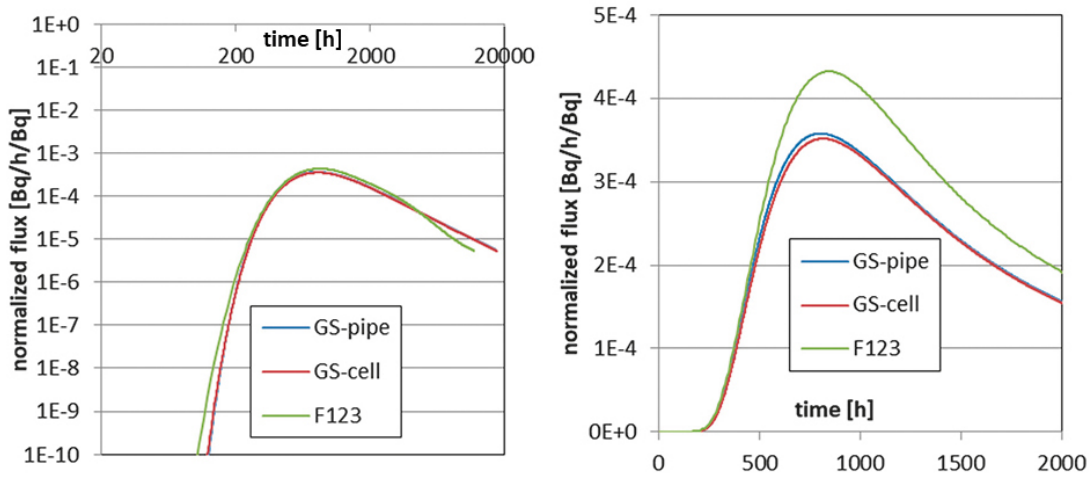
Figure 3-13. *Comparison of the calculated breakthrough curves of WPDE-2 by individual models for Na-22.*
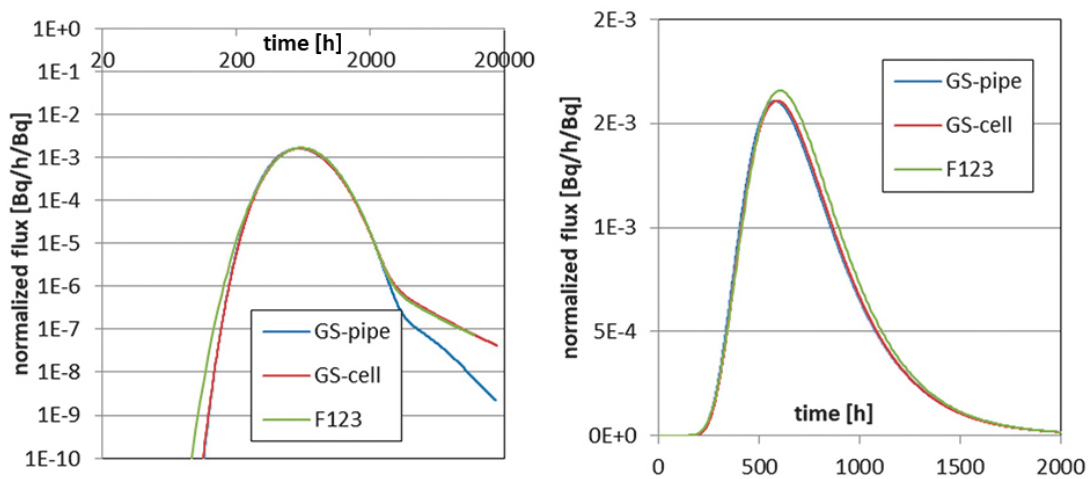
Figure 3-14. *Comparison of the calculated breakthrough curves of WPDE-2 by individual models for Cl-36.*
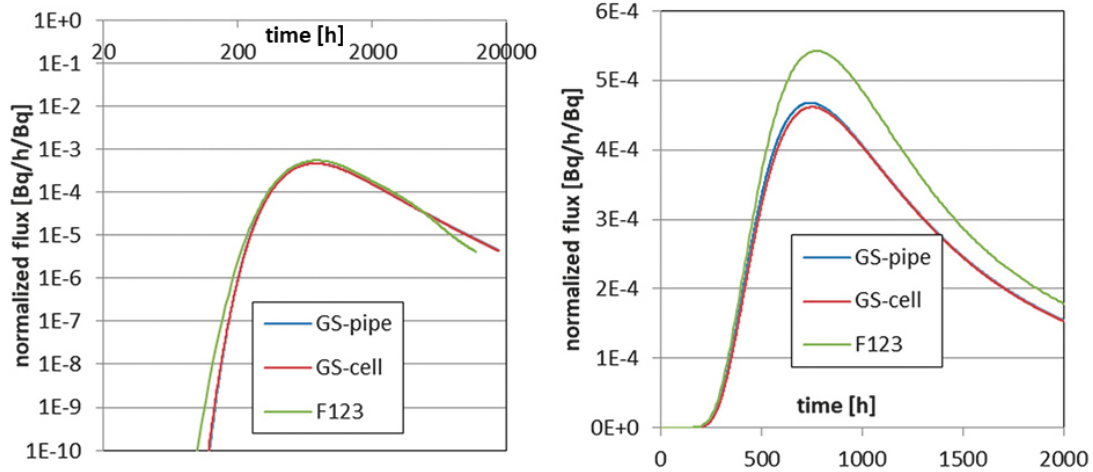
Figure 3-15. *Comparison of the calculated breakthrough curves of WPDE-2 by individual models for Sr-85.*
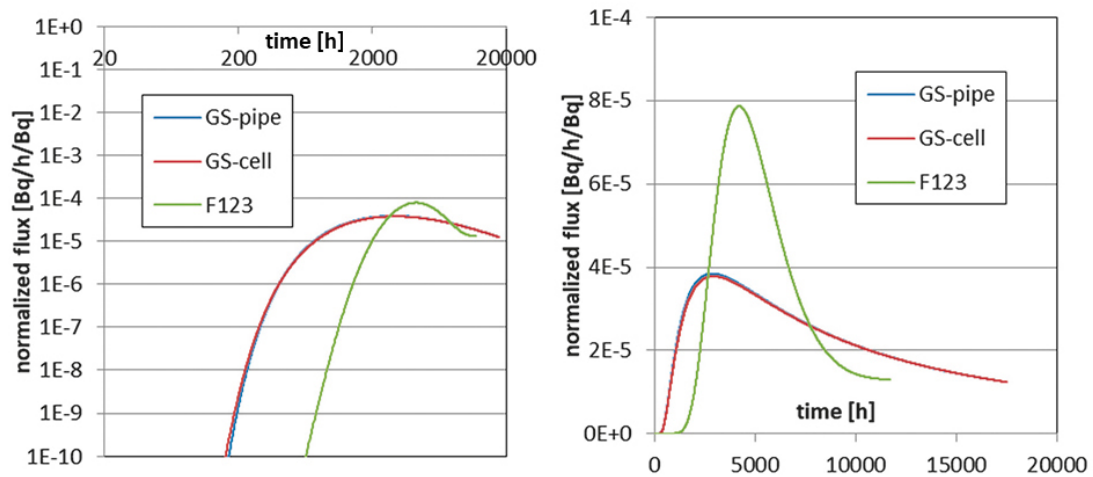
Figure 3-16. *Comparison of the calculated breakthrough curves of WPDE-2 by individual models for Ba-133.*

3.4 Calculations and comparisons of sensitivity

In the task description (Löfgren and Nilsson 2019), the issue of sensitivity and uncertainty was mentioned, but without direct specification. Terms are often used in different contexts with different meanings. During the processing, we worked on the following considerations:

- The purpose of the task can be considered preparation for the future evaluation of measured data, i.e. estimation of what parameters can be estimated from the model and measurement conformity or whether the difference between model and data is due to an inaccurate value of the parameter (the measurement falls within the uncertainty limits of the model) or an erroneous model, i.e. with certain incorrect assumptions or simplifications (the measurement falls outside the uncertainty limits).

- The calculation with uncertainty was indirectly defined by the format of the required table for the output, i.e. upper/lower prediction.

- The standard deviations presented together with the measured data in the literature were used as a basis for the uncertainty of the parameters. Specific references are given in Table 3-7. In certain cases, the values had to be modified with their own estimation to make the calculation meaningful (the variance was greater than the value).

- The term "sensitivity" could be meant as a basis for uncertainty for individual parameters, but also directly as a numerical value. For the latter, the calculations were performed using the methodology outlined in Section 3.4.1 below.

- Using the procedure stated in the above point, a partial basis for evaluating the conformity of data with measurement was obtained without the need to evaluate full-fledged uncertainty limits (which would be computationally demanding) and it is possible to determine whether the influence of the parameter is similar for individual models/software or results – it is possible to assess whether the difference is within or outside the limits of the influence of the parameter.

- Correct calculation of uncertainty requires a calculation with all of the combinations of parameter changes, i.e. for N parameters of 2^N calculations. Given that several parameters have a minimal effect, including all for PGR rocks, the CTU team made such calculations for three parameters: Porosity and diffusion coefficient of VGN rock and either dispersivity for non-sorbing tracers or a sorption coefficient for sorbing tracers.

3.4.1 Methodology for calculating sensitivity

Sensitivity as a value means the ratio between the change of the model result and the change in the parameter, the derivative of the corresponding function expressing the dependence of the selected model result (e.g. point or integral values) on the parameters. It is possible to approximate using regular differential formulas and by using the calculation of the model with perturbed parameters. In our case, considering the limits of the uncertainty intervals of the parameter is naturally not an approximation of the derivative, but we use the same principle for a quantitative comparison of the influence of the parameters on each other.

To make the values independent of the units and scale of different quantities, we also consider normalising the result and parameter values. The formula used for this is

$$s = \frac{\left(\frac{y_2}{y_1}\right)-1}{\left(\frac{b_2}{b_1}\right)-1} = \frac{y_2-y_1}{b_2-b_1}\frac{b_1}{y_1}, \tag{3-1}$$

where $y(b)$ is a function expressing the dependence of the result of the model y on the value of parameter b, the values marked by index 1 have the meaning of reference values and the values with index 2 express the changed values. The formula is used in the same way for the upper and lower limits, the result is naturally significantly different due to the "non-infinitesimal" interval.

Values are chosen as model results (scalar criteria), which are selected on the same principle as in Task 9A, as follows:

- Maximum value of concentration in the breakthrough curve [kg/h/kg].

- Time to reach the maximum concentration [h].

- Peak width of the breakthrough curve defined as the time interval between 50 % of the maximum in the increasing section and in the decreasing section [h].

The mentioned values are obtained by postprocessing the results of the model. They have a discrete form, i.e. individual time steps. Therefore, the values are determined with an accuracy of one step of time discretisation, which is either 1 h or 8 h. In the latter case, the result is often "zero sensitivity", where the position of the value on the curve remains in the same time step.

The selected parameter limits are shown in Table 3-7. The reference values are identical to those considered for comparison in the previous Section 3.3. The value of Porosity Cl-36 is understood as the available porosity (considering anion exclusion), determined experimentally as a capacity factor. In most cases, the limits are chosen according to the stated standard deviations of the measurement. In the case of Porosity VGN for Cl-36, the lower limit was chosen to be approximately half the value instead of the standard deviation, which is greater than the value.

Table 3-7. Boundary values of parameters for sensitivity and uncertainty calculations. TD indicates the task description (Löfgren and Nilsson 2019).

Parameter	Reference	Minimum	Maximum	Source
Longitudinal dispersivity [m]	0.19	0.1	0.28	Defined by GWFTS
Porosity VGN [-]	0.0082	0.0011	0.03	Tab 2-8 TD
Porosity PGR [-]	0.005	0.0026	0.0077	Tab 2-8 TD
Porosity VGN [] Cl-36	0.000175	0.0001	0.0006	Tab 2-9 TD
Porosity PGR [] Cl-36	0.013	0.011	0.015	Tab 2-9 TD
K_d Na-22 VGN [m^3/kg]	0.0013	0.001	0.0016	Tab 2-11 TD
K_d Na-22 PGR [m^3/kg]	0.0008	0.0005	0.0011	Tab 2-11 TD
K_d Sr-85 VGN [m^3/kg]	0.0011	0.0008	0.0014	Tab 2-11 TD
K_d Sr-85 PGR [m^3/kg]	0.0011	0.0008	0.0014	Tab 2-11 TD
K_d Ba-133 VGN [m^3/kg]	0.06	0.04	0.08	Tab 2-11 TD
K_d Ba-133 PGR [m^3/kg]	0.08	0.06	0.1	Tab 2-11 TD
D_e HTO VGN [m^2/s]	1.83E−13	1.2E−13	2.8E−13	Tab 2-9 TD
D_e HTO PGR [m^2/s]	5.7E−13	5.1E−13	6.3E−13	Tab 2-9 TD
D_e Na-22 VGN [m^2/s]	4.65E−13	3.7E−13	5.6E−13	Kaukonen et al. 1997
D_e Na-22 PGR [m^2/s]	4.65E−13	3.7E−13	5.6E−13	Kaukonen et al. 1997
D_e Cl-36 VGN [m^2/s]	5E−15	2E−15	8E−15	Tab 2-9 TD
D_e Cl-36 PGR [m^2/s]	5E−13	4E−13	6E−13	Tab 2-9 TD
D_e Sr-85 VGN [m^2/s]	3.3E−13	2.5E−13	4.1E−13	Skagius et al. 1999
D_e Sr-85 PGR [m^2/s]	3.3E−13	2.5E−13	4.1E−13	Skagius et al. 1999
D_e Ba-133 VGN [m^2/s]	1.47E−13	1.17E−13	1.77E−13	Widestrand et al. 2007
D_e Ba-133 PGR [m^2/s]	1.47E−13	1.17E−13	1.77E−13	Widestrand et al. 2007

3.4.2 Results

The comparison of sensitivity values for the individual criteria and parameters is presented in Table 3-8 to Table 3-12. These have a uniform form for the five evaluated radionuclides except for the missing sorption coefficients for HTO and Cl-36. In the upper part of the table there are the calculated values of the model (quantitative criteria characterising the breakthrough curve) and in the lower part are equally arranged sensitivity values determined according to the Equation (3-1).

The comparison also complements the graphs of the breakthrough curves in Section 3.3 – for a large part of the criterion values, we can see the order matching corresponding to the optical agreement of the graphs. On the contrary, there is a noticeable difference in the different Ba-133 breakthrough curves from the Flow123d program, with the approximate agreement of both GoldSim variants. In the case of consistent values, the sensitivity is usually acceptable, but there are two specific cases

- In the case of low sensitivities, there is sometimes a zero value for one program versus a non-zero value for another program. This is due to the foregoing methodology with discrete time steps, and precisely because it is a sensitivity at the boundary of resolution, there is no practical sense to deal with it.

- In the case of the dispersion effect, an anomaly occurs from the usual effect of higher dispersion on earlier detection and the lower peak, and vice versa. This occurs in various forms in all of the sorbent radionuclides, especially in both GoldSim variants.

The standard dispersion effect corresponds to the negative sensitivity at the position and peak size at min and max (decrease in value at higher dispersion or increase in value at lower dispersion) and is therefore seen uniformly in all of the software programs for HTO and Cl-36 (see the graphs in Figure 3-17). In the case of Na-22 and Sr-85, very similarly in both GoldSim variants, for reference the minimum peak size and both dispersion changes lead to an increase, i.e. the sensitivity to min and max has the opposite sign. In the case of Flow123d, the effect is not in this form, but a sensitivity imbalance for min and max dispersion can be observed, oriented towards the phenomenon observed in GoldSim. For Na-22, this is demonstrated in the graph in Figure 3-18. For Ba-133, the GoldSim dependency trend fully reverses, i.e. the peak increases at a higher dispersion and decreases at a lower dispersion.

The non-monotonicity of the dependence is not typical, and the identification of the minimum is an unexpected coincidence. On the other hand, it cannot be said that this would be a random effect as a whole, as it manifests itself consistently – slightly sorbing radionuclides as a transition between non-sorbing and more sorbing, as well as the same oriented effect in several different numerical schemes.

Other sensitivities in non-sorbing radionuclides are negligible. The effect of porosity is on the downward part of the curve (the position of the line in the log-log axes), which is not affected by the criteria (Figure 3-19). The visible effect on the graphs and values are relatively consistent between different values in the case of diffusion and sorption of sorbing radionuclides, which are mainly reflected in the peak size. Even in the case of different curves between Flow123d and GoldSim for barium, the trend of the influence by the parameters may be considered similar (Figure 3-20).
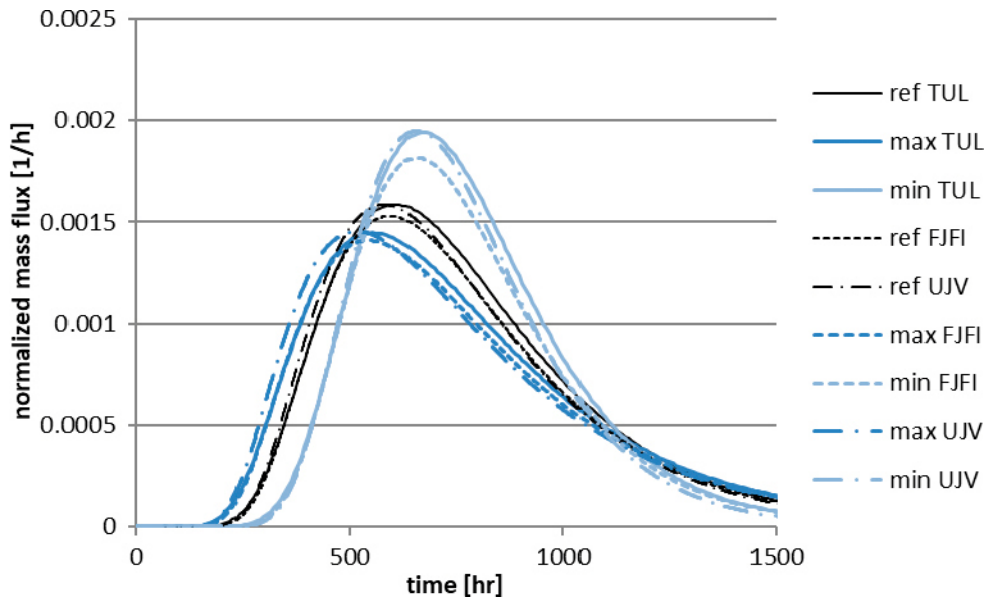
Figure 3-17. *Sensitivity of HTO breakthrough curves in WPDE-2 to dispersion (min/max according to Table 3-7) with a comparison of three calculations.*
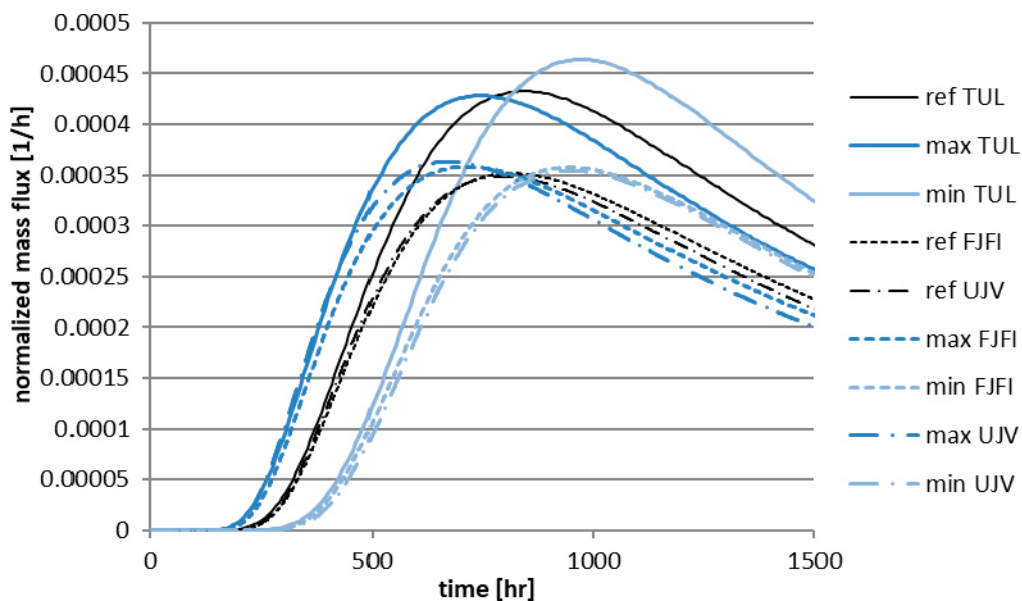
Figure 3-18. *Sensitivity of N-22 breakthrough curves in WPDE-2 to dispersion (min/max according Table 3-7) with a comparison of three calculations.*
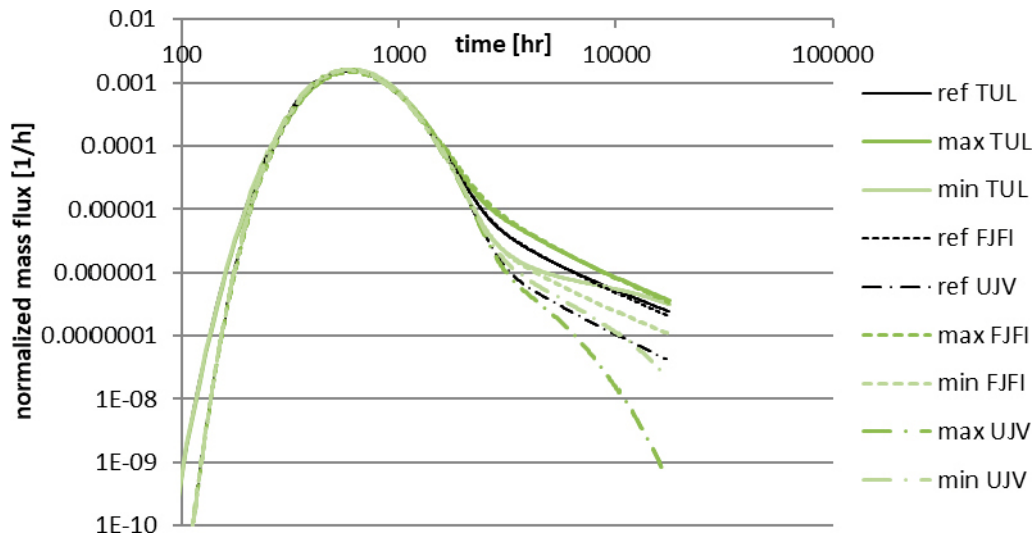
Figure 3-19. Sensitivity of HTO breakthrough curves in WPDE-2 to porosity (min/max according to Table 3-7) with a comparison of three calculations.
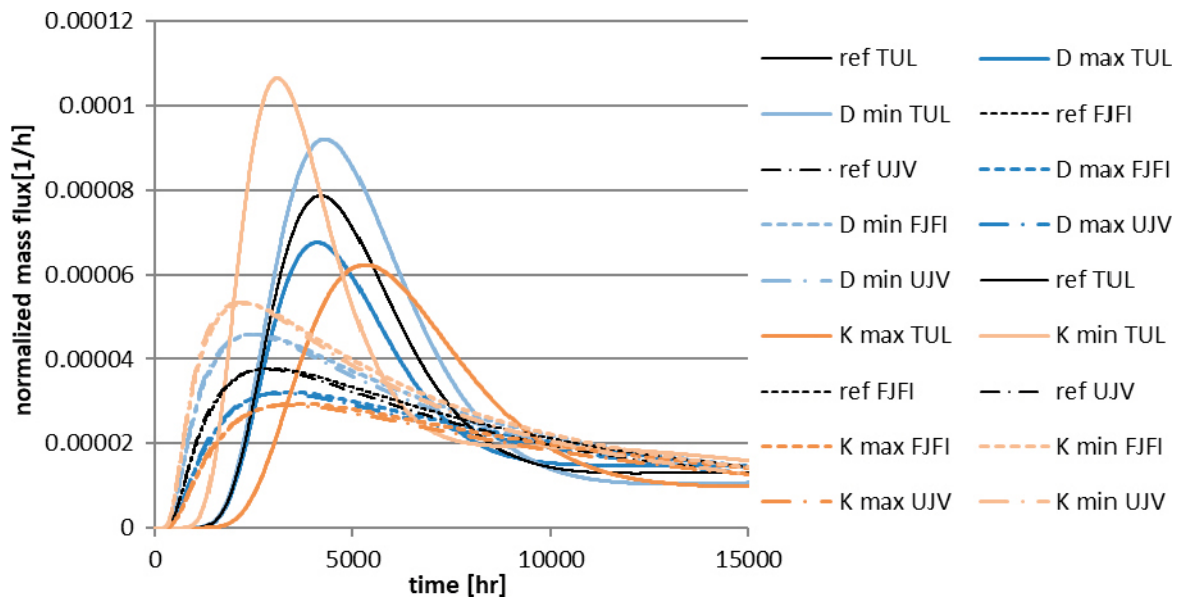
Figure 3-20. Sensitivity of Ba-133 breakthrough curves in WPDE-2 to the effective diffusion coefficient (D) and sorption coefficient (K) (min/max according to Table 3-7) with a comparison of three calculations.

Table 3-8. Results of the evaluation of the sensitivity of the breakthrough curve criteria to the model parameters for HTO.

	HTO	Maximum position [h]			Peak width [h]			Maximum value [1/h]		
	Parameter	GS-pipe	F123d	GS-cell	GS-pipe	F123d	GS-cell	GS-pipe	F123d	GS-cell
Criterion value	Reference	581	602	594	560	576	568	1.59E−3	1.59E−3	1.53E−3
	Dispersion max	518	554	543	596	624	606	1.46E−3	1.45E−3	1.41E−3
	Dispersion min	657	674	657	467	496	486	1.96E−3	1.94E−3	1.82E−3
	De VGN max	582	610	594	562	576	571	1.58E−3	1.56E−3	1.51E−3
	De VGN min	581	602	593	559	576	565	1.60E−3	1.60E−3	1.55E−3
	De PGR max	581	602	594	560	576	568	1.59E−3	1.59E−3	1.53E−3
	De PGR min	581	602	594	560	576	568	1.59E−3	1.59E−3	1.53E−3
	poro VGN max	581	610	597	560	584	580	1.60E−3	1.54E−3	1.46E−3
	poro VGN min	581	602	591	562	576	560	1.59E−3	1.63E−3	1.58E−3
	poro PGR max	581	602	594	560	576	568	1.59E−3	1.59E−3	1.53E−3
	poro PGR min	581	602	593	560	576	567	1.59E−3	1.59E−3	1.53E−3
Sensitivity to the parameter	Dispersion max	−2.3E−1	−1.7E−1	−1.8E−1	1.4E−1	1.8E−1	1.4E−1	−1.8E−1	−1.9E−1	−1.6E−1
	Dispersion min	−2.8E−1	−2.5E−1	−2.2E−1	3.5E−1	2.9E−1	3.0E−1	−4.8E−1	−4.7E−1	−4.0E−1
	De VGN max	3.2E−3	2.5E−2	0.0E+0	6.7E−3	0.0E+0	1.0E−2	−1.0E−2	−2.6E−2	−2.7E−2
	De VGN min	0.0E+0	0.0E+0	4.9E−3	5.2E−3	0.0E+0	1.5E−2	−1.0E−2	−3.2E−2	−3.3E−2
	De PGR max	0.0E+0	0.0E+0	0.0E+0	0.0E+0	0.0E+0	0.0E+0	−3.0E−3	−3.8E−3	−4.5E−3
	De PGR min	0.0E+0	0.0E+0	0.0E+0	0.0E+0	0.0E+0	0.0E+0	−3.0E−3	−4.0E−3	−4.7E−3
	poro VGN max	0.0E+0	5.0E−3	1.9E−3	0.0E+0	5.2E−3	7.9E−3	8.4E−4	−1.1E−2	−1.7E−2
	poro VGN min	0.0E+0	0.0E+0	5.8E−3	−4.1E−3	0.0E+0	1.6E−2	5.3E−3	−3.0E−2	−3.9E−2
	poro PGR max	0.0E+0	0.0E+0	0.0E+0	0.0E+0	0.0E+0	0.0E+0	4.3E−4	−2.2E−3	−3.0E−3
	poro PGR min	0.0E+0	0.0E+0	3.5E−3	0.0E+0	0.0E+0	3.7E−3	8.0E−4	−3.0E−3	−4.0E−3

Table 3-9. Results of the evaluation of the sensitivity of the breakthrough curve criteria to the model parameters for Na-22.

	Na-22	Maximum position [h]			Peak width [h]			Maximum value [1/h]		
	Parameter	GS-pipe	F123d	GS-cell	GS-pipe	F123d	GS-cell	GS-pipe	F123d	GS-cell
Criterion value	Reference	802	842	815	1368	1368	1371	3.58E−4	4.33E−4	3.52E−4
	Dispersion max	678	746	715	1294	1352	1332	3.71E−4	4.28E−4	3.58E−4
	Dispersion min	958	970	945	1338	1288	1343	3.65E−4	4.64E−4	3.58E−4
	De VGN max	832	866	845	1488	1520	1492	3.21E−4	3.95E−4	3.15E−4
	De VGN min	771	818	784	1244	1240	1247	4.06E−4	4.78E−4	4.00E−4
	De PGR max	804	850	817	1376	1376	1380	3.55E−4	4.30E−4	3.49E−4
	De PGR min	800	842	812	1358	1352	1361	3.61E−4	4.35E−4	3.55E−4
	poro VGN max	802	842	816	1368	1360	1375	3.58E−4	4.35E−4	3.51E−4
	poro VGN min	802	842	814	1368	1368	1370	3.58E−4	4.32E−4	3.52E−4
	poro PGR max	802	842	815	1368	1368	1371	3.58E−4	4.33E−4	3.52E−4
	poro PGR min	802	842	815	1368	1368	1371	3.58E−4	4.33E−4	3.52E−4
	Kd VGN max	836	882	849	1503	1488	1507	3.17E−4	3.84E−4	3.11E−4
	Kd VGN min	767	802	779	1228	1240	1231	4.13E−4	4.96E−4	4.06E−4
	Kd PGR max	806	850	819	1382	1376	1386	3.53E−4	4.27E−4	3.47E−4
	Kd PGR min	798	842	810	1349	1344	1353	3.64E−4	4.39E−4	3.58E−4
Sensitivity to the parameter	Dispersion max	−3.3E−1	−2.4E−1	−2.6E−1	−1.1E−1	−2.5E−2	−6.0E−2	7.6E−2	−2.1E−2	4.0E−2
	Dispersion min	−4.1E−1	−3.2E−1	−3.4E−1	4.6E−2	1.2E−1	4.3E−2	−4.0E−2	−1.5E−1	−3.5E−2
	De VGN max	1.8E−1	1.4E−1	1.8E−1	4.3E−1	5.4E−1	4.3E−1	−5.0E−1	−4.3E−1	−5.1E−1
	De VGN min	1.9E−1	1.4E−1	1.9E−1	4.4E−1	4.6E−1	4.4E−1	−6.5E−1	−5.2E−1	−6.7E−1
	De PGR max	1.2E−2	4.7E−2	1.2E−2	2.9E−2	2.9E−2	3.2E−2	−3.7E−2	−2.9E−2	−4.1E−2
	De PGR min	1.2E−2	0.0E+0	1.8E−2	3.6E−2	5.7E−2	3.6E−2	−4.2E−2	−3.3E−2	−4.7E−2
	poro VGN max	0.0E+0	0.0E+0	4.6E−4	0.0E+0	−2.2E−3	1.1E−3	3.7E−5	2.3E−3	−1.3E−3
	poro VGN min	0.0E+0	0.0E+0	1.4E−3	0.0E+0	0.0E+0	8.4E−4	3.1E−4	1.2E−3	−1.3E−3
	poro PGR max	0.0E+0	0.0E+0	0.0E+0	0.0E+0	0.0E+0	0.0E+0	9.3E−6	1.2E−4	−9.9E−5
	poro PGR min	0.0E+0	0.0E+0	0.0E+0	0.0E+0	0.0E+0	0.0E+0	1.9E−5	7.8E−5	−9.9E−5
	Kd VGN max	1.8E−1	2.1E−1	1.8E−1	4.3E−1	3.8E−1	4.3E−1	−5.0E−1	−4.9E−1	−5.0E−1
	Kd VGN min	1.9E−1	2.1E−1	1.9E−1	4.4E−1	4.1E−1	4.4E−1	−6.7E−1	−6.4E−1	−6.7E−1
	Kd PGR max	1.3E−2	2.5E−2	1.3E−2	2.7E−2	1.6E−2	2.9E−2	−3.6E−2	−3.4E−2	−3.9E−2
	Kd PGR min	1.3E−2	0.0E+0	1.6E−2	3.7E−2	4.7E−2	3.5E−2	−4.6E−2	−4.2E−2	−4.9E−2

Table 3-10. Results of the evaluation of the sensitivity of the breakthrough curve criteria to the model parameters for Cl-36.

	Cl-36	Maximum position [h]			Peak width [h]			Maximum value [1/h]		
	Parameter	GS-pipe	F123d	GS-cell	GS-pipe	F123d	GS-cell	GS-pipe	F123d	GS-cell
Criterion value	Reference	580	602	590	557	568	557	1.61E−3	1.66E−3	1.61E−3
	Dispersion max	517	554	541	593	616	597	1.47E−3	1.46E−3	1.48E−3
	Dispersion min	656	666	653	464	480	475	1.98E−3	2.17E−3	1.92E−3
	De VGN max	580	602	590	557	568	557	1.61E−3	1.66E−3	1.61E−3
	De VGN min	580	602	590	557	568	557	1.61E−3	1.66E−3	1.61E−3
	De PGR max	580	602	590	557	568	557	1.61E−3	1.66E−3	1.61E−3
	De PGR min	580	602	590	557	568	557	1.61E−3	1.66E−3	1.61E−3
	poro VGN max	580	602	590	557	568	557	1.61E−3	1.66E−3	1.61E−3
	poro VGN min	580	602	590	557	568	557	1.61E−3	1.66E−3	1.61E−3
	poro PGR max	580	602	590	557	568	557	1.61E−3	1.66E−3	1.61E−3
	poro PGR min	580	602	590	557	568	557	1.61E−3	1.66E−3	1.61E−3
Sensitivity to the parameter	Dispersion max	−1.8E−1	−2.6E−1	−1.7E−1	−2.3E−1	−1.7E−1	−1.8E−1	1.4E−1	1.8E−1	1.5E−1
	Dispersion min	−4.9E−1	−6.4E−1	−4.1E−1	−2.8E−1	−2.2E−1	−2.3E−1	3.5E−1	3.3E−1	3.1E−1
	De VGN max	−6.0E−4	−6.7E−4	−6.8E−4	0.0E+0	0.0E+0	0.0E+0	0.0E+0	0.0E+0	0.0E+0
	De VGN min	−6.0E−4	−8.6E−4	−9.0E−4	0.0E+0	0.0E+0	0.0E+0	0.0E+0	0.0E+0	0.0E+0
	De PGR max	−2.4E−3	−5.2E−3	−6.0E−3	0.0E+0	0.0E+0	0.0E+0	0.0E+0	0.0E+0	0.0E+0
	De PGR min	−2.4E−3	−5.7E−3	−6.6E−3	0.0E+0	0.0E+0	0.0E+0	0.0E+0	0.0E+0	0.0E+0
	poro VGN max	4.9E−5	−2.9E−4	−4.5E−4	0.0E+0	0.0E+0	0.0E+0	0.0E+0	0.0E+0	0.0E+0
	poro VGN min	1.5E−4	−5.3E−4	−7.3E−4	0.0E+0	0.0E+0	0.0E+0	0.0E+0	0.0E+0	0.0E+0
	poro PGR max	4.0E−4	−3.1E−3	−5.0E−3	0.0E+0	0.0E+0	0.0E+0	0.0E+0	0.0E+0	0.0E+0
	poro PGR min	4.8E−4	−3.5E−3	−5.4E−3	0.0E+0	0.0E+0	0.0E+0	0.0E+0	0.0E+0	0.0E+0

Table 3-11. Results of the evaluation of the sensitivity of the breakthrough curve criteria to the model parameters for Sr-85.

	Sr-85	Maximum position [h]			Peak width [h]			Maximum value [1/h]		
	Parameter	GS-pipe	F123d	GS-cell	GS-pipe	F123d	GS-cell	GS-pipe	F123d	GS-cell
Criterion value	Reference	741	778	752	1 121	1 120	1 124	4.68E−4	5.43E−4	4.62E−4
	Dispersion max	634	690	666	1 087	1 128	1 113	4.75E−4	5.32E−4	4.63E−4
	Dispersion min	873	882	862	1 057	1 040	1 068	4.91E−4	5.88E−4	4.82E−4
	De VGN max	765	794	775	1 213	1 208	1 215	4.20E−4	4.98E−4	4.14E−4
	De VGN min	716	746	727	1 026	1 040	1 028	5.32E−4	6.01E−4	5.26E−4
	De PGR max	743	778	754	1 128	1 128	1 132	4.64E−4	5.39E−4	4.57E−4
	De PGR min	739	770	750	1 113	1 112	1 114	4.73E−4	5.47E−4	4.67E−4
	poro VGN max	741	770	753	1 121	1 112	1 126	4.68E−4	5.46E−4	4.60E−4
	poro VGN min	741	778	752	1 121	1 120	1 123	4.68E−4	5.43E−4	4.62E−4
	poro PGR max	741	778	752	1 121	1 120	1 124	4.68E−4	5.43E−4	4.62E−4
	poro PGR min	741	778	752	1 121	1 120	1 124	4.68E−4	5.43E−4	4.62E−4
	Kd VGN max	767	802	779	1 224	1 224	1 227	4.15E−4	4.80E−4	4.09E−4
	Kd VGN min	713	738	723	1 014	1 016	1 017	5.41E−4	6.24E−4	5.34E−4
	Kd PGR max	743	778	754	1 129	1 128	1 133	4.63E−4	5.37E−4	4.57E−4
	Kd PGR min	739	770	749	1 111	1 112	1 113	4.74E−4	5.49E−4	4.68E−4
Sensitivity to the parameter	Dispersion max	3.3E−2	−4.2E−2	4.4E−3	−3.0E−1	−2.4E−1	−2.4E−1	−6.4E−2	1.5E−2	−2.1E−2
	Dispersion min	−1.1E−1	−1.7E−1	−9.0E−2	−3.8E−1	−2.8E−1	−3.1E−1	1.2E−1	1.5E−1	1.1E−1
	De VGN max	−4.2E−1	−3.4E−1	−4.3E−1	1.3E−1	8.5E−2	1.3E−1	3.4E−1	3.2E−1	3.3E−1
	De VGN min	−5.6E−1	−4.4E−1	−5.7E−1	1.4E−1	1.7E−1	1.4E−1	3.5E−1	2.9E−1	3.5E−1
	De PGR max	−3.8E−2	−3.0E−2	−4.3E−2	1.1E−2	0.0E+0	1.1E−2	2.6E−2	2.9E−2	2.9E−2
	De PGR min	−4.5E−2	−3.4E−2	−5.0E−2	1.1E−2	4.2E−2	1.1E−2	2.9E−2	2.9E−2	3.7E−2
	poro VGN max	4.4E−5	2.2E−3	−1.3E−3	0.0E+0	−3.9E−3	5.0E−4	0.0E+0	−2.7E−3	6.7E−4
	poro VGN min	3.7E−4	−5.2E−4	−1.3E−3	0.0E+0	0.0E+0	0.0E+0	0.0E+0	0.0E+0	1.0E−3
	poro PGR max	8.3E−6	1.4E−4	−7.7E−5	0.0E+0	0.0E+0	0.0E+0	0.0E+0	0.0E+0	0.0E+0
	poro PGR min	1.7E−5	1.4E−4	−7.7E−5	0.0E+0	0.0E+0	0.0E+0	0.0E+0	0.0E+0	0.0E+0
	Kd VGN max	−4.2E−1	−4.3E−1	−4.2E−1	1.3E−1	1.1E−1	1.3E−1	3.4E−1	3.4E−1	3.4E−1
	Kd VGN min	−5.7E−1	−5.5E−1	−5.7E−1	1.4E−1	1.9E−1	1.4E−1	3.5E−1	3.4E−1	3.5E−1
	Kd PGR max	−3.8E−2	−4.0E−2	−4.2E−2	9.9E−3	0.0E+0	9.8E−3	2.6E−2	2.6E−2	2.9E−2
	Kd PGR min	−4.5E−2	−4.4E−2	−5.0E−2	9.9E−3	3.8E−2	1.5E−2	3.3E−2	2.6E−2	3.6E−2

Table 3-12. Results of the evaluation of the sensitivity of the breakthrough curve criteria to the model parameters for Ba-133.

	Ba-133	Maximum position [h]			Peak width [h]			Maximum value [1/h]		
	Parameter	GS-pipe	F123d	GS-cell	GS-pipe	F123d	GS-cell	GS-pipe	F123d	GS-cell
Criterion value	Reference	2858	4202	2926	10179	4016	10366	3.84E−5	7.87E−5	3.78E−5
	Dispersion max	2123	3690	2309	8421	4104	9011	4.36E−5	7.81E−5	4.15E−5
	Dispersion min	3924	4938	3826	11893	3592	11806	3.46E−5	8.67E−5	3.46E−5
	De VGN max	3262	4106	3334	11925	3960	12120	3.27E−5	6.76E−5	3.22E−5
	De VGN min	2448	4306	2508	8412	4112	8588	4.67E−5	9.21E−5	4.59E−5
	De PGR max	2894	4194	2966	10333	4008	10543	3.78E−5	7.77E−5	3.71E−5
	De PGR min	2818	4210	2881	10003	4032	10168	3.91E−5	7.97E−5	3.86E−5
	poro VGN max	2858	4130	2926	10179	3944	10366	3.84E−5	7.99E−5	3.78E−5
	poro VGN min	2858	4226	2926	10179	4032	10365	3.84E−5	7.84E−5	3.78E−5
	poro PGR max	2858	4202	2926	10179	4008	10366	3.84E−5	7.87E−5	3.78E−5
	poro PGR min	2859	4202	2926	10179	4016	10366	3.84E−5	7.87E−5	3.78E−5
	Kd VGN max	3515	5306	3596	13020	5064	13233	2.99E−5	6.23E−5	2.94E−5
	Kd VGN min	2185	3098	2241	7279	2992	7443	5.43E−5	1.07E−4	5.32E−5
	Kd PGR max	2900	4290	2974	10365	4120	10582	3.77E−5	7.68E−5	3.70E−5
	Kd PGR min	2808	4114	2870	9959	3912	10118	3.93E−5	8.06E−5	3.88E−5
Sensitivity to the parameter	dispersion max	2.9E−1	−1.5E−2	2.1E−1	−5.4E−1	−2.6E−1	−4.5E−1	−3.6E−1	4.6E−2	−2.8E−1
	dispersion min	2.1E−1	−2.1E−1	1.8E−1	−7.9E−1	−3.7E−1	−6.5E−1	−3.6E−1	2.2E−1	−2.9E−1
	De VGN max	−7.3E−1	−6.9E−1	−7.3E−1	6.9E−1	−1.1E−1	6.8E−1	8.4E−1	−6.8E−2	8.3E−1
	De VGN min	−1.1E+0	−8.3E−1	−1.0E+0	7.0E−1	−1.2E−1	7.0E−1	8.5E−1	−1.2E−1	8.4E−1
	De PGR max	−7.7E−2	−6.2E−2	−8.7E−2	6.2E−2	−9.3E−3	6.7E−2	7.4E−2	−9.8E−3	8.4E−2
	De PGR min	−8.9E−2	−6.3E−2	−1.0E−1	6.9E−2	−9.3E−3	7.5E−2	8.5E−2	−2.0E−2	9.4E−2
	poro VGN max	1.3E−6	5.8E−3	−4.3E−5	0.0E+0	−6.4E−3	0.0E+0	0.0E+0	−6.7E−3	0.0E+0
	poro VGN min	8.1E−6	4.3E−3	−4.3E−5	0.0E+0	−6.6E−3	0.0E+0	0.0E+0	−4.6E−3	1.1E−4
	poro PGR max	−4.8E−7	4.6E−4	−2.1E−6	0.0E+0	0.0E+0	0.0E+0	0.0E+0	−3.7E−3	0.0E+0
	poro PGR min	1.6E−6	5.1E−4	−2.2E−6	−7.3E−4	0.0E+0	0.0E+0	0.0E+0	0.0E+0	0.0E+0
	Kd VGN max	−6.7E−1	−6.3E−1	−6.6E−1	6.9E−1	7.9E−1	6.9E−1	8.4E−1	7.8E−1	8.3E−1
	Kd VGN min	−1.2E+0	−1.1E+0	−1.2E+0	7.1E−1	7.9E−1	7.0E−1	8.5E−1	7.6E−1	8.5E−1
	Kd PGR max	−7.6E−2	−9.6E−2	−8.5E−2	5.9E−2	8.4E−2	6.6E−2	7.3E−2	1.0E−1	8.3E−2
	Kd PGR min	−9.1E−2	−9.8E−2	−1.0E−1	7.0E−2	8.4E−2	7.7E−2	8.6E−2	1.0E−1	9.6E−2

3.5   Calibration of the model for measurement

The calibration was performed at a later stage of the project, after publication of the measured data by the management of GWFTS, using only the Flow123d model. A new computational mesh, only two-dimensional, was created for all of the simulations described below. This was done with the aim of achieving acceptable demands on time, but not at the expense of the model's predictive ability. The third dimension is emulated by the cross_section parameter (Flow123d, representing the thickness or cross-section of elements with dimension less than 3), whose value changes continuously according to the following:

$cs = 6.2832 \cdot y,$

which ensures the asymmetry of the task (the y-axis direction is perpendicular to the fracture). The equivalence of outputs was verified by test calculations.

Figure 3-21 analyses the predictive model of the WPDE-2 experiment (HTO tracer) with the measured data (both axes of the graph are on a logarithmic scale). The image shows the following facts characterising the degree of agreement between the predictive model and the measured data.

- Non-zero value of the measured data from the start of the simulation time – given by the sequence of performed experiments, will be discussed in a separate text below.

- Leading edge – measured data increase to a maximum far before the simulation results reach a maximum. This is strange, as the flow through the artificial fracture was monitored throughout the experiment and fluctuates only negligibly around the value given in the task description (and used in the simulation). The degree of influence of the presence of the rock matrix in the model on the course of the leading edge was tested by the simulation of a separate fracture. The result of this model is shown in Figure 3-21 represented by a pink curve. It is apparent that the inclusion of a rock matrix for the conservative tracer only affects the course of the falling edge, the leading edge and the value, and the position of the maximum has no observable effect. Molecular diffusion and hydrodynamic dispersion, which are simulated in the fracture, have no effect on the position of the maximum, only on its value and on the degree of dispersion ("width" of the breakthrough curve). This implies that the leading edge of the measured data cannot be replicated in the current configuration of the experiment model. One can only guess what causes the rapid onset of the concentration at the outlet. A possible explanation is the inaccuracy (lack of concentration) of the borehole seal, which may have resulted in a preferential pathway. The irregularities on the walls of the borehole could also have been influenced, or the horizontal orientation of the borehole in which the experiment is installed (the borehole has fallen by approximately ten degrees) could not be completely horizontal.

- Maximum value – here the blind prediction shows good agreement with the measured data.

- Falling edge – parameters of the rock matrix for the conservative tracer have an influence especially on the rate of decrease of the falling edge. It is on its course that efforts are focused on the model reproduction of the measured data (see below).
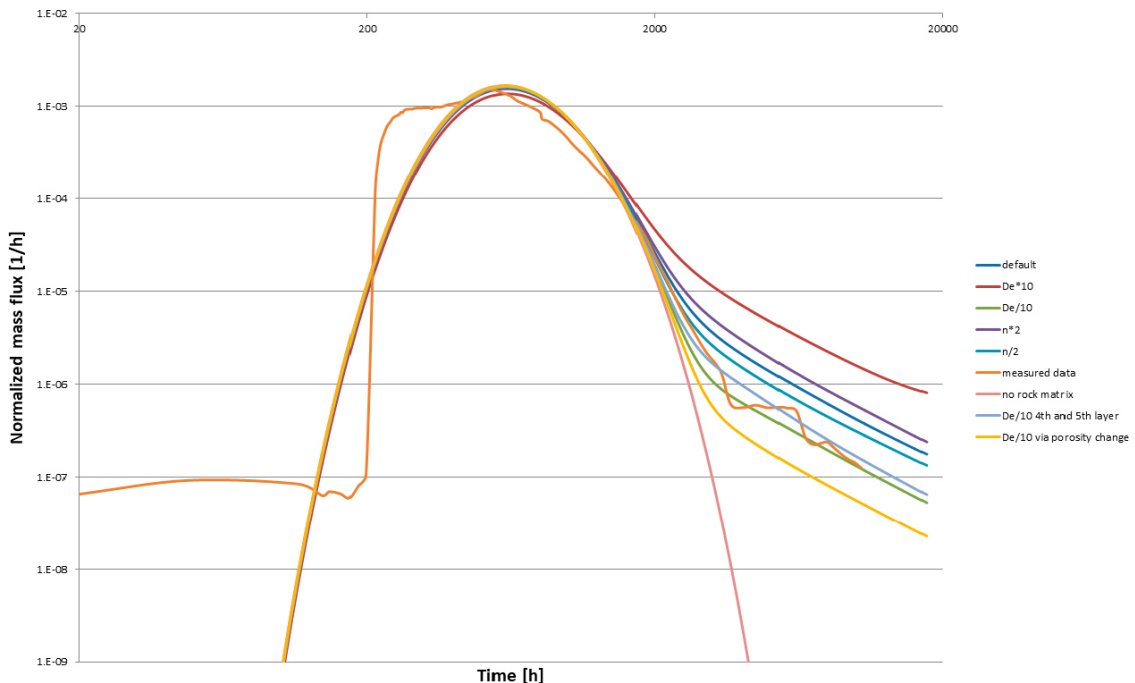
Figure 3-21. *WPDE-2 – Additional simulation, measured data – HTO.*

Because HTO is a conservative tracer, the only simulated process in the rock matrix is molecular diffusion. Therefore, only two parameters were available to fit the measured data: effective diffusivity D_e and porosity n.

$$D_e = D_w \cdot n \cdot \tau = D_w \cdot n^{4/3},$$

where D_w is the diffusion coefficient in free water and τ is the geometric factor (tortuosity), which Flow123d calculates as the cubic root of the porosity without user intervention. The inputs for the model are D_w and n, D_e is calculated internally.

A sensitivity analysis was performed, whereby the porosity parameter was changed to twice and half its baseline and the effective diffusivity parameter to a tenth and ten times its baseline (change in D_w). Effective diffusivity was also indirectly changed when porosity was changed (see Table 3-13). The results of this sensitivity analysis are shown in Figure 3-21. At the same time it was verified whether there is equality in the model in the sense that it does not matter if we change the porosity or diffusivity in the open water in order to change the effective diffusivity (the resulting value is always the same). In Figure 3-21 it is apparent that the course of the simulated breakthrough curve is significantly different if one-tenth of the initial value of effective diffusivity is achieved by changing the D_w (the curve marked "D_e/10") or by changing n (the curve marked "D_e/10 via porosity change"). The change in porosity does not mean only an implied change in D_e, but also a change in the pore volume available for transporting the tracer.

Table 3-13. Effect of porosity change on effective diffusivity.

Change the porosity (multiplier)	Implied change D_e (multiplier)
2	2.5198
1/2	1/(2.5198) = 0.39685

Figure 3-21 shows that good agreement with the measured data was achieved when the effective diffusivity was reduced to one tenth of its initial value over the entire volume of the rock matrix. It would be difficult to justify such a change in value that was measured (albeit with inherent uncertainty). We could easily say that the real value of the geometric factor (tortuosity) is different from its rough estimate, calculated as the cubic root of the porosity, which to some extent may be true. Instead, an additional series of calculations was performed, where the effective diffusivity was changed only in part of the rock matrix. For this purpose, the computational grid representing the rock matrix was divided into concentric layers, whose thicknesses are given in Table 3-14. The total thickness of the simulated rock matrix is 250 mm. The series of calculations showed that for a very good agreement with the measured data (see Figure 3-21), it is sufficient to enter a reduced value of the effective diffusivity only in the fourth and fifth model layers. The change in effective diffusivity to a tenth of the initial value was made by changing the porosity, which means that from the fourth layer onwards the porosity is approximately five and a half times lower than in the first three layers. Therefore, a higher (measured) diffusivity value is used only in the first two and a quarter millimetres of the rock matrix, which is consistent with the theory that a Borehole Disturbed Zone (BDZ) was created around the borehole in which the experiment is located, with higher porosity and, accordingly, higher effective diffusivity. The effective diffusivity value stated in the task description was measured on samples from the drill core, i.e. not on intact rock. In this case, a continuous decrease in porosity with depth would probably be better than a steep decrease, but the idea behind it would not change.

Table 3-14. WPDE-2 – division of the rock matrix into layers.

Layer	Thickness [mm]
1	0.5
2	0.7
3	1.05
4	30
5	217.75

Figure 3-22 shows an analysis of the conformity with the measured data for the selected sorbing tracers. The simulation of all of the sorbing tracers is similar in relation to the measured data, so, in the interest of brevity, we will limit ourselves to a single one, Sr-85. It may be seen from the figure that, compared to a conservative tracer, the breakthrough curves are much more sensitive to the parameter of effective diffusion. It affects not only the rate of decline of the descending part of the curve, but also the maximum value and the time it is reached. Even for the sorbing tracer, a good agreement with the measured data was achieved by reducing the effective diffusivity to one tenth. This is important as it would be difficult to justify using different porosity values for different tracers in the same rock matrix (naturally, if there is no reason to assume anion exclusion). Interestingly, a very good agreement was also achieved when simulating a one-tenth value of the linear sorption distribution coefficient compared to the initial value. This could be justified by the fact that K_D is measured on the crushed part of the drill core, so lower values can be expected in intact rock. However, the reasoning for using a decrease in porosity (and the implied change in D_e) is more plausible as it is consistent for all of the tracers. As with HTO, the measured breakthrough curve for Sr-85 has a significantly faster onset than the simulated curves. The possible justifications are the same as those presented in the analysis of the results for HTO.
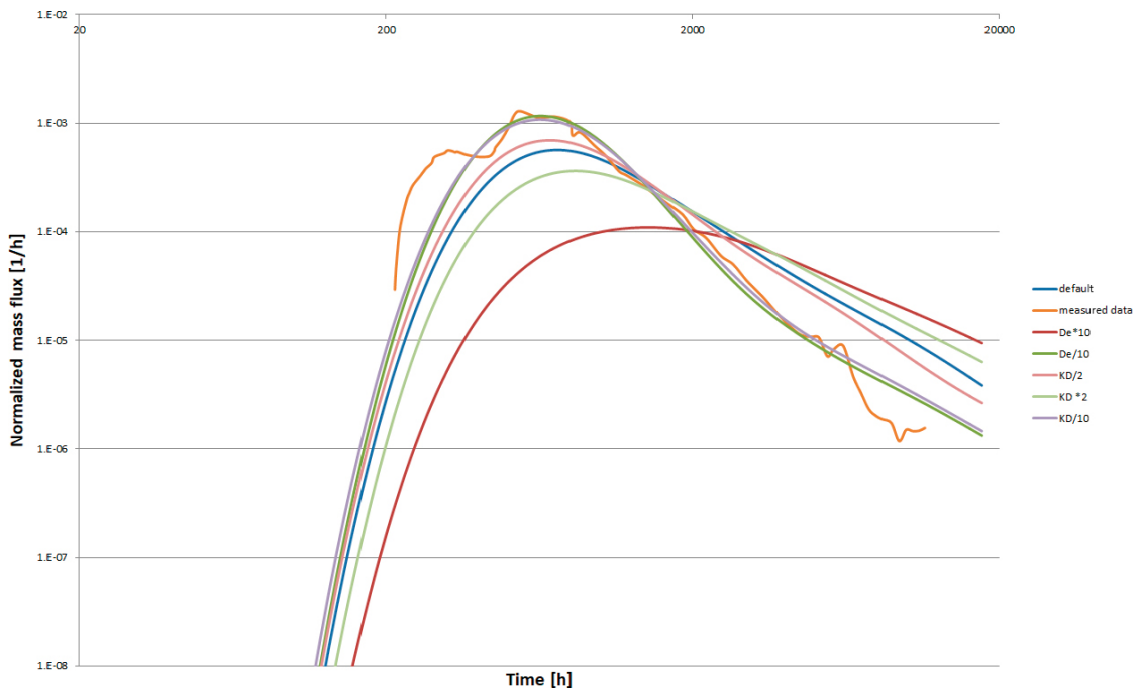
Figure 3-22. *WPDE-2 – Additional simulation, measured data – Sr-85.*

3.6　Additional analyses

3.6.1　Influence of the order of experiments

Both experiments (WPDE-1 and WPDE-2) were performed sequentially in the same experimental section. Since all three tracers from the first experiment were used in the second (together with the other two), it is necessary to verify how the residual amount in the rock matrix influences the result of the simulation. Figure 3-23 shows the result of this verification for HTO along with the measured data from both experiments. Simulations of both experiments were performed with a one-tenth value of effective diffusivity compared to the baseline (in the whole volume of rock matrix). The simulation periods specified in the task description could not be followed as the second experiment began during the simulation period of the first experiment. The timeline of this sequential model is based on real dating with only a small uncertainty consisting in the fact that it was not possible to trace exactly when the flow through the artificial fracture was changed (in the results of the simulation, the time of this change is very clear). However, the error in the estimation should be no more than a few days. From Figure 3-23 it is evident that there was a very good agreement between the model and measured data and that the non-zero leading edge value at the beginning of the WPDE-2 experiment was also explained. However, the residual amount of HTO present in the rock matrix prior to the start of the second experiment did not have an appreciable effect on the results of the model.

3.6.2　Influence of the discretisation of Flow123d

The strong influence of discretisation of the rock matrix in the vicinity of the fracture (i.e. at the interface of two environments with significantly different properties) was mentioned above. Figure 3-24 shows this effect for the strongest sorbing tracer, Ba-133. The green curve represents the result of a simulation performed on a basic variant of a discretisation mesh involving two thin layers of rock matrix elements surrounding a fracture that was used for all of the tracers (for a comparison see Section 3.3). Furthermore, the figure shows the results of simulations on modified meshes, where their gradual refinement results in shifting of the leading edge to the left, while decreasing the maximum mass flow value. By way of comparison, the figure also shows the result of the GoldSim model (Section 3.2.1 which approximates the results of the Flow123d model, which approaches a gradual refining of the computing mesh. The initial discretisation was sufficient to simulate weaker sorbing tracers, with the refinement of the mesh no longer having any noticeable effect. The best agreement with the measured data was achieved with a 4x finer mesh compared to the default variant, but it should not be taken too seriously, because the presented outputs are from a model with parameters
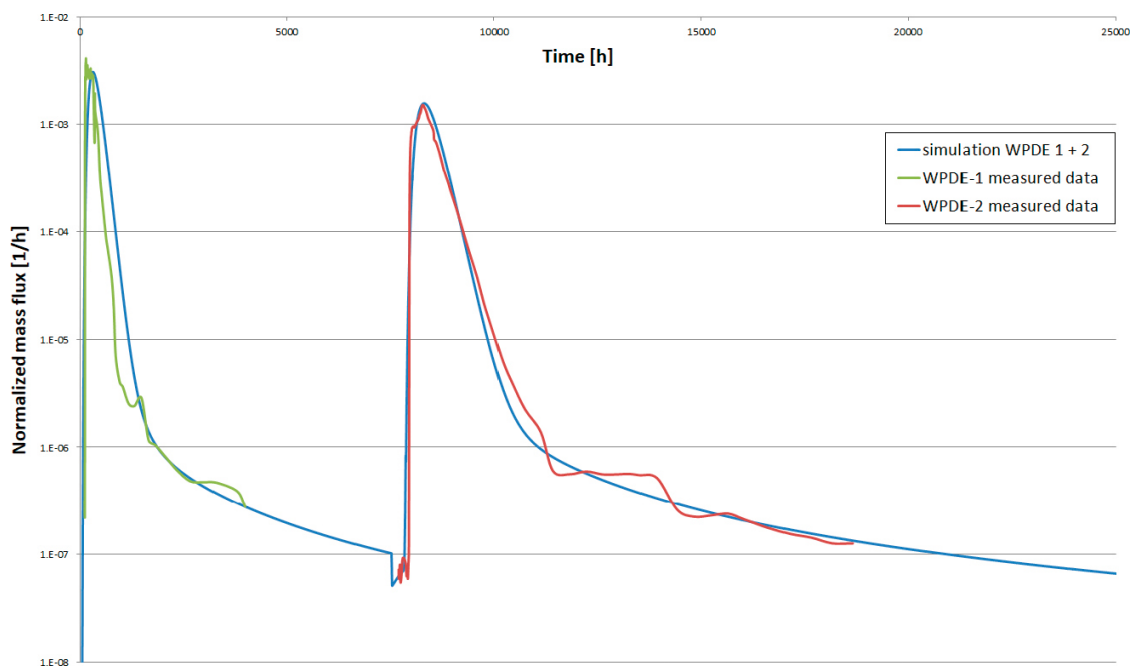
Figure 3-23. *WPDE – sequential simulation of both experiments – results – HTO.*
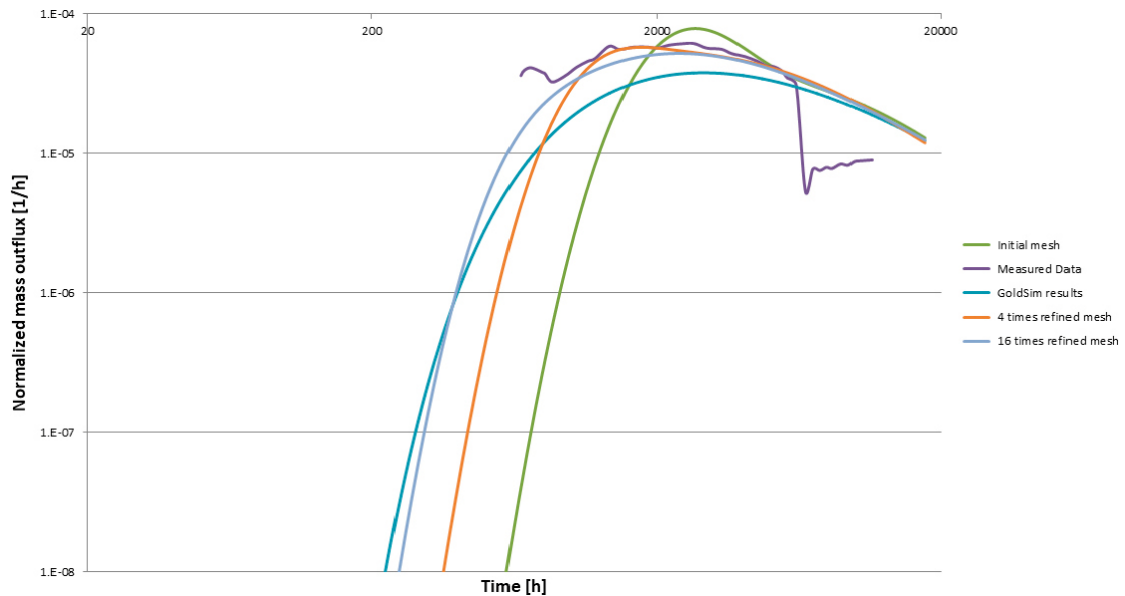
Figure 3-24. *WPDE-2 – Ba-133 – effect of discretisation, comparison between measured data and results of the GoldSim model.*

used for a blind prediction, i.e. without adjusting the effective diffusivity, which for the remaining tracers provided better compliance between the model and the measured data. From this comparison it can be concluded that increased attention should be paid to discretisation at the fracture/rock interface, especially when simulating the transport of several sorbent radionuclides. However, it cannot be said in advance what degree of discretisation is sufficient. It is definitely not advisable to use an exaggeratedly fine mesh, as a growing number of elements take their toll in the form of long computational times and memory requirements.

3.6.3   Influence of discretisation and variants in MT3D

An overview of selected alternative model variants is given in Table 3-15 (reduced relative to the complete set in the interim report Hokr et al. 2016). The following aspects of the solution were examined:

• In MT3DMS, transport parameters are entered exclusively into computational cells; however, some parameters (e.g. dispersivity) defined at the computational cell interface are entered to the numerical solution of the transport equation.

• In the standard version of MT3DMS (simulated variants without "HARM"), the parameters at the model cell interface are calculated as a weighted average of values, where the weight is the distance between the centres of the cells and the common interface.

• The basic model variants marked as "var0-HARM" were simulated in a modified version of MT3DMS, in which the parameters entering the dispersion term of the transport equation, i.e. dispersivity and diffusion coefficient at the interface of the model cells, are calculated as a harmonic mean of values in the cells.

Table 3-15. Overview of presented modified model variants.

Tracer	Identification and description of the model variants	
HTO	var0	Basic variant with dispersivity of 20 cm and a constant fracture, width of the first cell in the rock of 1 mm
	var0_DISP0	Variant with zero dispersivity and a constant fracture, width of the first cell in the rock of 1 mm
	var0_DISP100	Variant with reduced dispersivity of 10 cm and a constant fracture, width of the first cell in the rock of 1 mm
	var0_DISP280	Variant with increased dispersivity of 28 cm and a constant fracture, width of the first cell in the rock of 1 mm
	varAPER_DISP0	Variant with zero dispersivity and a fracture with a variable aperture, width of the first cell in the rock 1 mm, harmonic average of dispersion parameters at the boundary between the cells
Na-22	var0	Basic variant with dispersivity of 20 cm and a constant fracture, width of the first cell in the rock of 1 mm
	var0-HS	Basic variant with dispersivity of 20 cm and a constant fracture, width of the first cell in the rock of 1 mm, a thickened computer mesh with a width of the first cell in the rock of 0.1 mm
	var0-HARM	Basic variant with dispersivity of 20 cm and a constant fracture, width of the first cell in the rock of 1 mm, harmonic average of dispersion parameters at the boundary between the cells

Commentary on the effect of discretisation:

- In the case of sorbing tracers, such as Na-22, the result of the simulation in MT3DMS may be affected by a significant error due to improper discretisation mesh, see Figure 3-25. In the variant "var0" there is a clear overestimation of the transport processes taking place in the rock matrix and a significant slowdown of the breakthrough of the tracer by the experimental set-up. This is due to the combination of several phenomena – the order of magnitude differences in parameter values between adjacent fracture-rock cells, the same cell size at the fracture-rock interface, and the numerical solution of the transport equation used in MT3DMS. In order to suppress this error and to refine the simulation, it is necessary to refine (make denser) the computational mesh in places where the order differences of values of transport parameters are entered, i.e. at the interface of the rock fracture. A more precise result is presented in variant "var0-HS", in which the size of the computational cells (to 0.1 mm) at the interface of the rock matrix with the artificial fracture is reduced 10 times.

- A very similar result as in variant "var0 HS", but on the model with the original unrefined mesh, was achieved in the modified version of MT3DMS with harmonic averaging of parameters – see the breakthrough curve of variant "var0 HARM".

Comment on the effect of dispersion (Figure 3-26):

- Modified variants are presented for the HTO tracer and for the dispersivity values of 0, 100 and 280 mm ("DISP0", "DISP100" and "DISP280").

- Lower dispersion is expected to cause a narrowing of the breakthrough curve in the introductory "advection-dispersion" section and an increase in maximum value (and vice versa a higher dispersion leads to a widening of the curve and a lower "peak").

- The change in dispersion is not expected to affect the slope of the breakthrough curve in the "diffusion-sorption" part.

- In variant "varAPER_DISP0" (Figure 3-26), the effect of dispersion in the fracture was simulated for the HTO tracer by means of the variable aperture of the fracture. The dispersivity was set to zero, the uneven aperture was simulated in such a way that the artificial fracture is not completely symmetrical with a constant aperture of 1.25 mm – half the cross-sectional area of the fracture was left with an aperture of 1.25 mm, a quarter with less aperture 0.25 mm and with a larger aperture of 2.25 mm. The results show a very similar curve of the breakthrough curve as in the variant with the given dispersion "DISP_100" (the aperture variability replaces the given dispersion), but with a steeper onset caused by the preferential flow in the profile with a larger aperture.
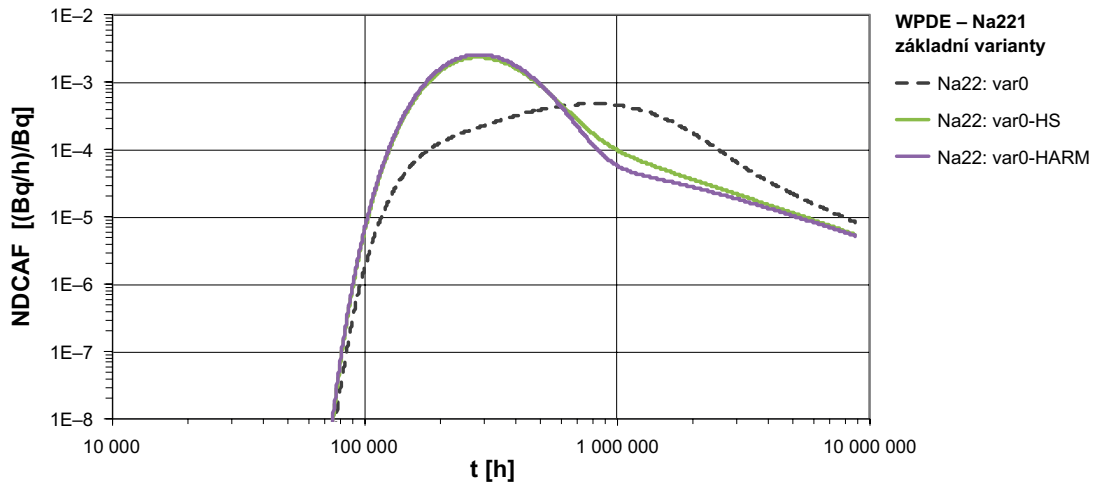
Figure 3-25. *Effect of the model discretisation on the course of the breakthrough curve for Na-22 (var0).*
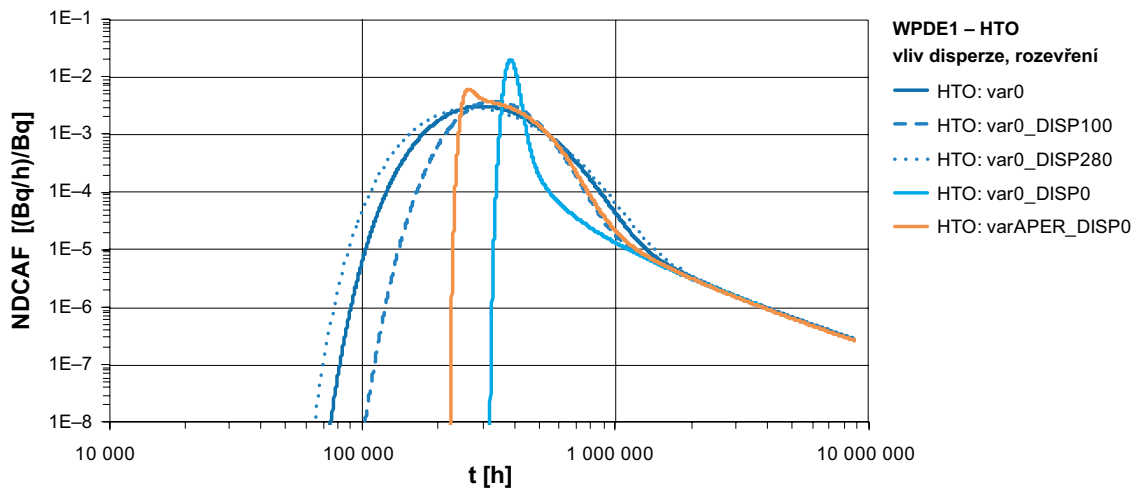
Figure 3-26. *Effect of dispersion and aperture of the fracture on the course of the breakthrough curve of HTO.*

3.7 Conclusions from the modelling of WPDE

Simulations of the WPDE experiments may generally be used to deduce several conclusions for the models of transport processes in a fractured porous environment. Considering that advective flow dominates in fractures and that the rock matrix has the function mainly of retardation mechanisms of molecular diffusion and sorption, it is possible to state that:

- For conservative tracers – the molecular diffusion parameter has no significant effect on the retardation rate. If the source of the tracer in the model is represented by an initial concentration distribution or a time-limited source element, then the effect of the effective diffusivity value is significant for the character of the falling edge of the breakthrough curve.

- For sorbing tracers – both molecular diffusion and linear sorption parameters have a strong influence on the retardation rate (higher effective diffusivity and higher distribution coefficient of linear sorption both mean a higher retardation rate). If both of these parameters are used to calibrate the model, the equivalence of the models is evident. Any possible change in the parameter value must be physically justifiable.

- Parameter values – if the values tabulated in the available literature are used in the simulation, it should be understood how they were measured. Values obtained from the crushed core samples are unlikely to be the same as from intact rock.

- EDZ, BDZ – if the transport processes are simulated in an environment where boreholes or tunnels are located, it is likely that the rock will be disturbed in their immediate vicinity and that in this disturbance zone the rock matrix will have different parameters (both diffusion and sorption).

- Discretisation – greater attention should be paid to discretisation at the fracture/rock interface, especially when simulating the transport of stronger sorbing tracers. It may have a significant effect on the accuracy of the outputs of the model.

4 Solution of task LTDE-SD (Task 9B)

This chapter describes the solution of Task 9B based on the data from the LTDE-SD experiment. The task description is referred to in the GWFTS documentation. It focuses primarily on inverse modelling and, as in the case of Task 9A, a comparison between investigators on fixed data is performed as the initial step. Unlike sub-tasks 9A and 9C, the measured data were published by SKB before the start of the project and therefore known to the investigators.

The solution presented in this chapter was developed before the task coordinators within GWFTS revised the interpretation of several of the measurements. In particular, distinguishing relevant data and "background" in the activity values led to disappearance of the long tails at low concentrations for the strongly sorbing tracers. The revision of the measured data was distributed at a time when the investigators' participation in other sub-tasks 9C and 9D was in the project schedule. New inverse problem calculations were not required based on executive meetings decisions. The data update was reflected in a separate solution using the micro-DFN concept in the framework of the next Chapter 5, which was performed throughout the implementation of the project.

4.1 Summary of the task description and the data

The LDTE-SD experiment was conducted in the Äspö underground laboratory in Sweden (Nilsson et al. 2010, Löfgren and Nilsson 2020). The subject of the experiment was observation of the diffusion transport of radionuclides in the rock (granodiorite) matrix in-situ at a depth corresponding to the concept of the DGR. A significant aspect is the large number of radioactive tracers used with different migration and geochemical characteristics and the relation of matrix conditions within a compact block and the potentially disrupted or altered matrix adjacent to the fracture – in the experiment there were two volumes of tracer cocktails in two locations (around the borehole and around the fracture), which were interconnected and mixed (Figure 4-1). The available data from the experiment are the evolution of the concentration (activity) of the tracer in the reservoir and the profiles of the concentrations (activity) of the tracers in the rock obtained from differently located drill cores from the point of contact with the solution towards the rock. The cores around the fracture (the "stub" section) are marked A, and the cores from around the borehole (the "slim hole") are marked D (Figure 4-2).

The task description of Task 9B is defined in the report (Löfgren and Nilsson 2020), which states the essential aspects of the modelled experiment. These include the specific steps of injecting the solution into volumes in contact with the rock, the materials used, the drilling procedure after completion of the experiment, and the sample division plan (for guidance, see Figure 4-3). Nevertheless, a number of uncertainties remained in the methodology regarding the possibility of artificially influencing transport and detected concentrations by an experimental procedure (which was discussed during the project at meetings of GWFTS). The aim of the modelling is to explain the observed concentrations through understanding the ongoing phenomena, with the motivation to design alternative conceptual models or to consider unplanned effects in the experiment.

The task description is divided into two phases, closely linked:

- 9B-1: Modelling of the transport of six radionuclides in two selected A profiles and two D profiles, with the aim of fitting the concentration distribution in the rock along the length of the profile after dismantling, using the time course of the concentration in the reservoir (tank) as input data. As described in Löfgren and Nilsson (2020).

- 9B-2: Modelling the experiment as a whole, i.e. fitting both the profiles and the time course, using only the total initial activity as input data. The task description also extends the number of considered radionuclides. As described in Löfgren and Nilsson (2020).

- The aim of 9B-3 was to predict the concentration distribution in cores not yet analysed. As described in Löfgren and Nilsson (2020).

The second case, therefore, also includes the question of the balance of the tracers, which in some cases proved to be problematic (e.g. detection of only part of the injected amount).
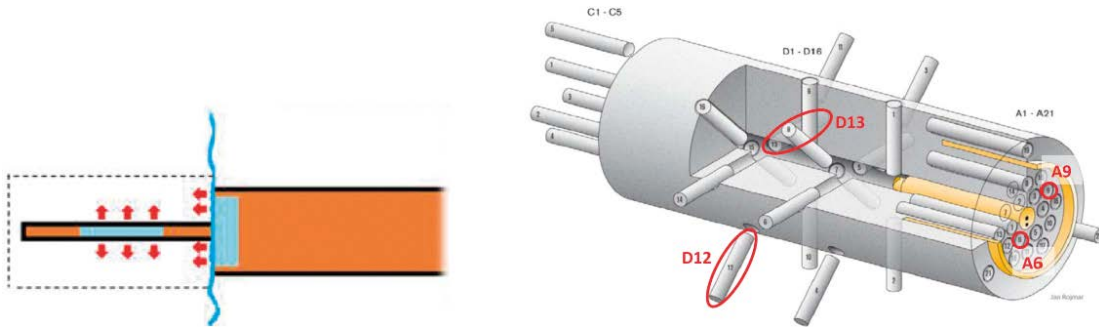
Figure 4-1. *Configuration of the LTDE-SD experiment: Left: boreholes intersecting the fracture, placement of the radionuclide solution, direction of migration and position of the drill block. Right: configuration of core drilling sampling and selection of the profile for Task 9B-1 (below). In yellow, the insulation separating the 177 mm core area that was in contact with the radionuclides while the exterior should theoretically be unaffected. (Löfgren and Nilsson 2020).*
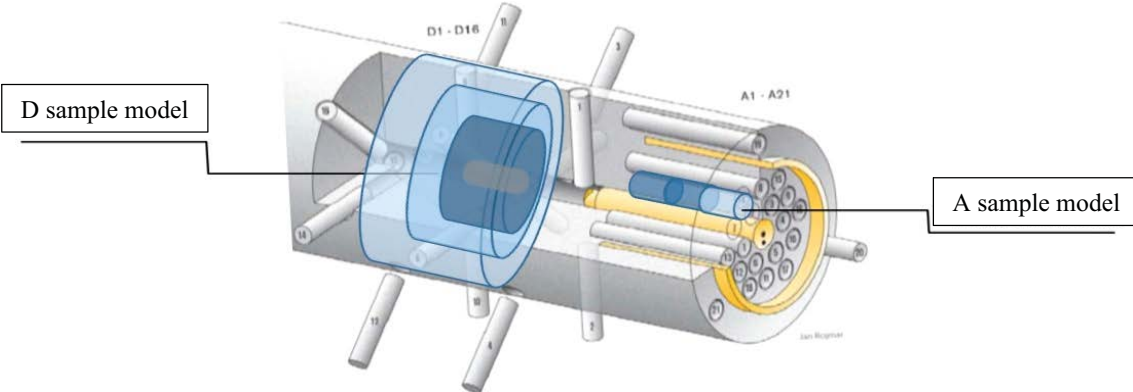
Figure 4-2. *Configuration of the LTDE-SD experiment showing the geometric significance of the models for two sample types (axisymmetric for D and one-dimensional for A).*
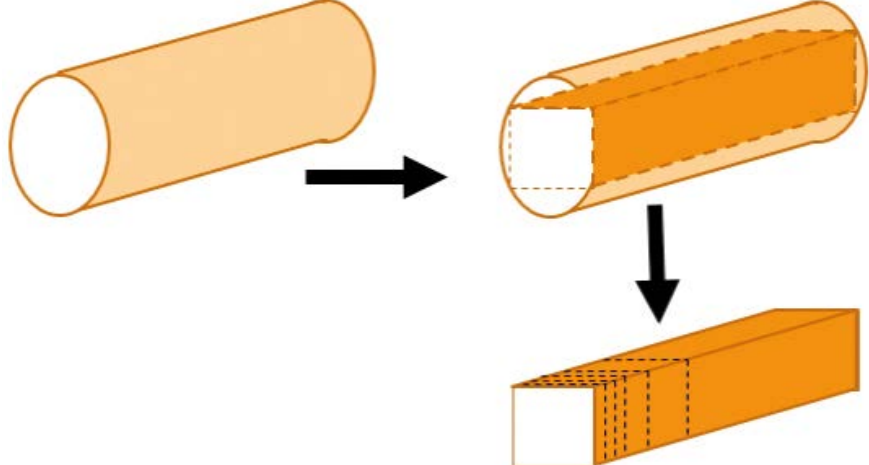
Figure 4-3. *Diagram of the preparation of the analysed samples from the drill core (taken from Löfgren and Nilsson 2020).*

Table 4-1. Parameters (distribution coefficient, formation factor, and porosity) used for the initial calculations of the comparison of models on profiles A and D of the LTDE-SD experiment, according to Nilsson et al. (2010).

	K_d [m³/kg]				F_f [-]	$Por.$ [-]
	Na-22	Cl-36	Ni-36	Cs-137		
A-profile (fracture)	1.20E−04	1.00E−08	1.60E−01	4.80E−01	4.80E−04	5.00E−02
D-profile (borehole)	2.90E−04	1.00E−08	1.50E−02	2.20E−02	2.20E−05	2.10E−03

Figure 4-4 shows the dimensions and location of the experimental sections (their contact with the rock is highlighted in red) and the packers. A 26 mm diameter seal was coaxially placed in the borehole experimental section, the volume of this experimental section was 146 ml, the area (surface of the cylinder shell) of its contact with the fracture was 0.034 m². The thickness of the fracture experimental section was 3.25 mm, its volume was 80 ml and the area (the content of annulus) of its contact with the rock was 0.0236 m². The experimental sections were interconnected, and there was forced circulation during the experiment. Their total volume, including the supply piping and other operating parts, was 1 140 ml.

A known initial amount of tracer was dissolved in the solution that circulated through the experimental sections for a specified period of time. Tracers diffused into the rock matrix, where some were additionally sorbed. At the end of the experiment, the rock around was drilled out and after some time the samples were cut and analysed. Thereby, activity profiles (concentrations) of the individual tracers with depth (distance from the contact with the solution) were obtained.

The results of the experiment are interesting because the measured concentration profiles were different than expected. A predictive model of concentration profiles is described in Widestrand et al. (2010) and an inverse model is described in Nilsson et al. (2010). The final parameter values are shown in Table 4-1. Regardless of the selected parameters, the difference between the model results and the measured profiles was considerable (Figure 4-5). Both models used Fick's diffusion in a homogeneous medium together with linear sorption.
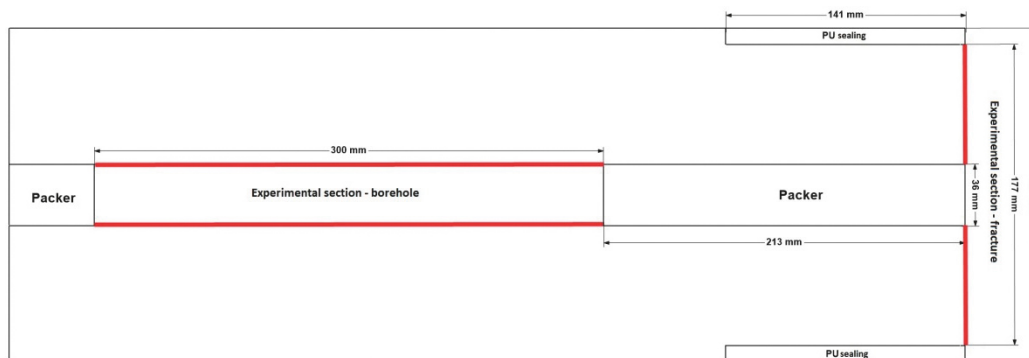
Figure 4-4. *LTDE-SD – dimensions and locations of the experimental sections.*
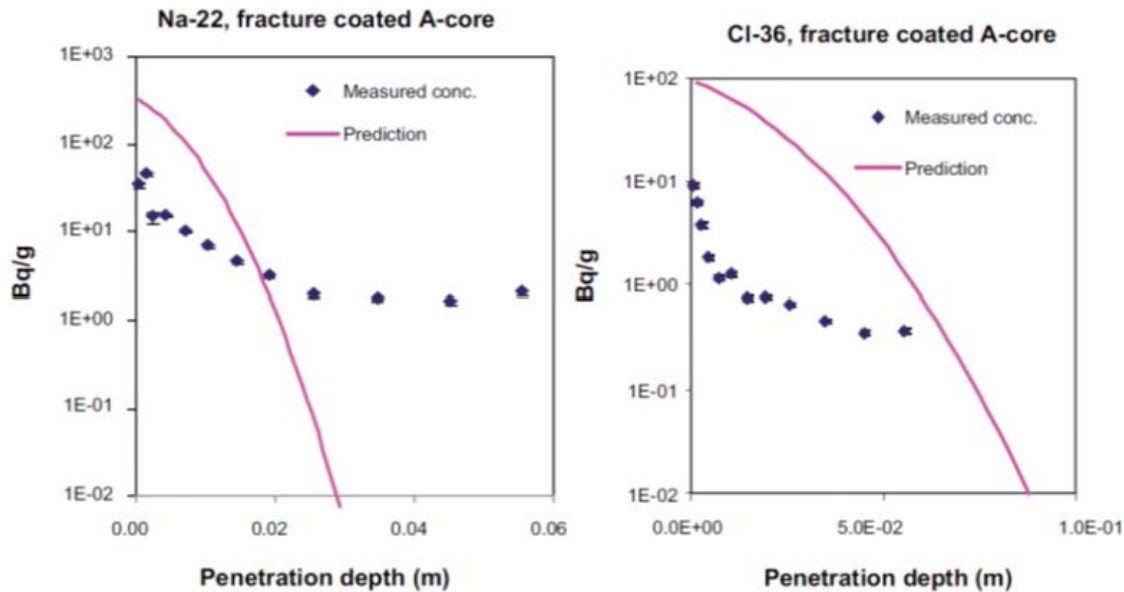
Figure 4-5. *Results of the in-situ diffusion experiment LTDE-SD – concentration profiles for Na-22 and Cl-36. Measured data vs the model. Taken from Nilsson et al. (2010, Figures 4-1a and 4-2a).*

4.2 Comparison of models in the introductory example

The concept of the task description, in terms of finding alternative conceptual models and calibrating the parameters leading to optimal model compliance with the measurement, is not suitable for a specific comparison of software programs with each other. For the needs of SÚRAO in this sub-project, we added a "preparatory" task with fixed data to the task description of GWFTS, in otherwise identical conditions of the task description of Task 9B-1. This made it possible to compare the software in a solution of a similar conceptual model, to check the correct understanding of the physical meaning of the input parameters (with respect to the software inputs), without the ambition of the model results matching the experiment.

The calculation is similar to the initial modelling performed by the LTDE-SD implementation team (Nilsson et al. 2010, Chapter 4), from which the input data are used and, therefore, it is possible to compare with these results.

The model considers diffusion and sorption in a homogeneous rock matrix in the geometry of either 1D perpendicular to the fracture for the A profile or 1D radially (axially symmetrical model) for the D profile. The length was chosen as a distance exceeding the expected range of migration, in the range of 100 to 300 mm (the investigators' choice was limited by computational demands). The borehole radius in the radial model was 18 mm. The specific implementations and settings in each software program and the parameters used are outlined in the main features, with further details in the interim report (Hokr et al. 2016) and in relation to the solution of the inverse model 9B-1, which was based on the same configuration (Sections 4.3 and 4.4).

4.2.1 Input data

The rock parameters are given in Table 4-1, taken from the report Nilsson et al. (2010). Sorption coefficients were differentiated for radionuclides, and other parameters were common. The original value of the Cl-36 was several orders of magnitude higher and we consider this an error. The sense of the assumed value of 10^{-8} is understood only to be a formal choice of a number close to zero. The diffusion coefficient in free water was the same for all of the radionuclides (2×10^{-9} m^2/s), i.e. D_e was also the same for all radionuclides.

How the process of dismantling the experiment after the end of the contact of the tracer cocktail with the rock affects the ongoing diffusion transport and the meaning of the resulting analyses in relation to the interpreted diffusion in the in-situ phase proved to be quite demanding with a number of ambiguities. Table 4-2 shows the times of different types of rock handling. The analysis of possible

influences was not the subject of this comparison, but it was possible to estimate how much the ongoing diffusion after rock extraction under ideal conditions would affect the resulting profile. Therefore, points have been chosen that represent the main changes in the theoretical configuration of the model:

- b.c.1: in-situ experiment with contact with the tracer
- b.c.2: separate rock block without contact (insulated or uninsulated)
- b.c.3: separate individual micro-boreholes

In the comparative calculation, only the first phase was separated and the remaining time was set in the form of a boundary condition on the area of contact with the tracer (no further changes in geometry were considered). Outputs were made at three points, the first of which was a factual comparison with the calculations of Nilsson et al. (2010), i.e. approximately 200 days, another two after two phases of further ongoing diffusion, where a tendency towards measured profile shapes can be expected.

Table 4-2. Selection of key moments of the experiment and analysis, as identified from various sources, and the related changes in transport conditions. The last column shows the corresponding possible changes to the boundary conditions of the model (see Section 4.2.1).

		Day from the start	Day after the end	Data in the task description	Results	Boundary condition
Start of the cocktail	27/09/2006					b.c. 1
End of the cocktail	12/04/2007	197	0		model point 1 (equi. 196–198 d)	
Drilling out	26/04/2007	211				
Covering with epoxy resin	03/08/2007	310			model point 2	b.c. 2
Separation	06/08/2007	313				b.c. 3
Start of the micro-borehole	08/08/2007	315				
End of the micro-borehole	13/08/2007	320	123	120		
Start of the cutting	01/12/2007	430				End of diffusion
Cutting	31/12/2007	460	263	240–290 (p.265)		
Cutting	02/01/2008	462	265		model point 3 (equi. 460–470 d)	
End of the cutting	31/01/2008	491				

4.2.2 Results of the comparison

The calculation was performed for eight variants – four radionuclides with different parameters on two geometries corresponding to the groups of profiles A (perpendicular from the fracture) and D (radially from the borehole). There are three outputs for each time point. The whole set of calculations was performed by Flow123d (TUL) and GoldSim (Cell Net variant – CTU), two were selected also for MT3DMS (PROGEO). The results are shown against the background of the measured profile data used for Task 9B-1 (indicative comparison) and compared to the results of Nilsson et al. (2010), corresponding to the simulation after 197 days (the data were only graphically read from the original figures).

Out of a total of eight, only five variants are presented, due to the similarity between profiles A and D of the sorbent tracers. The four cases of the A-sections are shown in Figure 4-6 to Figure 4-9 and both calculated variants of MT3DMS are included, the second being the D-profile of Cl-36 (Figure 4-10). The results are in reasonable agreement with each other, although there are certain differences in the slope of the profiles. The results of Nilsson et al. (2010) have a steeper profile in most cases, but here we do not have full control over the uniformity of the model inputs. For the results of TUL, CTU and PROGEO, if there is a difference, then it is in the part of the curve with lower values. If we take into

account that these numbers are several orders of magnitude less than the maximum (specified boundary condition), they may be caused only by the inaccuracy of the numerical algorithm, or the effect of the difference of the boundary conditions of zero flow and zero concentration or the distance of the boundary condition.

In all cases, we can observe the time development during the experiment (up to 197 d) and between the dismantling and analyses (up to 460 d). The diffusion taking place later on changes the profile to a shape closer to the analysed profiles, but the change is far from sufficient to fully explain the difference.
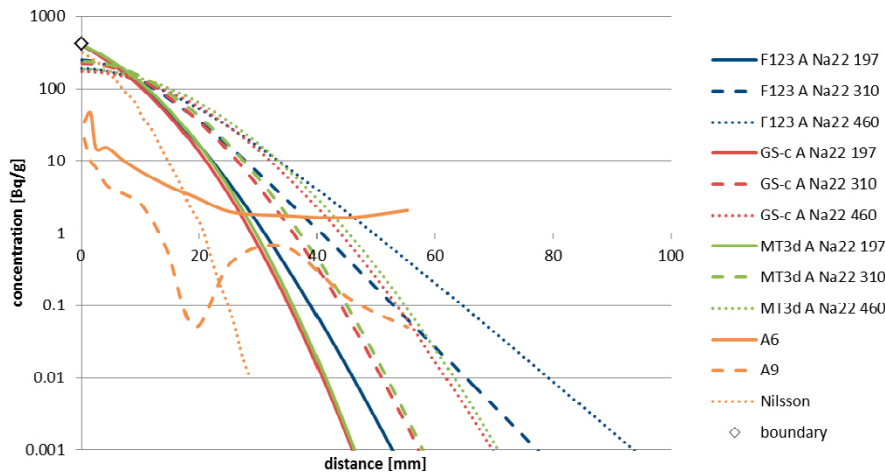
Figure 4-6. *Comparison of profiles of Na-22 calculated by Flow123d, GoldSim (Cell Net) and MT3DMS for Type A and times 197 d, 310 d and 460 d, versus the measurement of profiles A6 and A9 and the original calculation in Nilsson et al. (2010).*
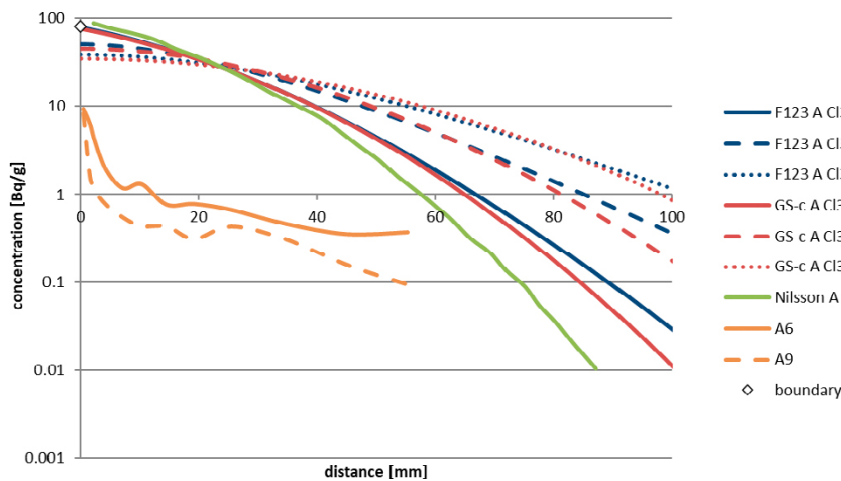
Figure 4-7. *Comparison of profiles of Cl-36 calculated by Flow123d, GoldSim (Cell Net) for Type A and times 197 d, 310 d and 460 d, versus the measurement of profiles A6 and A9 and the original calculation in Nilsson et al. (2010).*
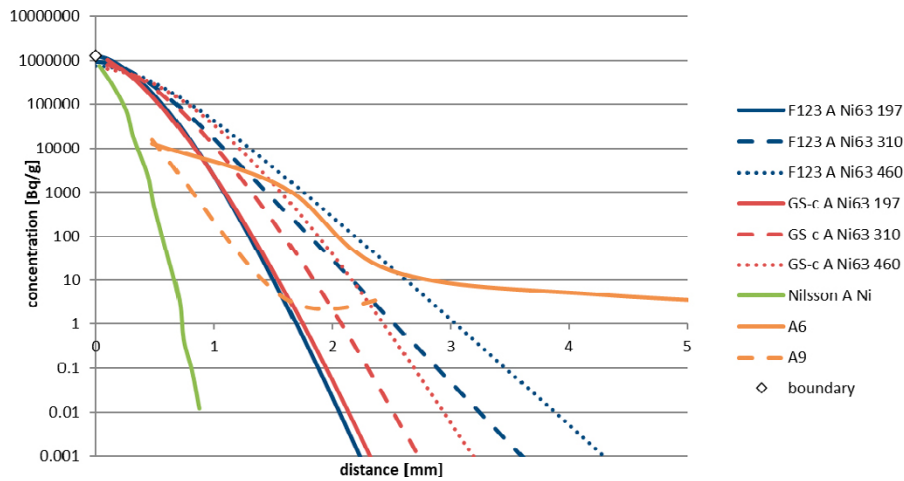
Figure 4-8. *Comparison of profiles of Ni-63 calculated by Flow123d, GoldSim (Cell Net) for Type A and times 197 d, 310 d and 460 d, versus the measurement of profiles A6 and A9 and the original calculation in Nilsson et al. (2010).*
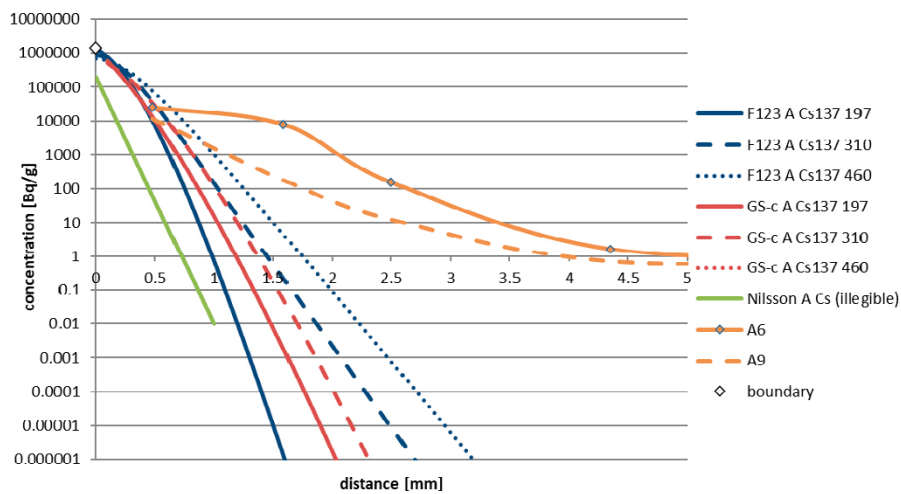
Figure 4-9. *Comparison of profiles of Cs-137 calculated by Flow123d, GoldSim (Cell Net) for Type A and times 197 d, 310 d and 460 d, versus the measurement of profiles A6 and A9 and the original calculation in Nilsson et al. (2010).*
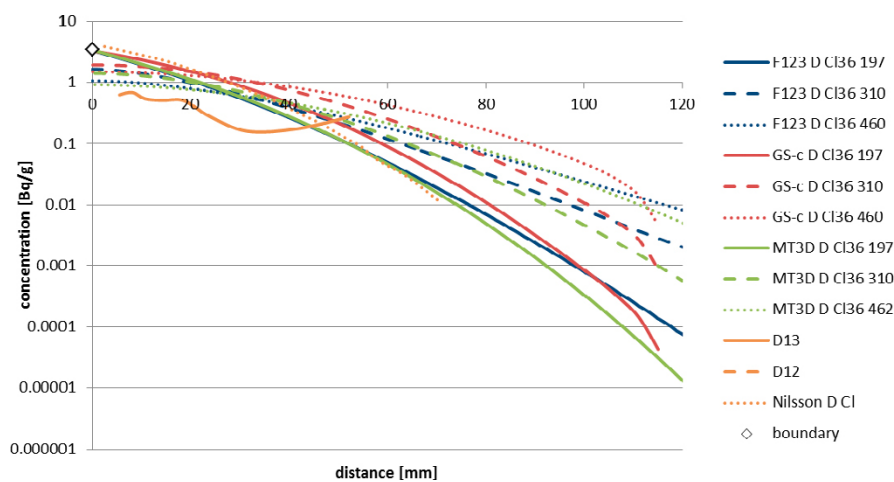
Figure 4-10. *Comparison of profiles of Cl-36 calculated by Flow123d, GoldSim (Cell Net) and MT3DMS for Type D and times 197 d, 310 d and 460 d, versus the measurement of profiles D12 and D13 and the original calculation in Nilsson et al. (2010).*

4.3 Inverse model in Flow123d

During the simulation of the experiment, we first used a model with diffusion and linear sorption in a homogeneous medium. Outputs of the model (concentration profiles) agreed qualitatively with the courses shown in purple in Figure 4-5 as expected and are also presented in the previous Section 4.2. This confirmed that a certain degree of heterogeneity needs to be introduced into the model to improve agreement with the measured data.

In accordance with the instructions of the coordinators of GWFTS, the simulations were divided into two stages:

- Stage 1 – the task was to replicate the measured concentration (activity) profiles in the rock matrix. Tracer concentrations in the solution (their development over time) taken from the task description (Löfgren and Nilsson 2020) – measured values as input data.

- Stage 2 – takes over the parameters from Stage 1. The model was extended by simulating the development of tracer concentrations in the solutions, the mass balance was monitored.

4.3.1 Stage 1

Six tracers (Na-22, Cl-36, Co-57, Ni-63, Ba-133 and Cs-137) were simulated. For each of them four measured profiles were used, two drilled from the experimental section – fracture (core A) and two from the experimental section – borehole (core D). We only used profiles from A cores to calibrate the model in the first stage, as their simulations could be performed in 1D, which resulted in significant time savings in launching multiple models associated with the calibration. The character of the measured concentration profiles is the same for both A and D cores, and we assumed that the model parameters obtained during calibration of the A cores will also be transferable to the D cores.

Efforts to model the measured profiles were based on the assumption of a disturbance zone near the borehole (BDZ). So we considered the rock as being heterogeneous in terms of the parameters continuously changing with increasing depth (distance from borehole/fracture plane).

The geometry of the model is a line 0.1475 m long. Its computer mesh is equidistant with a step of 0.1 mm. The model domain was divided into three sub-domains (physical groups) to give us more degrees of freedom while prescribing the parameters of the model. The boundaries between the sub-domains were defined at a depth of 3 and 25 mm (or 3 and 30 mm for Cl-36).

Diffusion and linear sorption processes were simulated.

The simulation period was 434 days. The rock matrix was in contact with the solution for the first 189 days. For the rest of the period, only diffusion in the matrix itself with zero mass flow across the border is simulated (the total amount of the individual tracers in the matrix no longer changes). This covers both the experiment itself and the time between the end of the experiment and the analysis of the samples, during which the cores were packaged and stored.

The transport of tracers (radionuclides) in the rock matrix is controlled by three parameters (porosity, effective diffusivity and a distribution coefficient of linear sorption). Their values were subject to calibration, which was performed manually to reflect the trend of the measured concentration profiles rather than their exact values, in which case a more suitable calibration would be automatic.

Radioactive decay was not considered, since all of the measured activities reported in the task description were converted to values that would correspond to a non-decaying tracer (decay corrected).

The porosity was considered to be linearly decreasing with increasing depth (distance from the borehole wall) in the first two physical groups, while the third remains constant. Its values, as results of the calibration, are given in Table 4-3 and are shown in Figure 4-11. Importantly, the same porosity value was used for all of the tracers, except for Cl-36, where we assume anion exclusion.

The distribution coefficient of linear sorption also decreased with increasing depth: steeply in the first physical group, slower (or not at all) in the second, and in the third it remained constant. Cl-36 was simulated as a conservative tracer. Its values (results of the calibration process) are shown in Figure 4-12 (depending on depth, for the first two physical groups).

Table 4-3. LTDE-SD – dependence of the porosity value on depth (distance from the borehole wall).

Depth [m]	Porosity [-]	Depth [m]	Porosity Cl-36 [-]
0	0.02	0	0.01
0.003	0.005	0.003	0.001
0.025	0.002	0.03	0.0005
0.1475	0.002	0.1475	0.0005
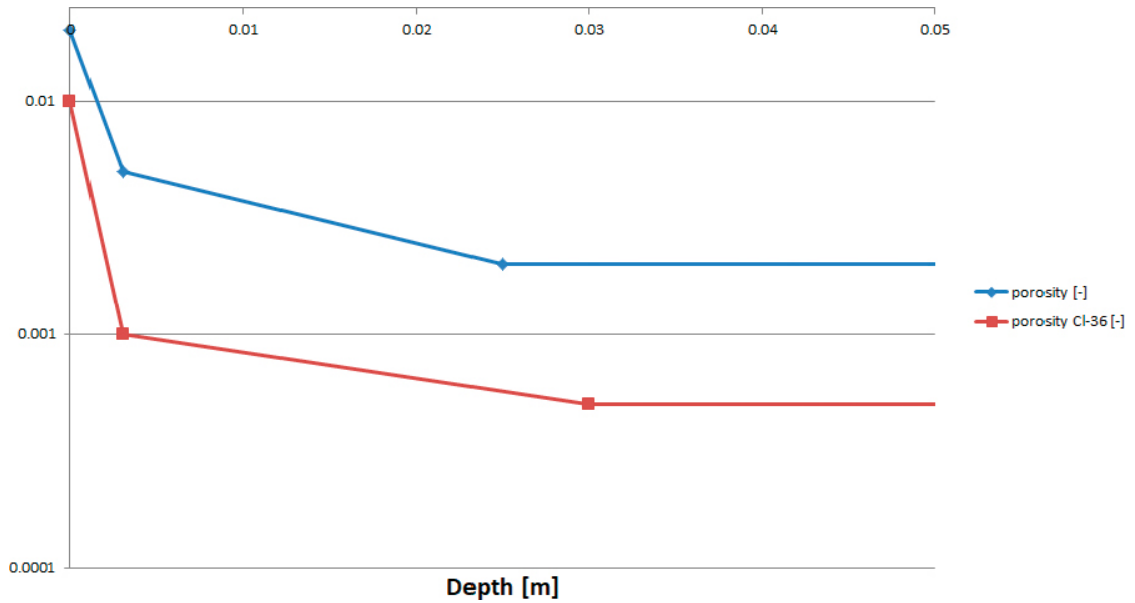
Figure 4-11. *LTDE-SD – dependence of the porosity value on depth (distance from the borehole wall).*
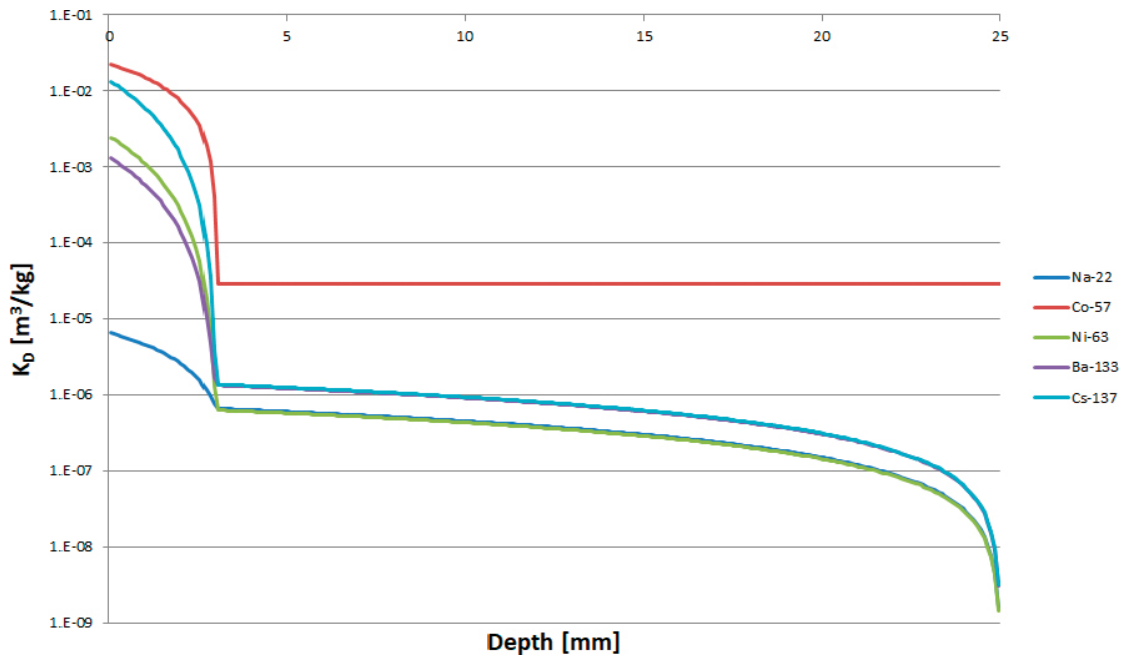
Figure 4-12. *LTDE-SD – dependence of the value of distribution coefficient of linear sorption on depth (distance from the borehole wall).*

The last parameter is effective diffusivity, which is calculated from the diffusivity in free water, the geometric factor and porosity. The diffusivity value in open water is always constant for all of the tracers throughout the calculation area (Table 4-4, the results of the calibration process). Since the value of effective diffusivity is dependent on the porosity, whose value varies with depth, the value of effective diffusivity also varies with depth.

Table 4-4. LTDE-SD – values of diffusivity in free water for the individual tracers.

Tracer	Diffusivity in free water [m²/s]
Na-22	5e−10
Cl-36	1.462e−9
Co-57	2e−9
Ni-63	5e−10
Ba-133	2e−9
Cs-137	2e−9

Figure 4-13, Figure 4-14, Figure 4-15, Figure 4-16, Figure 4-17 and Figure 4-18 show the simulated concentration profiles (results of the calibrated model) along with the profiles measured on the A6 and A9 cores. Each figure includes the profiles on a linear scale, which better documents the development (steep decrease) of the concentrations in the first few millimetres of the rock matrix, and on the right a logarithmic scale, which better shows the agreement of the model with the data measured further away from contact of the rock with the tracer solution. The measured concentration profiles were tabulated in units [Bq/g]. Outputs of the model, concentrations in the liquid phase, had to be recalculated according to the relation:

$$c = c_l \cdot a \cdot \frac{n + K_D \cdot \rho_S}{\rho_l \cdot n + \rho_S},$$

where c [Bq/g] is the resulting concentration, c_l [kg/m³] is the liquid phase concentration (output of Flow123d), a [Bq/g] is the specific activity, K_D [kg/m³] is the linear sorption distribution coefficient, n [-] is the porosity, ρ_S [kg/m³] is the density of the rock and ρ_l [kg/m³] is the density of the liquid (water).

It can be said that a relatively good agreement with the measured data was achieved. A better agreement could be achieved by further calibrating or dividing the computational domain into more than three physical groups, which would increase the number of degrees of model freedom (calibratable parameters). However, since the accuracy with which the profiles were measured is debatable (as is evident, for example, in the oscillations in the measured data), it would not make much sense to aim for a better agreement. The essential thing is to describe the trend.

The realistic nature of the parameters used, which were obtained by the manual calibration process, remains an open question. The decrease in porosity and distribution coefficient of the linear sorption in the first layers of the simulation domain is explained by the presence of the BDZ – near the contact with the tracer solution, the rock may be disrupted by the work accompanying the preparation of the experiment. This may cause an increase in the porosity and, consequently, an increase in the sorption coefficient caused by the larger available sorption surface.

It should be noted that, as implied by the principle of equifinality, the combination of parameters found is probably not the only one that will provide a good agreement between the model and the measured data. For example, it is possible that the decrease in porosity should be steeper, while with a decrease in sorption, the parameter should be more moderate.

In order to verify whether the parameters used in the model are meaningful, the apparent diffusivity (including its development in dependence on depth) was calculated for each tracer according to the relation:

$$D_a = D_w \cdot \frac{\tau}{R} = D_w \cdot \frac{\tau}{1 + \frac{\rho_S \cdot K_D}{n}},$$

where R [-] is retardation. The apparent diffusivity shall not be higher than the diffusivity in open water for any of the tracers at any depth. Confirmation of this is shown in Table 4-5. This does not naturally prove that the used parameters are correct, only that they do not conflict with the physical ones.

Table 4-5. LTDE-SD – comparison of maximum apparent diffusivity with diffusivity in open water.

Tracer	Diffusivity in open water [m²/s]	Apparent diffusivity [m²/s] – maximum
Na-22	5e−10	7.21e−11
Cl-36	1.462e−9	3.13e−10
Co-57	2e−9	6.48e−12
Ni-63	5e−10	6.30e−11
Ba-133	2e−9	2.52e−10
Cs-137	2e−9	2.52e−10
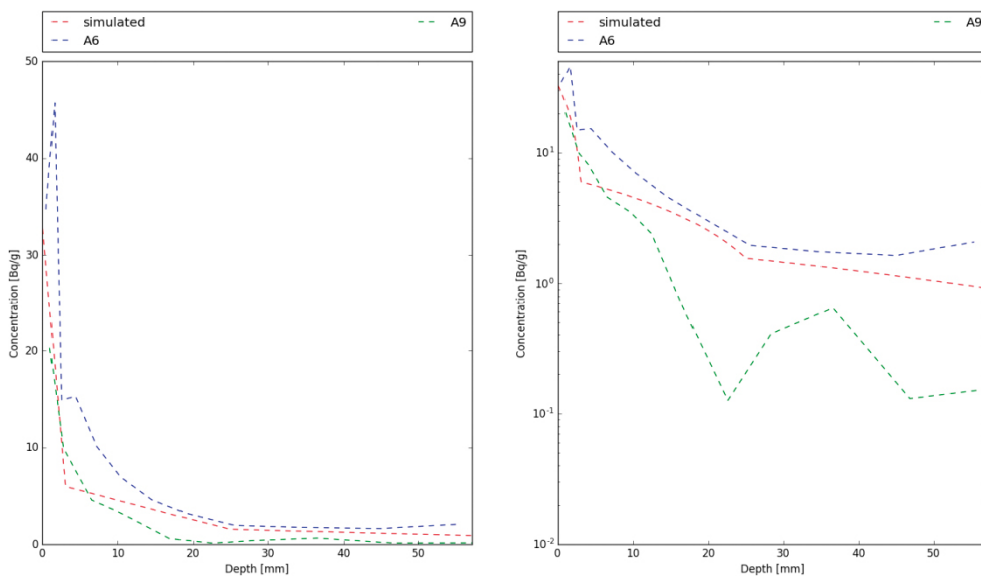
Figure 4-13. LTDE-SD – concentration profiles in the rock in a linear (left) and logarithmic (right) scale – Na-22.
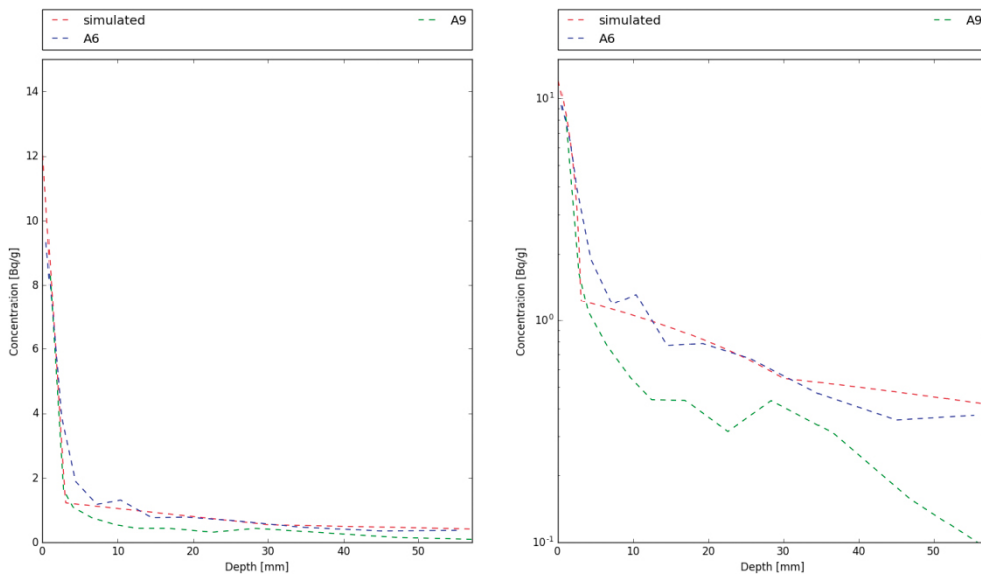
Figure 4-14. LTDE-SD – concentration profiles in the rock in a linear (left) and logarithmic (right) scale – Cl-36.
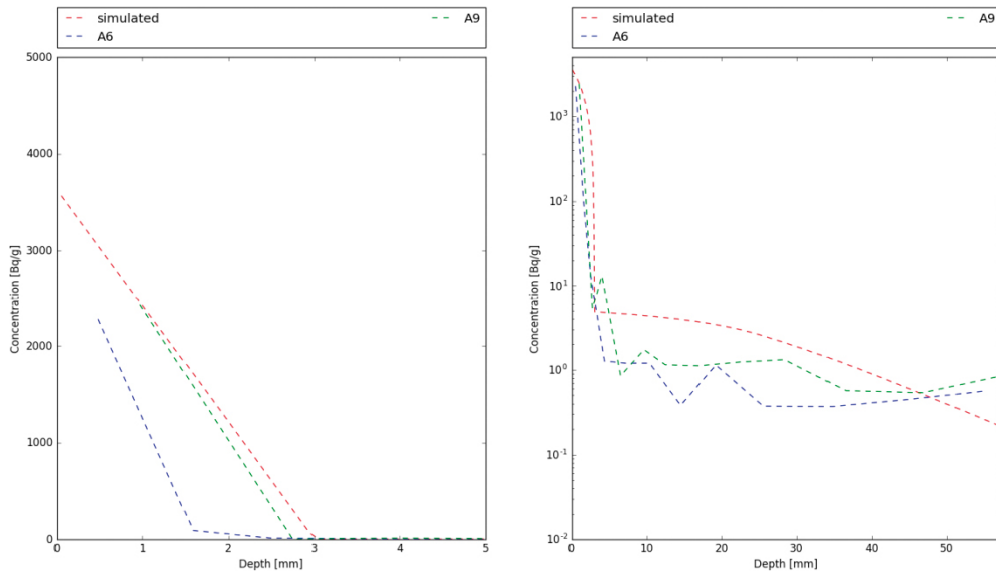
Figure 4-15. *LTDE-SD – concentration profiles in the rock in a linear (left) and logarithmic (right) scale – Co-57.*
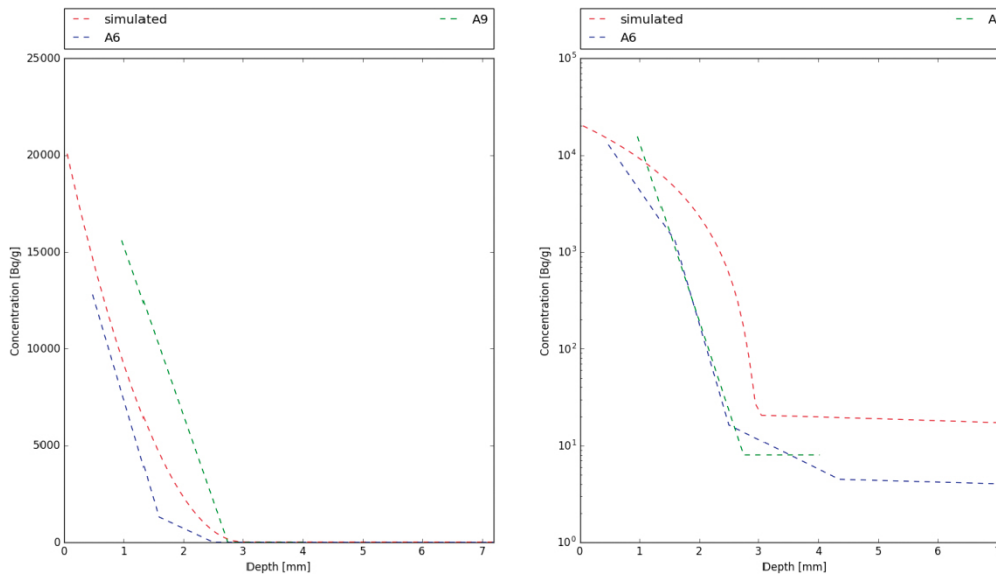
Figure 4-16. *LTDE-SD – concentration profiles in the rock in a linear (left) and logarithmic (right) scale – Ni-63.*
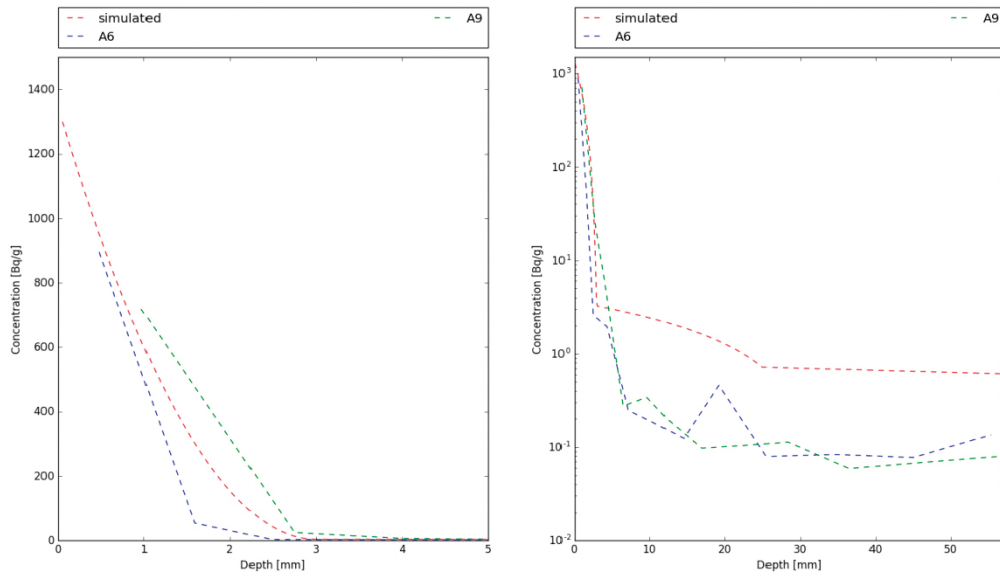
Figure 4-17. *LTDE-SD – concentration profiles in the rock in a linear (left) and logarithmic (right) scale – Ba-133.*
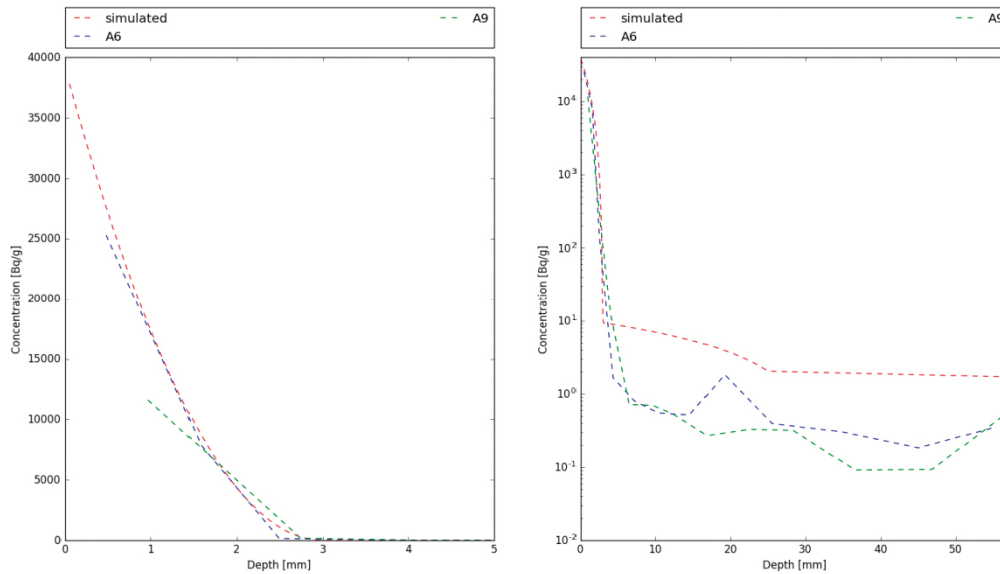
Figure 4-18. *LTDE-SD – concentration profiles in the rock in a linear (left) and logarithmic (right) scale – Cs-137.*

4.3.2 Stage 2

The second stage of the LTDE-SD modelling consisted of extending the model by simulating the development of tracer (radionuclide) solution. These concentrations were used as boundary conditions for transport at the solution-rock interface.

The solution model is superior to the Flow123d model as it enables its execution, modification of its inputs and evaluation of its outputs.

The initial state of the solution was derived from the data given in the task description: the initial volume of the solution was 1 150 ml. The initial concentrations of the individual tracers were calculated based on the injected activity.

Changes in the state of the solution were caused by:

1. Sampling – the volumes of the samples taken and the times when the sampling took place are known from the task description. They do not cause a change in the concentration but a change in the volume of the solution together with the mass of the tracers dissolved in the solution.

2. Mass flow to/from the rock matrix – calculated on the basis of the outputs (mass balance) of Flow123d

The solution model monitors the time, volume of solution, and mass of the tracers dissolved in it. It calculates the boundary condition for transport simulations that repeatedly run with a simulation period of 1 day (1 hour during the first day). After each single run of the transport model, the solution model evaluates the Flow123d outputs (mass flow across the boundary representing the solution-rock interface) and recalculates the masses of the tracers in solution. Before each transport model run, the solution model checks whether a sampling occurred. If so, it will appropriately adjust the volume of the solution and the weight of the tracers dissolved therein.

The development of the concentration in the solution is described by the first order differential equation. The solution model solves it numerically, using an explicit one-step method. The simulation period of the partial transport models is therefore a step of time discretisation of the solution model, which on the one hand influences the accuracy of the numerical solution and on the other hand is important for its stability (Anderson 1995).

The geometry of the experiment is complicated, its representation by a 3D computer mesh was difficult to use due to the high demands on the fineness of the mesh near the solution-rock interface (the created mesh had tens of millions of elements). Therefore, we used a simplification, which should have no or negligible impact on the accuracy of the outputs (especially in the context of other model uncertainties). The experiment was represented by two separate geometries:

1. 1D geometry – for calculation of the interaction between the rock and the experimental section – fracture. Both the geometry and the discretisation mesh are identical to those used and described in Stage 1. The surface area of the solution-rock interface is 0.0236 m^2.

2. 2D geometry – for calculation of the interaction between the rock and experimental section – borehole. Created as a sector of an annular circle (with a sector angle of $\pi/90$ radians). Representing the entire annulus would unnecessarily increase the computational demands. The area of the solution – the rock interface is 0.034/180 m^2 (when evaluating the outputs of Flow123d the mass flow was multiplied by 180).

Whenever a solution model calls Flow123d, it runs two instances of it (one for each geometry) and evaluates the outputs of both.

Except for transport boundary conditions, all of the model parameters are identical to Stage 1 (including the overall simulation timeframe). Selected results of the simulations made during Stage 2 are presented below.

The best agreement with the measured concentration values in the solution was achieved for Cs-137 (see Figure 4-19).The agreement was worse for the other tracers, as shown for Ni-63 (Figure 4-20). The figure shows a very rapid decrease in the measured concentrations during the first hours of the experiment. Due to the different boundary conditions, the agreement between the simulated and measured concentration profiles in the rock also naturally deteriorated (see Figure 4-21, cf. Figure 4-16). If we

tried to improve the agreement of the measured and simulated development of the concentration in the solution, we would have to increase the total mass of the tracer in the rock matrix approximately two-fold, which would make the agreement of the profiles even worse. Therefore, the result does not indicate an error in the rock matrix parameters, but a mass balance error that can be caused either by measurement errors in the activity either in the solution (where the measurement uncertainties are very obvious from oscillations in a time series) or when a tracer is bound to the experimental equipment.

A partial conclusion is that it is better to use the initial injected amount of tracers and simulate the development of the concentration in the solution (to monitor the mass balance) rather than to use error-ridden measurements as a boundary condition. Although the simulated and measured temporal evolution of the tracer concentration in the solution is not the same for all of the tracers, the resulting differences in the boundary condition of transport at the solution-rock interface do not deteriorate the qualitative agreement of the concentration profiles in the rock, even though the quantitative agreement may deteriorate. The qualitative agreement means that the validity of the assumption of a decline in the rock parameters with depth remains; improving the quantitative agreement may be achieved by additional calibration
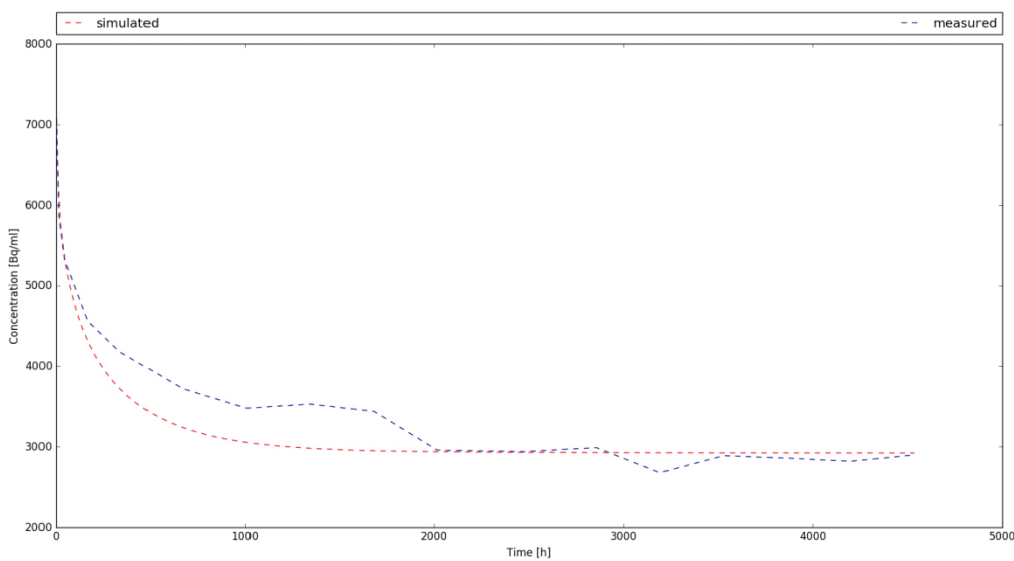
Figure 4-19. *LTDE-SD – solution model – Cs-137.*
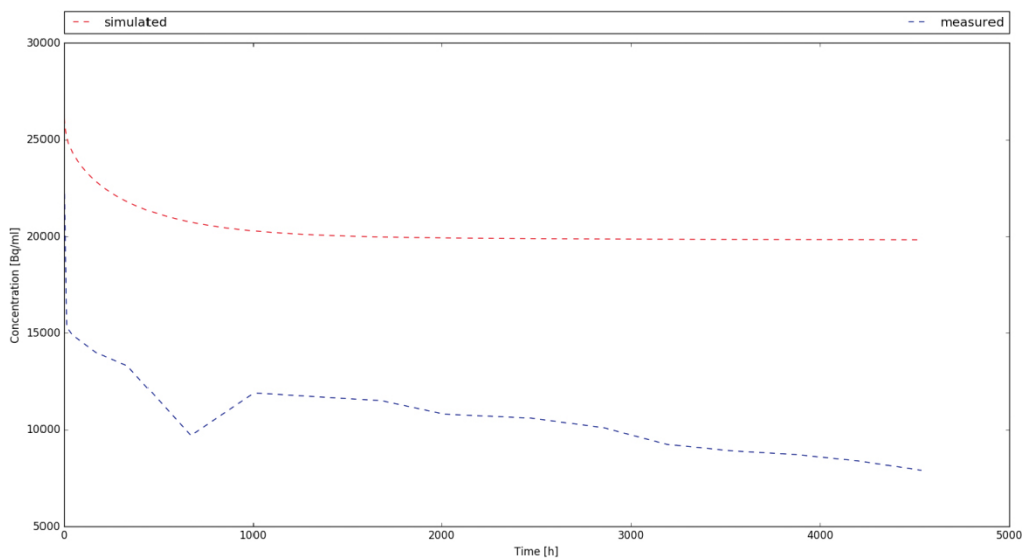
Figure 4-20. *LTDE-SD – solution model – Ni-63.*
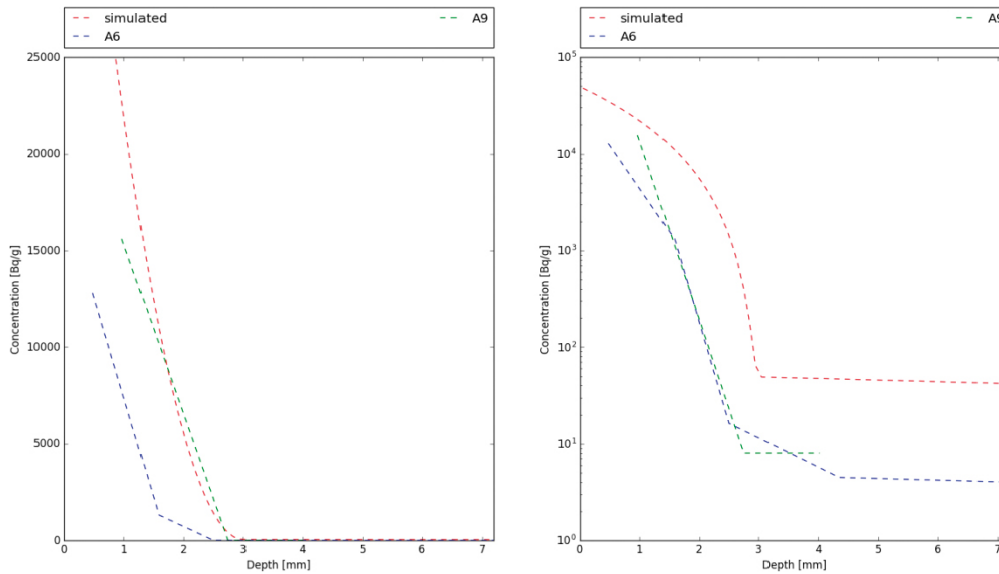
Figure 4-21. *LTDE-SD – Stage_2 – concentration profiles in the rock in a linear (left) and logarithmic (right) scale – Ni-63.*

4.4 Inverse model in GoldSim

4.4.1 Stage 1

For an interpretation of the measured data from the in-situ experiments of LTDE-SD, a model was created in the program environment of GoldSim. The commercial license (GoldSim + RT (Enterprise)) version 12.0 was used. This model represents diffusion into the rock using a 1D finite volume grid (Cell element). In order to model the heterogeneous nature of the rock environment, the 1D grid was divided into 15 parts (Figure 4-22), as in the in-situ experiment, each containing its rock environment and its transport pathway divided into five parts (Figure 4-23). The boundary condition at the input was defined on the basis of experimental concentration data (the INPUT part). This model was used to optimise the selected transport parameters so that the calculated profile curves represent the shapes of the detected profiles as closely as possible.

Optimisation of the values of selected parameters is based on finding the minimum of the objective function, which in our case was the sum of the squared concentration differences between the model and the experimental values in a given rock location (only in places where the experimental data were measured, there is no interpolation of the measured values) divided by the experimental values (Figure 4-24). The objective function is minimised with respect to the selected parameters. For each of these parameters, it is necessary to enter an initial value and an upper and lower limit in GoldSim. The optimisation is done in GoldSim using "Box's complex method" described in Box (1965). This method is based on the creation of an initial "complex" for each of the optimised parameters. The initial "complex" is a set of valid solutions that meet al. of the requirements specified by the user. This complex contains twice as many valid solutions as the number of optimization variables. the algorithm searches the solution space iteratively, replacing the least optimal members of the complex with more optimal ones until the solution converges. If there is no convergence in a certain number of steps, then an error message appears. GoldSim allows the user to define the accuracy of the optimisation. It chooses from four precision options: "Low", "Medium", "High" and "Maximum". The accuracy indicates how the initial complex will be generated. For "Low" accuracy, a minimum number of parameter values is generated, i.e. $2n$ values, where n is the number of optimised parameters. For "Medium" accuracy, $5n$ is generated and for "High" and "Maximum" $10n$ values, and for the initial complex the selection of $2n$ is the most suitable. The degree of accuracy also varies by ending the optimisation. For "Low" accuracy, the optimisation is ended after a new value of the optimised function does not differ by more than 1 % from the previous one or after 100 attempts. For "Medium" accuracy, these conditions are 0.1 % and 1 000, for "High", 0.001 % and 10 000, and for "Maximum", 0 % and 1 000 000.
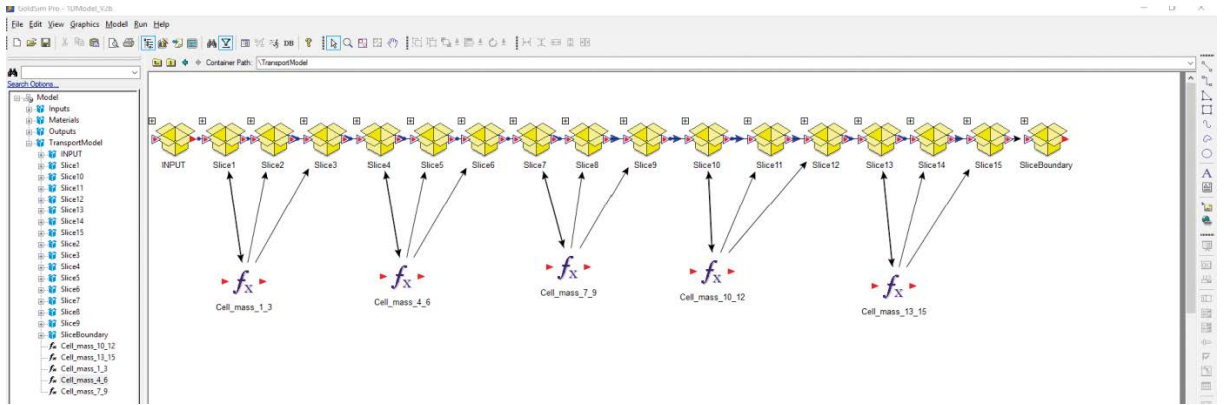
Figure 4-22. *Division of the 1D network into 15 separate parts in the graphical interface of GoldSim.*
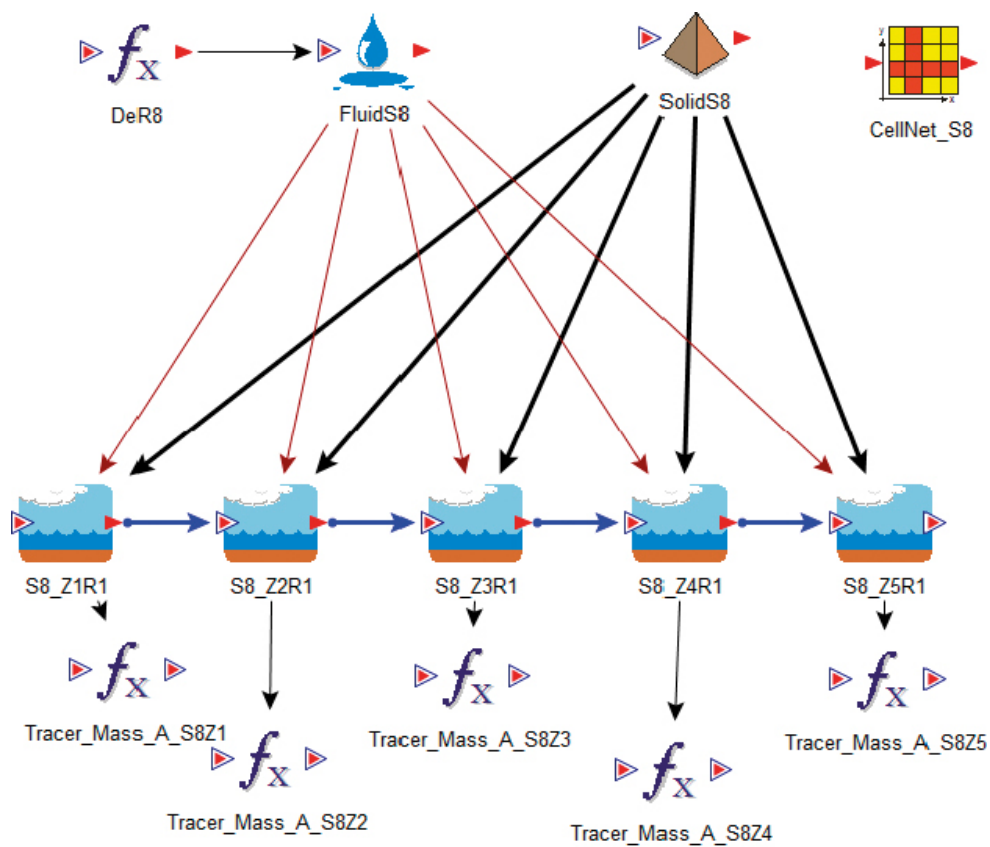
Figure 4-23. *One of 15 separate parts of the 1D network in the graphical interface of GoldSim. In the separate parts are defined the values of the transport parameters using the FluidS8 and SolidS8 elements. The actual sub-network of the finite volumes was made up of five Cell elements (S8_Z1R1- S8_Z5R1), with diffusion lengths varying for the separate sections similar to the thickness of the individual sections taken from the rock.*
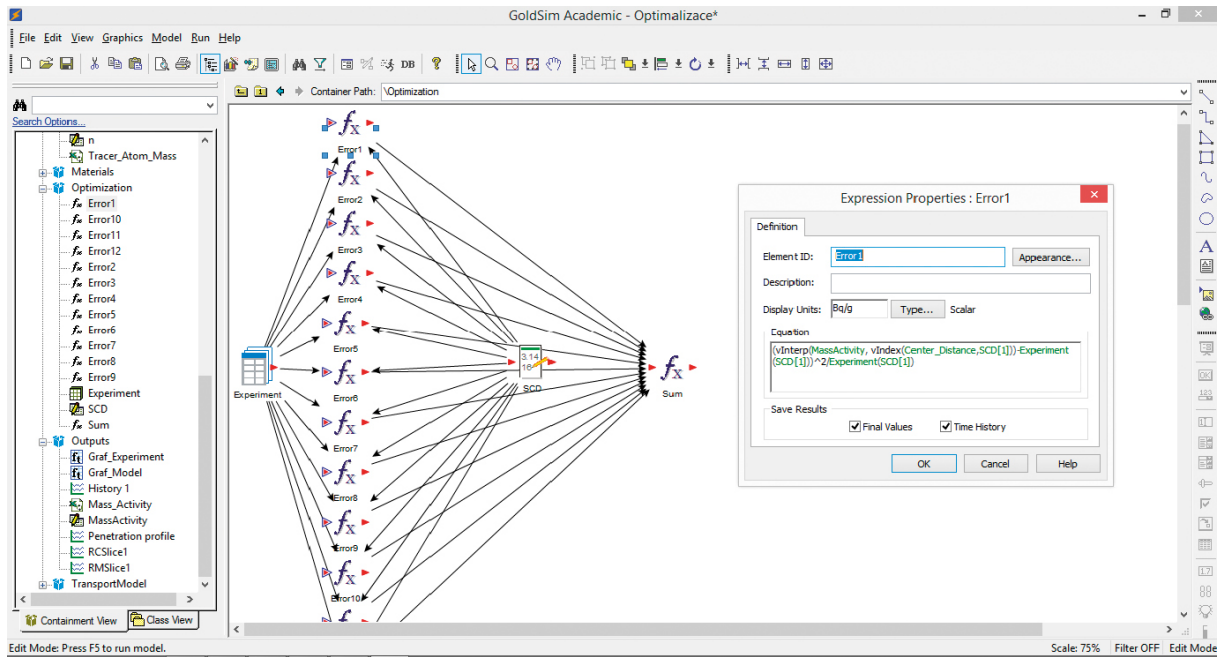
Figure 4-24. *Description of the objective function for optimisation in the graphical environment of GoldSim.*

At first, heterogeneity in the model was represented by one variable, the diffusion coefficient D_e, whose value increased with distance from the source. It is not possible to solve an optimisation problem in which specific coefficients D_e, K_d, ε would be chosen in each separate part, because we have only one experimental value for each separate part. We optimised three parameters (D_{e0}, α, n) of our chosen function for the increase in D_e

$$D_e = D_{e0} + \alpha d^n, \tag{4-1}$$

which to the point of the rock at distance d is assigned a given value of D_e.

Figure 4-24 illustrates how the purpose function is defined in the graphical environment of GoldSim. The right window shows the formula for calculating the sum of squares of the concentration difference at the first experimental point. The model reads the distances at which the concentration was determined and finds the model value at the same distance from the source. The Sum function (objective function) then calculates these differences for all of the measured points.

Figure 4-25 shows the profiles for Cl-36⁻ in the A6 core, where the red curve corresponds to the experimental values and the green profile to the model values with optimised distance dependence parameters D_e. The minimum difference between the experimental and model data was reached for $D_{e0} = 1.002 \times 10^{-14}$ m²/s, $\alpha = 3.18 \times 10^{-6}$, $n = 3.13$. Other transport parameters were read from an Excel file (e.g. $K_d = 10^{-8}$ m³/kg, $\varepsilon = 0.03$). For this functional dependence, D_e approaches to the diffusion coefficient value in free water from a distance of 10 cm (see Figure 4-26) and consequently D_p is even larger, which is physically impossible. This suggests that the model used may not include all of the processes that contributed to the transport curve.

The same model was used for the experimental data in core A6 for the sorbing ion, specifically Na-22. The same dependence of coefficient D_e on the distance from the source was used. The coefficients α and n of this dependence were the same as in the case of Cl-36, the other was the value $D_{e0} = 5.314 \times 10^{-14}$ m²/s. Other parameters, which gave the best agreement of the model results with the experimental results, were $K_d = 2.72 \times 10^{-5}$ m³/kg, $\varepsilon = 0.03$. The calculated and measured profiles for Na⁺ are shown in Figure 4-27.
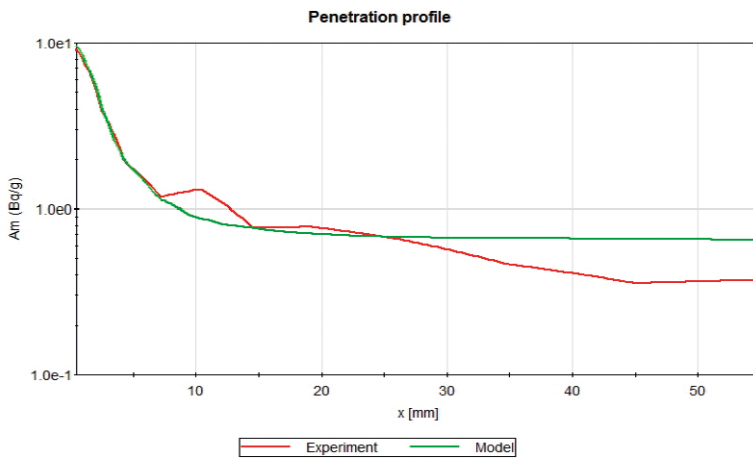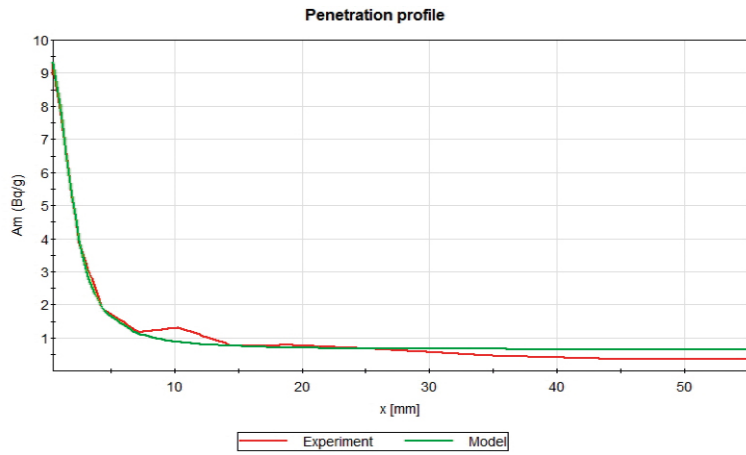
Figure 4-25. *Comparison of experimental and model profile of Cl-36 activity in the rock layer.*
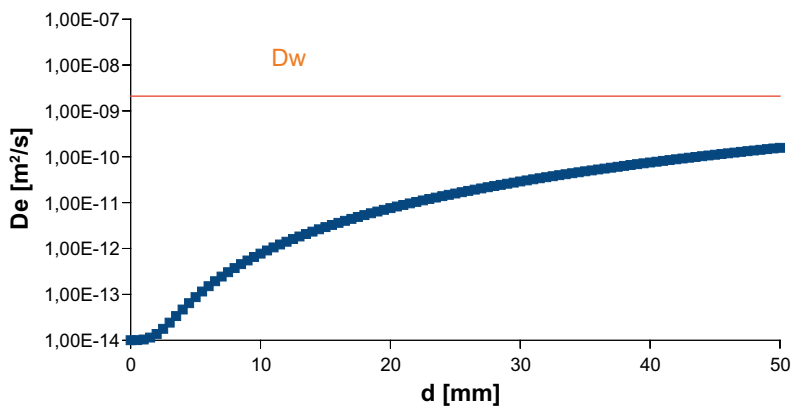
Figure 4-26. *Dependence of the D_e Equation (4-1) on the distance from the source for the Cl-36 for the optimal parameter values $D_{e0} = 1.002 \times 10^{-14}$ m²/s, $\alpha = 3.18 \times 10^{-6}$, n = 3.13. The orange line indicates the limit value of the diffusion coefficient in water.*
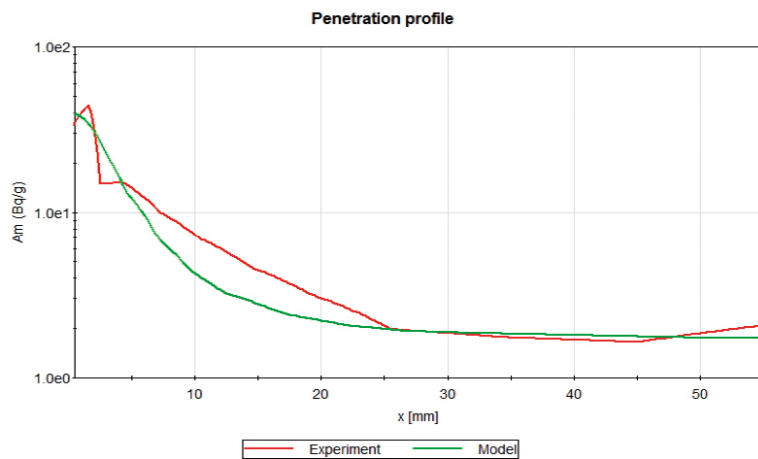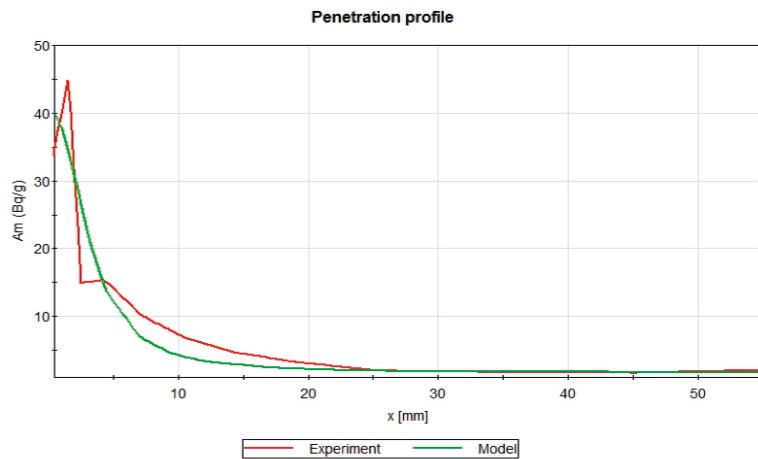
Figure 4-27. *Comparison of experimental and model profile of Na-22 activity in the rock layer.*

4.4.2 Stage 2

In the subsequent stage, an extended model was developed in the GoldSim program environment, which also contains both sample types (A, D). Figure 4-2 shows the location of the models of both samples; the position of sample A is random, due to the adjustable cross-sectional area of the cylinder, the sample model may represent the entire volume of the rock from which the samples were taken. The extended model allows simultaneous simulation of the transport of several radionuclides. For a more general description of the heterogeneous rock environment, a second "rock environment" was introduced in each Cell element. This second rock environment is a network of micro-fractures (Figure 4-28), which have different transport properties and may represent a preferential transport pathway. The following text provides a more detailed description of the implemented changes. Finally, the model allows the user to solve the transport task only on the basis of initial radionuclide activities.

Radionuclides considered

The extended model solves the transport of the following five radionuclides in parallel: Na-22, Cl-36, Ni-63, Ba-133 and Cs-137. The input amount of these radionuclides is entered either in the form of the time courses of concentrations, whereby in each time step the concentration in the input cell is interpolated from the experimental data using the Time Series element or the initial mass of the radionuclides in the input cell is entered only.
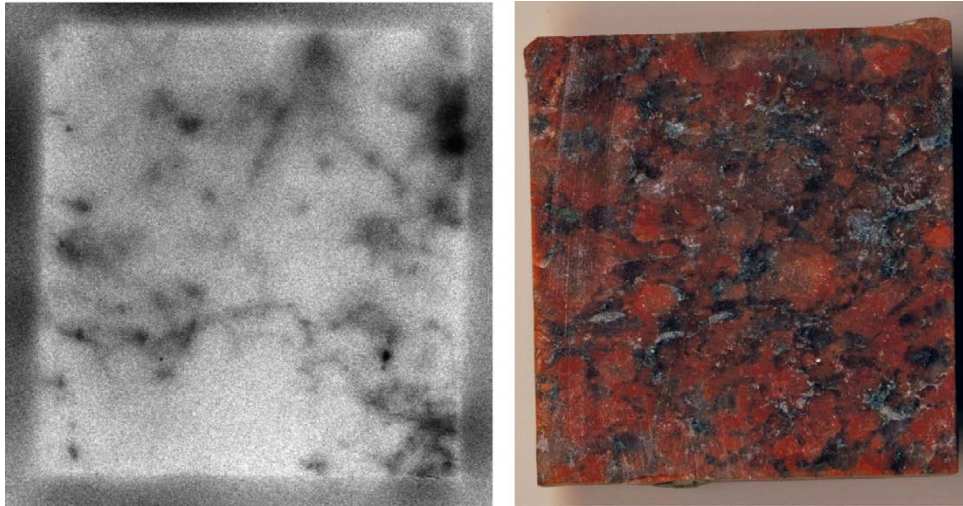
Figure 4-28. *Autoradiograph (left) and photograph (right) of the cutting of sample A.9. The black-coloured parts in the autoradiograph may be interpreted as a network of micro-fractures, which represent preferential transport pathways. Taken from Löfgren and Nilsson (2020).*

Model of the D sample

Model of the D sample was constructed using a 1D finite volume grid (Cell) with cylindrical geometry (Figure 4-29), with a constant *Z* coordinate of 300 mm (along the borehole), and with the *R* coordinates shown in Table 4-6 for all 76 Cell elements. These 76 Cell elements were divided into three groups (shown in Figure 4-2 by different shades of blue, and in Figure 4-29 by different colours), the first group containing ten elements with a radius of 18–19 [mm], followed by the second group containing five elements with a radius of 19–20 [mm] and the remaining third group containing 61 elements with a radius of 20–145 [mm]. Each group has its own two model rock environments (preference zone of micro-fractures and grain volume).
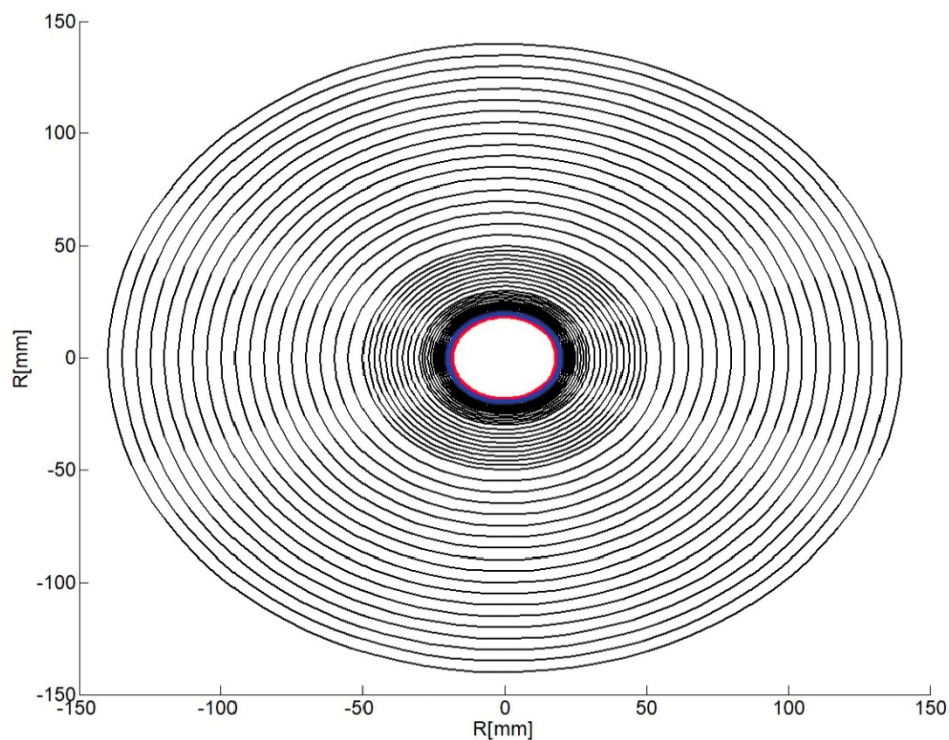
Figure 4-29. *Detail of the geometry of the cylindrical grid of the model of the D sample; the different areas of the various different model rocks (spatially variable parameters) are represented by different colours.*

Table 4-6. Cylindrical grid R-coordinates representing the D samples.

Index	R [mm]	Index	R [mm]	Index	R [mm]	Index	R [mm]	Index	R [mm]
R1	18	R17	20.5	R33	34	R48	66	R64	98
R2	18.1	R18	21	R34	36	R49	68	R65	100
R3	18.2	R19	21.5	R35	38	R50	70	R66	102
R4	18.3	R20	22	R36	40	R51	72	R67	104
R5	18.4	R21	22.5	R37	42	R52	74	R68	106
R6	18.5	R22	23	R38	44	R53	76	R69	108
R7	18.6	R23	23.5	R39	46	R54	78	R70	110
R8	18.7	R24	24	R40	48	R55	80	R71	115
R9	18.8	R25	24.5	R41	50	R56	82	R72	120
R10	18.9	R26	25	R42	52	R57	84	R73	125
R11	19	R27	26	R43	54	R58	86	R74	130
R12	19.2	R28	27	R44	56	R59	88	R75	135
R13	19.4	R29	28	R45	58	R60	90	R76	140
R14	19.6	R30	29	R45	60	R61	92	R77	145
R15	19.8	R31	30	R46	62	R62	94		
R16	20	R32	32	R47	64	R63	96		

Rock environment

The basic properties of the rock environment are defined in the model by density, porosity and K_d. The density was considered to be $2\,700$ kg/m^3 for all rock environments in the studies performed; the porosity and K_d values were considered differently and were optimised so that the modelled profiles curves were as close as possible to those detected. Each Cell element, which is part of the transport pathways representing the A and D samples, contains two rock media (designated as solid1 and solid2). The relative representation of the two rock environments in the model is controlled by an input parameter that has been optimised as well as the porosity and K_d values relative to the detected profiles – marked in the results table as "solid2/solid".

Results of the selected study

For sorbing radionuclides Ni-63, Ba-133 and Cs-137, the input was used in the form of concentration time courses as well as the results from the same sample (A6). In contrast to the study for Na-22 and Cl-36 (where a relatively good agreement was achieved based on the spatially variable value of the diffusion coefficient D_e), we used the constant $D_e \equiv D_{e0}$ and optimised, in addition to D_{e0}, K_d and the relative representations of the rock environment. In order to achieve an agreement between the simulated and experimental profiles, we had to consider higher values of effective diffusion coefficient D_{e0} for sorbing radionuclides than for Cl-36 (Table 4-7) and in particular a large representation of rock with zero sorption (for d> 10 mm 99 % non-sorbing rock, see Table 4-8). The resulting profiles are shown in Figure 4-30.

Summary of results obtained to-date

The results of the performed studies show that in order to represent the tail parts of the profiles it is necessary to take into consideration the high diffusion coefficients for non-sorbing radionuclides, and for sorbing radionuclides the sorption of radionuclides on very limited parts of the rock volume. This can be interpreted so that the detected profiles cannot be explained by a model that includes transport governed by Fick's law only. Analysis of the experiment shows that it cannot be ruled out that advective flow or osmosis may occur during the experiment due to pressure gradients or desiccation, respectively. On the other hand, the autoradiographs of the sample sections correspond qualitatively to the conclusion that the transport of tracers was limited to a small volume of the rock.

Table 4-7. Selected parameters used to simulate the profiles included in Figure 4-30. Parameter values were optimised with respect to the detected profiles.

Parameter	Cl-36	Ba-133	Cs-137	Na-22	Ni-93
K_d [m^3/kg] – solid1	1.0E−14	2.5E−03	4.0E−02	5.0E−05	4.0E−02
K_d [m^3/kg] – solid2	1.0E−14	1.0E−10	1.0E−10	1.0E−14	1.0E−10
D_{e0} [m^2/s]	4.1E−14	8.0E−13	1.0E−11	1.0E−13	2.0E−12

Table 4-8. Relative representation of the rocks and their porosities, which were used to simulate the profiles shown in Figure 4-30 (result of the optimisation).

Model layer	1	2	3	4	5	6	7	8
solid2/solid	0.20	0.20	0.20	0.20	0.20	0.99	0.99	0.99
ε1	0.009	0.008	0.006	0.003	0.003	0.003	0.003	0.003
ε2	0.003	0.003	0.003	0.003	0.003	0.003	0.003	0.003

Model layer	9	10	11	12	13	14	15	Boundary
solid2/solid	0.99	0.99	0.99	0.99	0.99	0.99	0.99	0.99
ε1	0.003	0.003	0.003	0.003	0.003	0.003	0.003	0.003
ε2	0.003	0.003	0.003	0.003	0.003	0.003	0.003	0.003
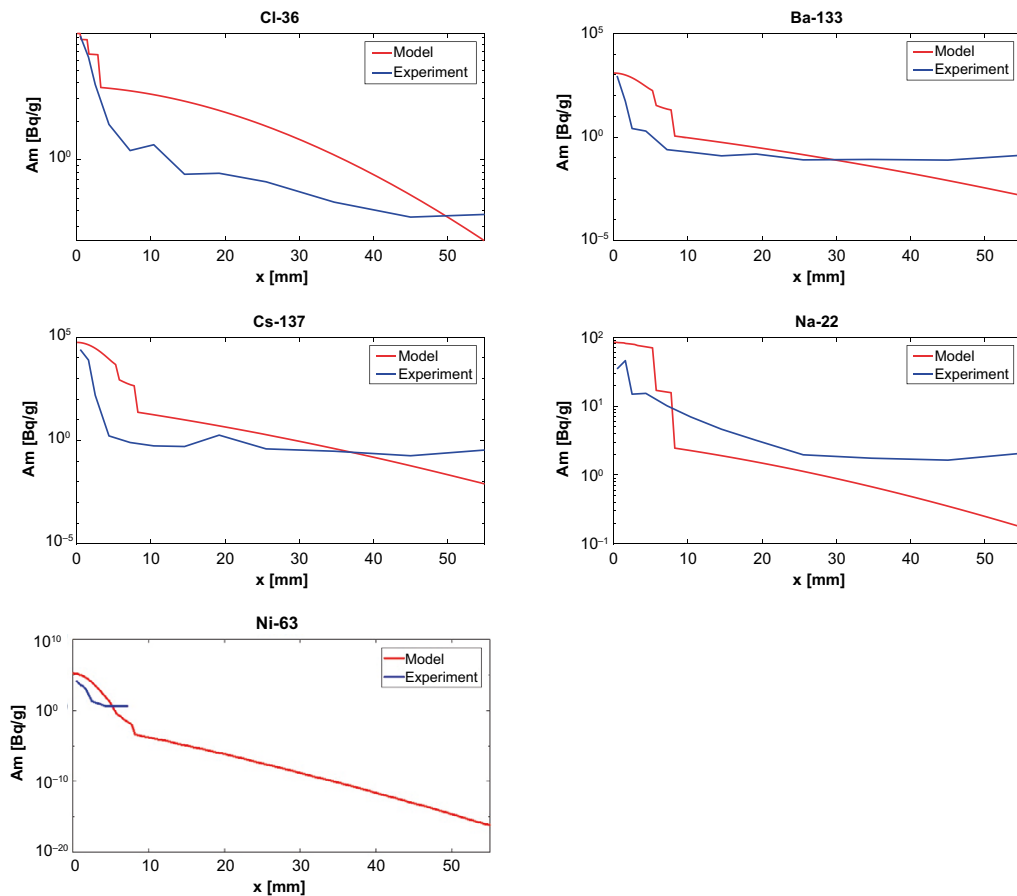
Figure 4-30. Comparison of experimental and model profiles of the activity of five radionuclides in the rock layer.

4.5 Conclusions for simulation of transport processes in the geosphere

The simulations of the LTDE-SD experiment provided the following conclusions for the simulation of transport processes in the geosphere:

- The presence of a disturbance zone (EDZ, BDZ) in the vicinity of boreholes and the fracture must be taken into consideration, the thickness and characteristics of which depend on the selected extraction/drilling method. The parameters of the disturbance zone can be very different from those of unaffected rock. In particular, a higher porosity and associated sorption rate can be expected in the such zone.

- In-situ experiments provide qualitatively new information. Laboratory experiments are always made on samples that have been affected. Inverse models of in-situ experiments can provide parameters affecting transport processes in the solid massif.

- The sorption measure in intact and unaffected rock can be up to several orders of magnitude lower than the parameters found in the laboratory.

5 Modelling LTDE-SD using the micro-DFN concept

The micro DFN/CPM transport models were processed in relation to the solution of Task 9B. This section summarises the general methodology for the preparation of the micro-DFN/CPM models, which was applied to the specific task description and results of the LTDE-SD experiment. The input materials used at the level of the micro-scale of the rock matrix are summarised, and the computational software and the methodical procedure for the construction and implementation of the transport model are described.

The LTDE-SD diffusion experiment (see Section 4) was performed in a rock environment without open fractures, in which the transport of tracers is bound to the micropore space of the matrix – this is formed solely by a network of interconnected micro-fractures, which have the character of flat discrete elements with very little apertures. Volumetric micropores, characteristic for a porous medium, are practically absent from granitic rocks (if they exist, they are always connected to a network of micro-fractures, which predetermines the resistance characteristics of the environment).

The difference between the simulation of the diffusion experiments using the classical concept (labelled as macro-CPM) and the micro-DFN concept is mainly in the characterisation of the parameters of the rock matrix. While in the macro-CPM approach, the transport parameters of the rock matrix are more or less homogeneous and average for the whole simulated volume, in the micro DFN approach, the model parameters representing the rock matrix are based on the observed microstructure of the simulated rock and are, therefore, very heterogeneous in space. The macro-CPM model is then comparable in its parameters to a certain (larger) representative volume of the micro-DFN domain (the micro DFN model after up-scaling and averaging the values).

The micro-DFN transport models were processed in relation to the solution of Task 9B and were applied on the specific task description and results of the LTDE SD experiment. Some of the modelling procedures applied in other projects (e.g. PAMIRE – Havlová et al. 2017) and the results of laboratory diffusion experiments performed on samples from the Grimsel site were also used (LTD project – Havlová et al. 2016). The results of the transport experiments indicated several aspects of the behaviour of radioactive tracers in granitic rocks, which cannot be described based on a simplified concept using homogeneous properties of the rock matrix (preferably one value of the diffusion coefficient, porosity etc.). The microstructure of the rock matrix is very complex and spatially highly heterogeneous.

The main objective of micro-DFN modelling was to apply the measured microstructure data (which include micro-fractures at a millimetre scale and affect the overall heterogeneity of the intact rock matrix), to design and develop procedures to model micro-scale experiments, and to better understand the diffusion and sorption processes occurring in the rock matrix for individual radionuclides.

5.1 Summary of the input data

A limited amount of input data describing the microstructure of the studied rock was available during the solution of Task9 – autoradiographs of two samples from the Äspö site impregnated with C-14-PMMA. Rock micrographs at a resolution of 25 mm/pixels were not taken on samples directly from the tested sections of the LTDE-SD experiment, but on samples from its vicinity. The characteristics of the microstructure of the rock matrix with significant micro-fractures over the entire sample are evident from the micrographs in Figure 5-1 and Figure 5-2.

At the microscale level of the rock matrix, the evaluated 3D images from the microtomography of the samples were also available, and documented the spatial distribution of mineral grains. However, the resolution of the method does not allow for the visualisation of the spatial network of the micro-fractures – the aperture of the micro-fractures is significantly less than the resolution of the microtomography method used. In terms of generating a micro-fracture network model, no specific (numerical) input data were available for the task description of the DFN models in the framework of the solution of Task 9, e.g. statistical evaluation of lengths or number of micro-fractures from the images, distribution of the apertures of the micro-fractures from the images or Hg porosimetry, etc.
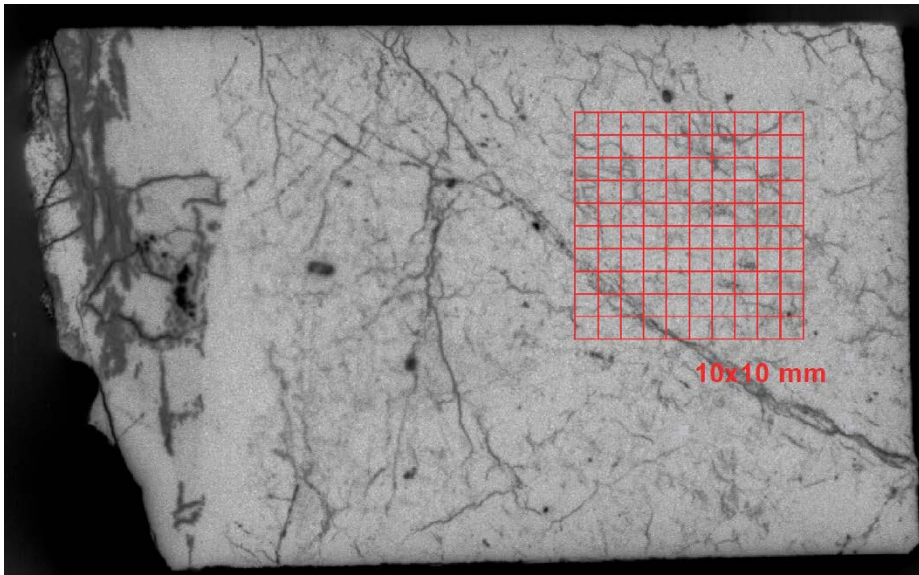
Figure 5-1. *Microstructure image obtained by the C-14-PMMA method – sample LTDE-SD1 (DD18, 2017).*
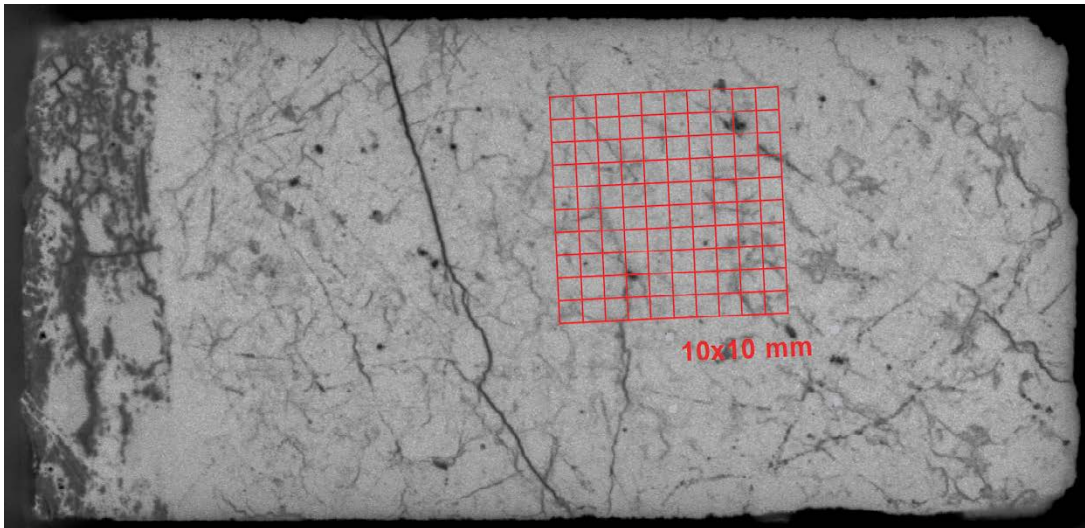
Figure 5-2. *Microstructure image obtained by the C-14-PMMA method – sample LTDE-SD2 (DD18, 2017).*

5.2   Methodology of micro-DFN modelling

The basic methodology used in the micro-DFN modelling during the solution of the Transport 4 project is summarised in the following sections:

1. Processing and analysis of microstructure images of the rock matrix – evaluation of bases and determination of geometrical parameters of micro-fractures (in particular evaluation of the lengths, number and density of micro-fractures, etc.).

2. Generation of a micro-DFN model, i.e. a stochastic 3D micro-fracture network – only significant micro-fractures with a minimum size of 10 mm are included in the model. The domain size is $10 \times 10 \times 20$ cm; the shape of the generated micro-fractures is square; spatial and directional distribution, frequency of micro-fractures and their size are generated randomly according to selected parameters and statistical functions (power dependence between number and size of micro-fractures); The aperture of the micro-fractures is also generated randomly according to the given parameters, but it has a direct link to the size of the micro-fractures (increasing the size of the micro-fractures increases the value of the aperture).

3. Up-scaling of the micro-DFN model to the micro-CPM model with a computational element size of $1 \times 1 \times 1$ mm. During the up-scaling, the transport parameters are calculated for the elements in which the generated micro-fracture network takes place. Other elements outside of this fracture network form the "background" and include less significant and small open micro-fractures (along with more significant micro-fractures but that form an interconnected network and also contribute to the transport), which are represented in the model as a continuous homogeneous environment. The assembled micro-CPM model is simpler than the micro-DFN model, but retains the heterogeneity and properties of the micro-DFN model and is more suitable for transport simulations.

4. Calculation of the transport task on the assembled micro-CPM model, continuous evaluation of model results, comparison with measured data and optimisation (calibration) of transport parameters.

The following programs were used during the solution of the micro-DFN models:

- ConnectFlow (v11.5.2 and v12.0) – the program was used as a user interface (GUI) for pre- and post-processing of input/output files, for generating a micro-fractured DFN based on the selected statistical distribution of input parameters and upscaling of the micro-DFN model to the micro-CPM model.

- Groundwater Vistas (v6 and v7) – the program was used as a pre-processor (GUI) to build a transport micro-CPM model and generate input text files for MT3DMS.

- MT3DMS (v5.3) – the program was used to calculate transport tasks on the up-scaled CPM models.

- ParaView (v5.3.0) – the program was used for spatial visualisation of model geometry and model results.

- Python scripts (v2.7.3) for pre- and post-processing of input and output data – the user interface of the ConnectFlow and Groundwater Vistas software is prepared primarily for the implementation of hydraulic models and some of the necessary functions are not available for relatively specific assignments of transport diffusion tasks solved within Task9B. Therefore, a number of purpose-built scripts had been prepared and used for handling and batch processing of transport models (for building and running variant transport micro DFN/CPM models and for processing and evaluation of model outputs).

5.3 Results of the micro-DFN modelling

In the initial phase of the micro-DFN model, images of rock matrix samples from the studied site were analysed. The work focused on the evaluation of the character of three basic components (see Figure 5-3), which appear in nearly all of the samples (in different granite rocks from different locations):

- The borehole disturbed zone (BDZ) at the edge of the sample specimen due to drilling. The BDZ is not visible on the micrograph (Figure 5-3 – left) because the samples were taken from the rock in contact with an open macro-fracture (it would theoretically be possible to include the whole part of the sample above the green line in the BDZ, which is a material fill of the fracture or a mineralised coating with a very high porosity, and not a rock matrix; therefore, the sample corresponds in nature to the test interval A of the LTDE experiment, where the coating of the fracture had a thickness of a few millimetres and was not continuous) and not from the rock on the contact with the wall of the borehole (test interval D). Nonetheless, a disturbed zone of a maximum of hundreds of micrometres was observed on micrographs taken in other projects; therefore, the BDZ is entered only in the first row of the computational cells, i.e. with a thickness of 1 mm.

- Longer significant micro-fractures – these may be unfilled micro-fractures (cracks) across several mineral grains or altered zones of densely interconnected very short micro-fractures. These micro-fractures represent the connection of the rock matrix over a longer distance and are generated in the model as a micro-DFN (mDFN).

- Less significant micro-fractures with small apertures, which are difficult to recognise for a given type of imaging (densely connected network or grey background of the image) – entered in the model as a continuous homogeneous environment (mCPM).
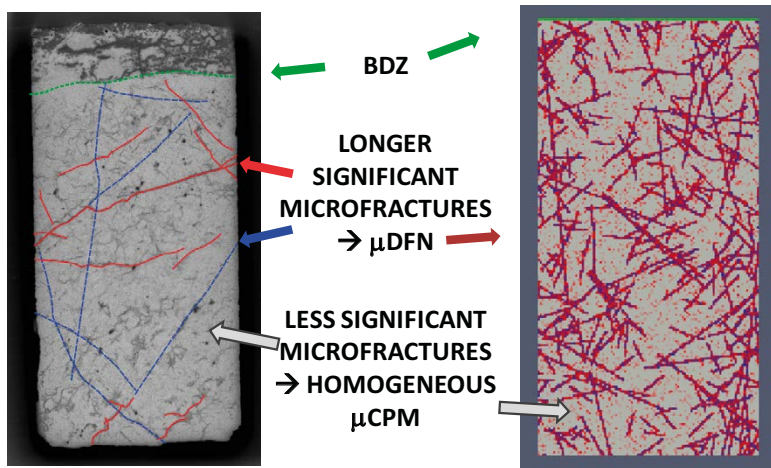
Figure 5-3. *Definition of the basic elements characteristic of the rock matrix – BDZ, longer significant micro-fractures and less significant micro-fractures forming the background of the image. Rock matrix micrograph (LTDE-SD2 sample) on the left and a micro-CPM model with a randomly generated network of micro-fractures in the cross-section on the right.*

5.3.1 Optimisation of the micro-fracture density

During the creation of the micro-DFN of more significant micro-fractures, the influence of parameter A of the power function defining the relationship between the number of fractures n(L) and their size L on the resulting density of the micro-fractures in the model was tested:

$$n(L) = A \cdot L^{-3}.$$

For the selected values of parameter A, Figure 5-4 shows cross-sections of the generated networks showing the differences in the density of the micro-fractures. The outputs were evaluated only in a simplified form by a visual comparison of the generated model networks and the real micro-fractures on the images. For other model works, lower values of 0.1–0.2 of parameter A were used, for which the model network of the micrographs corresponds better to the number of micro-fractures.
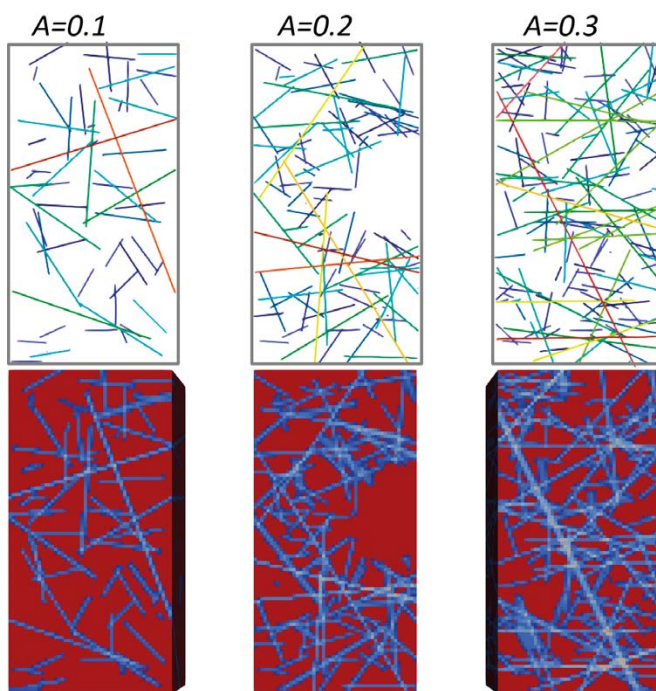
Figure 5-4. *Cross-sections generated by micro-fracture networks for different values of parameter A of the power function. Above: cross-sections of the micro-DFN model, below: models converted to the micro-CPM model.*

5.3.2 Influence of the background micro-fractures on the transport results

The influence of less significant background micro-fractures on the penetration of the tracer into the rock matrix was investigated in the task with a uniform micro-DFN. Transport parameters of significant micro-fractures were entered identically for all variants of the task:

- Pore diffusion coefficient (D_p) at the level of the coefficient in free water, i.e. $1.2E{-}3$ mm^2 s^{-1}.

- Porosity of micro-fractures recalculated from a specified (generated) aperture of 0.1-0.3 mm.

- Sorption in the micro-fractures is negligible, i.e. they represent a preferential pathway.

The transport parameters of the smaller micro-fractures in the background were specified as variants and are included in Table 5-1.

Table 5-1. Specified values of the transport parameters of the background micro-fractures.

Variant	D_p (mm$^2 \cdot$s^{-1})	Porosity (-)	K_d (m$^3 \cdot$kg^{-1})
VAR_444	1.0E−4	1.0E−4	1.0E−4
VAR_446	1.0E−4	1.0E−4	1.0E−6
VAR_556	1.0E−5	1.0E−5	1.0E−6
VAR_638	1.0E−6	1.0E−3	1.0E−8

Figure 5-5 shows the distribution of model activities for the individual combinations of transport parameters. Figure 5-6 shows the profile of the penetration of the tracer depending on depth (for a comparison, the measured values of the Cl-36 experiment are also shown in the graph). The graph shows a different profile in the VAR_444 variant, which has the highest sorption coefficient value, see the tracer penetration to a shallow depth in the figure of concentration distribution. Interestingly, there is a relatively small difference in the penetration for the remaining three variants, although e.g. VAR_556 has a very different distribution of activities in space (a combination of higher sorption and diffusion coefficients, but lower porosity than in VAR_638).
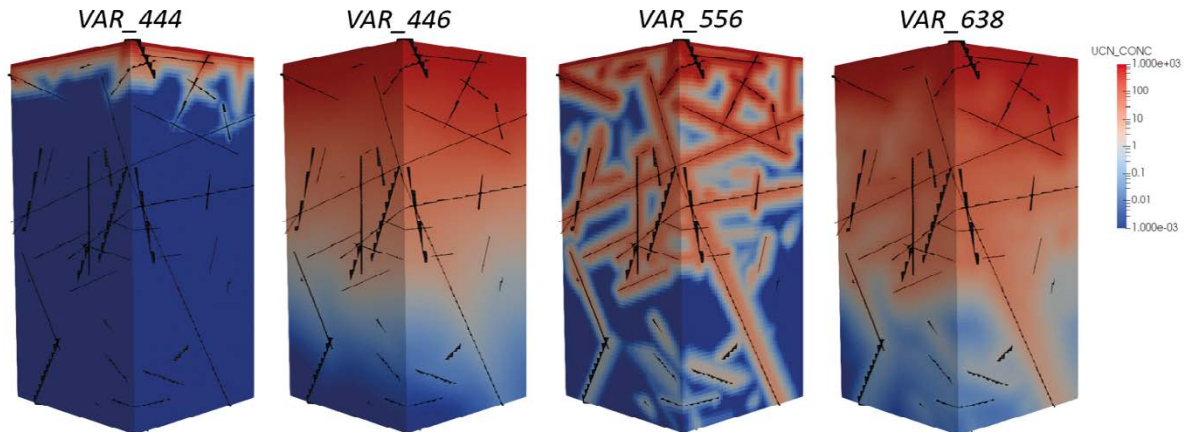
Figure 5-5. *Variant simulations of the penetration of the tracer for various settings of transport parameters of smaller micro-fractures in the background – spatial distribution of activity in the 3D domain.*
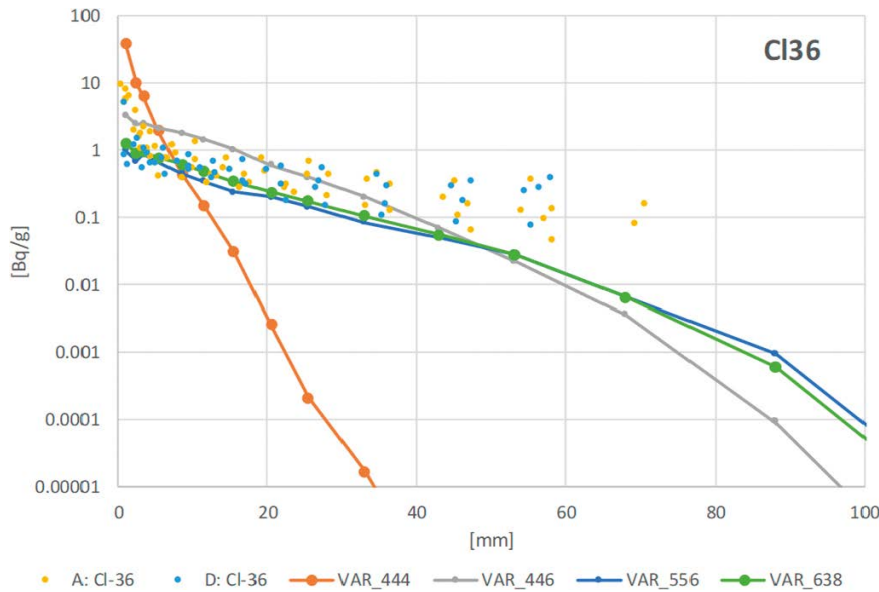
Figure 5-6. *Variant simulation of the penetration of the tracer for various settings of transport parameters of smaller micro-fractures in the background – amount of tracer in cross-sections by the model domain.*

5.3.3 Simulation of the diffusion of the sorbing tracer

During the micro-DFN modelling, laboratory measurement of the diffusion coefficient of the Cs-134 tracer in the diffusion cell for the sample of Aare granite (measured in the LTDIII experiment) was simulated. For the LTDE experiment (Task9B), detailed results of diffusion coefficient measurements (breakthrough curves from diffusion cells) were not available; however, these data are very valuable as calibration data, especially for sorbing tracers, where it is possible to use breakthrough curves from the output as well as the input cell.

The simulation of the diffusion experiment (1D diffusion through a 1 cm-wide disk of rock located in the diffusion cell) was performed for a slightly modified concept of the micro-scale of the rock matrix, see Figure 5-7. No microstructure imaging of the C14 PMMA was performed for the Aare granite. On the other hand, data were obtained from the relative proportions of minerals together with the results of measurements of sorption coefficients for individual minerals, whereby a significant sorption to biotite was observed. The rock matrix was conceptually divided into two zones:

1. BDZ on both bases of the sample.

2. Randomly generated distribution of the main minerals "inside" the sample.
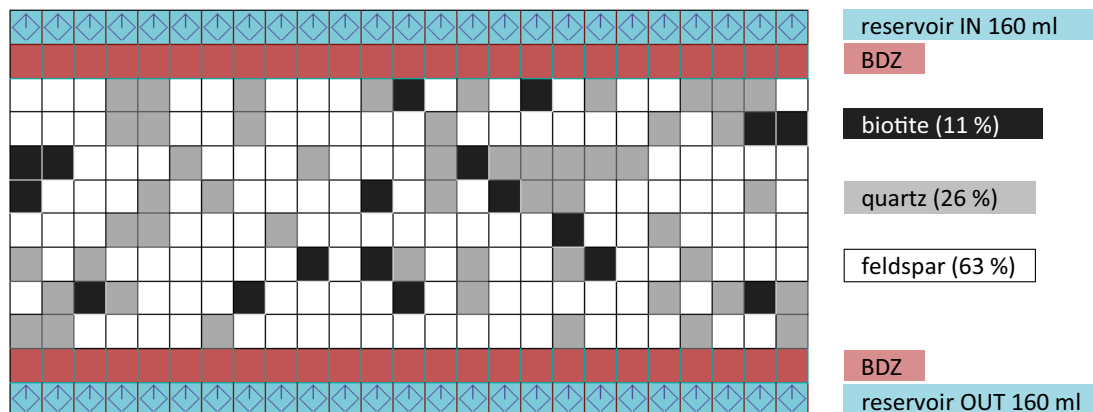
Figure 5-7. *Laboratory diffusion experiment LTDIII – concept of rock matrix without significant micro-fractures with division of the domain according to the percentage of minerals (Aar granite).*

Micro-DFN preferential pathways were not included in the model (the question is how and if they are significant for sorbing tracers). A total of 12 parameters were calibrated – porosity, pore diffusion coefficient and sorption distribution coefficient for BDZ, biotite, quartz and feldspar. The breakthrough curves were captured very accurately, see the comparison of measured and model curves in the graph in Figure 5-8. Table 5-2 shows the resulting calibrated values:

- In agreement with the measurements, the maximum value of the sorption coefficient for biotite was evaluated in the model.

- The very similar values of all parameters of BDZ and feldspars were interesting (values of BDZ are slightly higher). Given the dominant representation of feldspars in the sample (63 %) this could indicate that the size and influence of the BDZ on transport in the rock matrix will not be so significant.

Table 5-2. Laboratory diffusion experiment LTDIII – calibrated values of transport parameters of individual minerals and the BDZ layer.

	por [-]	D_p [$m^2 \cdot s^{-1}$]	K_p [$m^3 \cdot kg^{-1}$]
Biotite	0.0026	1.76E−10	4.10E−2
Quartz	0.0061	4.20E−10	9.58E−3
Feldspar	0.0163	1.12E−9	2.41E−3
BDZ	0.0195	1.56E−9	3.34E−3

5.3.4 Simulation of the LTDE experiment – evaluation of the results

In the final processing of the micro-DFN model of the LTDE experiment, a total of 2 400 simulations were performed with a variable specification of BDZ transport parameters, a micro-fracture domain (significantly longer micro-fractures represented by the DFN) and a homogeneous continuous domain. Transport parameters, i.e. porosity, pore diffusion coefficient and distribution sorption coefficient, were chosen randomly for each model variant within preselected limits of values (the limits were entered that overlapped values higher and lower than the real measured values – it is necessary to bear in mind that it is a model simplification of rock matrix micro space, for which detailed data is not available so that the model can be assembled with a higher degree of accuracy – unrealistic values of parameters at the microscale level can replace e.g. complex interconnection of micro-fractures, high variability of micro-fractures etc.). The whole model procedure from entering the randomly-generated values of the transport parameters, through the calculation and exporting of the model results of the variants was automated using Python scripts. Therefore, the simulations may be performed in parallel and on several computers.
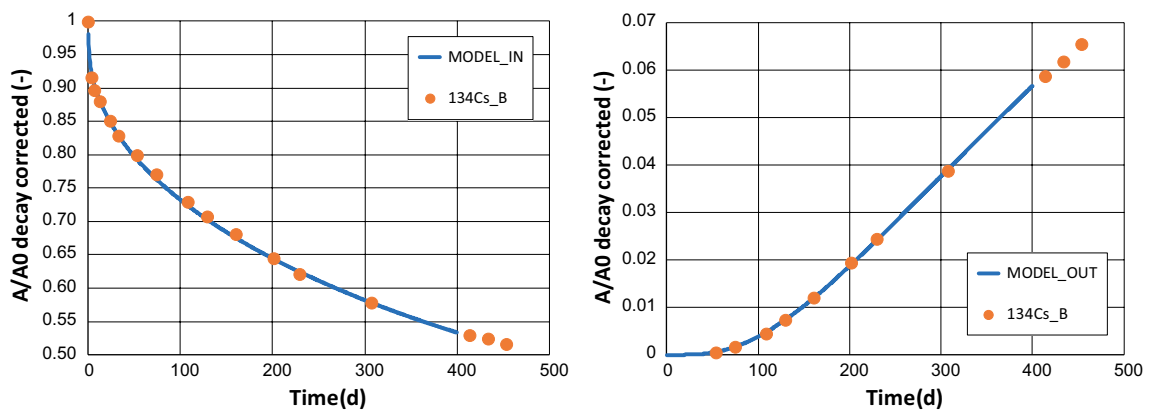
Figure 5-8. *Laboratory diffusion experiment LTDIII – comparison of the measured breakthrough curves with results of the calibrated model (inlet reservoir on the left, outlet reservoir of the diffusion cell on the right).*

The simulation was evaluated in the form of a graphical comparison of the measured and model data for the cross-sections of the model domain and the temporal evolution in the source reservoir. No classical model calibration, i.e. gradually refined model parameters, was performed as this would be extremely time consuming, with a total of nine parameters needing to be calibrated for each of the three tracers Cl-36, Na-22 and Cs-137. A procedure where only combinations of model parameters for which the model results correspond to measurements were selected from all of the simulated variants, was used.

The values of the calibrated parameters are summarised in Table 5-3 to Table 5-6 (the value ID indicates the number of the model for linking the parameters to the results of the model). Figure 5-9 to Figure 5-11 provide a comparison of the measured data and the model results. The values of the parameters for the individual tracers and model domains are relatively varied; therefore, a combination of all of the parameters is important. Certain trends can be observed in the calibrated parameters of the individual model domains, but a clear evaluation of the results of micro DFN models is not so simple:

- The calibrated data generally show relatively low porosity values (for some variants several orders of magnitude lower than the measured values).

- On the contrary, a relatively high pore diffusion coefficient D_p (in some cases even higher than the diffuse coefficient in open water) was calibrated. This model behaviour requires a more in-depth analysis. For example, the combination of higher D_p and low porosity in the BDZ may be related to the discretisation of the model, where BDZ is assumed to be to a maximum distance of 1 mm. The combination would suggest a significantly lower thickness of the BDZ.

- The results of the model confirmed negligible values of distribution coefficient K_d for Cl-36 and a significantly higher sorption value for Cs-137.

- A relatively big problem that influenced the direction of the micro-DFN modelling during the solution of Task9B was the development of the measured data for Cs-137. The original data showed strong preferential behaviour of this tracer (the low activity should have resulted in it reaching a relatively long distance). An explanation of this behaviour was the main motivation for using the micro-DFN model with its ability to capture the heterogeneity of the rock matrix. However, after a few years, the Cs-137 measurement data was revised, and recommendations were made that measured values below 1 Bq/g (values measured in deeper samples) are not representative. The measured results of all of the tracers have a relatively predictable course, which could probably be understood by a simpler model based purely on the CPM concept.

- In the case of the Na-22 tracer, it was not possible to find an optimal combination of parameters that would best fit the activity in both the cross-section and source. The problem is most likely due to erroneous data, where the overall balance of the tracer does not fit the experiment. After extrapolation of the measured activity in the individual sections into the whole of the affected volume of rock, the activity of Na-22 in the rock is significantly lower than the loss of activity in the source (although the loss is small with respect to the total injected amount).

- From the point of view of obtaining more an accurate evaluation and results, it would be appropriate to include simulations of laboratory experiments determining the diffusion coefficients on samples (e.g. calibration of measurements in diffusion cells) in the whole process. No raw data were available from SKB for these models (only evaluated parameters, which is insufficient for the model).

Table 5-3. Cl-36 – calibrated transport parameters of the micro-DFN model.

ID	Porosity [-]			D_p [m$^2 \cdot$ s^{-1}]			K_d [m$^3 \cdot$ kg^{-1}]		
	BDZ	FRAC	MATRIX	BDZ	FRAC	MATRIX	BDZ	FRAC	MATRIX
#593	1.6E−3	2.9E−5	1.6E−7	4.8E−12	3.9E−8	4.3E−11	1.6E−8	1.8E−8	2.4E−2
#1533	2.8E−5	7.8E−4	1.1E−7	8.3E−8	3.6E−11	1.0E−6	3.0E−6	1.7E−7	1.4E−8
#876	2.1E−7	2.0E−3	6.3E−3	7.7E−9	1.7E−12	3.8E−8	1.2E−7	2.7E−7	7.5E−8

Table 5-4. Na-22 – calibrated transport parameters of the micro-DFN model for cross-sections of the model domain.

ID	Porosity [-]			D_p [m$^2 \cdot$ s^{-1}]			K_d [m$^3 \cdot$ kg^{-1}]		
	BDZ	**FRAC**	**MATRIX**	**BDZ**	**FRAC**	**MATRIX**	**BDZ**	**FRAC**	**MATRIX**
#959	1.1E−5	2.2E−8	5.0E−4	3.4E−9	4.8E−6	5.1E−6	4.8E−4	5.2E−7	5.8E−5
#22	1.5E−6	5.7E−2	6.1E−6	7.9E−9	2.9E−8	3.1E−11	1.9E−5	4.7E−5	3.4E−3
#545	2.3E−8	1.2E−2	5.6E−2	3.2E−7	9.5E−11	1.0E−7	3.2E−4	5.5E−2	2.7E−7
#1065	2.2E−7	5.1E−7	2.5E−5	5.3E−8	1.4E−9	8.6E−6	1.5E−4	3.6E−2	9.6E−6
#1925	3.3E−3	1.3E−4	3.6E−6	3.8E−9	6.5E−12	7.1E−7	2.4E−5	9.6E−4	4.5E−8

Table 5-5. Na-22 – calibrated transport parameters of the micro-DFN model for the evolution in the inlet reservoir.

ID	Porosity [-]			D_p [m$^2 \cdot$ s^{-1}]			K_d [m$^3 \cdot$ kg^{-1}]		
	BDZ	**FRAC**	**MATRIX**	**BDZ**	**FRAC**	**MATRIX**	**BDZ**	**FRAC**	**MATRIX**
#640	3.5E−5	1.7E−4	7.3E−4	1.9E−7	2.4E−10	3.0E−10	3.7E−4	5.5E−5	2.9E−6
#2365	4.0E−2	6.1E−7	1.0E−3	1.3E−10	1.7E−7	4.1E−10	5.3E−4	1.9E−4	7.7E−8
#985	2.5E−7	6.8E−5	5.0E−3	7.1E−6	8.2E−11	5.7E−8	1.2E−3	1.5E−2	8.7E−8
#508	1.1E−5	3.1E−2	8.3E−5	1.2E−7	5.7E−11	1.1E−6	3.6E−4	8.0E−5	3.1E−8
#2359	2.2E−4	5.0E−7	1.0E−2	1.6E−9	1.7E−7	3.1E−8	2.7E−4	5.1E−4	1.7E−5

Table 5-6. Cs-137 – calibrated transport parameters of the micro-DFN model.

ID	Porosity [-]			D_p [m$^2 \cdot$ s^{-1}]			K_d [m$^3 \cdot$ kg^{-1}]		
	BDZ	**FRAC**	**MATRIX**	**BDZ**	**FRAC**	**MATRIX**	**BDZ**	**FRAC**	**MATRIX**
#136	3.4E−6	3.8E−5	3.3E−3	3.1E−6	1.4E−10	3.9E−10	1.2E−2	2.0E−5	7.4E−4
#1668	3.7E−6	4.4E−6	9.6E−5	5.9E−7	2.6E−6	4.5E−9	8.3E−3	1.0E−1	1.3E−5
#2182	3.4E−2	5.1E−7	1.6E−2	5.0E−10	3.2E−10	6.6E−10	2.7E−3	5.3E−2	5.2E−3
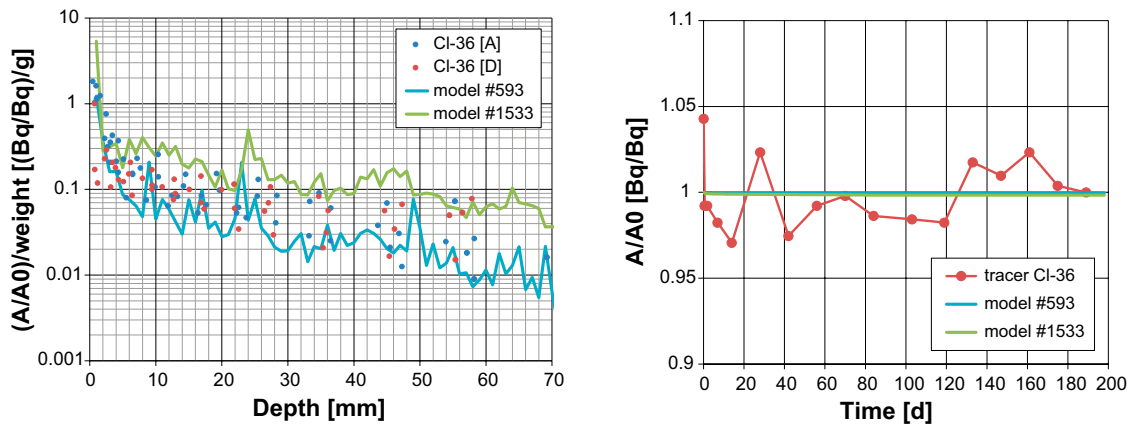
Figure 5-9. Cl-36 – comparison of measured data and model results – cross-sections of the sample and model domain on the left, course of the activity in the source reservoir on the right.
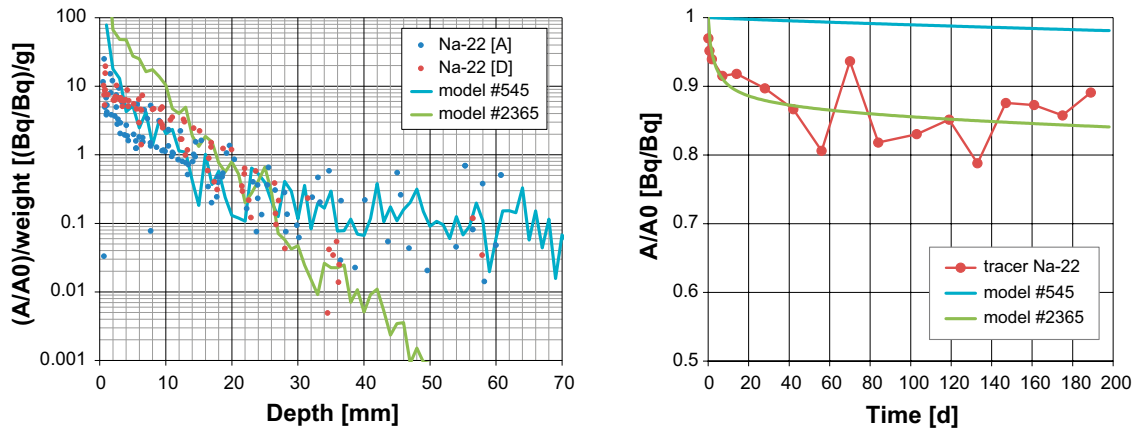
Figure 5-10. *Na-22 – comparison of measured data and model results – cross-sections of the sample and model domain on the left, course of the activity in the source reservoir on the right.*
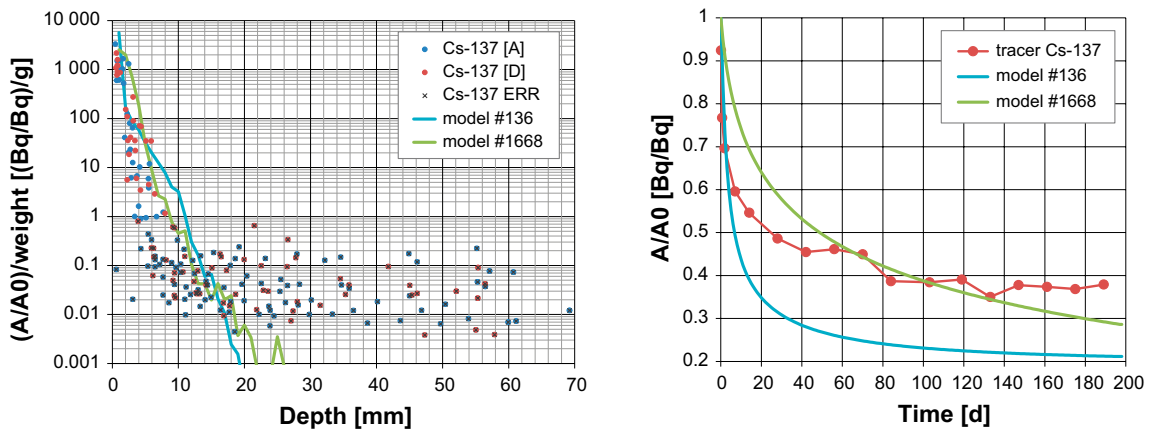
Figure 5-11. *Cs-137 – comparison of measured data and model results – cross-sections of the sample and model domain on the left, course of the activity in the source reservoir on the right.*

6 Solution of task TDE (Task 9C)

This subtask focuses on the predictive modelling of an in-situ through-diffusion experiment (TDE) as part of the REPRO project performed by POSIVA in ONKALO, Olkiluoto, Finland.

Formally, the content of Task 9C was only a prediction, but after closing the solution stage and submitting the results of the models by the individual investigators, and publishing them at project meetings, the data from the experiment, which was actually ongoing at the time of the processing of the model and continues at the time of this report, was released. Part of the report is a subsequent evaluation of agreement and differences between the models and the measurements. In addition, a model calibration (inverse model) was performed beyond the scope of the task description of Task 9 of GWFTS (but in accordance with its general aims). The research teams participated in the different parts to various different degrees, which is reflected in the structure of the sections and the presented comparisons.

6.1 Summary of the task description and the data

The TDE experiment was launched in November 2015. Information for the needs of the model solution in the framework of GWFTS is given in the task description (Andersson et al. 2020). The experiment takes place between three parallel sub-horizontal boreholes arranged in a right-angle triangle (Figure 6-1 – No. 324, 326 and 327, the entire designation is ONK-PP324, etc.). Borehole 326 serves as an injection borehole and the other two as monitoring boreholes. The geometry of the experiment is motivated by the effort to capture the migration of tracers in the directions perpendicular and parallel to the rock foliation. Each of the boreholes has a radius of 28.25 mm.

Sections measuring 1 m are open within the boreholes, the transverse distance between the borehole walls is 10–15 cm, and the mutual difference of position between the boreholes in the direction of the axes is in units up to the first tens of centimetres (Table 6-1). The open sections are at a distance of 11–12 m from the tunnel wall and next to them are so-called guard sections (separated by other packers), interconnected internally and externally, which reduce the hydraulic gradient around the experiment. The packer sections are connected to the apparatus in the underground laboratory by a circulation system with documented volumes of its individual parts (Table 6-2). The device presented in the WPDE experiment is used, i.e. the borehole is fitted with a cylinder and a solution flows through the slot between the cylinder and the borehole wall.
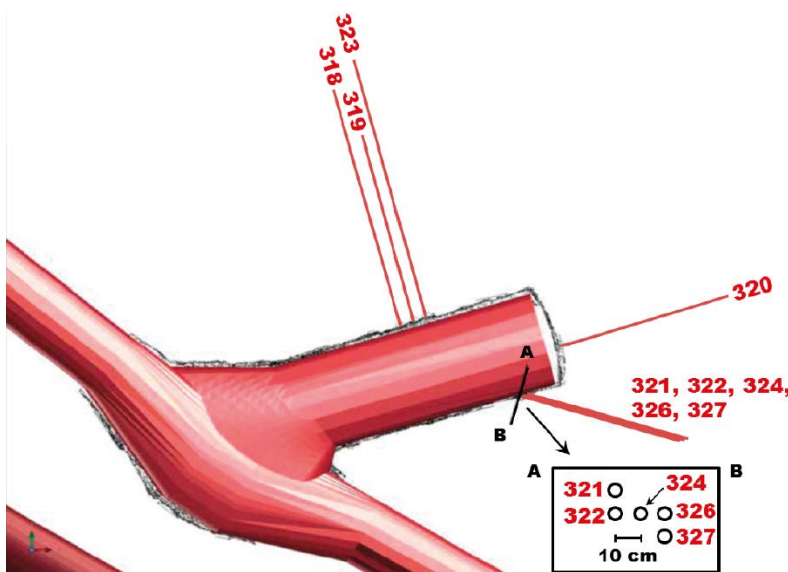
Figure 6-1. *Borehole assembly at and around the TDE experiment – the injection borehole is number 326 and the monitoring boreholes are 324 and 327 (taken from Andersson et al. 2020).*

Table 6-1. Task 9C – coordinates of the centres of the open boreholes and the distance between the boreholes.

Bore hole	X [m]	Y [m]	Z [m]	Distance from ONK-PP326 [m]		
				centre-centre Original task description	wall-wall Original task description	wall-wall Revised task description 11/2018
ONK-PP324	0.43	0.48	−0.31	0.2665	0.153	0.15
ONK-PP326	0.34	0.23	−0.29			
ONK-PP327	0.33	0.27	−0.45	0.1652	0.119	0.115

Table 6-2. Task 9C – volumes of solutions in boreholes, including the supply piping (a detailed differentiation of individual contributions to the total volume is included in the task description, see Andersson et al. 2020).

Borehole	Volume of solution in the borehole [mL]	
	Original task description	Revised task description 11/2018
ONK-PP324	268	291
ONK-PP326	252	290
ONK-PP327	268	313

A "cocktail" containing the following tracers was injected: HTO, Na-22, Cl-36, Ba-133 and Cs-134. Both the decreasing concentrations in injection borehole 326 and increasing concentrations in boreholes 324 and 327 are monitored. Concentrations are measured both by online detection of total gamma activity inside the boreholes and on the basis of samples of documented volumes, which are replaced by synthetic groundwater of the same volume without the tracer. Table 3-1 of the task description (Andersson et al. 2020) includes the total injected activities and detection methods.

The aim of modelling is to predict the course of activity or the concentrations in the boreholes over a period of 10 years, although the breakthrough of heavier sorbing tracers is not expected. The model includes the full balance of the tracers in the individual rock forms and individual parts of the experimental apparatus. Decay-corrected activities, i.e. concentrations corresponding to a conservative tracer, are evaluated, and the results presented below are also processed in this way.

The parameters for the model (Table 6-3) are set the same by all investigators in the case of data from the task description (Andersson et al. 2020): porosity based on Table 5-4 as an average of 13 samples from experimental borehole sections, effective diffusion coefficient of tritium from Table 5-5 as the average of three samples and the sorption coefficient for Na-22 and Ba-133 from Table 5-8 (value for VGN rock). The task description did not state the effective diffusivities for sodium and barium, which were taken from the task description of Task 9A (the experiment performed in the same rock). Furthermore, the parameters used for Cs-134 are taken from the data from the LTD-III experiment (Havlová et al. 2016). Data for Cl-36 were interpreted differently, either considering the anion exclusion (TUL, ÚJV) according to the data from Task 9A, or as the reference porosity (CTU).

Table 6-3. Model transport parameters of the used tracers.

	$\varepsilon(-)$	K_d (m³·kg⁻¹)	D_e (m²·s⁻¹)	D_w (m²·s⁻¹)
H-3	0.0094	0	3.90E−13	2.30E−09
Na-22	0.0094	0.0013	4.65E−13	1.33E−09
Cl-36 (TUL, ÚJV)	0.000175	0	5E−15	2.03E−09
Cl-36 (CTU)	0.0094	0	3.40E−13	2.03E−09
Ba-133	0.0094	0.060	1.47E−13	1.69E−09
Cs-134	0.0094	0.031	3E−13	2.07E−09

The technical data of the experiment in the task description was revised during the task solution and the models were subsequently modified. The data presented in this report correspond to the final version and, therefore, may differ from those presented at the executive meetings and stated in the interim reports. The main changes of input parameters are included in Table 6-1 and Table 6-2.

Several problematic aspects were encountered during the measurement i.e. problems with the circulation in PP324 meant the borehole had to be flushed and the piping re-installed, leading to an ambiguous interpretation of the arrival of HTO. A continuous increase starts after 1 000 days; however, qualitatively the first arrival of HTO should be considered about 300 days, of course without realistic concentration values.

6.2 Implementation of the models

6.2.1 Solution of Task 9C using Flow123d

This is an ad-hoc balance model with Flow123d at its core. The model evaluates the concentrations in the boreholes, which are then used as boundary conditions for a transport simulation in Flow123d. The input of the model are the injected activities (or masses) of the individual tracers together with the volumes of solutions (effective part of the experimental section together with the inlets) in each of the boreholes. Flow123d runs the model with a given time step, evaluates the mass balance (Flow123d output) and recalculates the concentrations in the boreholes. It also sets the last known concentration distribution in the rock matrix as the initial condition for the next step of the calculation. The model may also simulate the sampling.

Diffusion (migration process) and linear sorption (retardation process) are simulated in Flow123d. Advection is considered only in the context of test calculations (see Section 6.4).

Several simplifications were made to prepare the model:

- The rock matrix is simulated as being homogeneous in the prediction. Possible heterogeneity of the model is considered in the inverse model.

- Experimental artefacts (e.g. concentration leaks during the experiment) are not considered. The presence of these artefacts is known, but not sufficiently documented. Their omission from the existing simulations was carried out based on a recommendation from the task leaders.

- Geometry of the model (and thus the discretisation mesh) is only 2D. This simplification was adopted in order to reduce computational requirements.

- Zero mass flux as a boundary condition of the transport is prescribed at the outer boundary of the simulated domain. This boundary condition is necessarily incorrect because the model domain is finite, and its boundaries are not at a significant distance from the experimental section. An alternative would be to prescribe a zero concentration at the boundary, which is no more accurate. The solution would be to extend the model domain, whereby reducing the impact of the boundary condition (at the expense of increased computational requirements).

- An ideal mixing of the tracers in the water volumes is assumed.

- The pressure gradient and advective transport are not considered. The pressure difference was measured between the individual boreholes during the experiment. The effect of the pressure gradient on the model results was tested separately (see below).

The geometry of the model is given by the position of three boreholes according to Table 6-1. For 2D geometry, the depth of the individual boreholes in the experimental sections is irrelevant. However, in a 3D model, it would have to be taken into account.

The computational area was discretised by triangular elements with local refinement around the boreholes (0.25 mm) and at their joints (2.5 mm). In the remainder of the area the size of the elements was 10 mm. The resulting mesh consists of 39 325 elements (Figure 6-2).
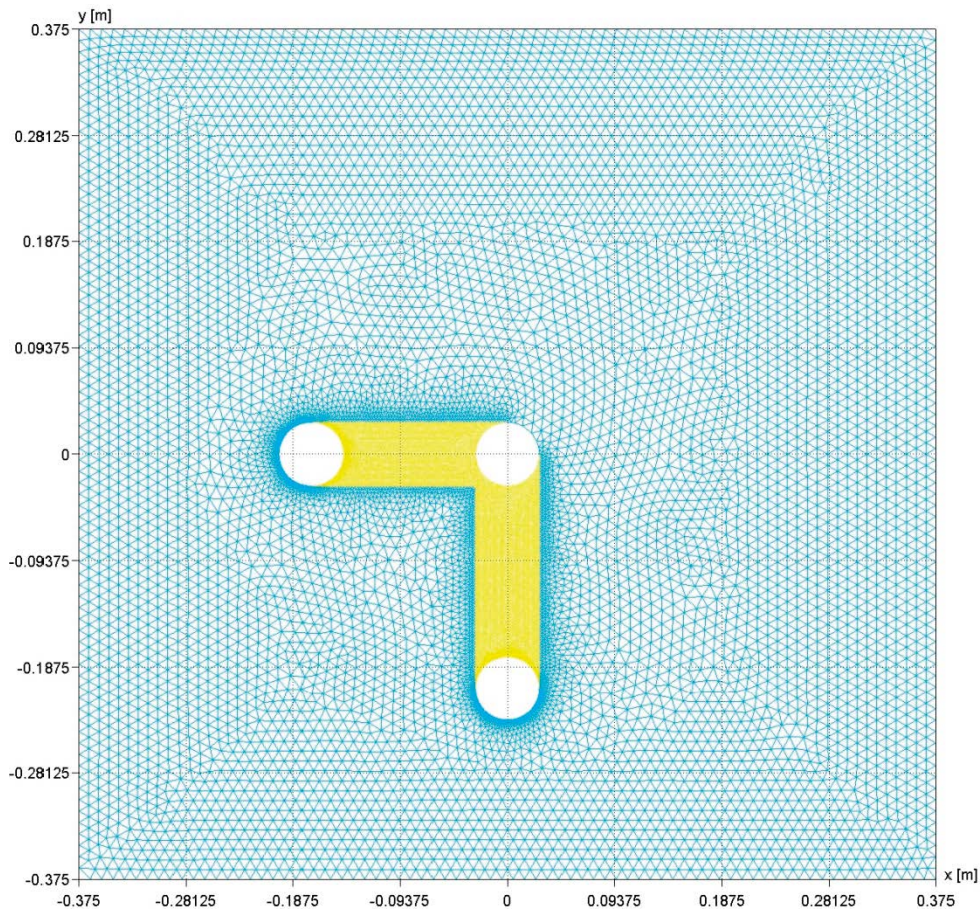
Figure 6-2. *Task 9C – Flow123d – computational mesh of the model.*

Our aim was to simulate the transport, where the only driver of concentration spreading is molecular diffusion. Therefore, the flow model parameters were set to minimise the pressure gradients and thereby also the flow velocities. The hydraulic conductivity of the rock matrix is constant throughout the region K = 2.8731×10^{-12} m/s (calculated from the average permeability k=3.825×10^{-19} m²). A zero piezometric head is prescribed as a boundary condition at the edge of the injection borehole, with a homogeneous Neuman boundary condition (zero flow) used on the remaining model boundaries. The transport model parameters are summarised in Table 6-3.

The boundary conditions of transport on the circumference of the boreholes are given by the concentrations of tracers in the borehole solution (they change over time). A homogeneous Neuman boundary condition is prescribed at the outer boundary of the model. The initial volumes of the solutions in each borehole are shown in Table 6-2. The volumes of the solutions change during the experiment due to sampling. However, this was not included in the predictive simulation due to the absence of input data in that time. Nevertheless, the model is ready for this.

The total simulation period was set to 10 years according to the requirements of the task leaders. The internal step of the balance model was different for the individual tracers (0.1 year for HTO, 0.01 year for Na-22 and Cl-36 and 0.005 year for Ba-133 and Cs-134). Strongly sorbing tracers needed a shorter time step to avoid oscillations (given by the stability limit of the explicit method). In Flow123d, the discontinuous Galerkin method (implicit in time) was used to calculate the transport in the individual steps.

The results of the simulations are presented in Section 6.3 in the comparison of the results of the individual investigators.

6.2.2   Solution of Task 9C using GoldSim (ÚJV)

The subject of the experiment in the initial phase of the solution was to simulate the transport of radionuclides H-3, Na-22, Cl-36, Ba-133, Cs-134 from the specified section in the injection borehole to the specified section on each of the two monitoring boreholes. The following features were omitted from the experiment:

1. Unsteady pressure conditions in defined sections of the borehole.

2. Changes in the radionuclide activity in the boreholes due to the sampling (taking a certain amount of water of a given activity, subsequently replacing this volume with water without a tracer).

3. Radioactive decay.

Due to these assumptions, diffusion transport is simulated, where the breakthrough of radionuclides through the rock environment is retarded by their sorption in the rock matrix.

The GoldSim program (commercial license, version 12.0) was used to solve Task 9C and the "Cell pathway" component was selected. The use of this component is a volumetric approach, where the model area is represented by a network of interconnected cells (Cell Net). The concentration of the radionuclide in one cell can be varied both by diffusion and/or advection transport between adjacent cells, and by radioactive decay of the radionuclide itself, or of the parent radionuclide contained within the cell. The control equations for the "Cell pathway" component were described in the interim report (Hokr et al. 2015) during the solution of Task 9A and recalled in chapter 2 of this report.

The results of the comparison between the two variants of a preliminary 1D radial model (Interim Report – Hokr et al. 2017) showed that the presence (position) of the monitoring borehole influenced the development of the activity in the injection borehole in all cases. In variant 1, the activity in the monitoring boreholes is also influenced by the position of the boundary condition c = 0, which is at an insufficient distance. A new model was used for the subsequent solution.

The task is solved in 2D, discretisation of the model area was solved separately for non-sorbing radionuclides (H-3, Cl-36) and for strongly sorbing radionuclides (Ba-133, Cs-134). In the case of the transport simulation of Na-22, such detailed discretisation was not as necessary as in the case of strongly sorbing radionuclides. On the other hand, the degree of discretisation used for non-sorbing radionuclides was insufficient. The discretisation for strongly sorbing radionuclides has a fundamental influence on model results, while maintaining the transport parameters. In the case of insufficiently detailed discretisation, different results are obtained for different types of discretisation of the model area. For this reason, the choice of discretisation was given great attention.

For non-sorbing radionuclides, two types of discretisation with different division between injection (IB) and monitoring (MB) boreholes (10 and 20 parts between IB and MB, respectively) were tested, with the results being very similar in both cases. The model area consists of 37 cells in the x-axis direction and 37 cells in the y-axis direction, and a total of 1 369 cells in the model. For highly sorbing radionuclides, suitable discretisation was searched until the spreading of the resulting radionuclide in the model region was dependent only on the change of model parameters. In the case of highly sorbing radionuclides, the model area does not contain the monitoring borehole due to the transport of the monitored nuclides over a significantly shorter distance than that between the boreholes. The geometry of the model region for non-sorbing radionuclides is shown in Figure 6-3 and Figure 6-4 and for the sorbing radionuclides in Figure 6-5 and Figure 6-6, and in table form in Table 6-4 to Table 6-6. Two variants, uniform and non-uniform, were tested for highly sorbing radionuclides. The uniform region consists of 41 cells in the x-axis direction and 41 cells in the y-axis direction, and a total of 1 681 cells in the model; the non-uniform region consists of 51 cells in the x-axis direction and 51 cells in the y-axis direction.

As the boundary condition on the outer sides of the model area, there is zero flow of radionuclides across the boundary; therefore, for non-sorbing radionuclides, an area extending far beyond the monitoring borehole is selected. Additional monitoring boreholes are located on the outer boundary of the model area in all of the models, in which an increase in radionuclide activity is monitored in order to confirm the validity of the selected boundary condition.

The injection and monitoring boreholes are simulated as square areas of 4.44 × 4.44 cm and 100 cm in length, the dimensions of a circular borehole with a díameter of 5.65 cm were converted to the foregoing dimensions of the square borehole, in order to maintain the same surface area.

Table 6-4. Discretisation of the model area for non-sorbing radionuclides, values are in cm.

Non-sorbing radionuclides

Model name	Step in the x direction between IB – MB	Step in the y direction between IB – MB	Length of the area in the x direction	Length of the area in the y direction
Coarser discretisation	1.19	1.53	80.28	100.68
Finer discretisation	0.595	0.765	80.28	100.68

Table 6-5. Uniform discretisation of the model region for sorbing radionuclides, values are in cm.

Sorbing radionuclides

Model name	Step in the x direction	Step in the y direction	Length of the area in the x direction	Length of the area in the y direction
Coarser discretisation	0.595	0.595	28.24	28.24
Finer discretisation	0.2975	0.2975	16.34	16.34
The finest discretisation	0.149	0.149	10.39	10.39

Table 6-6. Non-uniform discretisation of the model region for sorbing radionuclides, values are in cm.

Sorbing radionuclides

Model name	Step in the x direction	Step in the y direction	Length of the area in the x direction	Length of the area in the y direction
Discretisation non-uniform_1	0.01/0.02/0.05/0.1/0.2	0.01/0.02/0.05/0.1/0.2	8.24	8.24
Discretisation non-uniform _2	0.01/0.04/0.08/0.16/0.32	0.01/0.04/0.08/0.16/0.32	10.54	10.54
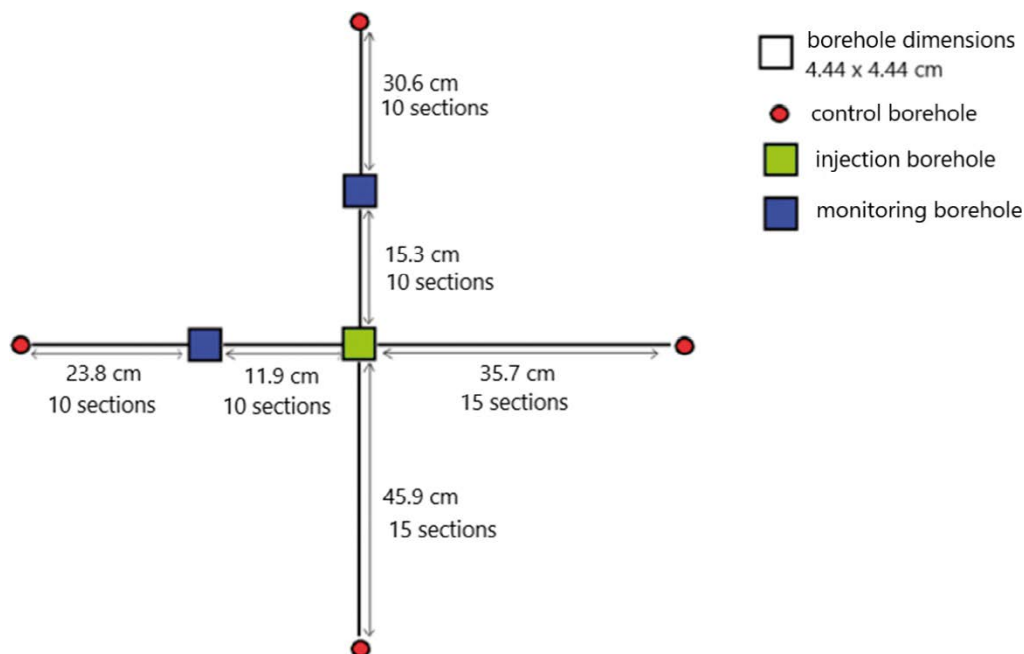
Figure 6-3. Representation of discretisation for non-sorbing radionuclides, coarser division of the model area between the monitoring and injection boreholes.
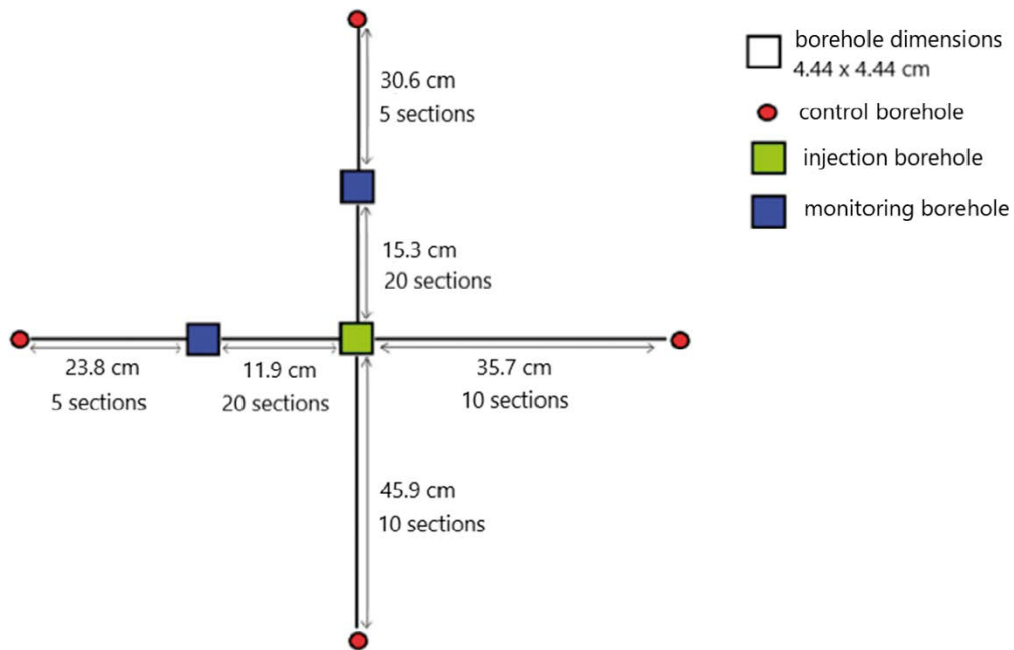
Figure 6-4. Representation of discretisation for non-sorbing radionuclides, finer division of the model area between the monitoring and injection boreholes.
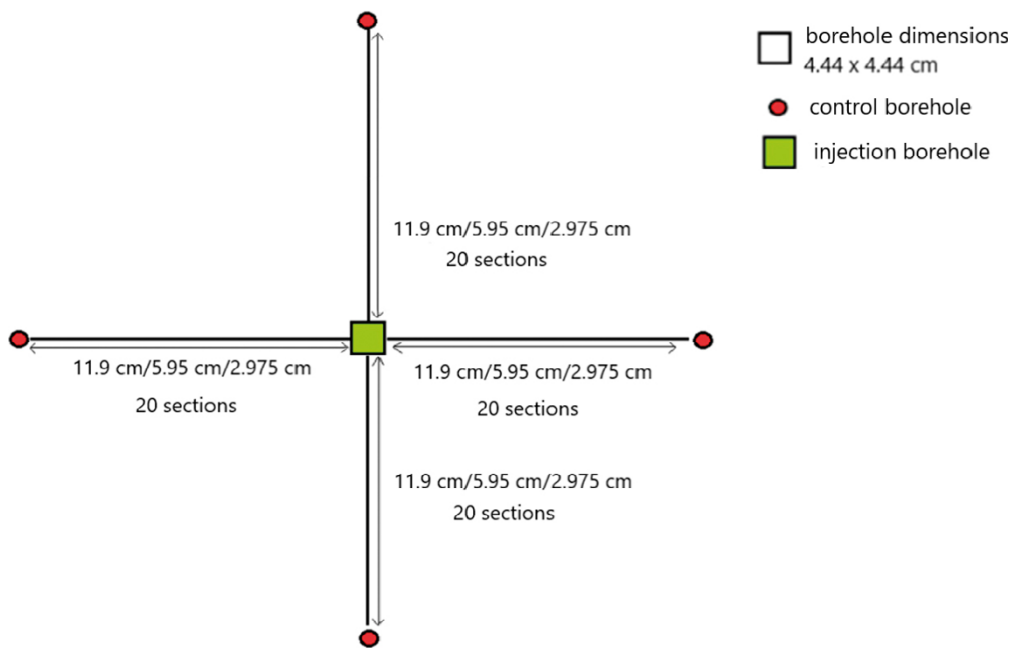
Figure 6-5. Representation of uniform discretisation for sorbing radionuclides, size and discretisation of the model area was made in three variants.
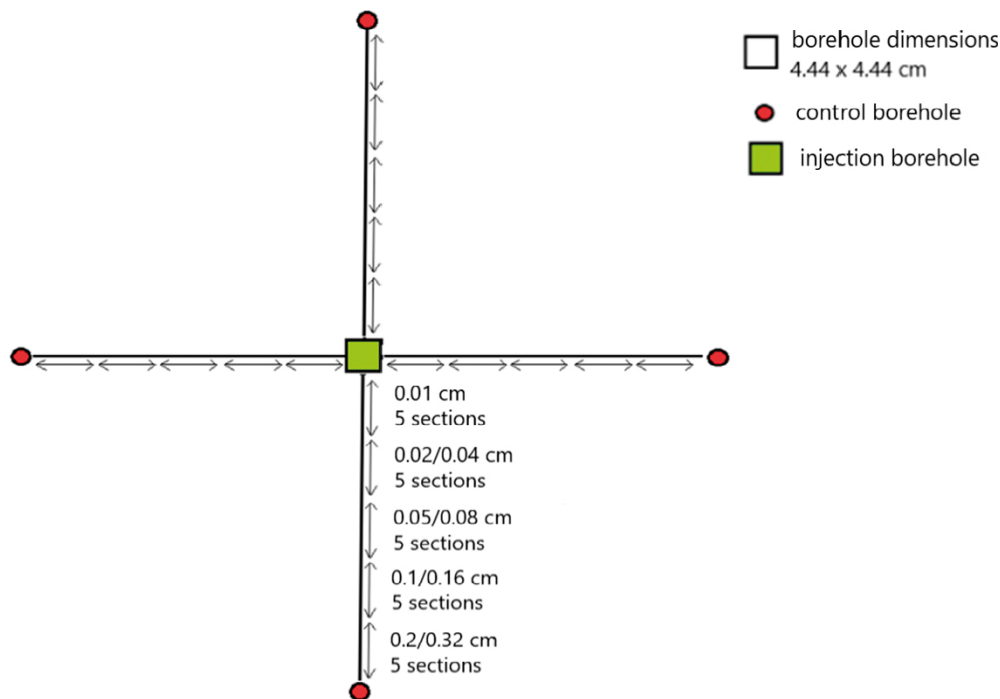
Figure 6-6. Representation of non-uniform discretisation for sorbing radionuclides, discretisation of the model area was made in two variants, the discretisation in the x-axis direction is the same as the discretisation in the y-axis direction.

After experience with Task 9A, the porosity fraction, which assumes that not all pores are available for contaminant transport, was not used due to the fact that the results from ÚJV were not comparable with those of other research groups. In Task 9C, another porosity was only selected for Cl-36, similar to Task 9A. The model parameters used are shown in Table 6-3 and commented on in the introduction (Section 6.1).

The results of the discretisation evaluation are presented as part of the comparison with other models (Section 6.3).

6.2.3 Solution of CTU (GoldSim and analytical variant)

A model was created at the Faculty of Nuclear Sciences and Physical Engineering of CTU to represent the boreholes and the surrounding rock using a planar network of Cell elements. The network diagram is shown in Figure 6-7. The network was designed to allow the simulation of five radionuclides with K_d values from the interval $K_d = [0, 0.001]$ $[\mathrm{m^3 \cdot kg^{-1}}]$. Therefore, we chose a non-equidistant grid refined around the boreholes where the highest concentrations of sorbing radionuclides can be expected. The grid was generated automatically, the volumes and diffusion areas of the elements corresponding to the boreholes were manually adjusted to agree with the cylindrical shape of the boreholes.

The model does not allow the modelling of advective flow, which may have occurred due to possible pressure gradients between the boreholes during the experiment. A finer grid model was created as a control. The results and the comparison between the two types of discretisation showed that radionuclides H-3 and Cl-36 are able to break through the observation boreholes due to diffusion. On the contrary, sorbing radionuclides, especially Ba-133, Cs-134, do not break through and at the same time the transport results for the monitoring boreholes are sensitive to discretisation. Therefore, we proposed to use the 1D radial model around the injection borehole as an alternative for the sorbing radionuclides. To estimate the radius of the domain in which the 1D model around the injection borehole may be considered, we used an analytical solution to the diffusion transport problem of a hollow cylinder with boundary conditions defined inside and at the edge of the cylinder shell. The diffusion equation in the radial coordinate r may be written in a 1D form.

$$\frac{\partial c}{\partial t} = \frac{1}{r}\frac{\partial}{\partial r}\left(rD\frac{\partial c}{\partial r}\right).$$
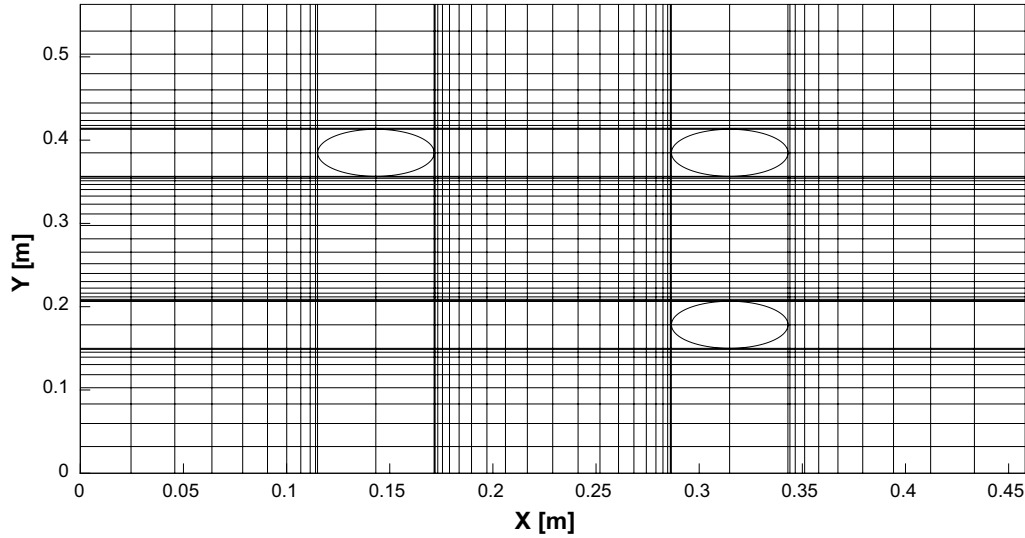
Figure 6-7. *Planar 2D grid in GoldSim for Task 9C.*

If on the inner surface ($x=a$) is maintained a constant concentration $C_a > 0$, and on the outer surface, ($r=b$), a constant zero concentration, $C_b = 0$, and if the concentration within the layer is initially ($t=0$) zero, $C_0 = 0$, then the concentration in the layer can be expressed by the series (Huang and Yen 2002)

$$C(r,t) = C_a \left\{ -\frac{ln\left(\frac{r}{b}\right)}{ln\left(\frac{b}{a}\right)} + \pi \sum_{n=1}^{\infty} \frac{J_0^2(b\alpha_n)[J_0(r\alpha_n)Y_0(a\alpha_n) - Y_0(r\alpha_n)J_0(a\alpha_n)]}{J_0^2(a\alpha_n) - J_0^2(b\alpha_n)} e^{-D\alpha_n^2 t} \right\},$$

where J_0 is the Bessel function of the first kind, Y_0 is the Bessel function of the second kind and α_n are the roots of the equation:

$$J_0(a\alpha)Y_0(b\alpha) - J_0(b\alpha)Y_0(a\alpha) = 0.$$

For a stationary case, the 1D diffusion equation is simplified to

$$\frac{d}{dr}\left(r\frac{dC}{dr}\right) = 0.$$

The solution equation for the considered boundary conditions has the form

$$C(r) = -\frac{C_a ln(r/b)}{\ln(b/a)}.$$

Flow through the layer in the stationary case has the shape

$$J_\infty = -D\frac{dC}{dr} = \frac{DC_a}{\ln\left(\frac{b}{a}\right)}\frac{1}{r}.$$

Flow through the outer surface ($r = b$) is

$$J_\infty^b = -D\left(\frac{dC}{dr}\right)_{r=b} = \frac{DC_a}{b\ln(b/a)}.$$

Based on a comparison of the analytical and numerical solutions, we designed and implemented a single non-equidistant 1D radial grid, which we used for all three of the considered radionuclides. The spacing of the elements over a length of 115 mm, starting at a radius of 28.25 mm, forms a geometric sequence. The step for the borehole with 100 elements is approximately 0.4 mm and the step at the opposite end is about 2.2 mm. Using this model we obtained results for Na-22, Ba-133 and Cs-134.

6.3   Comparison of the solution with the reference variants

Processing of the models by the three research institutions on the basis of an agreed uniform choice of input data enabled a direct comparison of the results and mutual verification, and in certain cases, determination of hypotheses regarding the effects on the accuracy of the calculation. The presented results correspond to the final variants after they were corrected based on partial comparisons at the executive meetings, in particular by modifying the discretisation.

Figure 6-8 shows the course of the concentrations for HTO in both the injection borehole and the detection boreholes. All of the results have a corresponding trend, slight deviations of the values are appropriate to the different processing of the geometry approximation (both GoldSim calculations) and to the differences in the numerical scheme. The lower increase in concentration in borehole 327 relative to borehole 324 corresponds to their different distances from the injection borehole.

Comparison of Cl-36 (Figure 6-9) is only performed between GoldSim (ÚJV) and Flow123d (CTU), where anion exclusion was applied in the same way (uniform parameters). Similar to HTO, the differences are appropriate to the differences in geometry and the effects of the numerical scheme.

The results for Na-22 are given only in the form of a drop in the injection borehole (calculated concentrations in the detection or control borehole of the ÚJV model, were many orders of magnitude below the detection level of the laboratory measurements) in Figure 6-10. In this case, an effect of discretisation around the injection borehole was already observed, similar to the previous tasks. The results with the finest discretisation are presented, in the case of the ÚJV model, in a uniform and non-uniform variant. The differences are mainly in the slope of the initial drop and may be explained precisely by the discretisation, given the delimitation by both variants of the ÚJV model. Despite certain differences, the models may be used with sufficient accuracy to interpret the measured data, which themselves are burdened with a comparatively large error. The results do not include the 1D model from CTU, which were likely affected by the external boundary condition.

For heavily sorbing tracers Ba-133 and Cs-134 (Figures 6-11 and 6-12), the differences between the models are significantly larger. In the long-term, the results fit into up to one order of magnitude range. On the other hand, the curves form an almost systematic series and it can therefore be assumed that this is a quantitatively escalating phenomenon, not a "gross" error in the input data. This again indicates the influence of discretisation. Considering that Flow123d uses the same discretisation in all cases, the agreement with the fully refined 1D model is sufficient.
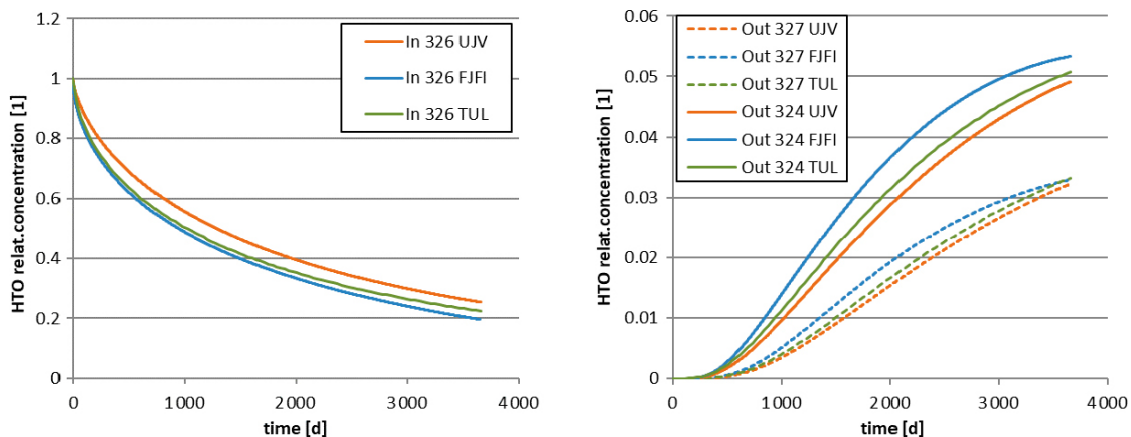
Figure 6-8. *Comparison of results of individual investigators/software for the reference parameters – tracer HTO, course in the injection borehole on the left and in both detection boreholes on the right.*
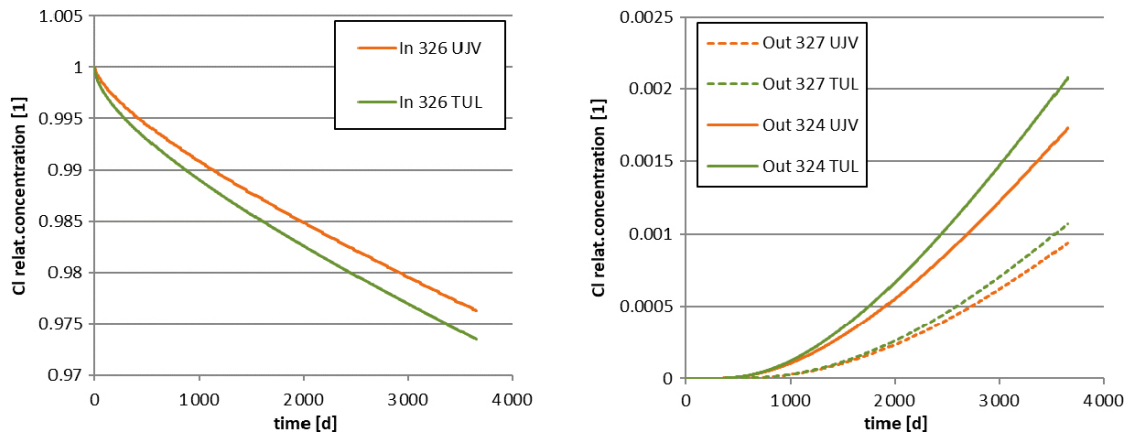
Figure 6-9. *Comparison of results of individual investigators/software for the reference parameters – tracer Cl-36, course in the injection borehole on the left and in both detection boreholes on the right.*
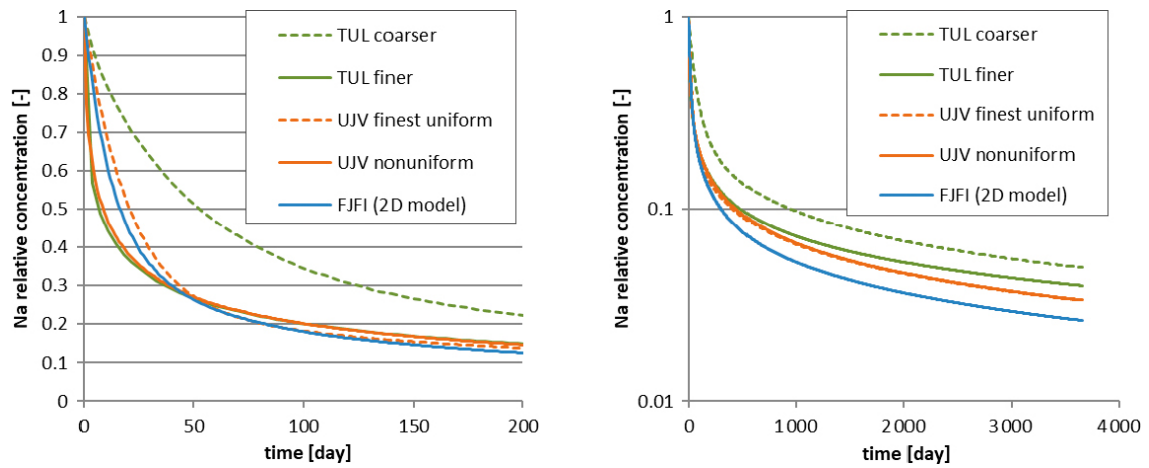
Figure 6-10. *Comparison of results of individual investigators/software for the reference parameters – tracer Na-22, course in the injection borehole in two different axis scales.*
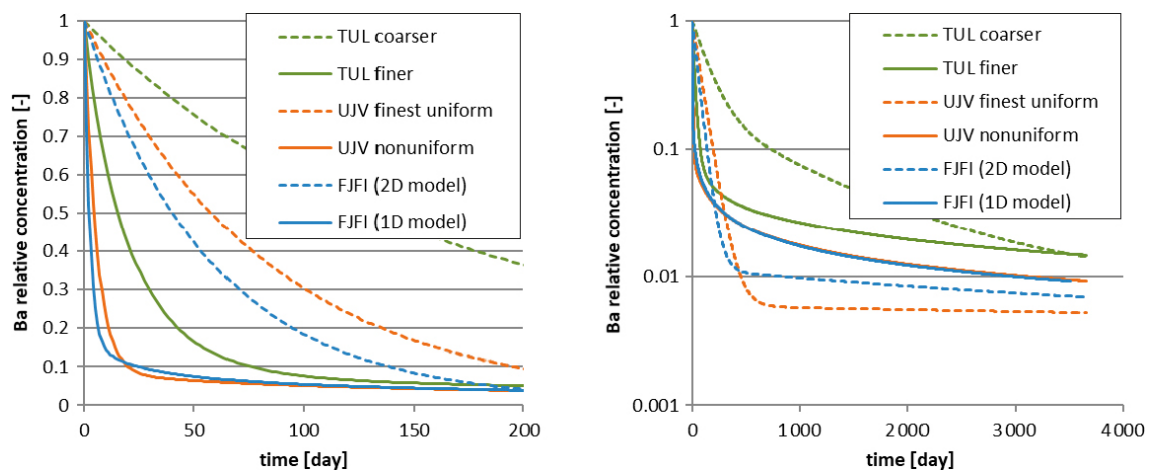
Figure 6-11. *Comparison of results of individual investigators/software for the reference parameters – tracer Ba-133, course in the injection borehole.*
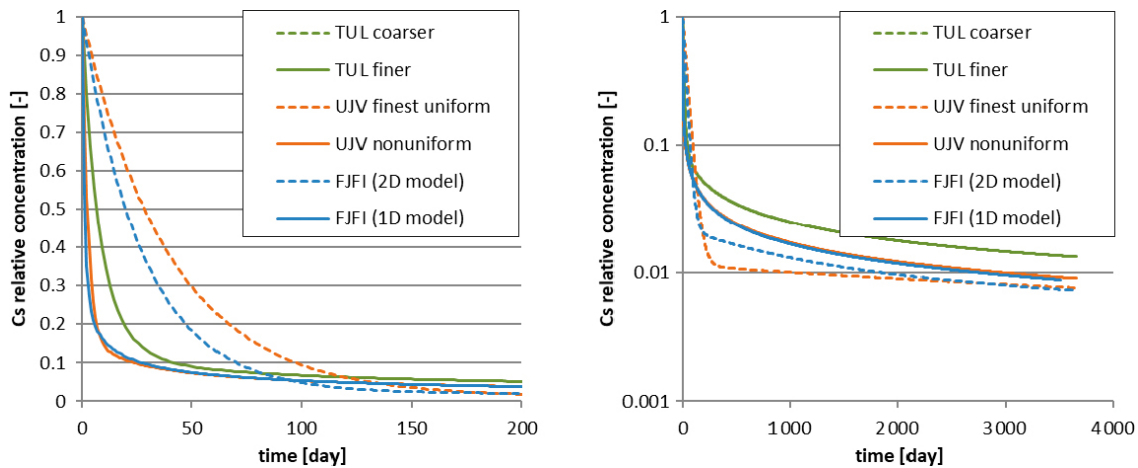
Figure 6-12. *Comparison of results of individual investigators/software for the reference parameters – tracer Cs-134, course in the injection borehole.*

A partial comparison of the influence of discretisation was performed in the framework of the models of the individual investigators. In the ÚJV model, the H-3 and Cl-36 variants were finer and coarser, and the differences were only very small in the source and detection boreholes. Figure 6-13, Figure 6-14 and Figure 6-15 show the fundamental influence of the discretisation of the model region for sorbing radionuclides. Although the size of the model area in the finest discretisation and discretisation non-uniform_2 versions is similar, a more detailed division around the monitoring borehole in the discretisation non-uniform_2 version yields different results than the uniform division in the finest discretisation version. When comparing the model versions discretisation non_uniform_1 and discretisation non_uniform_2 (Table 6-6), it is clear that by further decreasing the step size of the division of the model area no other results are obtained, so the discretisation level in the variant discretisation non-uniform_2 is sufficient. This was confirmed for other tracers, Ba-133 and Cs-134.
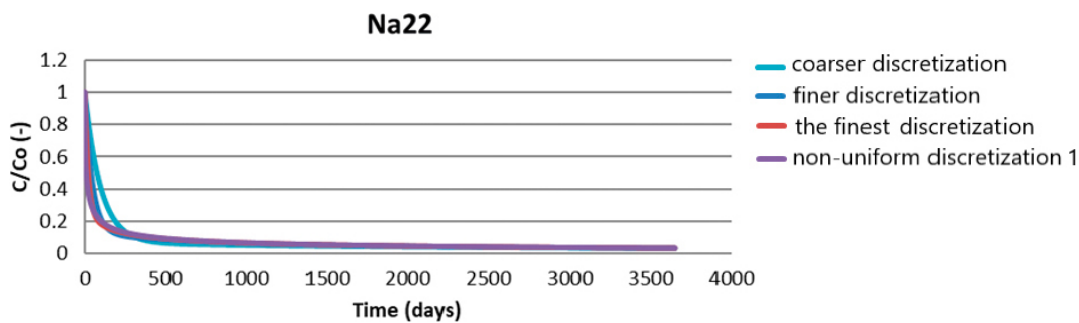
Figure 6-13. *Development of Na-22 activity in the injection borehole for the four considered types of discretisation of the ÚJV-GoldSim model.*
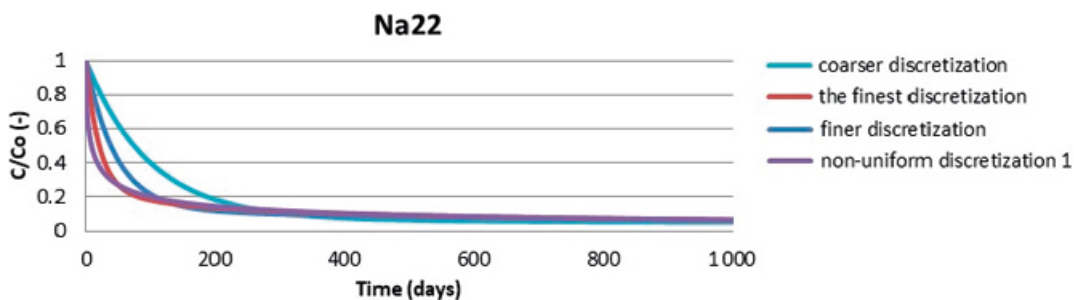
Figure 6-14. *Detail of the development of Na-22 activity in the injection borehole for the four considered types of discretisation of the ÚJV-GoldSim model.*

SKB P-20-22
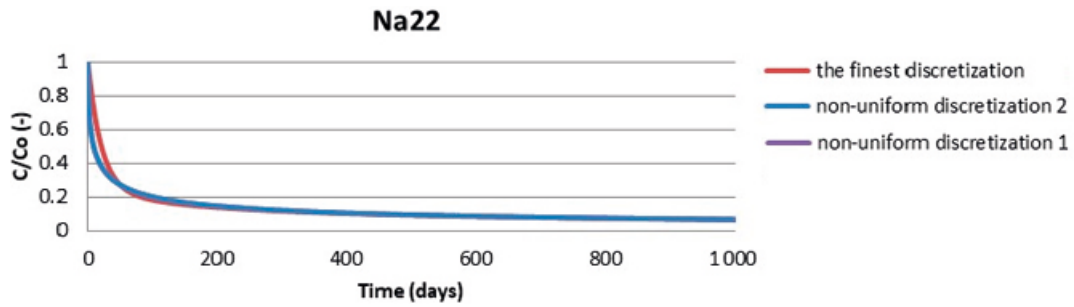
Figure 6-15. *Detail of the development of Na-22 activity in the injection borehole according to the ÚJV-GoldSim model – comparison of uniform and non-uniform division of the model area, curves for the non-uniform division of the area overlap.*

6.4 Analysis of the influence of advection

Due to the pressure gradient documented between the experimental sections of the individual boreholes, it can be assumed that in addition to diffusion and sorption, advection will also be an important transport process.

Three simulations were performed, two based on an artificial constant pressure gradient in a given direction, and the third based on pressure differences taken from the task description. All three simulations were performed for the conservative tracer HTO.

In the first simulation, the pressure gradient was set so that the advection was from the injection borehole to the monitoring boreholes. During the first year of the simulation period, the pressures were balanced, for the remainder of the simulation (up to 10 years) a boundary flow condition in the form of a piezometric head equal to 10 m was prescribed at the boundary of the injection borehole. This corresponds to a pressure difference of 0.1 MPa. The development of the relative activity in the individual borehole is shown in Figure 6-16 and Figure 6-17.
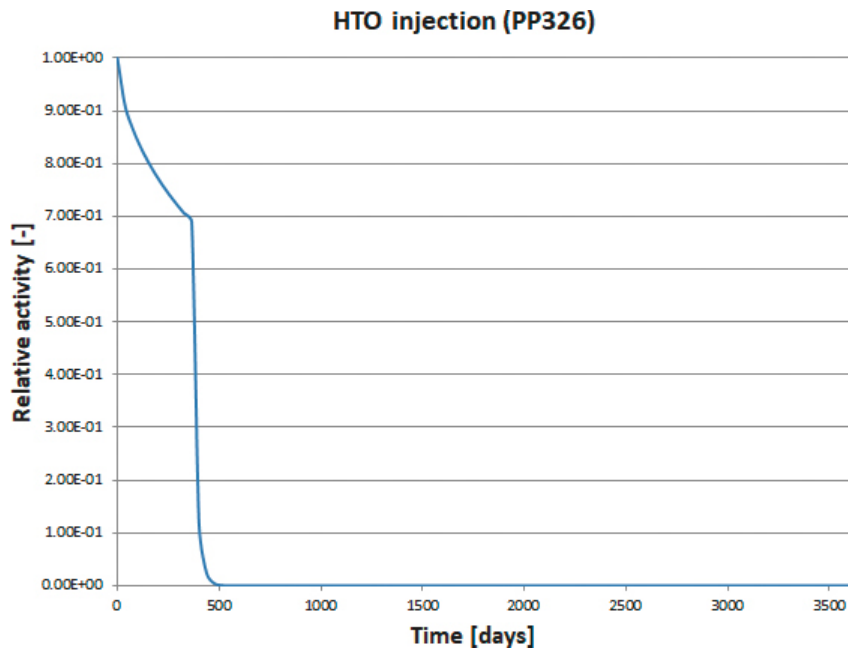
Figure 6-16. *Task 9C – Flow123d – influence of pressure gradient – artificial pressure gradient – advection towards the monitoring boreholes – dependence of relative activity on time in the injection borehole.*
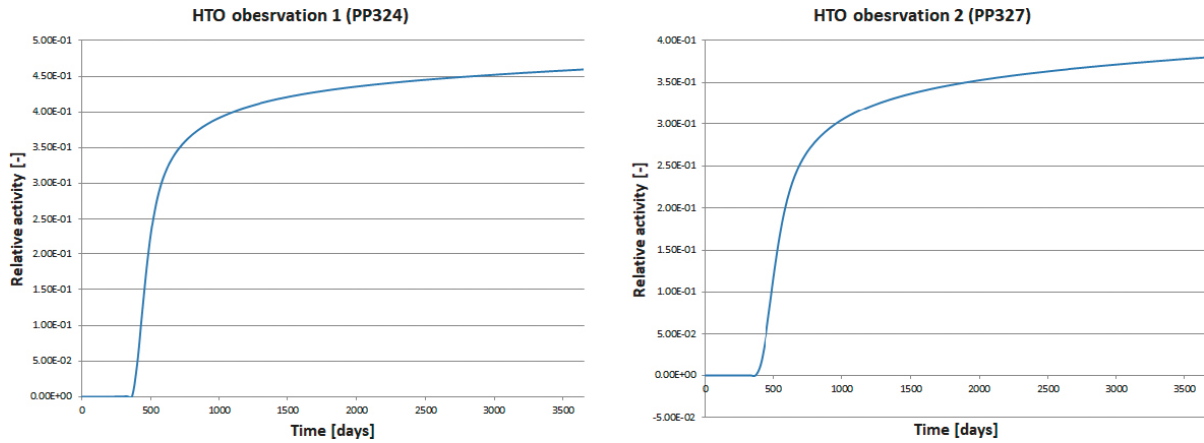
Figure 6-17. *Task 9C – Flow123d – influence of pressure gradient – artificial pressure gradient – advection towards the monitoring boreholes – dependence of relative activity on time in the monitoring boreholes.*

It is apparent from the results that after the "switching on" the advection, the transport of the tracer towards the monitoring borehole will be significantly accelerated.

In the second simulation, the pressure gradient was set so that the advection was from the monitoring boreholes towards the injection borehole. During the first year of the simulation period, the pressures were balanced, for the remainder of the simulation (up to 10 years) a boundary flow condition in the form of a piezometric head of 10 m was prescribed for the monitoring boreholes. This corresponds to a pressure difference of 0.1 MPa. The development of the relative activity in the individual boreholes is shown in Figure 6-18 and Figure 6-19.
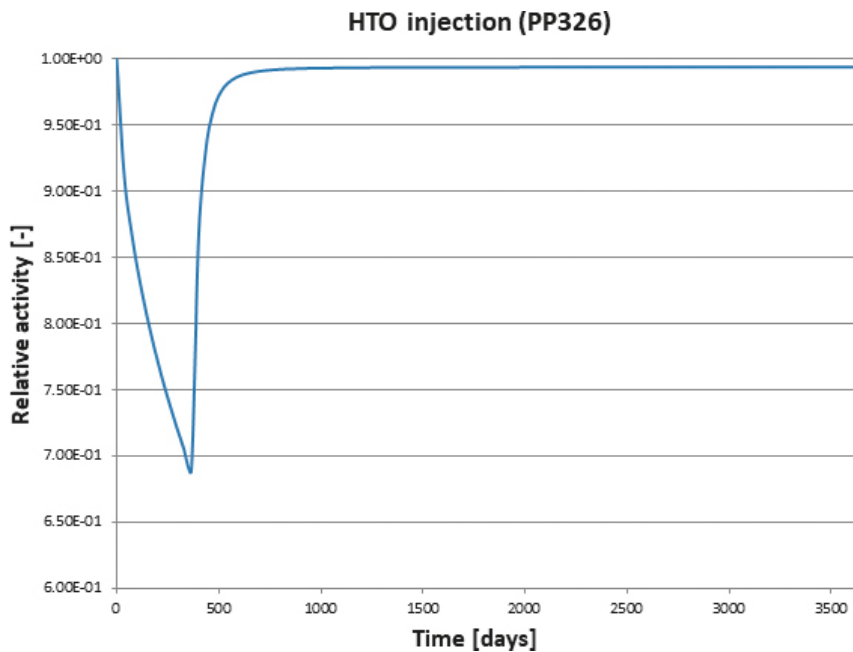
Figure 6-18. *Task 9C – Flow123d – influence of pressure gradient – artificial pressure gradient – advection towards the injection borehole – dependence of relative activity on time in the injection borehole.*
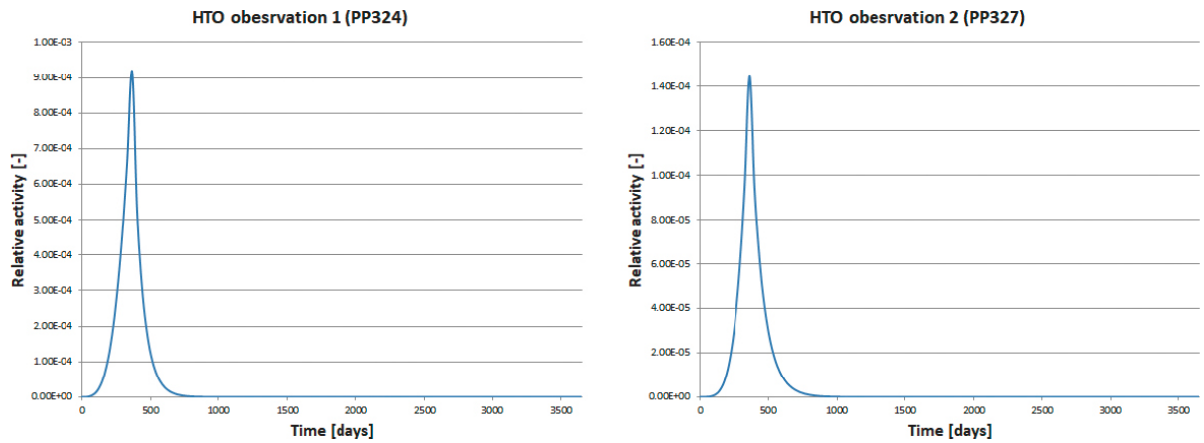
Figure 6-19. *Task 9C – Flow123d – influence of pressure gradient – artificial pressure gradient – advection towards the injection borehole – dependence of relative activity on time in the monitoring boreholes.*

It is apparent from the results that after the advection has been "switched on", the direction of migration of the tracer back to the injection borehole will quickly reverse. This is also documented by the visualisation of the concentration field in Figure 6-20.

In the third simulation, the pressure gradient was given by the measured data (pressures in the boreholes), which was part of the task description. The model in each step adjusts the boundary flow conditions based on the measured data (Figure 6-21). In the times between the two measurements, the pressures are calculated by the linear interpolation method. The simulation period was shortened to the range of measured data (629 days).
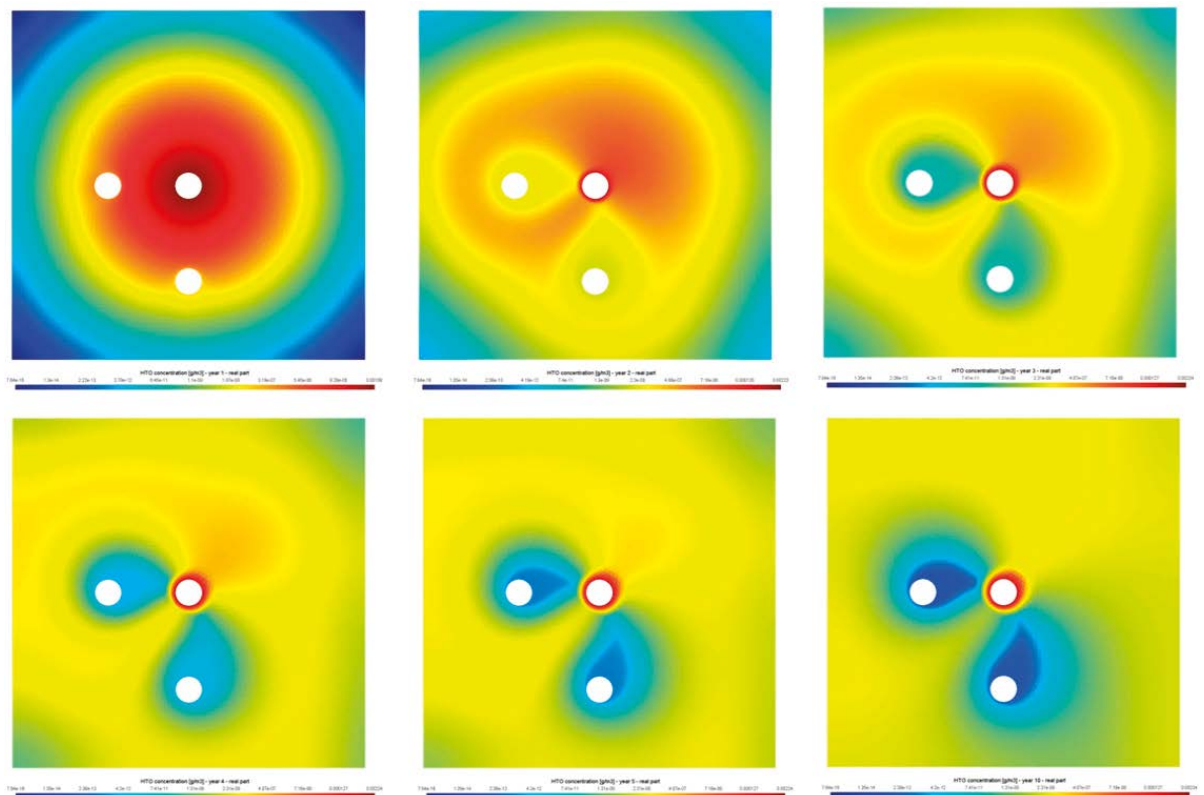
Figure 6-20. *Task 9C – Flow123d – influence of pressure gradient – artificial pressure gradient – advection towards the injection borehole – development of the concentration field (in time 1, 2, 3, 4, 5 and 10 years).*
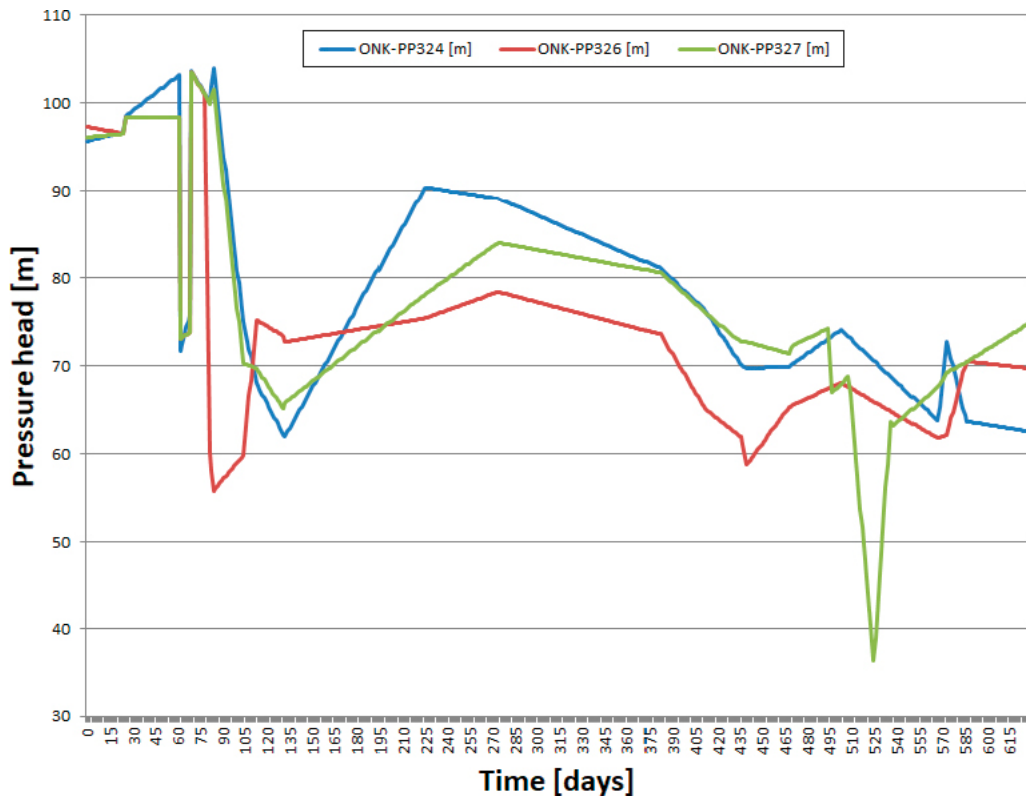
Figure 6-21. *Task 9C – Flow123d – influence of pressure gradient – measured pressure gradient – development of boundary conditions of flow dependence of the relative activity on time in the monitoring boreholes.*
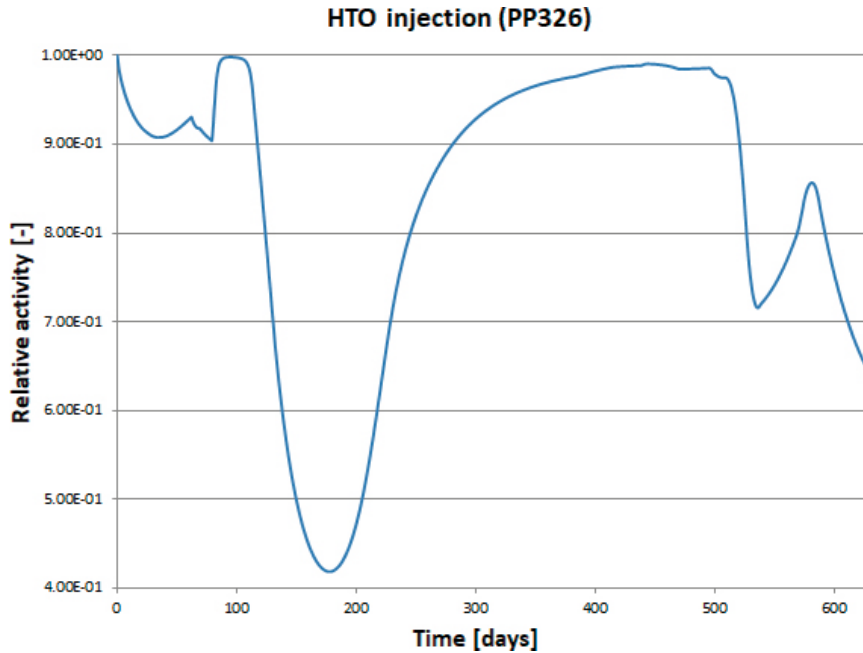
Figure 6-22. *Task 9C – Flow123d – influence of pressure gradient – measured pressure gradient – dependence of the relative activity on time in the injection borehole.*
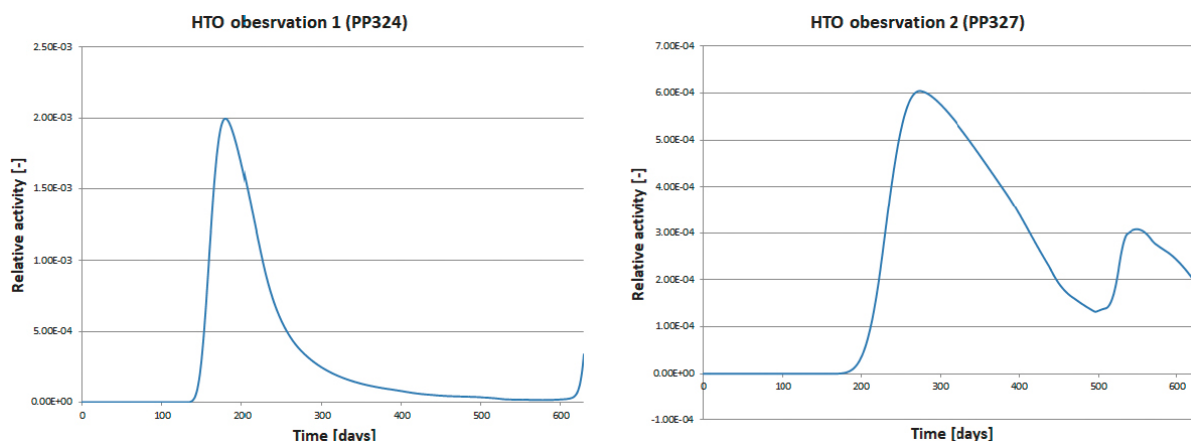
Figure 6-23. *Task 9C – Flow123d – influence of pressure gradient – measured pressure gradient – dependence of the relative activity on time in the monitoring boreholes.*

The development of the relative activity in the individual boreholes is shown in Figure 6-22 and Figure 6-23. As a result, as the direction of the pressure gradient changes, the direction of migration of the tracer also changes.

To conclude, the pressure gradient and the advection it induces may have a significant effect on the simulation results. However, it is debatable whether the measured borehole pressures reflect the actual hydraulic conditions at the site of the experiment or whether this is an experimental artefact.

6.5   Inverse model in Flow123d (TUL)

The aim of the inverse model was to achieve an agreement between the results of the simulation and the measured data by changing the parameters. Specifically, the time courses of concentrations of individual tracers were evaluated, especially in the injection borehole. In the monitoring boreholes the concentrations of some of the tracers did not reach measurable values during the duration of the experiment; therefore, agreement between the simulation and the measurements is evaluated only to a limited extent.

Compared to the blind prediction described above, several changes were made to the model. These were partly motivated by an update to the task description and partly by the need to modify the model to make it more feasible and flexible to calibrate its parameters. These changes included:

- Update of the water (solution) volumes in the experimental sections (according to new version of the task description):
    - ONK-PP324 (monitoring No. 1): 240 ml.
    - ONK-PP326 (injection): 254 ml.
    - ONK-PP327 (monitoring # 2): 262 ml.
- A new computer mesh considering the disturbance zone around each borehole.
- Implementation of sampling – during the course of the experiment, significant amounts of the solution were taken from the experimental sections, which are replaced by pure water, which has an obvious impact on the simulation results.
- Implementation of water/solution exchange in borehole ONK-PP324 at 1 028 days (for HTO and Cl-36, not used elsewhere).

Figure 6-24 shows the updated computational mesh. It consists of 38 868 triangular elements with the finest discretisation being near the boreholes. The figure shows the extent of the disturbance zone under consideration, which is 5 cm from the wall of each borehole. The mesh step sizes are 1 mm at the wall of the borehole, 2.5 mm at the BDZ interface and 10 mm in the rest of the model.
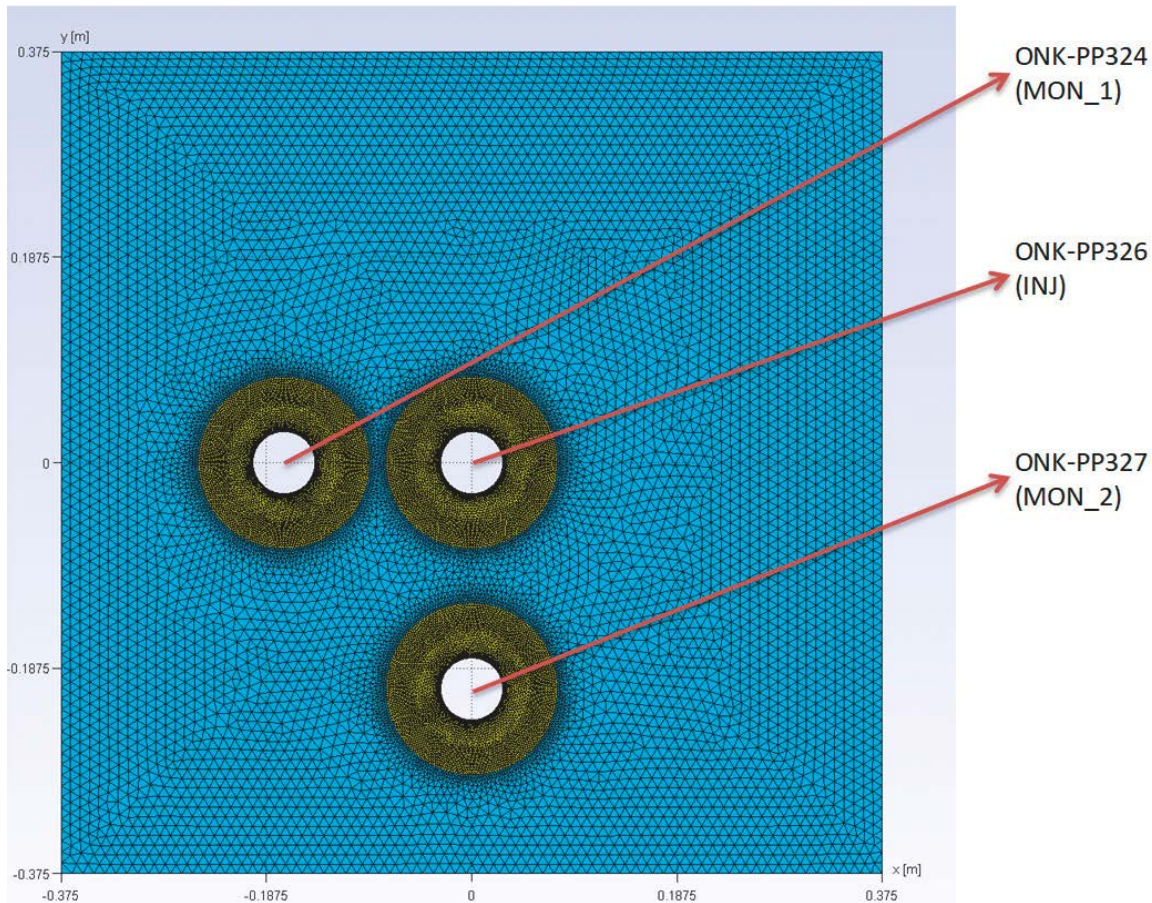
Figure 6-24. *Task 9C – Flow123d – updated computational mesh for the inverse model.*

To calibrate the model to the measured data, the concept of a linear decrease in porosity from the borehole wall towards the interface of the BDZ/intact rock was adopted. Figure 6-25 shows the distribution of porosity in the model area as from the manual calibration of the model.

Other model parameters that can be used to calibrate the measured data are effective diffusivity, which also depends on porosity, and linear sorption distribution coefficient (except for the conservative HTO and Cl-36 tracers). For clarity, the parameters resulting from the manual model calibration together with the parameters used in the blind prediction are shown in Table 6-7. For effective diffusivity in the disturbance zone, the maximum value (for the borehole walls) is always given in the table, the minimum value is the effective diffusivity in the intact rock. The character of the decrease follows the decrease in porosity, but not linearly, since the coefficient of effective diffusivity in Flow123d is proportional to the porosity powered by $\frac{4}{3}$. The table shows that in addition to the accepted concept of the linear decrease in porosity with depth, which also implies minor changes in the effective diffusivity, the calibration coefficient was primarily the distribution coefficient of linear sorption, which changed by several orders in both directions (compared to the values used in the blind prediction).

Figure 6-26 shows the results of the inverse model for HTO. The figure shows that by using the parameters given in Table 6-7, a very good agreement was achieved in the injection borehole. On the contrary, the simulated concentrations in the monitoring boreholes are significantly higher than the measured concentrations. Figure 6-27 shows the results of the model with the same parameters except for effective diffusivity in the intact rock, which is forty times lower. A better agreement is seen especially in monitoring borehole PP327, but the agreement in the injection borehole is worse. It is evident from the figure (also as in Figure 6-28) that the current model concept does not sufficiently capture the measured profiles in the monitoring boreholes since the measured values show an earlier onset in borehole PP327, which is further away from the injection borehole than borehole PP324. Moreover, it is situated perpendicular to the direction of foliation; a non-isotropic tensor of the coefficient of molecular diffusion, which would accentuate the PP326-PP327 direction, would be difficult to justify.
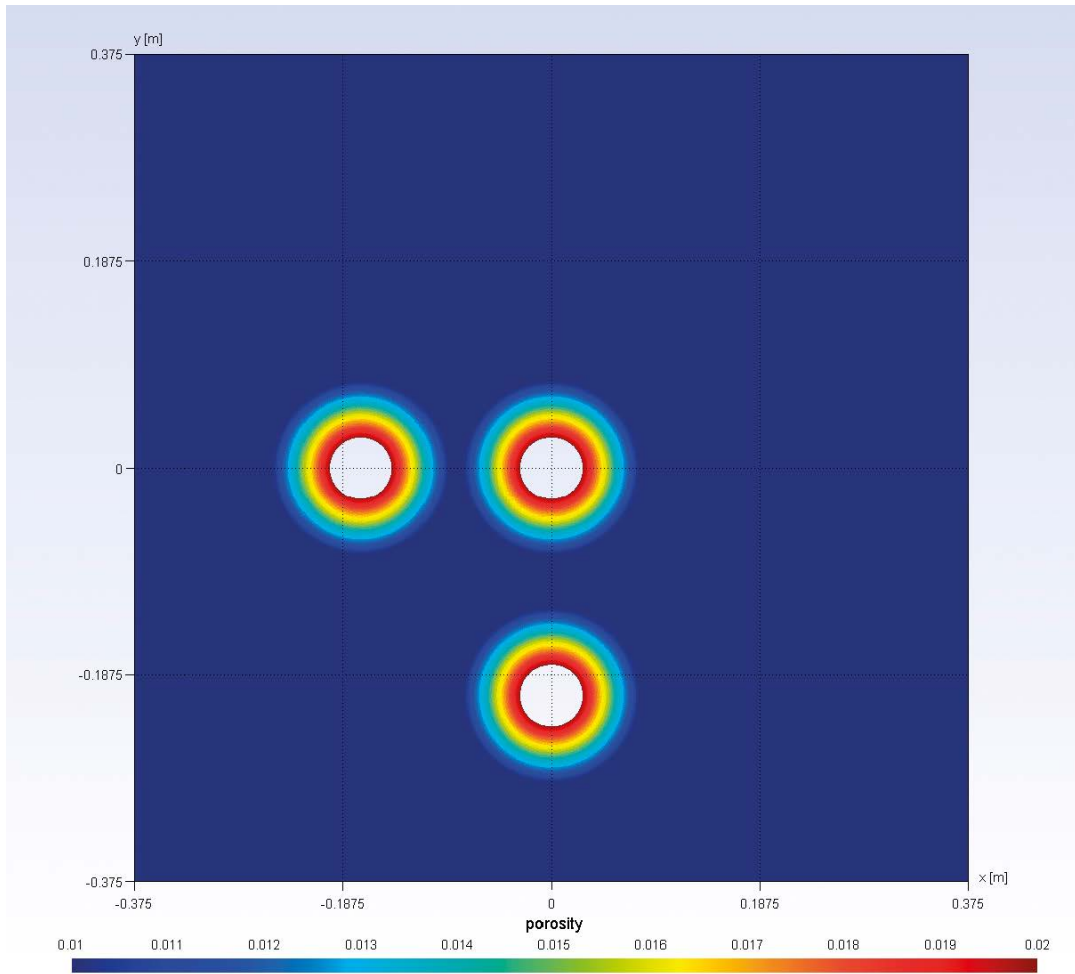
Figure 6-25. *Task 9C – Flow123d – distribution of porosity in the model area.*
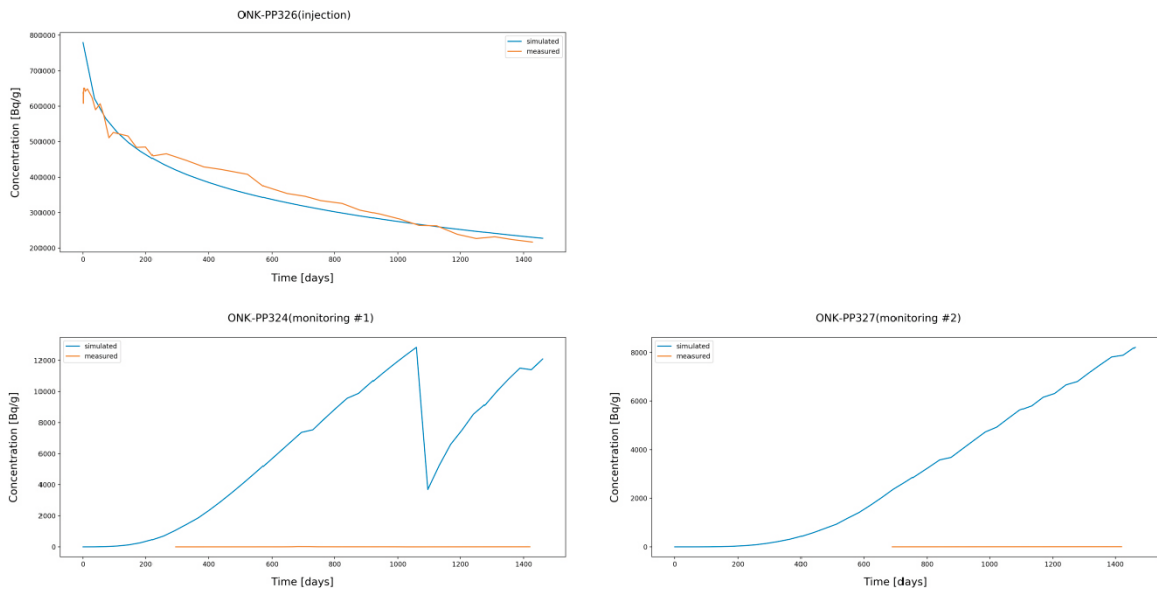
Figure 6-26. *Task 9C – Flow123d – results of the inverse model, HTO.*
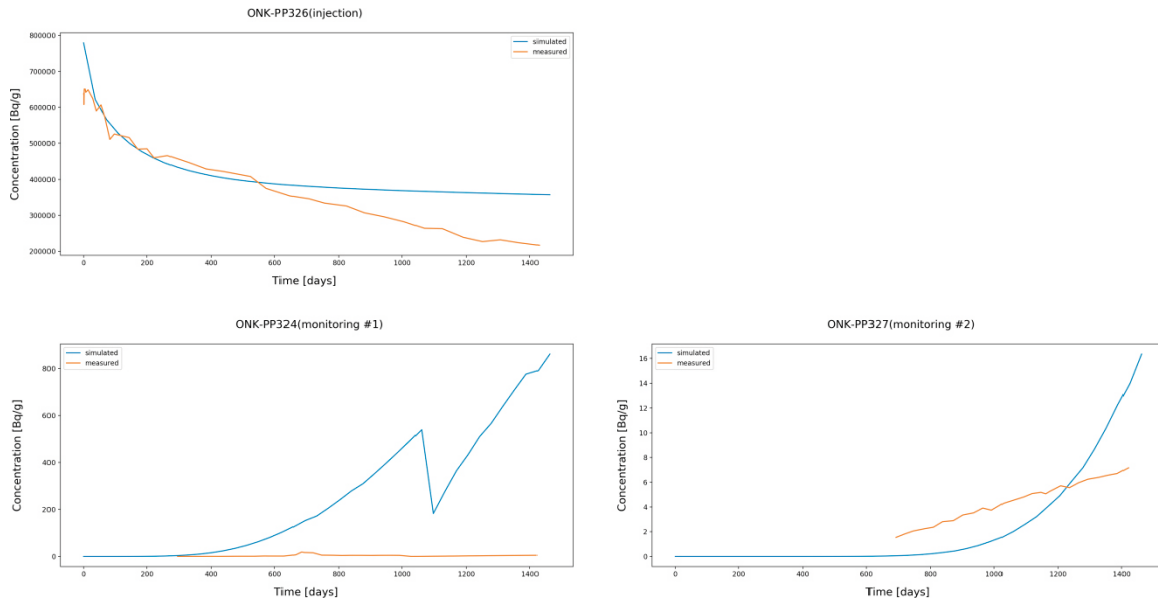
Figure 6-27. *Task 9C – Flow123d – results of the inverse model, HTO variant 2.*

Table 6-7. Task 9C – Flow123d – parameters resulting from calibration together with the blank prediction parameters.

Tracer	Porosity [-]	D_e BDZ max [m²/s]	D_e rock [m²/s]	K_D BDZ [m³/kg]	K_D rock [m³/kg]
Original (blind prediction)					
HTO	0.0094	-	3.90e−13	-	0
Cl-36	1.75e-4	-	5.00e−15	-	0
Na-22	0.0094	-	4.65e−13	-	0.0013
Ba-133	0.0094	-	1.47e−13	-	0.06
Cs-134	0.0094	-	3.00e−13	-	0.031
Modified (result of the manual calibration process)					
HTO	0.01–0.02	1.07e−12	4.24e−13	0	0
Cl-36	0.01–0.02	1.26e−13	5.02e−14	0	0
Na-22	0.01–0.02	1.27e−12	5.05e−13	1.3e−6	1.3e−6
Ba-133	0.01–0.02	8.20e−13	3.25e−13	0.6145	0.0307
Cs-134	0.01–0.02	8.20e−13	3.25e−13	0.6191	0.03095

Figure 6-28 shows the results of the inverse model for Cl-36. Again we see a good agreement in the injection borehole and a poor agreement in the monitoring boreholes. The same conclusions discussed in the previous paragraph apply here.

Figure 6-29 shows the results of the inverse model for Na-22. The agreement in the injection borehole is relatively good, with the curve representing the simulation results decreasing more sharply than the measurement curve. In order to achieve such an agreement, it was necessary to reduce the linear sorption distribution coefficient by three orders of magnitude. Again, agreement in monitoring boreholes is not good; the curves representing the results of the simulations clearly fluctuate, which documents the effect of sampling very well.

For Ba-133 and Cs-134, no activity was detected in the monitoring boreholes during the experiment. Similarly, there was no activity in the model outputs. Therefore, only the profiles in the injection borehole are depicted for these tracers, in Figure 6-30 for Ba-133 and in Figure 6-31for Cs-134, and in both cases for clarity with the logarithmic scale of the y-axis. In both cases, it is apparent that the simulated profile has an onset significantly higher than the measured profile (this is indeed true for all five tracers). The initial value of the simulated concentration in the injection borehole is calculated from the known volume of the experimental section and the known value of the injected amount (activity)

of the tracer. If we take these measurements as a paradigm, then the simulated curve cannot look otherwise. The measured curves would then be burdened with an experimental error, the origin of which we can only guess. In the case of Ba-133, the difference between the initial values of the profiles is not an order of magnitude; For Cs-134, however, the difference is large, so the aim of the calibration was to capture the trend, not to achieve full agreement.

In conclusion we can summarise that the chosen model concept is not able to reflect the measured profiles in the monitoring boreholes (for the reasons described above). In the injection borehole, the model can capture the trend, but the question of the initial concentration value remains open, whereby the measured value does not correspond to the amount injected. Alternatively, the model concept could consider the first measured value as the initial concentration value. The resulting parameters of the calibrated model would surely be different. Finally, it is worth mentioning that a similar combination of parameters could achieve similar model results. The selected parameters (see Table 6-7) are physically backed – realistic.
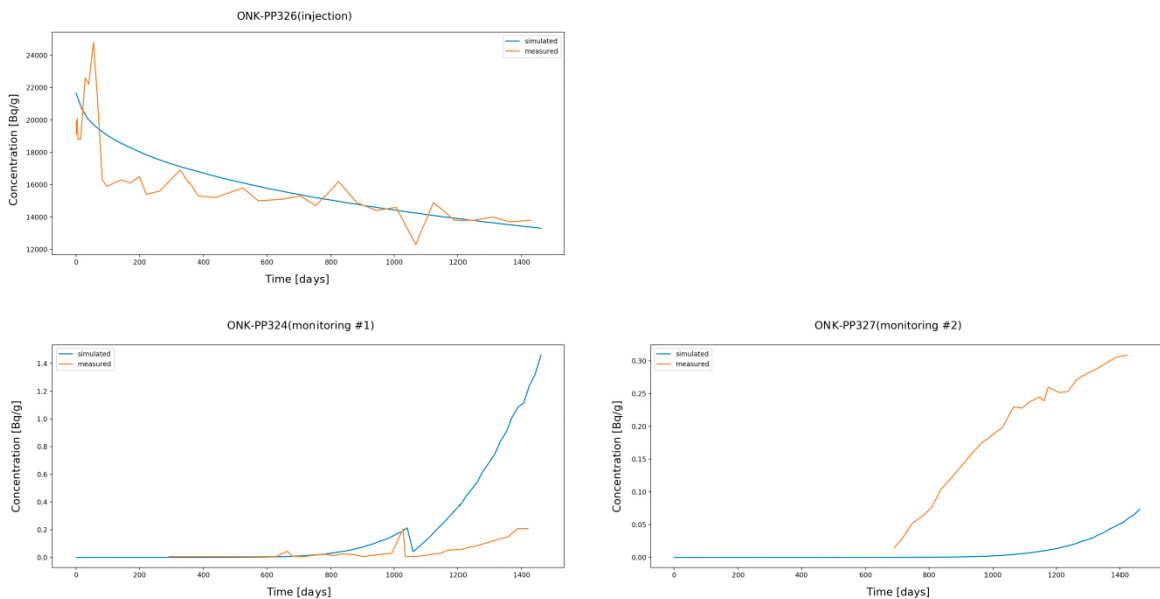
Figure 6-28. *Task 9C – Flow123d – results of the inverse model, Cl-36.*
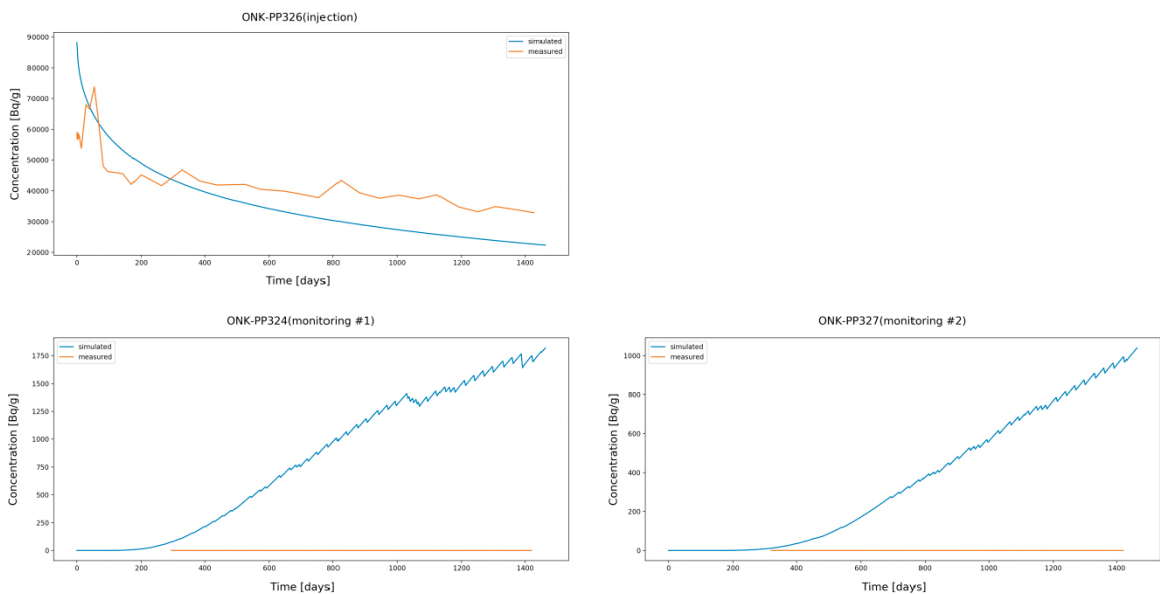
Figure 6-29. *Task 9C – Flow123d – results of the inverse model, Na-22.*
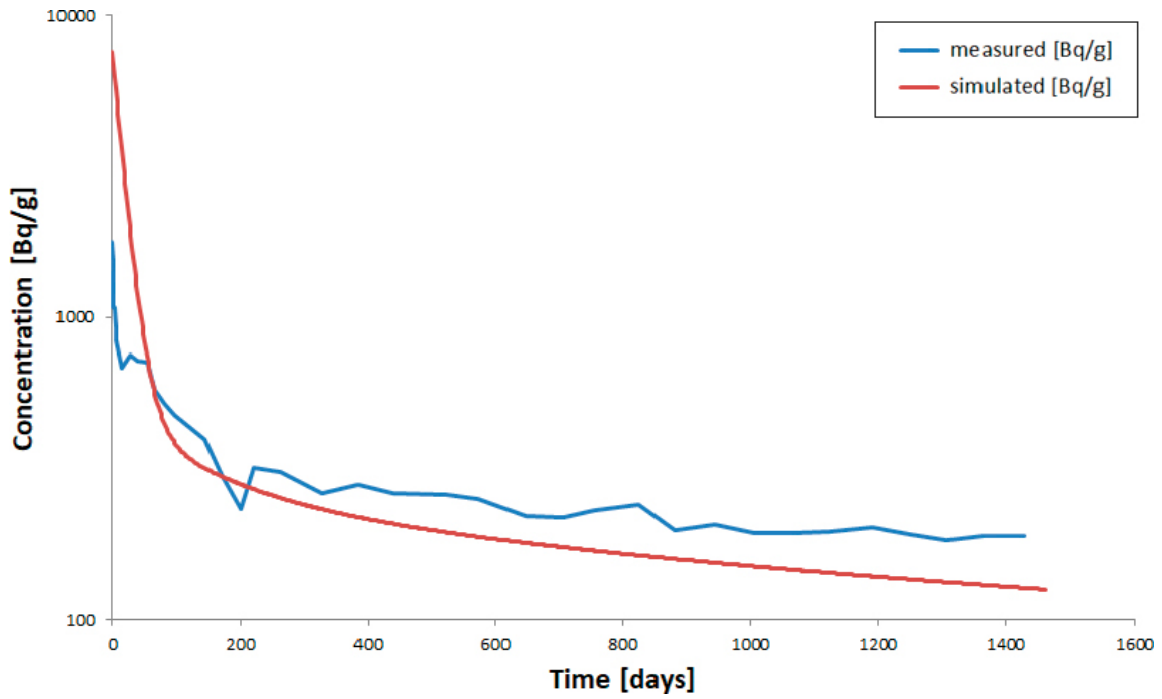
Figure 6-30. *Task 9C – Flow123d – results of the inverse model, Ba-133.*
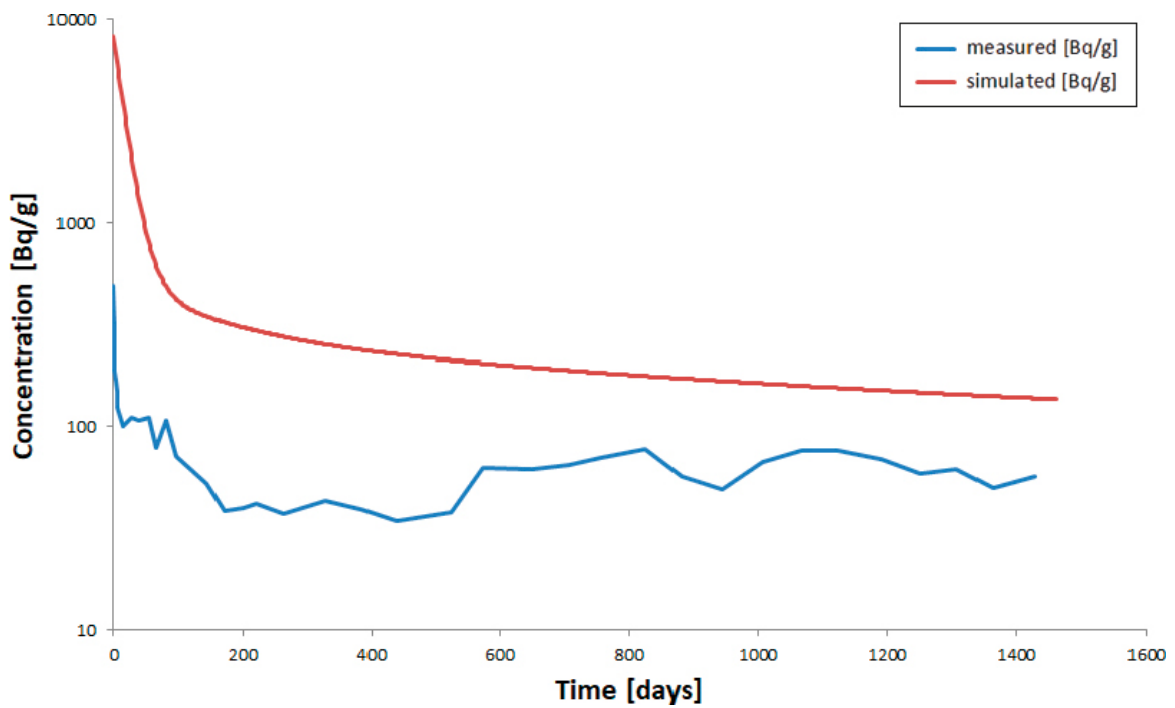
Figure 6-31. *Task 9C – Flow123d – results of the inverse model, Cs-134.*

6.6　Inverse model in GoldSim (ÚJV)

After the experimental data were released by the organiser, inverse modelling was performed, where the model parameters were changed in order to achieve the best agreement between the model and the measured results. Discretisation marked "finer discretisation" was used for the non-sorbing nuclides, (Table 6-4, Figure 6-4), and the discretisation of the sorbing radionuclides was marked "non-unifrom_1" (Table 6-6, Figure 6-6). The parameters of the model area remained homogeneous; the model area is not divided into closer and more distant zones around the boreholes.

In addition to the calibration of material parameters, attention was also paid during the inverse modelling to a critical evaluation of the measured data. In many cases (especially in the absence of data from the monitoring boreholes), similar model curves were achieved for different combinations of model parameters. The resulting model parameters are shown in Table 6-8, with other possible combinations in Table 6-9.

Table 6-8. Final calibrated parameters.

	Porosity	Kd (m³/kg)	De (m²/s)	Dw (m²/s)
H-3	9.40E−03	0.00E+00	7.00E−13	2.30E−09
Na-22	9.40E−03	5.00E−05	9.00E−14	1.33E−09
Na-22 cropped	9.40E−03	9.00E−05	3.00E−14	1.33E−09
Cl-36	9.40E−03	0.00E+00	2.00E−13	2.03E−09
Cl-36 cropped	9.40E−03	0.00E+00	3.50E−14	2.03E−09
Ba-133	9.40E−03	2.00E−03	1.47E−13	1.69E−09
Cs-134	9.40E−03	5.00E−03	3.00E−13	2.07E−09

Table 6-9. Variant model parameters.

	Porosity	Kd (m³/kg)	De (m²/s)	Dw (m²/s)
Na-22 var 1	9.40E−03	5.00E−05	9.00E−14	1.33E−09
Na-22 var 2	9.40E−03	9.00E−05	9.00E−14	1.33E−09
Na-22 var 3	9.40E−03	1.00E−05	2.00E−13	1.33E−09
Na-22 cropped var 1	9.40E−03	9.00E−05	3.00E−14	1.33E−09
Na-22 cropped var 2	9.40E−03	1.00E−05	6.00E−14	1.33E−09
Ba-133 var 1	9.40E−03	2.00E−03	1.47E−13	1.69E−09
Ba-133 var 2	9.40E−03	3.00E−03	1.47E−13	1.69E−09
Cs-134 var 1	9.40E−03	5.00E−03	3.00E−13	2.07E−09
Cs-134 var 2	9.40E−03	3.10E−02	5.00E−14	2.07E−09

H-3

A comparison between the measured and model results including the actual measured results is given in Figure 6-32 – Figure 6-35. Figure 6-32 shows that there is a sharp decrease in activity in the injection borehole during the first few hours. This decrease is attributed to the geometry of the experiment, it is not a property of the rock, which is characterised by the calibrated material parameters. Therefore, the data were cropped, and the initial activity was lowered by this cropping, so the initial amount injected is not 891 000 Bq/g, but 647 000 Bq/g.
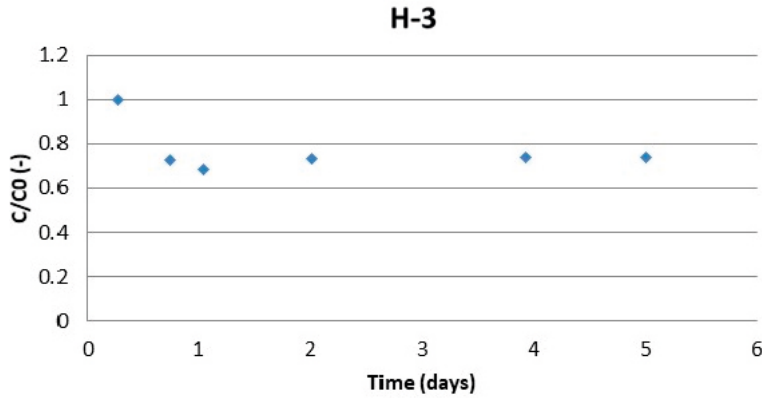
Figure 6-32. *Original measurement data, steep decrease during the first day attributed to the setup of the experiment.*
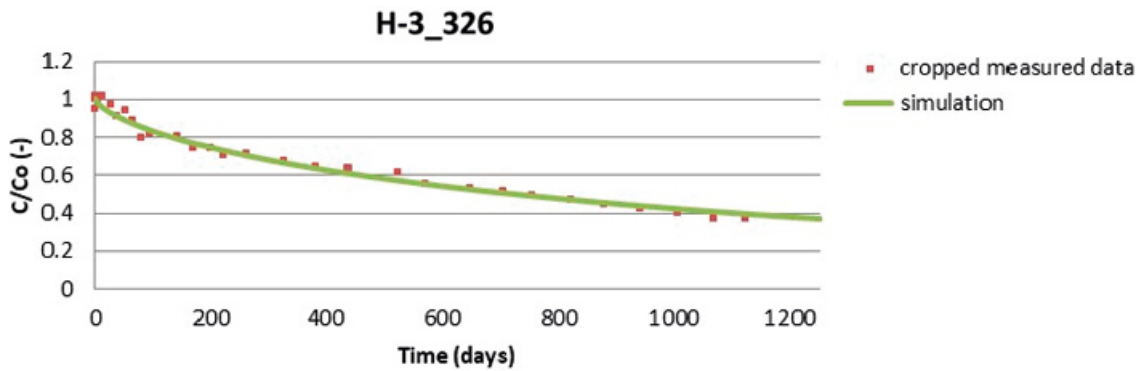
Figure 6-33. *Development of activity in the injection borehole.*
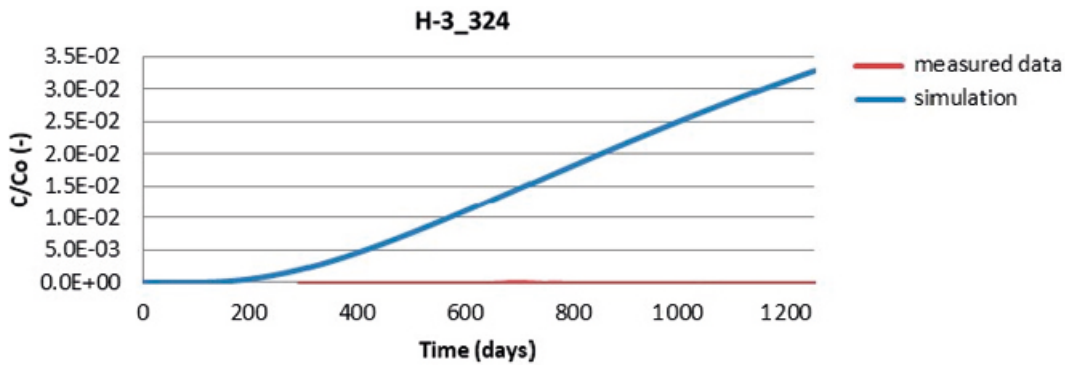
Figure 6-34. *Development of activity in the monitoring borehole.*
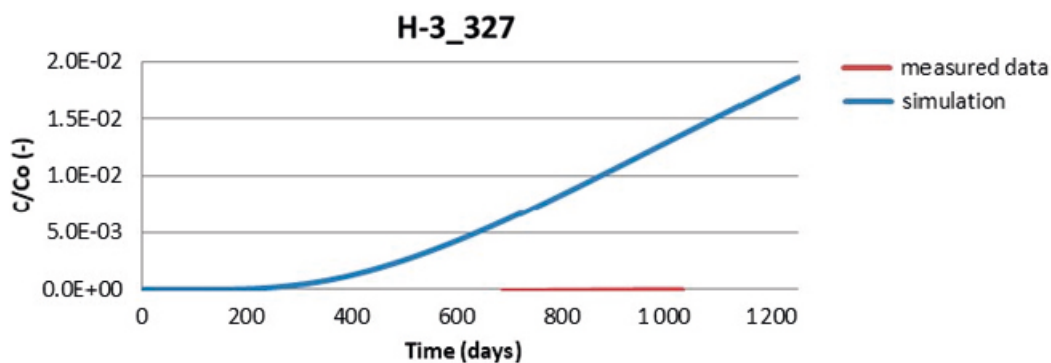
Figure 6-35. *Development of activity in the monitoring borehole.*

Na-22

Two variants of measured data were simulated for Na-22. Firstly, the original published data (Figure 6-36) and secondly, the cropped data (Figure 6-37). The graphs showing the uncropped data show an experimental artefact where the activity in the injection borehole during the measurement increases above the initial injected activity. Therefore, in the second (cropped) variant, the first 80 days during which this artefact occurred were neglected and the initial activity was set to an activity value of 80 days, i.e. an injected amount of 48 000 Bq/g (compared to the initial published value of 58 900 Bq/g). In both variants, we also faced a greater degree of freedom in the task due to the absence of data from the monitoring boreholes, whereby we obtained very similar model curves when combining the various parameters.
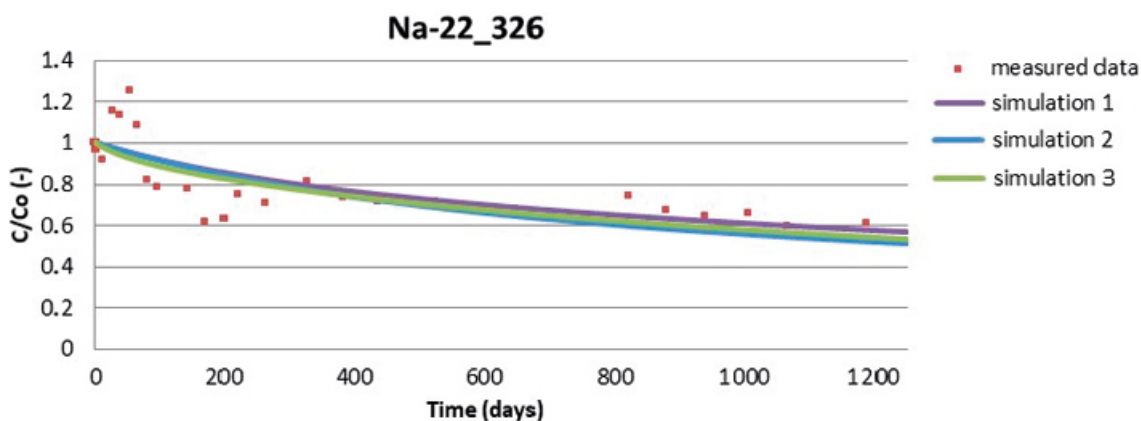
Figure 6-36. *Agreement between the measured and model results for the originally published data for the different combinations of model parameters.*
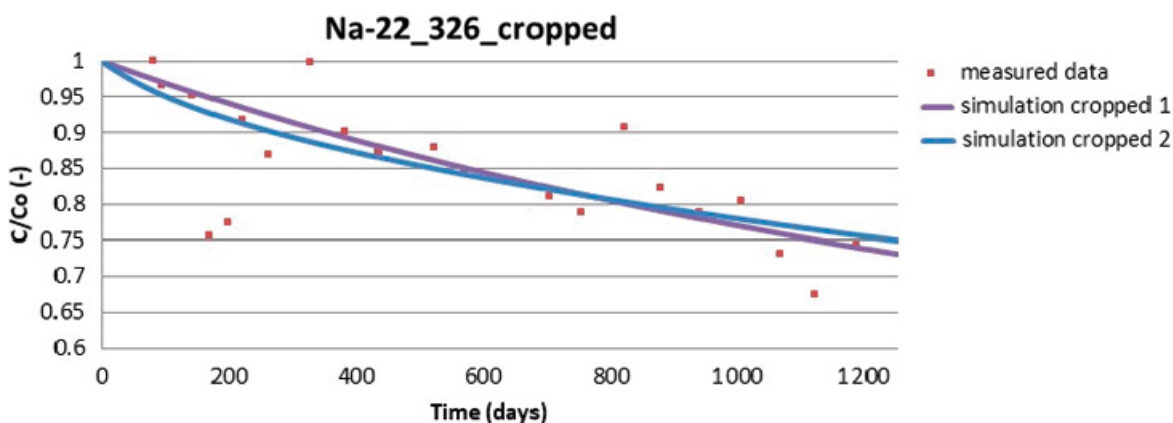
Figure 6-37. *Agreement between the measured and model results for the cropped data for the different combinations of model parameters.*

Cl-36

For Cl-36, there was the same problem with greater activity in the injection borehole during measurement than the originally injected activity as for Na-22. Therefore two sets of data were also used, the originally published and cropped data, with an initial injection amount of 16 300 Bq/g (compared to the originally published value of 19 900 Bq/g). The agreement between the measured and model results for the originally published data is shown in Figure 6-38, Figure 6-40 and Figure 6-41 and the agreement for the cropped data is shown in Figure 6-39, Figure 6-40 and Figure 6-41. Due to the presence of the monitoring boreholes, the same agreement in model curves was not achieved for the different combinations of model parameters. Therefore, the monitoring data reduces the degree of freedom of the mathematical model. The comparison of the development in the monitoring borehole shows that the rock environment is better described by the parameters obtained after cropping the original model parameters.
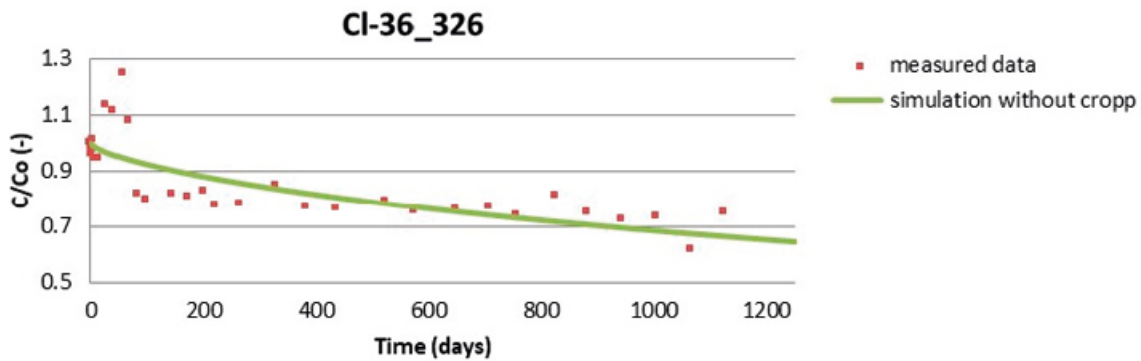
Figure 6-38. Agreement between the measured and model results for the originally published data, development of activity in the injection borehole.
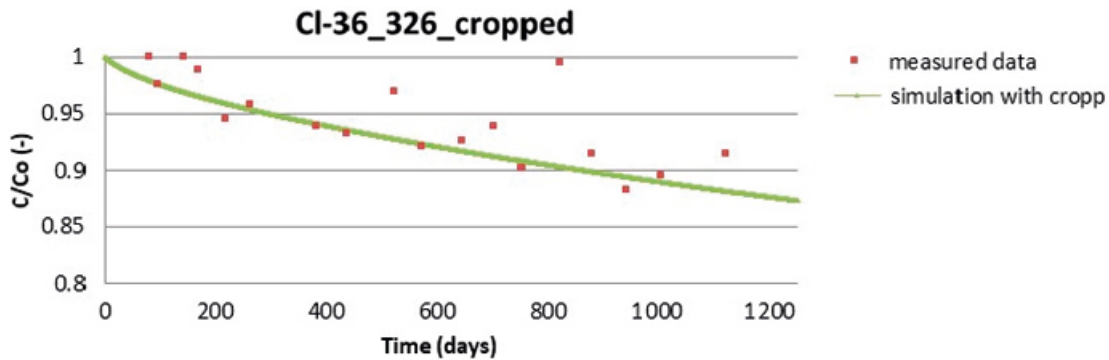
Figure 6-39. Agreement between the measured and model results for the cropped data, development of activity in the injection borehole.
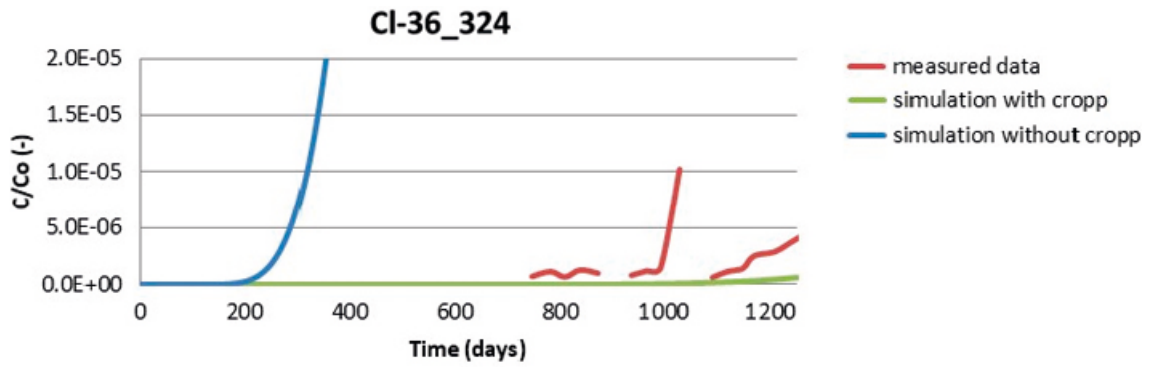
Figure 6-40. *Agreement between the measured and model results in the monitoring borehole.*
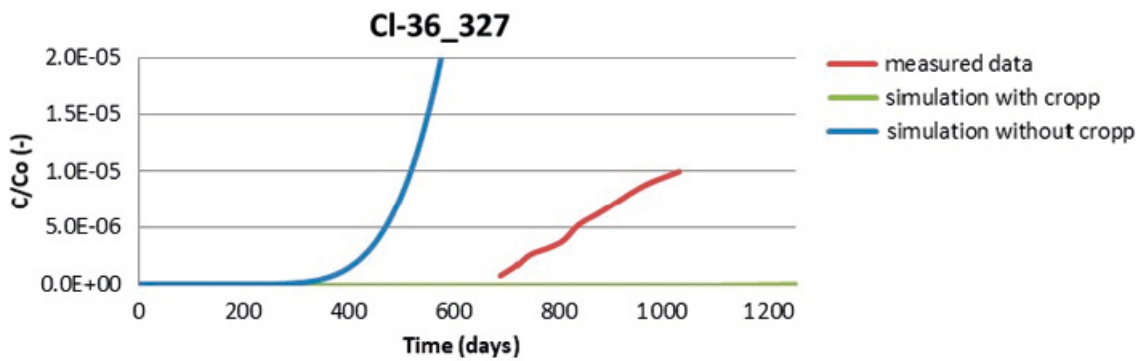
Figure 6-41. *Agreement between the measured and model results in the monitoring borehole.*

Ba-133

A comparison of the development of the measured and modelled activity in the injection borehole for Ba-133 is shown in Figure 6-42. The initial concentration was equal to the first measured value (no "cropping"). Due to the absence of data from the monitoring boreholes, similar modelling curves for different combinations of parameter are again achieved.
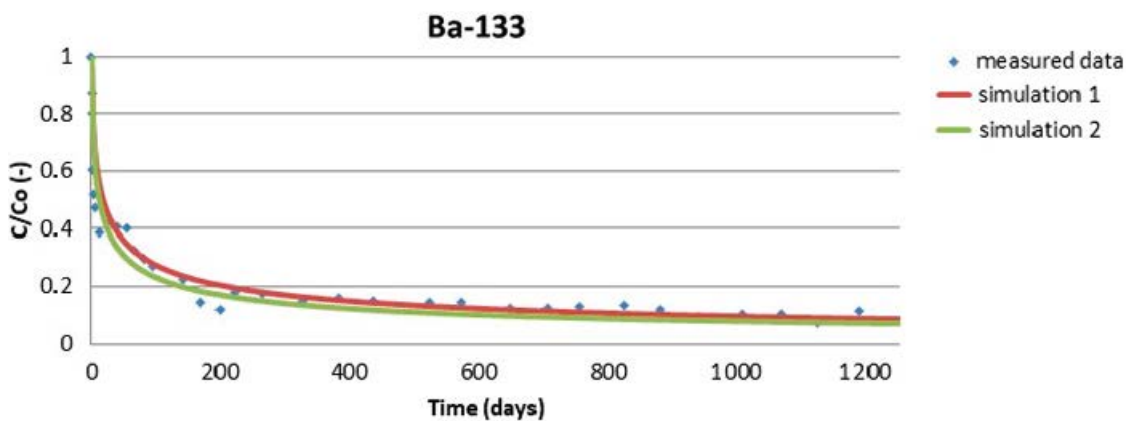
Figure 6-42. *Agreement between the measured and model results for different combinations of model parameters, development of activity in the injection borehole.*
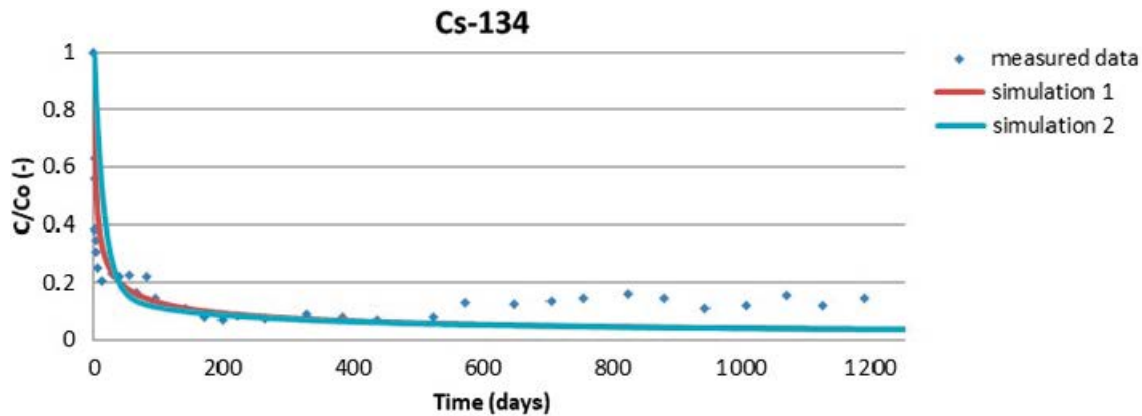
Figure 6-43. *Agreement between the measured and model results for different combinations of model parameters, development of activity in the injection borehole.*

Cs-134

A comparison of the development of the measured and modelled activity in the injection borehole for Cs-134 is shown in Figure 6-43. The initial concentration was equal to the first measured value (no "cropping"). Due to the absence of data from the monitoring boreholes, similar modelling curves for different combinations of parameters are again achieved. When calibrating the mathematical model, attention was given to data up to approximately day 500; the increase in activity after this time is attributed not to the behaviour of the rock environment, but to the setup of the experiment.

To specify the model parameters, it is recommended to drill out the rock around the experimental boreholes and measure the activities in the rock samples, thereby reducing the degree of freedom of the mathematical models. Furthermore, for sorbing nuclides, it should be verified that the resulting model curves are not dependent on the discretisation of the area, whereby a change in the discretisation of the areas would lead to different model curves for the same material parameters (Figure 6-14).

6.7 Inverse model in MT3D and the evaluation made by PROGEO

The solution of Task 9C at PROGEO was not originally planned. The motivation for solving Task 9C, in addition to the work performed out in the framework of the TF GWFTS and the associated contract of SÚRAO, was as follows:

1. More detailed knowledge of the implementation and results of the TDE experiment, analysis of instrumentation and errors in the experiment, analysis of measured data – the experiment is related to similar projects implemented by the co-investigator PROGEO: PAMIRE (Havlová et al. 2017), Transport 1 (Havlová et al. 2019), Fracture connectivity (Kryl et al. 2020).

2. Application of the MT3DMS program for simulation of a pure diffusion problem, possibilities of utilisation, analysis of software and computational solver behaviour.

3. Application of heterogeneous properties of the rock matrix on a larger scale – assignment of micro-connectivity according to the methodology used in the simulation of laboratory diffusion experiments in the Transport 1 project (utilisation of C14-PMMA micrographs) and influence on the results of simulations.

4. Calibration of the measured data and model evaluation of one selected tracer – HTO (however, very similar measured activities in the observation boreholes were measured for both non-sorbing tracers HTO and Cl-36).

Comments and suggestions on the implementation and results of the experiment obtained from the analysis of the task description for Task 9C and the provided results of measurements – several relatively significant and problematic events occurred during the implementation of the experiment, which very likely influenced the course and results of the experiment.

- The first problem was a leakage of approximately 40 ml of the solution from injection borehole PP326 within 60 to 90 days of the start of the experiment and a 15 % drop in source activity of all tracers (the leaked solution was supplemented with "pure" water).

- The leakage of the solution was accompanied by a drop and complete "spreading" of pressure conditions between the boreholes for the remainder of the experiment – the pressure difference between the "failed" connection of boreholes PP321/PP322 and the nearest borehole PP324 (approximately 10 cm away), and the other experimental boreholes PP326 and PP327 was relatively significant. The pressure in PP321/PP322 is 100 kPa higher than in the other boreholes(!); however, this difference is not mentioned in the presentations or the provided data (attention is devoted only to significantly smaller pressure differences between the three tested boreholes). The influence of these pressure gradients on the experiment is of course unknown, but purely theoretically it relates to a hydraulic conductivity of the rock matrix of 10^{-12} m $\cdot$ s^{-1} and porosity of 0.005 with an advective flow rate of the tracer of tens of centimetres per year(!).

- Recommendations for possible similar experiments performed at Bukov Underground Research Facility – in terms of instrumentation and the above-mentioned uncertainties regarding pressure differences, it seems much more beneficial to locate the boreholes in a cross-shape with a central source borehole.

- Observation boreholes PP324 and PP327 also had experimental problems – pressure, circulation, piping problems, etc. – representative breakthrough curves were only obtained from approximately 1 000 days for PP324 (after a complete re-installation of the test section) and 700 days for PP327.

- Despite the experimental problems, the measured data clearly show the relatively fast arrival of tracers HTO and Cl-36 in the observation boreholes – approximately 300 days for PP324 (the closer borehole; 12 cm) and 400 days for PP327 (15 cm).

- Interesting and unexpected comparisons of the breakthrough curves of the relative activity of HTO and Cl-36 in the observation boreholes (see Figure 6-44) – a linear shape probably indicates a steady flow between the source and observation boreholes, the effective diffusion coefficient is represented by the slope of the breakthrough curve and indicates a lower value for HTO than Cl-36(!).

- Very low relative activity of HTO and Cl-36 in the observation boreholes (five orders of magnitude lower than in the source borehole) correlates very well with the almost zero decrease in Cl-36 in the source borehole. However, the high decrease in HTO activity in the source borehole of 70 %, which is further commented on in the model results section, is ambiguous (and problematic from the point of view of overall balance).
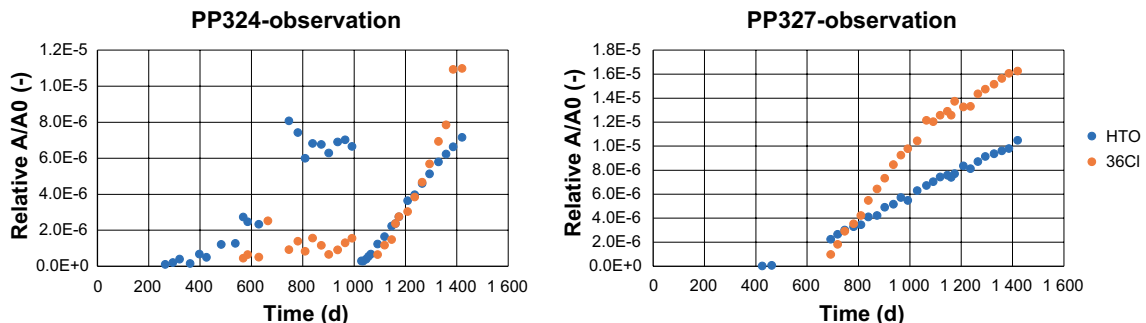
Figure 6-44. *Task 9C – measured relative activity of HTO and Cl-36 in observation boreholes PP324 and PP327.*

MT3DMS was used for solving the transport Task 9C, similar to the solution of other Task 9 tasks. The task is solved in a simplified one-layer model in 2D with a model domain consisting of a rectangular grid of computational cells 1 × 1 mm, see Figure 6-45. The axial symmetry of the task is used and only a quarter-circle slice with a 500 mm radius is simulated. The thickness of the model layer is 1 m and corresponds to the length of the tested borehole section. The source and observation boreholes are given as an open fracture (annulus) with the corresponding porosity (single-unit) so that the volume of water in the boreholes (total volume in the fracture and piping) corresponds to the task description. Therefore, no boundary conditions are prescribed for the source and observation boreholes, but only the initial values of activity in the source volume (according to the activity in the solution) and zero initial activity in the rock matrix and observation boreholes are defined.

Task 9C was solved as a purely diffusion model (zero hydraulic gradient, zero sorption), considering the experimental data to be compared with would be decay-corrected. The porosity and pore diffusion coefficient values were calibrated during the simulations to achieve a reasonable agreement between the measured and model breakthrough curves. In the models, homogeneous (same) values of transport parameters were entered in the whole space of the rock matrix. A disturbance zone (BDZ) with slightly higher parameter values was considered in the limited range of 1 mm from the borehole wall (a range of 1 mm was entered based on experience from previous modelling works). It should be emphasised that from the point of view of the geometry of the task and the mutual distance of 10–15 cm between the boreholes, we do not expect any significant influence of the BDZ on the transport of non-sorbing tracers HTO and Cl-36 (but it is important for sorbing tracers Na-22, Cs-134 and Ba-133).

The task was solved with a total of three variants, because for HTO it was not possible to calibrate the curve in the injection borehole and the observation borehole(s) at the same time:

1. Calibration of activity in injection borehole PP326 – comparison of the modelled and measured evolutions in the injection borehole and the observation boreholes is shown in Figure 6-46. The calibrated values of the rock matrix parameters are:
   - Porosity (n) −0.009 – this value compares relatively well to the measured porosity in the samples and values adopted by other co-investigators.
   - Pore diffusion coefficient (D_p) – 4.63×10^{-11} $m^2 \times s^{-1}$ – effective diffusion coefficient ($D_{eff} = D_p * n$) 4.17×10^{-13} $m^2 \times s^{-1}$ again corresponding to the measured values and the resulting values adopted by other investigators.
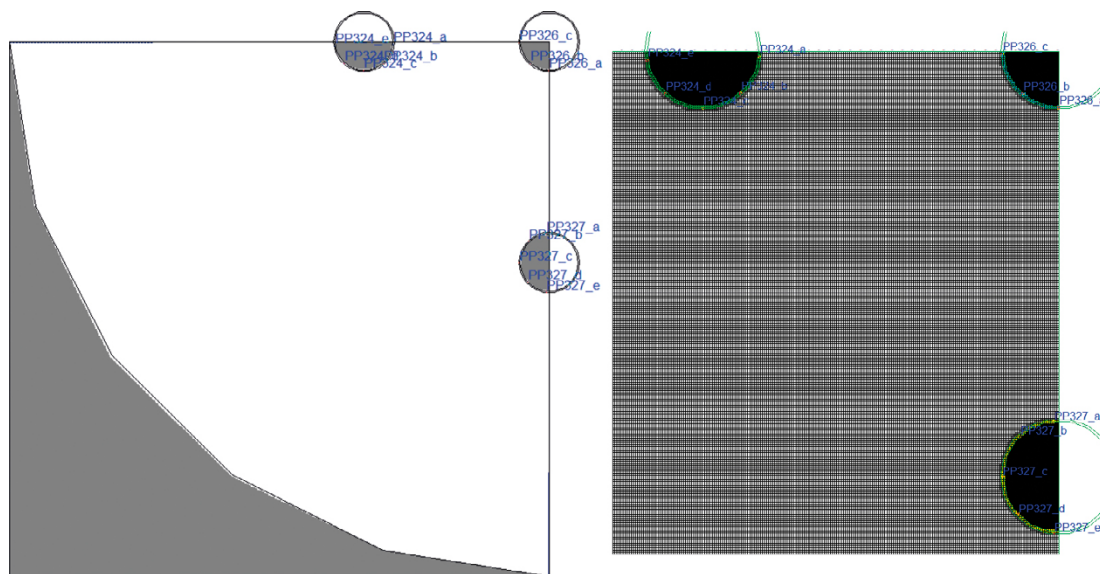
Figure 6-45. *Tack 9C – MT3DMS – discretisation of the model domain – size of the whole model 500 × 500 mm on the left, the cutting with the grid of model cells 1 × 1 mm on the right.*

The graph shows a very good agreement of the course of activity in the injection borehole. On the contrary, the measured and model activity in the observation boreholes is very problematic. The model values follow the trend of the measured values, but they are plotted on the secondary axis and are three orders of magnitude higher than the measured values(!). The problem is mainly in terms of the activity balance of HTO – a high drop in the injection borehole over the measured period of 1 500 days (by 70 % and 55 %, respectively, after deduction of 15 % through leakage) and practically zero activity in the rock matrices of the observation boreholes.

2. Calibration of activity in observation boreholes PP324 and PP327 – A comparison of the modelled and measured evolutions in the injection borehole and the observation boreholes is shown in Figure 6-47. The calibrated values of the rock matrix parameters are:

   - Porosity (n) – 0.000003 – extremely low calibrated value by more than three orders of magnitude lower (!) than the measured value.

   - Pore diffusion coefficient (D_p) – 7.5×10^{-11} m$^2 \times$ s^{-1} – comparable to the previous variant; however, effective the diffusion coefficient ($D_{eff} = D_p \times n$) 2.3×10^{-16} m$^2 \times$ s^{-1} is three orders of magnitude lower than the given low porosity. However, a value in the order of 10^{-16} corresponds to the value determined by the analytical calculation in Section 6.8.

The graph shows a very good agreement of the course of activity in both boreholes PP324 and PP327 (with respect to the almost same measured relative activities of HTO and Cl-36, the given calibrated values are valid for both tracers). The very low value of activity in the observation boreholes is associated with the modelled very low decrease in activity in the source borehole, which, while not corresponding to the measured decrease in HTO activity, agrees very well with the minimal decrease in the measured activity of Cl-36.

Therefore, the course of Cl-36 may be relatively well simulated in both the injection and observation boreholes using a low porosity value. The question is how to explain the mismatch between the low HTO activity in the observation boreholes and the high decrease in activity in the source borehole (or whether it is a measurement error, the effect of pressure differences between the boreholes or advective flow, etc.).

3. Application of micro-porosity – in an attempt to explain the uncertainties in the measured values of HTO, a variant with a heterogeneous distribution of the micro-porosity of the rock matrix was simulated according to the image obtained by the C14 PMMA method. This variant was only a test. Since the actual image from the given location was not available for such a large model domain (0.5×0.5 m), a modified micrograph (of a granite sample from other location) processed within SÚRAO's "Transport 1" project (Havlová et al. 2019) was used; see Figure 6-48. The aim was to verify whether the course of HTO activity could be explained by heterogeneities in the rock matrix. The model in this variant was not calibrated, but the results of the simulations yielded very similar conclusions to the previous two variants with a homogeneous distribution of porosity. Although in this variant the properties of the rock matrix between the boreholes are specified with a high degree of heterogeneity, the overall "behaviour" of the domain entered over a distance between boreholes of 11–15 cm is more or less homogeneous.
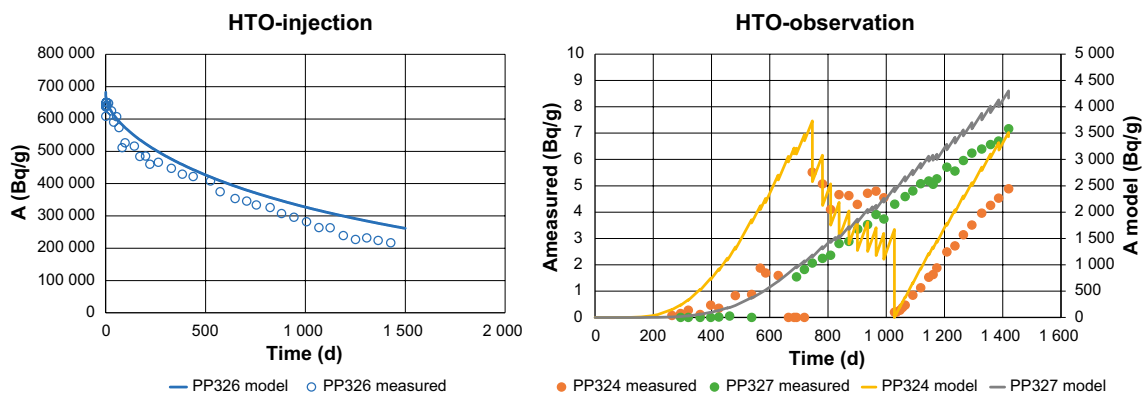
Figure 6-46. Task 9C – simulation of HTO in MT3DMS – Variant 1 – calibration of activity in injection borehole PP326. Comparison of the measured and model evolutions in the injection boreholes on the left and breakthrough curves in the observation boreholes on the right.
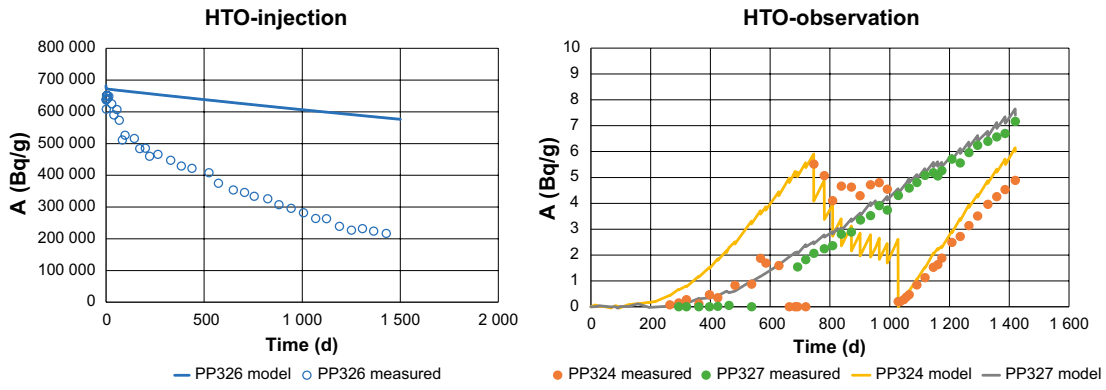
Figure 6-47. *Task 9C – simulation of HTO in MT3DMS – Variant 2 – calibration of activity in observation boreholes PP324 and PP327. Comparison of the measured and model evolutions in the injection boreholes on the left, in the observation boreholes on the right.*
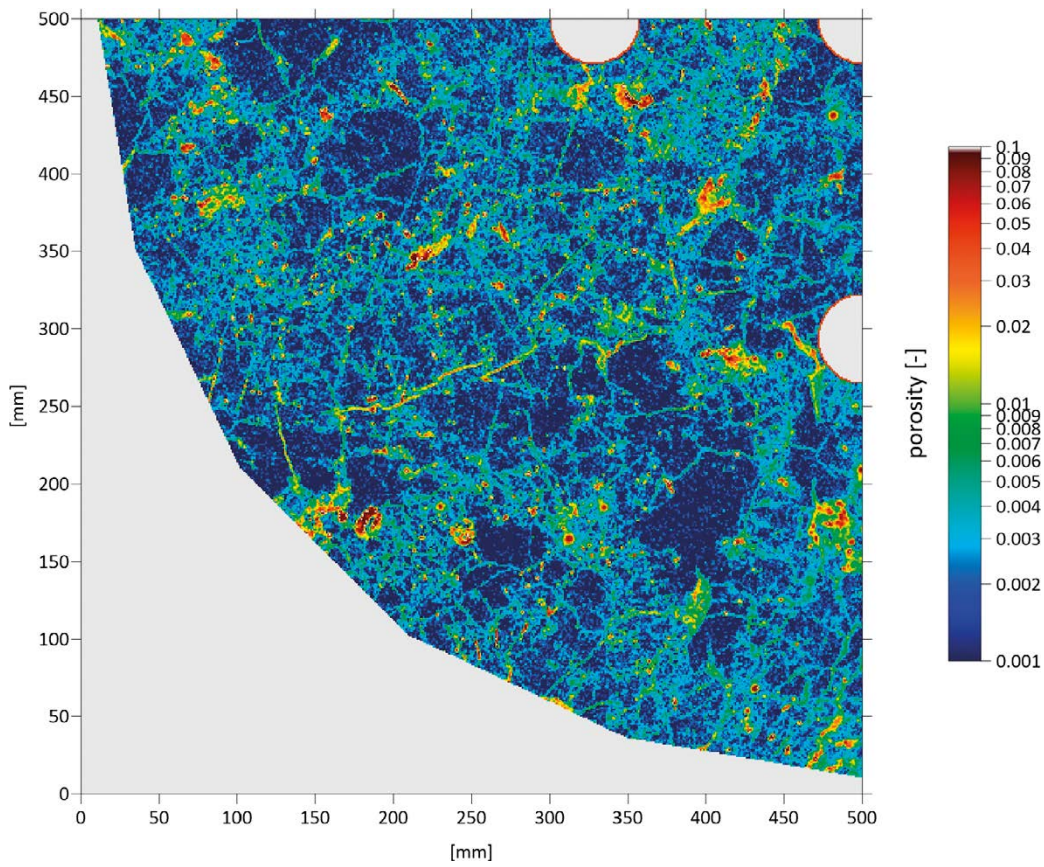
Figure 6-48. *Task 9C – Variant 3 – heterogeneous porosity based on the rock matrix micrograph.*

6.8   Simplified analytical solution (TUL)

Due to the fact that the course of the measured concentrations in the detection boreholes is linear over a relatively long period of time (Figure 6-49 left), this can be interpreted as a constant flux of tracer into the borehole. Therefore, it is possible to consider this process as a quasi-steady state transport with a stable concentration field between the injection and detection boreholes. Next, the geometry can be simplified into radial symmetry around the injection borehole (dilution in the detection borehole distributed throughout the perimeter) and a constant concentration assumed in the source and target boreholes (which is true for the given reservoir volumes and for a reasonably short period of time). The following applies for the steady transport in the angular segment φ corresponding to the dimensions of the detection borehole (Figure 6-50):

$$Q_c = \varphi d D_e \frac{c_1 - c_2}{\ln r_2/r_1},$$

where Q_c [kg/s] is the mass flux across a cylindric segment, d [m] is the length along the borehole axis (packer interval), D_e [m²/s] is the effective diffusion coefficient, $c_{1,2}$ [kg/m³] are the relative concentrations in the injection and detection boreholes respectively, r_1 [m] is the injection borehole radius, and r_2 [m] is the distance of the boreholes (a choice was from the centre of the injection to a half radius of the detection, Figure 6-50).

The flux must also be consistent with the balance in the monitoring borehole, i.e. with the rate of concentration increase, as follows

$$\frac{dc}{dt} = \frac{Q_c}{V}$$

where V [m³] is the detection borehole packer interval volume. Both formulas stay the same for consistent alternative expression of mass and concentration based on activity.

The slopes of the curves $\frac{dc}{dt}$ are shown in Figure 6-49 (in original units and after conversion to dimensionless) and in Table 6-10. On the basis of both relations, the corresponding effective diffusion coefficient is determined from the curve slope of the measurement (further columns in Table 6-10). Obviously, the obtained value is unrealistically low. Even if a concentration decrease was considered in the injection borehole (using final instead of initial concentration to represent the "steady-state"), only about factor of two is the effect on D_e (the last column of Table 6-10). Otherwise, the slow increase cannot be explained without the existence of at least part of the volume by with a low coefficient. At the same time, this value does not correspond to the rate of decrease in the source borehole (at a very low D_e, the decrease would practically not occur), so it can be expected that part of the affected rock matrix will have a value near the predicted value, but there will be a barrier in the monitored area with a several orders of magnitude lower coefficient.
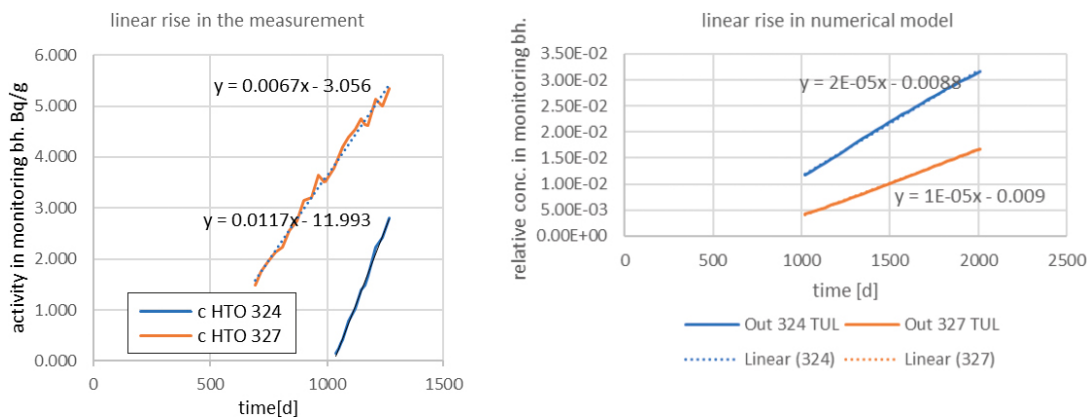
Figure 6-49. *Verification of assumption of a linear increase of concentrations in monitoring boreholes (324 327) and of the related steady-state diffusive transport. Linear regressions: left for the measured data (original units) and right for the numerical model result for a representative time interval (dimensionless).*
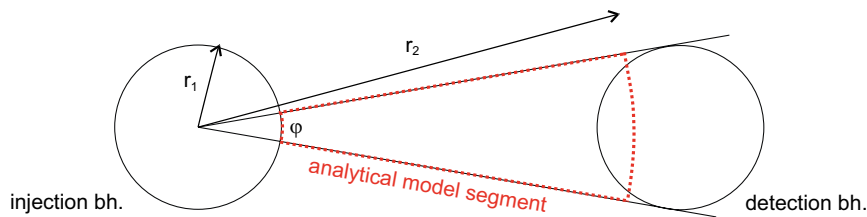
Figure 6-50. *Geometry for the steady-state radial symmetric model of TDE experiment – determining angle for ratio of mass captured by detection boreholes.*

Table 6-10. Input and results of the analytical solution and interpretation of mass flow rate between the boreholes (the concentration is evaluated as relative to the initial injection, i.e. dimensionless).

	dc/dt measured [1/s]	D_e fit analytical [m²/s]	D_e by considering decrease in the injection borehole [m²/s]
Borehole 324	2.14E−13	4.7E−16	9.4E−16
Borehole 327	1.19E−13	2.55E−16	4.6E−16

6.9 Alternative evaluation (CTU)

The time course of the relative concentrations in borehole PP324 is non-monotonous but, after the water exchange at approximately 1 000 days, the increase in concentrations over time is linear. To analyse and interpret this course, several calculations were performed at CTU using a 2D model created in GoldSim.

Based on the pilot calculations, it was determined that it is not possible to use a 2D model to simultaneously describe data measured in the injection borehole (PP326) and observation boreholes (PP324 and PP327). Therefore, we used the measured concentrations in injection borehole PP326 as the boundary conditions to calculate the time courses in PP324. Specifically, we applied the GoldSim Lookup Table element to interpolate the concentration in the Cell Pathway elements, which represented PP326 in each step. Because the 2D model is homogeneous, we searched for optimal *De* values for each observation borehole.

Figure 6-51 shows a comparison of concentration time courses in PP324, the black solid line corresponds to the detected data, the red line is the calculated values for the model without boundary conditions in PP324. The simulation was obtained for D_e = 4.35E−14 m²/s, which is an order of magnitude lower than expected (porosity of 0.0094). In the time interval up until the water exchange, i.e. up to approximately 1 000 days, the detected concentration was higher. On the contrary, the simulated increase afterwards is steeper. It can be expected that a higher concentration in the first interval resulted in diffusion from observation well PP324 into the matrix, which in turn may affect the diffuse flow into PP324 after the exchange, i.e. after 1 000 days. To verify this hypothesis, we constructed an alternative model that had a boundary condition on the time interval of 1–1 000 days in PP324 based on the detected data (red dashed line in Figure 6-51). The results of the simulation show that the influence of the boundary condition has no observable effect on the course of the concentration increase in PP324 during the course of the exchange.
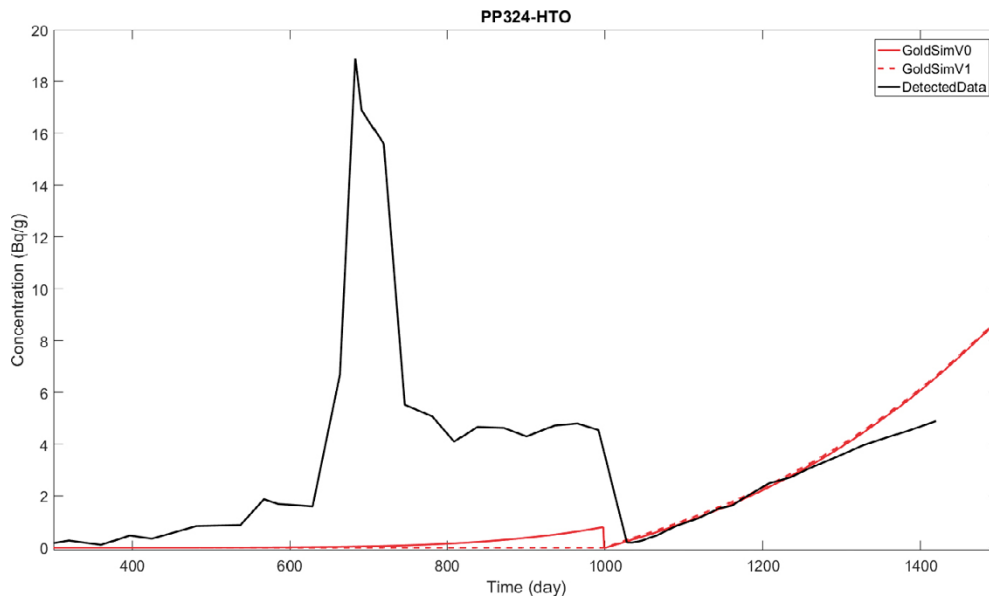
Figure 6-51. *Comparison of the time course of concentrations in PP324 for a model with PP324 without boundary conditions.*

6.10 Conclusions

The transport task solved in the framework of Task 9C is important from the point of view of modelling because of its relation to the ongoing in-situ diffusion experiment TDE (REPRO project). Simulation of the task, where specific measured data are available, is always better for comprehensive verification of the methodology of the modelling procedures, analysis, processing and evaluation of input and output data than simulation of a hypothetical task (with only input transport parameters, e.g. Task 9D). The experiment itself is interesting, because it can be used as a source of experience for the possible design of transport experiments, e.g. in the Bukov underground laboratory.

7 Solution of the transport task at the scale of a SA (Task 9D)

The aim of subtask 9D is to extrapolate the models and results from the scale of in-situ experiments to the scale and conditions considered in a safety assessment (SA). The configuration of the model is based on Task 9A and in sub-variants the properties and phenomena important in a real SA are added gradually. In the original plan issued by GWFTS, the basic ideas of the four variants were presented, in the end two, 9D-1 and 9D-2 were implemented, both by the Czech teams, authors of this report, and in the project as a whole.

Due to the limited involvement of other GWFTS teams in Task 9D, no comparison was made by the coordinator that could be included at the time of writing this report. The comparison is elaborated in detail between the co-authors of this report.

7.1 Summary of the task description and the data

The task is based on a synthetic simplified geometry (Figure 7-1), but with realistic parameters corresponding to the conditions of transport from the repository to the "interface with the biosphere", with a 1 km-long "fracture". Transport (advection and hydrodynamic dispersion) through one fracture, retention processes in the rock matrix (diffusion, sorption) and radioactive decay are considered. In addition to the scale, decay is a significant change from Task 9A. Two variants distinguish cases of hypothetical single tracers and a simplified decay series of uranium. The task description is detailed in the report (Crawford et al. 2021).

The relationship of the tasks at different scales, the in-situ WPDE experiment (9A) and the safety assessment (9D) is expressed by the parameters in Table 7-1. The accessibility of rock matrix by the tracers is expressed by the "F factor", which is the ratio of the wetted surface of the fracture to the flow rate expressed in (a/m). Task 9D is specified with the F-value of the SR-Site study, which is approximately three orders of magnitude higher than in the WPDE experiment. The transverse area of the fracture in the WPDE (annulus) is 2.17×10^{-4} m^2, which corresponds to the "flat" configuration of Task 9D:

- For diffusion into the matrix on only one side of the fracture, equivalent to a fracture width of 177 mm and an aperture of 1.22 mm (used for the models of TUL and PROGEO with explicit geometry).

- For diffusion into the matrix on both sides of the fracture equivalent to a fracture width of 88 mm and 2.44 mm (used for the models of CTU and ÚJV, using the "built-in" analytical solution of diffusion in the Pipe element of GoldSim).

The task description does not state a specific way of modelling the dispersion in the fracture, the default value of the Peclet number Pe=10 is proposed, which corresponds to a standard model of hydrodynamic dispersion and a task dimension of longitudinal dispersivity of 100 m.

The transverse dimension of the matrix domain is also not specified – the choice of finite or infinite distance is determined by the model used or a specific distance.

Rock matrix parameters are based on Task 9A and VGN rock is considered as the dominant type in the experimental series of REPRO. Specific parameters are given for the individual tracers for variants 9D-1 and 9D-2 in the subsections below. In both cases, anion exclusion is considered, i.e. effective diffusion coefficient an order of magnitude lower and the corresponding lower "transport porosity" (pore volume available for the tracer particles).
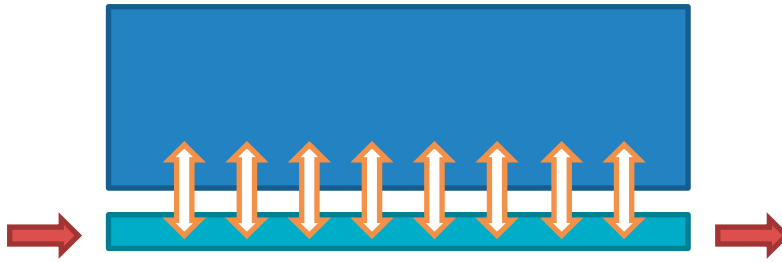
Figure 7-1. *Diagram of diffusion transport into the matrix in a scale corresponding to the safety calculation.*

Table 7-1. Parameters of flow and interaction of the rock matrix for Task 9D in the context of Task 9A (WPDE).

	WPDE-1	WPDE-2	SA Task 9D
q (m^3/a)	1.05×10^{-2}	5.26×10^{-3}	3.55×10^{-3}
v (m/a)	48.48	24.24	16.36
t_w (a)	0.0393	0.0786	61.12
F (a/m)	32.14	64.29	5×10^4

7.1.1   Step 9D-1 – hypothetical tracers

The task according to the configuration above is defined according to Crawford et al. (2021) for four hypothetical tracers (with parameters representing model cases of real radionuclides) marked A-D (Table 7-2) and four variants of other parameters marked a-d (Table 7-4). Of these, only the first two (a) with a pulse input (1 mol/a) of 1 000 years duration and no decay, and (b) with a continuous inlet flow of 1 MBq/a and decay were considered. The flow values are only technical; given the considered linearity of the model, they do not qualitatively affect the result.

The tracers primarily represent cases of sorption of varying size (Table 7-2), while the non-sorbing tracer A corresponds to the anion, with parameters considered for chlorine in Task 9A. The available porosity for tracer A is considered as before in Task 9A as 0.000436, as an assumption of authors, not just by the ratio of the D_e values as mentioned in the task description (Crawford et al. 2021). The tracers also have an increasing half-life the order from A to D. The density of rock was 2 741 kg/m^3.

Normalised breakthrough curves (time course of mass flow or output activity flow normalised by the input flow) and transverse profiles on the middle of the length of the task, at times that are different for each tracer, are prescribed as outputs (Table 7-3). The profile should be determined as total concentration (variant "a") or activity (variant "b") at the points of the profile, including both dissolved and sorbed forms. The work of the investigators in the form of analysis of the first versions of the models contributed to the selection of the given times, which are more suitable than those originally determined (it was included in the cited revision of the task description).

Table 7-2. Parameters of model tracers A-D according to the task description, the porosity corresponds to the relative volume of rock pores available for the given tracer.

Tracer	K_d (m^3/kg)	D_e (m^2/s)	$T_{1/2}$ (a)	porosity (-)
A (non-sorbing)	0	5×10^{-15}	20	0.000436
B (weakly sorbing)	10^{-4}	1.83×10^{-13}	1 000	0.0065
C (moderately sorbing)	10^{-3}	1.83×10^{-13}	10 000	0.0065
D (strongly sorbing)	0.1	1.83×10^{-13}	1 000 000	0.0065

Table 7-3. Times for profile output.

Tracer	Time for profile output [a]
A (non-sorbing)	500
B (weakly sorbing)	5 000
C (moderately sorbing)	50 000
D (strongly sorbing)	500 000

Table 7-4. Variants of the model according to the task description (calculations are performed for the first two).

Variant	Decay	Input boundary condition	Parameters
"a"	No	Pulse	Constant
"b"	Yes	Continual	Constant
"c"	No	Pulse	Variable
"d"	Yes	Continual	Variable

7.1.2 Step 9D-2 – decay series

The second variant 9D-2 considers real radionuclides bound together by a decay series. A simplified series of six radionuclides starting with U-238 was designed by the task proposer for the model task. Connection to the general decay process is shown in Figure 7-2. The half-life decreases with the sequence of products in the chain, so the secular equilibrium can be assumed (rates of particle formation and decay).

a) 4n+2 chain (spent nuclear fuel)

b) 4n+2 (naturally occurring/simplified)
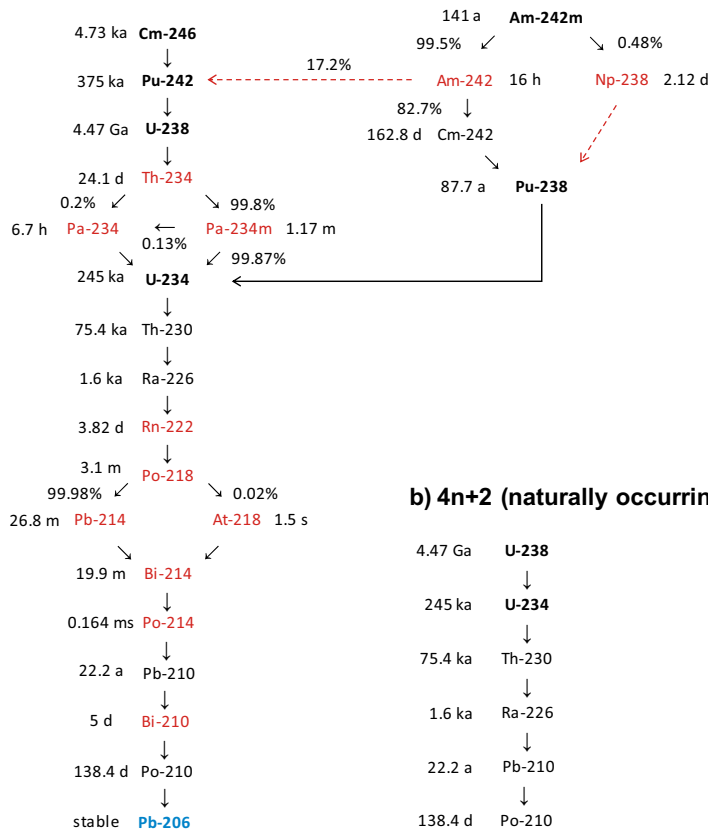
Figure 7-2. Derivation of a simplified decay series (taken from Crawford et al. 2021).

A continuous inflow of U-238 is specified only, with an activity flow of 1 MBq/a (again, it is only a technical choice). The radionuclides are assigned transport parameters according to Table 7-5.

Again, the breakthrough curves of the flow activity of the individual tracers normalised by the input flow of U-238 and the transverse profiles, evaluated in half of the length of the model at 100 ka, are required as outputs.

Table 7-5. Specified parameters of the considered radionuclides (according to Crawford et al. 2021), where the origin of the data is also explained).

Radionuclide	Dominant species	K_d (m³/kg)	D_e (m²/s)	$t_{1/2}$ (a)
U-238	$Ca_2UO_2(CO_3)_3$	8.0×10^{-2}	1.83×10^{-13}	4.47×10^9
U-234	$Ca_2UO_2(CO_3)_3$	8.0×10^{-2}	1.83×10^{-13}	2.45×10^5
Th-230	$Th(OH)_2(CO_3)_2^{2-}$	8	5×10^{-15}	7.54×10^4
Ra-226	Ra^{2+}	6.0×10^{-2}	1.83×10^{-13}	1.6×10^3
Pb-210	$PbCl^+$	2	1.83×10^{-13}	2.22×10^1
Po-210	$PoO(OH)_2$	2	1.83×10^{-13}	3.79×10^{-1}

7.2 Solution in Flow123d (TUL)

The concept of the model is based on a combination of a 1D fracture and a 2D rock matrix. The imaginary third dimension of the rock matrix (Flow123d input) is equal to 0.177 m, which ensures the correct value of the wetted surface (according to the task description). The fracture flow area is 217 mm², which corresponds to an aperture of 1.226 mm.

The fracture length is 1 000 m, the rock matrix thickness is 1 m (10 m in some calculations). The rock matrix is divided into layers of different thicknesses. The thinnest layer is closest to the fracture, further away the thickness of the layers increases. This was introduced to ensure finer discretisation near the fracture/rock interface.

The hydraulic conductivity in the fracture was calculated from the cubic law. The hydraulic conductivity in the rock matrix was calculated from the known permeability value (taken from the Task 9A task description). Parameters and boundary conditions of the flow are summarised in Table 7-6. The table shows that the resulting velocity (flux) in the fracture corresponds to the values given in the task description.

7.2.1 Task 9D-1

The transport model parameters are used according to Table 7-2 and other parameters specific for Flow123d are summarised in Table 7-6 and Table 7-7 (in addition, a fracture and a matrix are distinguished). The boundary condition of the transport was a constant mass flow of 1 kg/year (just a choice for convenience) on the inflow into the fracture, which does not affect the normalised breakthrough curves and the transverse profiles were converted to equivalent of the mass or activity flux in the task definition using the specific activity or molar weight.

Table 7-6. Task9D – Flow123d – parameters and BC flow model.

Hydraulic conductivity in the fracture	39.447e6 m/a
Hydraulic conductivity in the rock	3.096e−5 m/a
BC "inlet"	Total flow 16.36 m/a
BC "outlet"	Dirichlet Φ = 0 m
BC "remainder"	Homogeneous Neumann (zero flow)
Flow/rate	3.55e−3 m³/a ~ 16.36 m/a

Table 7-7. Task9D – Flow123d – transport model parameters.

	Rock matrix	Fracture
Porosity	0.0065 (4.3637e−4 for tracer A)	1
Longitudinal dispersivity	0 m	100 m
Transverse dispersivity	0 m	10 m

The results of transport simulations in the form of normalised breakthrough curves and concentration profiles at specified times in a line perpendicular to a fracture halfway through its length are part of a comparison in Section 7.6.

7.2.2 Task 9D-2

The transport model parameters are summarised in Table 7-5. The results of transport simulations in the form of normalised breakthrough curves are part of the cross-comparison in Section 7.6.

The breakthrough curves of the most sorbing members of the decay series are significantly different from the breakthrough curves from other investigators. We determined by the exclusion method that this is due to spatial discretisation of the rock matrix near the fracture/rock interface.

7.3 Variants of the solution at CTU

Task 9D was perceived by CTU as a task that applies the results obtained from modelling in-situ experiments analysed in previous tasks to the solution of the transport tasks corresponding to scenarios and scales typical for safety assessments. In accordance with the task description, we considered the model of an idealised fracture in the form of flat plates bounded on both sides by a homogeneous isotropic rock matrix of unlimited thickness (Figure 7-3).
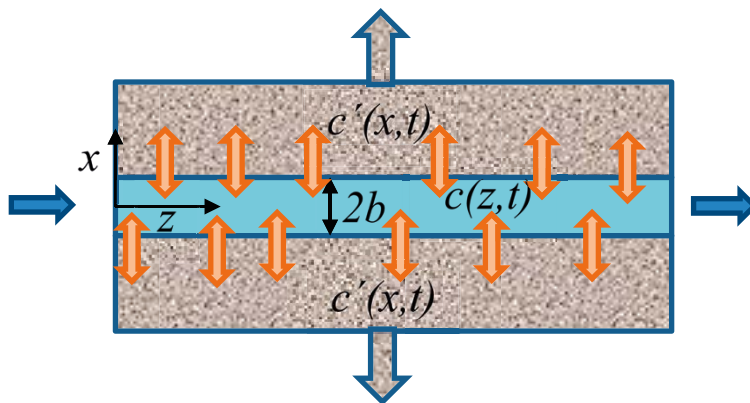
Figure 7-3. *Diagram of transport in an idealised fracture with aperture **2b**; the blue arrows indicate the direction of advective flow, orange arrows diffusion into the matrix, **c(z,t)** indicates the concentration of radionuclide in the flowing water, **c′(x,z,t)** the concentration in the pore water of the rock matrix.*

7.3.1 Analytical solution

The transport of radionuclides in this idealised fracture may be described using two sets of partial differential equations (Sudicky and Frind 1982). The first set of equations describes advective transport along the fracture in the direction of the z axis

$$\frac{\partial c_1}{\partial t} + v\frac{\partial c_1}{\partial z} + \lambda_1 c_1 - \frac{\varepsilon D_{p,1}}{b}\frac{\partial c_1'}{\partial x}\bigg|_{x=b} = 0 \tag{7-1}$$

$$\vdots$$

$$\frac{\partial c_n}{\partial t} + v\frac{\partial c_n}{\partial z} + \lambda_n c_i - \lambda_{n-1}c_{n-1} - \frac{\varepsilon D_{p,n}}{b}\frac{\partial c_n'}{\partial x}\bigg|_{x=b} = 0, 0 \leq z \leq \infty.$$

where x, z are spatial variables, t time change, $c_i = c_i(z,t)$ is the concentration of i-th radionuclide ($i\varepsilon[1,n]$) in the aqueous medium of the fracture, $c_i' = c_i'(x,z,t)$ is the concentration of the i-th radionuclide in the pore water of the rock matrix, v is the flow velocity in the fracture, λ_i the decay constant of i-th radionuclide, ε is the porosity of the rock matrix, $2b$ is the aperture of the fracture $D_{p,i} = \tau D_{w,i}$ is the diffusion coefficient of the i-th radionuclide in the pores, τ is the shape/geometric factor, $D_{w,i}$ is the diffusion coefficient of the i-th radionuclide in water.

The second set of equations describes diffusion and sorption in the rock matrix in the perpendicular direction, in the direction of the x axis

$$\frac{\partial c_1'}{\partial t} - \frac{D_{p,1}}{R_1}\frac{\partial^2 c_1'}{\partial x^2} + \lambda_1 c_1' = 0 \tag{7-2}$$

$$\vdots$$

$$\frac{\partial c_n'}{\partial t} - \frac{D_{p,n}}{R}\frac{\partial^2 c_n'}{\partial x^2} + \lambda_n c_n - \frac{R_{n-1}\lambda_{n-1}c_{n-1}'}{R} = 0, b \leq x \leq \infty,$$

where $R_i = 1 + (\rho_d K_{d,i}/\varepsilon)$ is the retardation coefficient of the i-th radionuclide, ρ_d is the bulk density of the material, $K_{d,i}$ is the equilibrium distribution coefficient of the i-th radionuclide.

The following initial and boundary conditions were considered

$$c_i(z,0) = 0, \; c_i(0,t) = c_{o,i}\delta(t) \tag{7-3}$$

$$c_i'(x,z,0) = 0, \; c_i'(b,z,t) = c_i(z,t), c_i'(\infty,z,0) = 0.$$

The analytical solution of this transport task for the concentration c_1 of the first radionuclide of the decay series can be written in the form (Sudicky and Frind 1982)

$$c_1(z,t) = \theta(t-T)c_{0,1}\frac{\gamma_1 z}{2\pi^{1/2}T^{3/2}}exp\left(-\frac{(\gamma_1 z)^2}{4T} - \lambda_1 t\right) \tag{7-4}$$

$$T = t - \frac{z}{v}, \; \gamma_1 = \frac{\epsilon\sqrt{R_1 D_{p,1}}}{bv},$$

where $\theta(t)$ is the Heaviside step function ($\theta(t) = 0$, for $t \leq 0$; $\theta(t) = 1$ for $t > 1$). For the other members of the decay series, it is not possible to express explicitly the dependence c_i on z and t due to the complexity of the calculation of the inverse Laplace transform.

We used the Equation (7-4) for c_1 to validate the model in GS, specifically to solve transport problems for four hypothetical radionuclides. Equation (7-4) describes the time dependence of the fracture end concentration in response to the Dirac unit impulse with initial and boundary conditions shown in Equation (7-3). To calculate the response for pulse flow for 1 000 years, in MATLAB® (R2016b) we created a function that first calculated the Equation (7-4) for the specified transport parameters and then calculated the convolution (MATLAB conv) with the rectangular function

$$U(t) = \begin{cases} 1; \text{for } 0 \leq t \leq 1\,000, \\ 0; \text{for } t < 0, \text{or } t \geq 1\,000. \end{cases}$$

We also used the analytical solution to design a further extension of the transport model in the framework of Task 9D. In Barten (1996), it has been shown that transport by a system of fractures connected in series can also be described by Equation (7-4), in which the parameters T and γ_1 are given as the sum of the parameters of the fractures. Therefore, we think that the heterogeneous nature of the fracture network should be represented by a more complex fracture system that will consist of interconnected parallel pathways.

7.3.2 Model in GoldSim

Figure 7-4 includes a diagram of the Task 9D model in GoldSim. The transport part of the model consists of five components. The Selector (FlInjection) component is used to specify a time-limited pulse flow, two Pipe pathway components (Pipe1 and Pipe2) represent a fracture with a rock matrix, the Container component (Matrix Diffusion) contains a planar network of 98 × 1 Cell pathway and calculates cross-sectional concentration profiles of radionuclides in the rock matrix in the middle of the fracture length. The Pipe pathway component contains the concentration of radionuclides in the water at the end of the fracture as the output. It does not allow to explicitly calculate the concentration profile in the rock matrix. Therefore, we split the fracture into two equal lengths and used the concentration at the output of the first Pipe pathway component (Pipe1) as a boundary condition for the Cell pathway network. In order to use the model for non-sorbing and sorbing radionuclides at the same time, we chose a network of 98 Cell pathway elements at an interval of (0, 10) [m] with a non-equidistant step extending from the fracture towards the matrix to calculate the concentration profile. We created two models in GoldSim, the first to solve the transport problem for four hypothetical radionuclides, and the second to solve the problem for the uranium (4n+2) decay series.
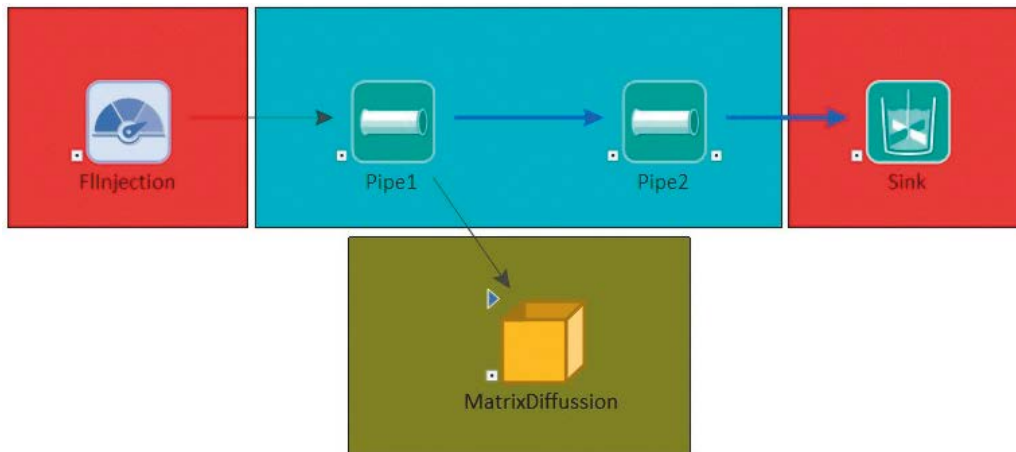
Figure 7-4. *Diagram of the transport part of the 9D model in GoldSim.*

7.4 Solution in GoldSim (ÚJV)

GoldSim version 12.0 was used to solve Task9D at the workplace of ÚJV Řež, a.s. The rock environment is considered homogeneous, its properties as isotropic. The Pipe pathway component was used for the solution of the task, a fracture of $1\,000\text{ m} \times 0.088\text{ m} \times 0.00244\text{ m}$ (length $\times$ width $\times$ transport aperture) was simulated as a whole (Figure 7-5). The fracture is simulated as free, without mineral infill. In the fracture, a dispersion of 10 % of the scale of the task was considered.

The following processes are simulated in the fracture:

- Advective transport

- Longitudinal dispersion

- Diffusion into rock matrix (exchange between mobile and immobile zones)

- Sorption

- Radioactive decay for selected tracers

The input was simulated in two ways, both as a $1\,000$-year pulse and as a constant input throughout the simulation. The groundwater flow rate of 0.00355 m^3/year was considered in the fracture, see Table 7-1. The parameters of the transport model were taken from the task description and are given in Table 7-2.

Task 9D2 follows on from Task 9D. Only the considered source, U-238, differs, with its decay products according to Figure 7-2. The injected amount of U-238 was 1 Bq/year. The parameters of the transport model were taken from the Task Description and are given in Table 7-5.

Figure 7-5. Method of fracture simulation in GoldSim, diagram of the mathematical model.

7.5 Solution in MT3D (PROGEO)

At PROGEO, a selected part of the tasks was simulated during the solution of Task 9D:

- Task 9D 1 for tracers A and C and for two boundary conditions "a" (pulse), "b" (constant source with radioactive decay),

- Task 9D 2 with the U 238 decay series.

MODFLOW2005 (for flow calculation) and MT3DMS and MT3D-USGS (for transport calculation) were used for the solution of transport Task 9D as well as for the solution of Task 9A, on which Task 9D is based. The conceptual model used in the solution of Task 9D is similar. Task 9D is solved by a one-layer model in 2D with a model domain formed by a rectangular grid of computational cells, see Figure 7-6. The fracture is entered in the upper row of the computational cells, i.e. it is oriented in the direction of the *x*-axis, diffusion into the rock matrix is in the direction of the *y*-axis. The length of the model domain is $1\,000$ m (corresponding to the fracture length), and width is 1 m (corresponds to the thickness of the rock matrix) and the thickness of the single-layer model is 0.177 m (corresponding to the TUL concept). The length of the computational cells in the fracture direction is a constant 1 m (i.e. a total of $1\,000$ columns). The width of the first row of the computational cells representing the fracture is 1.22 mm (corresponding to the fracture aperture). The width of the computational cells representing the rock matrix gradually increases from 0.1 mm to 170 mm (41 rows in total) in the direction from the fracture to the rock. A very small width of the rock matrix cells in contact with the fracture was used based on the experience of the solution of Task 9A, because it provides more accurate results of the transport simulation especially in the case of sorbing tracers. Time steps are set in a geometric series, starting at 0.001 years and increasing with a quotient of 1.05, when the input concentration is changed, the time step is restarted.
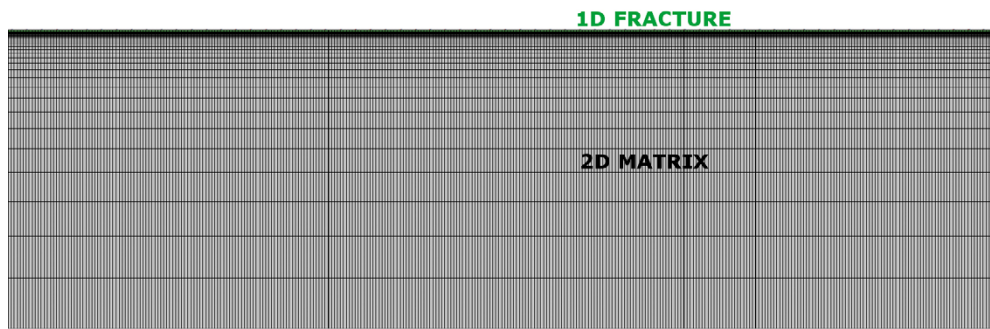
Figure 7-6. Task 9D – discretisation of the model domain in the PROGEO solution.

Flow values of the fractures and transport parameters of the rock matrix (porosity, diffusion coefficients, sorption coefficients, half-life) are taken from the joint task description and are the same for the other co-investigators.

The main aim of the simulation of Task 9D-1 in MODFLOW2005 and MT3DMS was to verify the possibility of performing this type of task (a combination of fracture flow and diffusion into the rock matrix) in programs that have been used in PROGEO for a long time, and with which we have very good experience in solving real hydrogeological tasks. Given the previous Task 9A, which was also solved at PROGEO, the aim was to verify the consistency of small-scale simulation results (Task 9A with a fracture length of 1.9 m) and then upscaling to a regional scale task (albeit simplified to a single fracture; Task 9D with fracture length of 1 000 m).

The motivation of the solution of Task 9D-2 was to verify and compare the results of the radionuclide decay series simulation in the MT3D USGS program – the decay series simulation is a new feature only added to this program in 2016 (earlier versions of the program, e.g. MT3DMS, did not allow this solution).

7.6 Comparison of the solutions

7.6.1 Task 9D-1

The breakthrough curves for the pulse input variants are shown both in the linear and in the logarithmic axes of the concentration, in order to see the shape of the decreasing concentration characteristic for diffusion from the matrix. The graphs in Figure 7-7, Figure 7-8, Figure 7-9 and Figure 7-10 show the individual tracers A-D. The comparison includes three (B, D) or four (A, C) numerical calculations, an analytical solution without dispersion or a model without dispersion (B, D), allowing for several partial evaluations.

The breakthrough curves are in qualitative agreement among the model variants for each tracer. Some deviations occur either on the linear axis only or on the logarithmic axis only. The most obvious effect is the course discretisation of Flow123d, while MT3D for the same conceptual model has a better agreement with the more accurate GoldSim. The deviations of the trend in the slope of the curve in the logarithmic axis are related to the different matrix thicknesses for each model, as demonstrated by the comparison in Section 7.7, and a similar comparison in Task 9A.

The shift of the analytical solution compared with all of the models of sorbing tracers B, C, D may seem surprising, but this phenomenon has also been observed for Task 9A in terms of sensitivity to dispersion in the fracture. The dispersion effect is also documented here by comparing the Flow123d solution with zero dispersion for tracers B and D, where the same shift occurs as in the analytical solution (however, numerical diffusions occur at different peak heights).

For variants with a continuous input, concentrations tend asymptotically to a constant value. The outputs are drawn in one form with a linear axis for all of the tracers in Figure 7-11. Again, you can see the effect of dispersion at the position of the leading part of the curve of all of the numerical models in contrast to the analytical solution. Slight differences in the asymptotic activity values are seen, more pronounced in tracer A, where each of the four models gives a different value. In this case, the dominant effect of time discretisation, probably related to the simultaneous calculation of transport and decay, was confirmed, where the discretisation effect becomes more apparent for rapid decay (Section 7.7).
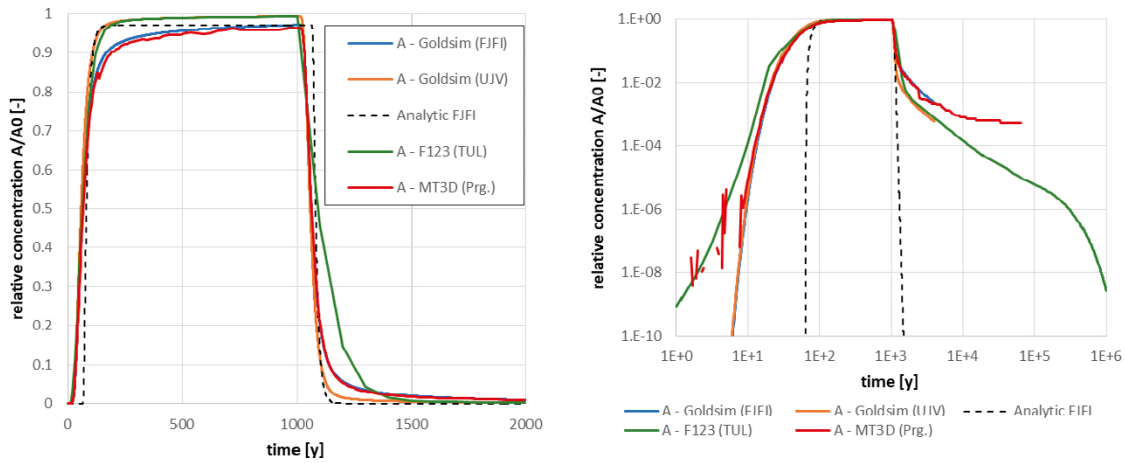
Figure 7-7. *Comparison of solution 9D-1-a breakthrough curves in two types of axis scales for tracer A (four models); in this case, the analytical solution is for the advection-only model (without the matrix diffusion).*
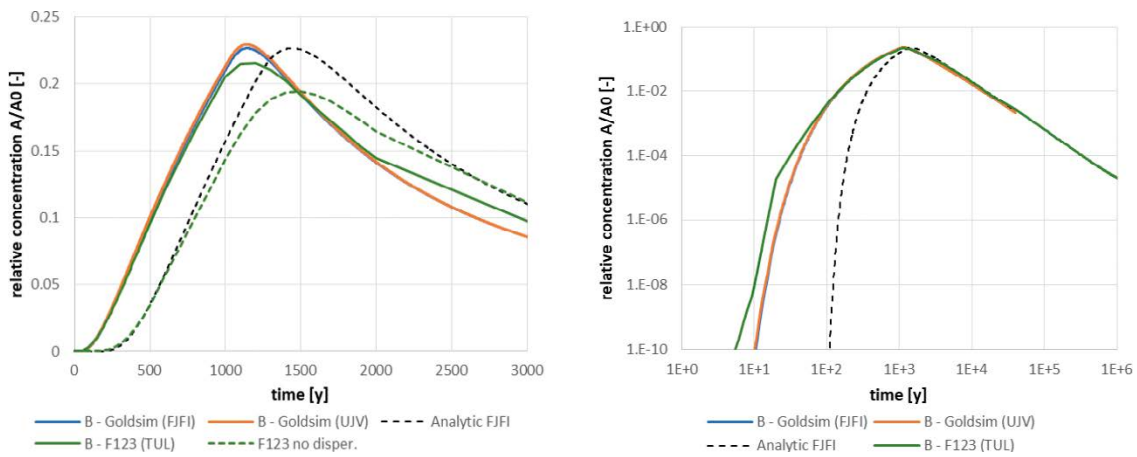
Figure 7-8. *Comparison of solution 9D-1-a breakthrough curves in two types of axis scales for tracer B (three models and variants without dispersion corresponding to the analytical solution).*
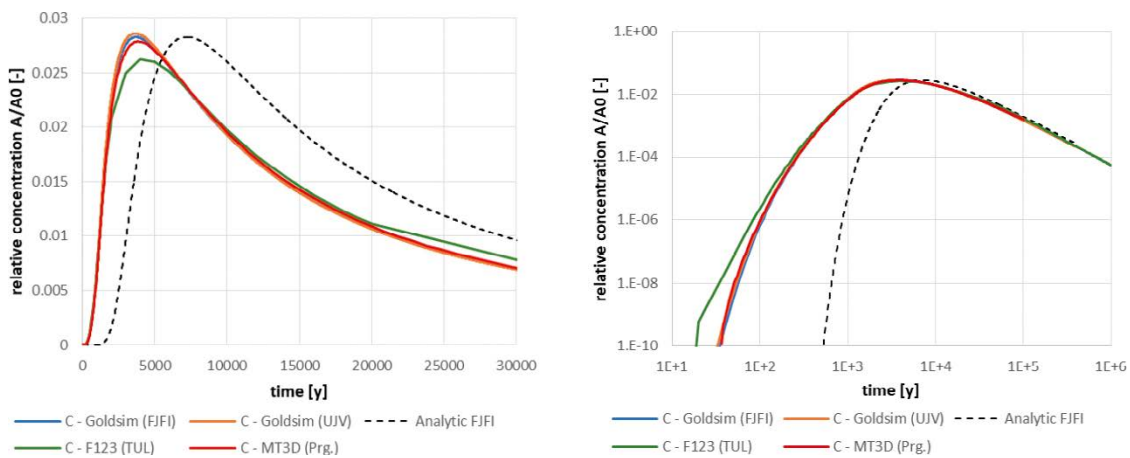
Figure 7-9. *Comparison of solution 9D-1-a breakthrough curves in two types of axis scales for tracer C (four models).*
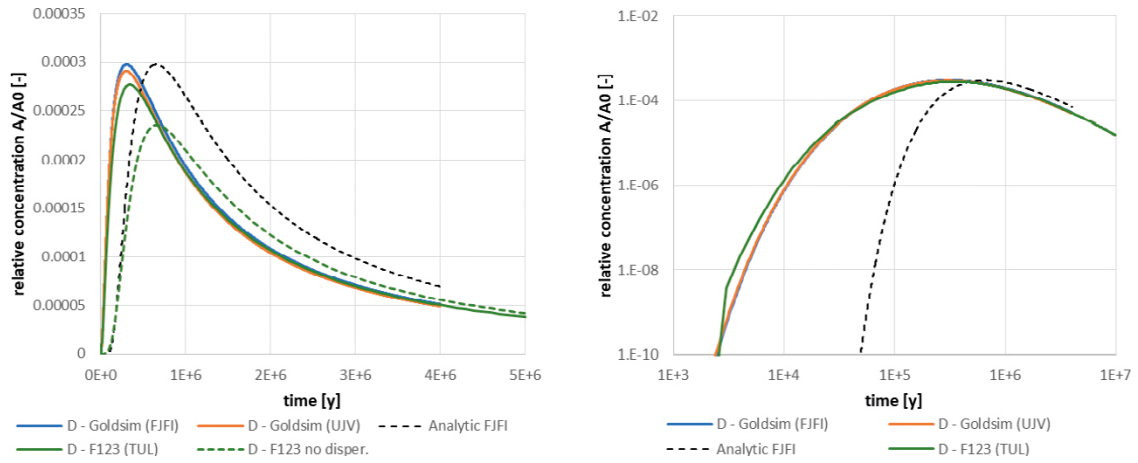
Figure 7-10. *Comparison of solution 9D-1-a breakthrough curves in two types of axis scales for tracer D (three models and variants without dispersion corresponding to the analytical solution).*
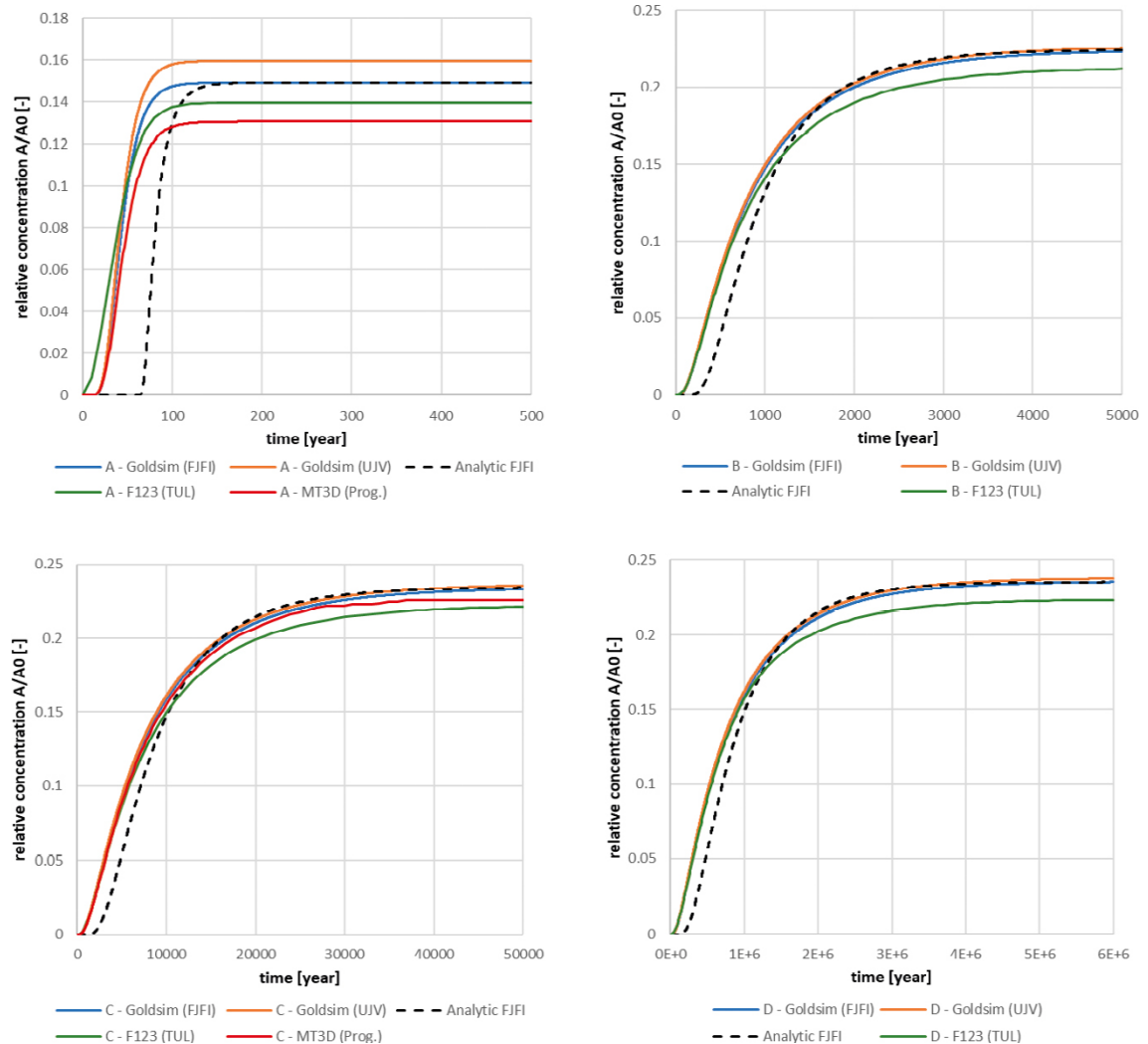
Figure 7-11. *Comparison of solution 9D-1-b breakthrough curves for all of the tracers (A – 4 models, B – 3 models, C – 4 models, D – 3 models).*

The comparison of the profiles in Figure 7-12 is only for the GoldSim (CTU) and Flow123d (TUL) models. The starting points of the fracture profiles differ slightly (in accordance with slight differences in breakthrough curves) and the trends are qualitatively identical. The results of Flow123d show the smoothness of the curves, which is probably due to the course discretisation and the effect of interpolation of points with values differing by one order of magnitude.

7.6.2 Task 9D-2

The comparison of the breakthrough curves is arranged so that the processing of the two GoldSim models (CTU and ÚJV) is presented in logarithmic axes over a longer period of time in Figure 7-13. The three models (GoldSim, Flow123d and MT3D) are compared in Figure 7-14 over a shorter period on linear axis scales. In the first case, an exact agreement is seen except for a slight deviation in the leading edge of the Th curve (these are values of one order of magnitude less than the maximum), as well as the differences in orders of magnitude between the activity values of the individual radionuclides, which cannot be captured on the linear axis. The results of Po and Pb are identical due to equilibrium at a short half-life and the same transport parameters.
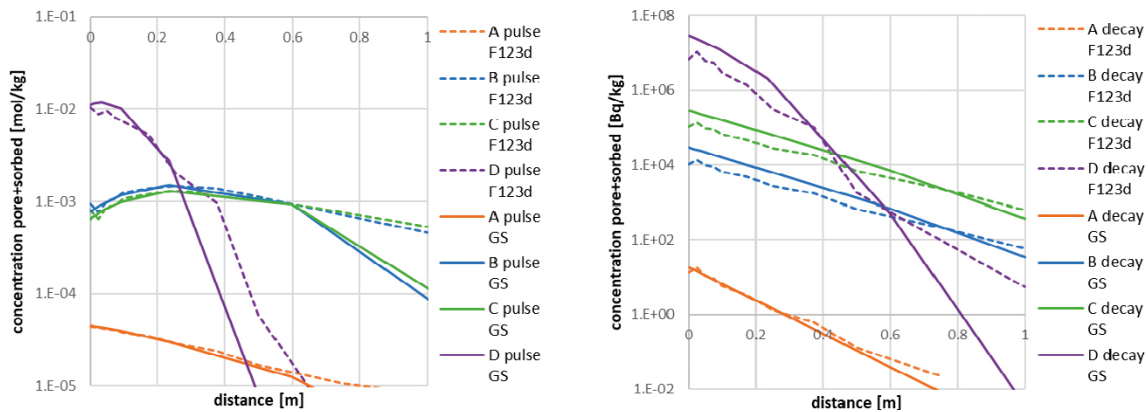
Figure 7-12. *Comparison of solution 9D-1 cross-sectional profiles of two models (Flow123d and GoldSim – GS) for all of the tracer., Pulse inflow without decay (variant a); continuous inflow with decay (variant b).*
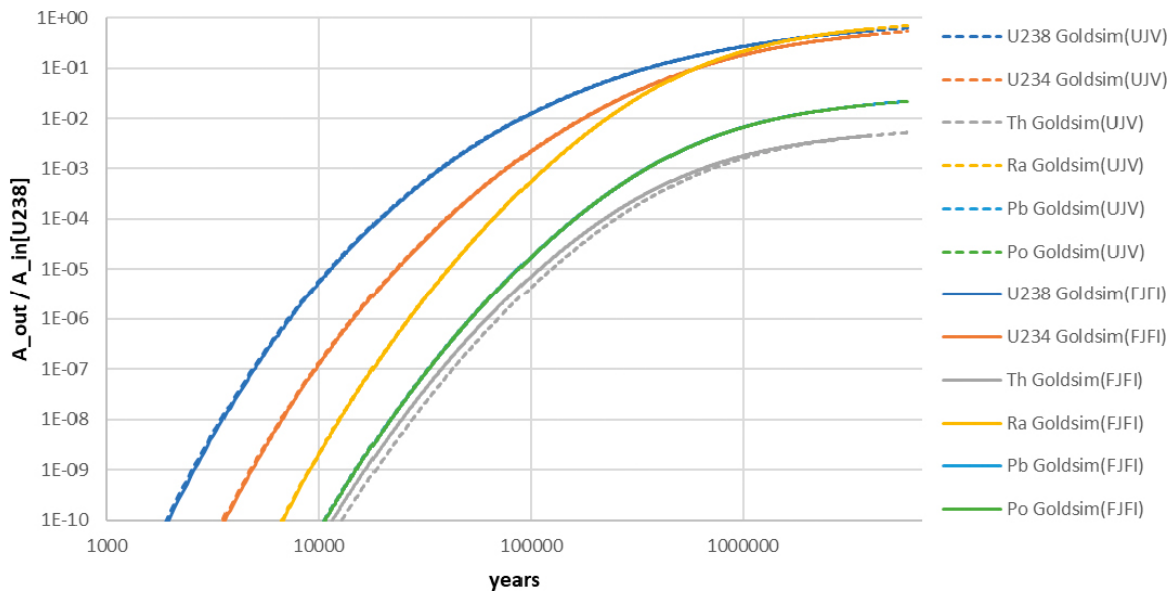
Figure 7-13. *Comparison of solution 9D-2 breakthrough curves for six radionuclides in the decay series (Pb is graphically indistinguishable from Po) – two independently processed GoldSim calculations.*
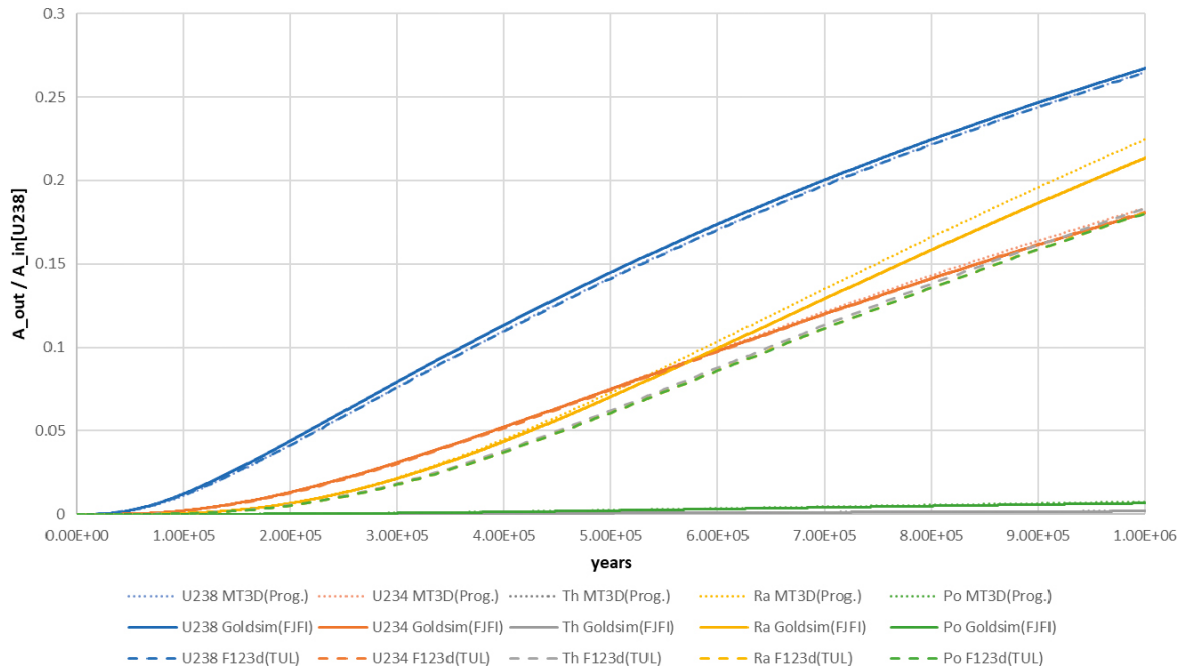
Figure 7-14. *Comparison of solution 9D-2 breakthrough curves for five radionuclides in the decay series (Pb is not plotted, it is graphically indistinguishable from Po) – calculations by three different software programs.*

In the second case, Figure 7-14 shows the agreement of the models for U-238, U-234 and Ra, while for the remaining radionuclides, Th, Pb and Po, the result of Flow123d is significantly different – in a similar order to the other radionuclides, while the rest agree with approximately two orders of magnitude lower values. This is more precisely quantified in Table 7-8 by values of activities at 1 Ma, i.e. selected points on the curves. It may be seen that in the three radionuclide cases with higher sorption (Th, Pb, Po), the deviation of the GoldSim and MT3D models is evident in the order of agreement. The hypothesis is again directed to the effect of discretisation in connection with high sorption.

As a control, U-238 was compared with the considered decay against the D-tracer without decay (Figure 7-15). A second auxiliary comparison is then given in the following section.
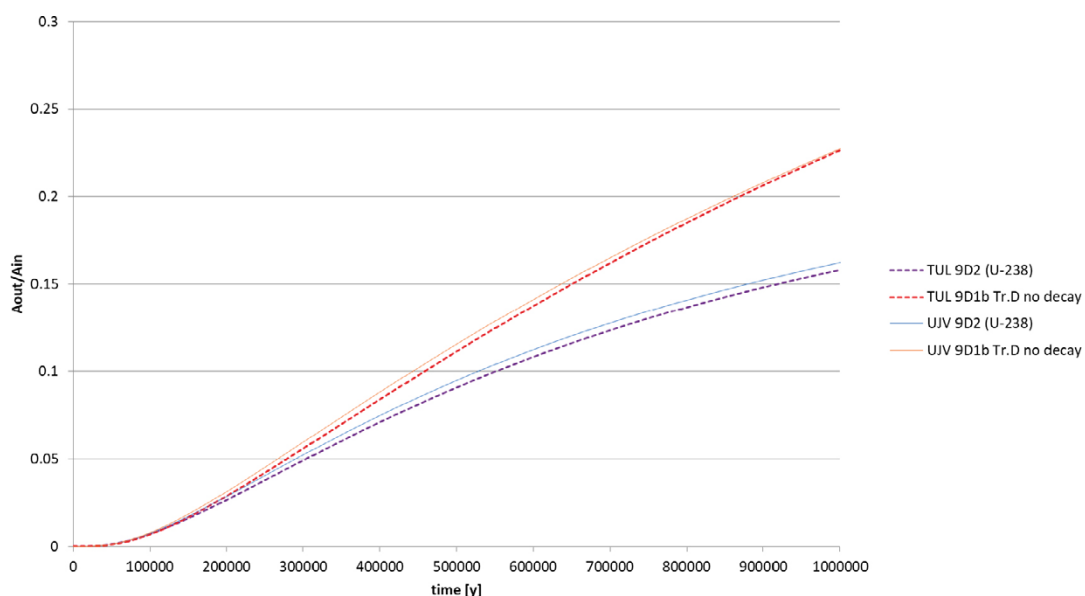
Figure 7-15. *A control comparison of the breakthrough curves of 9D-1 (tracer D) and 9D-2 (uranium) between Flow123d(TUL) and GoldSim (ÚJV).*

Table 7-8. Comparison of values on the breakthrough curve at 1 Ma (activity normalised by the input activity of U-238).

	U-238	U-234	Th-230	Ra-226	Pb-210	Po-210
GoldSim (CTU)	0.267	0.180	0.00179	0.213	0.00665	0.00662
GoldSim (ÚJV)	0.270	0.182	0.00161	0.213	0.00665	0.00662
MT3D-USGS	0.265	0.183	0.00185	0.224	0.00777	0.00748
Flow123d	0.265	0.181	0.183	0.180	0.180	0.180

7.6.3 Auxiliary task with uniform sorption

Due to the large differences in the breakthrough curves of the more sorbing radionuclides in 9D-2 and the observed problematic behaviour during large sorption in previous tasks, an auxiliary task was defined, differing by setting a uniform sorption coefficient $K_d = 8.0 \times 10^{-2}$ m³/kg for all of the radionuclides in the decay series. This corresponds to the parameters of uranium, while the other radionuclides are labelled "-alt". A comparison of the breakthrough curves is shown in Figure 7-16, which shows a good agreement between GoldSim and Flow123d, whereby confirming the mentioned cause of the difference in the results of the original task description for 9D-2. Table 7-9 compares the specific values of activity on the breakthrough curve.
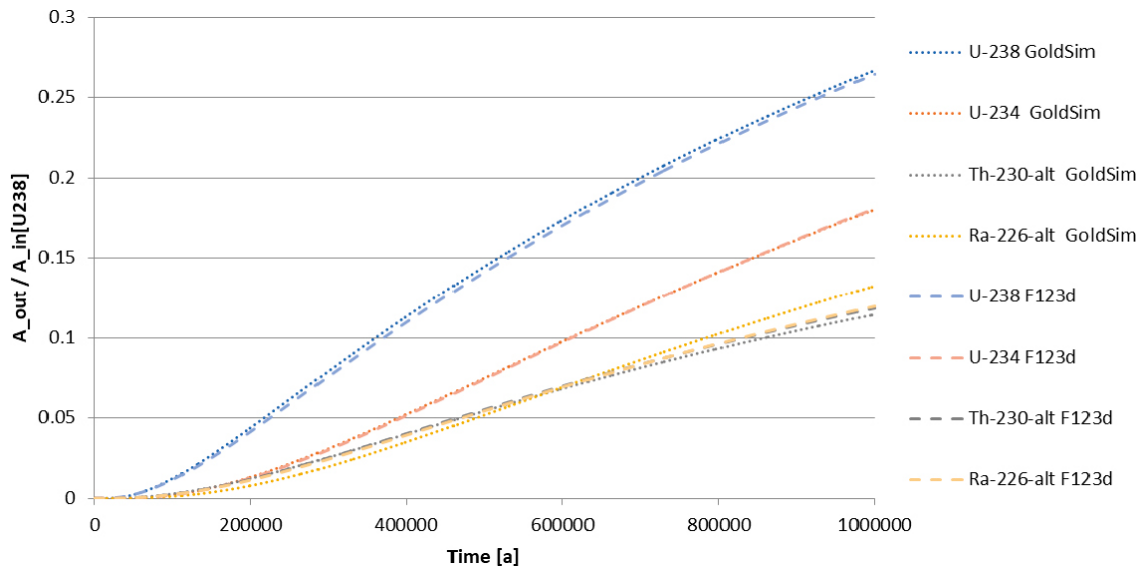
Figure 7-16. *Breakthrough curves of the auxiliary model (profiles Po and Pb are identical to Ra in both models).*
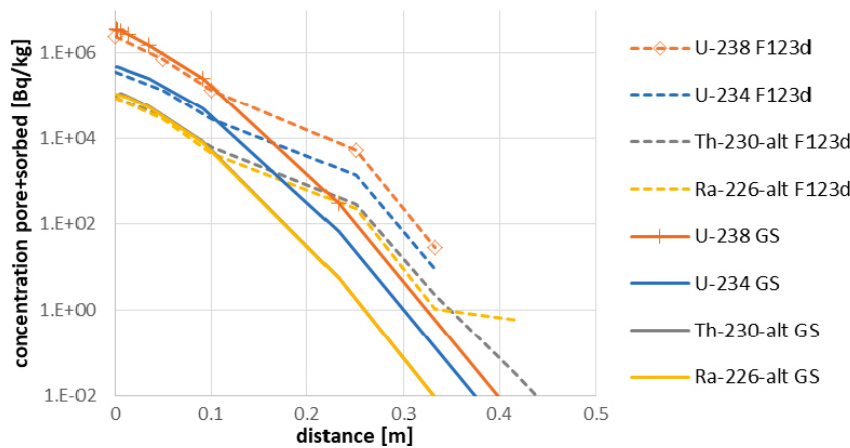
Figure 7-17. *Transverse profiles in the auxiliary model (Po and Pb profiles are identical to Ra in both models).*

The profiles of activity in the transverse direction in the rock matrix are shown in Figure 7-17. The agreement of parts of the curves near the fracture is good, the area with the separation of the course of the curves corresponds to the change in discretisation in the Flow123d model, which again confirms the combination of discretisation and large sorption as the main cause of the differences.

Table 7-9. Comparison of values on the breakthrough curve at 1 Ma (activity normalised by the input activity of U-238) for a modified task with uniform sorption.

	U-238	U-234	Th-230	Ra-226	Pb-210	Po-210
GoldSim	0.267	0.18	0.114	0.132	0.132	0.132
Flow123d	0.265	0.181	0.119	0.12	0.12	0.12

7.7 Sensitivity studies

Sensitivity to spatial discretisation

The sensitivity of the course of the breakthrough curves to the spatial discretisation of the model (especially near the fracture/rock interface) was tested. For this purpose, five variants of the mesh were created, where the individual layers of the rock matrix had different thicknesses. The variants are described in Table 7-10, where the columns indicate at what depth (distance from the fracture) the individual layers end. The layer distances correspond to discretisation triangle sides in the direction perpendicular to the fracture. The "Refined fine" variant was created from the mesh marked "Fine" by dividing each of its triangular elements into four triangles. The analysis results are shown in Figure 7-18, Figure 7-19, Figure 7-20 and Figure 7-21 (scenario 9D-1a: no decay, BC in the form of a 1 000-year-long pulse). It is evident that for the conservative tracer, the results are not dependent on spatial discretization; with increasing sorption the dependence becomes more and more pronounced. Therefore, we reach the same conclusions as in the case of Task 9A, where we stated that a very fine mesh is needed for strongly sorbing tracers near the fracture/rock interface.

Sensitivity to the discretisation time was also tested. It was determined that it is advisable to choose a finer time step, especially in the beginning of the simulation. The length of the time step must also be chosen with regard to the half-life of the individual tracers, in the event that radioactive decay is considered in the given scenario.

Table 7-10. Task9D – Flow123d – Mesh variants (the presented position of layer interface is also approximately the element size for the next layer, except the "Refined fine" – e.g. the zone between 0.5 m and 10 m is discretized by 0.5 m for "Fine").

Mesh marking	Layer 1 [m]	Layer 2 [m]	Layer 3 [m]	Layer 4 [m]	Layer 5 [m]
"Coarse"	0.2	0.4	1	2	10
"Medium"	0.1	0.2	0.5	1	10
"Fine"	0.05	0.1	0.25	0.5	10
"Refined fine"	0.05	0.1	0.25	0.5	10
"Thin"	0.005	0.01	0.03	0.1	1
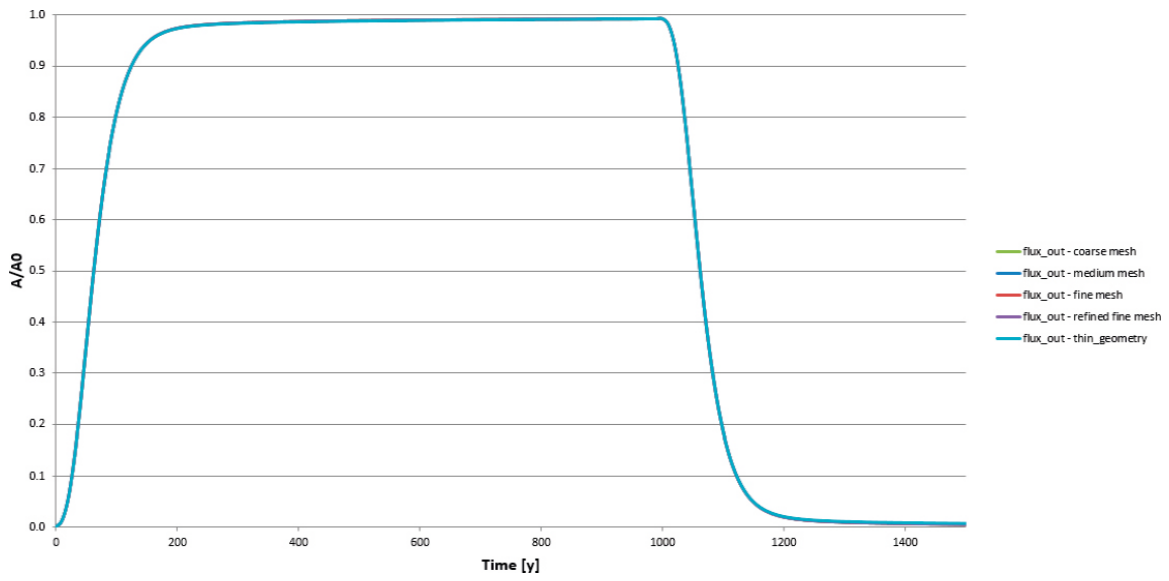
Figure 7-18. *Task9D – influence of spatial discretisation – tracer A.*
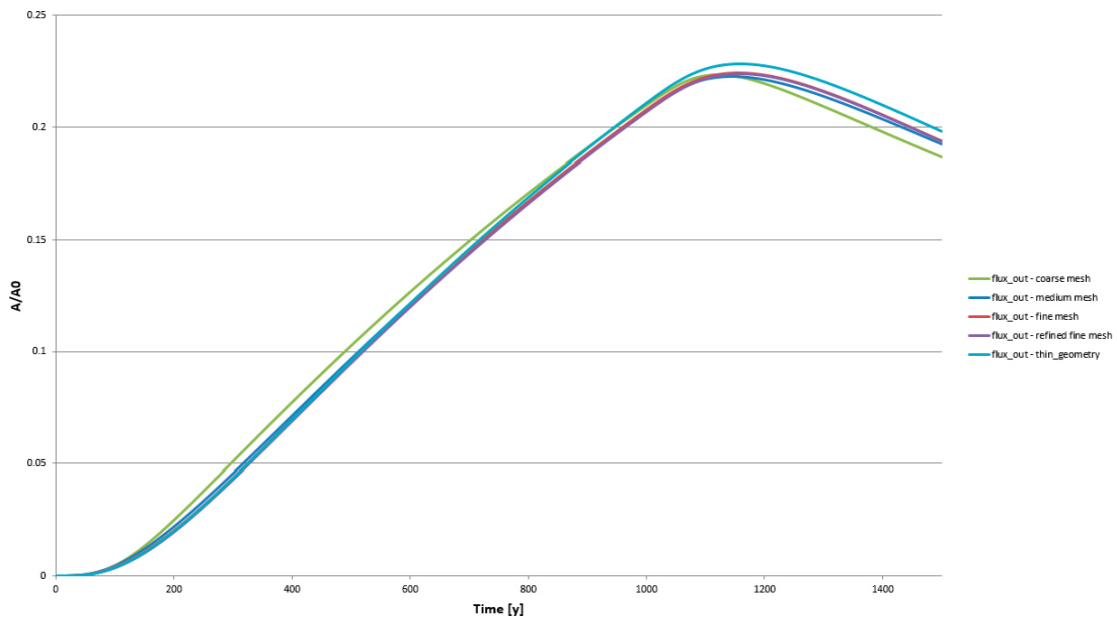
Figure 7-19. *Task9D – influence of spatial discretisation – tracer B.*
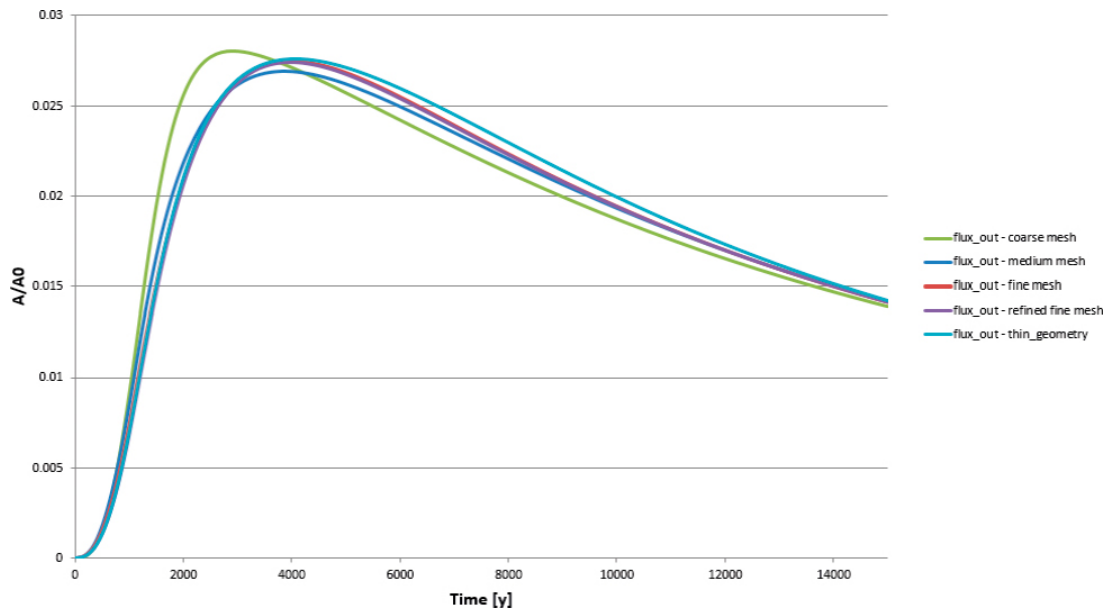
Figure 7-20. *Task9D – influence of spatial discretisation – tracer C.*
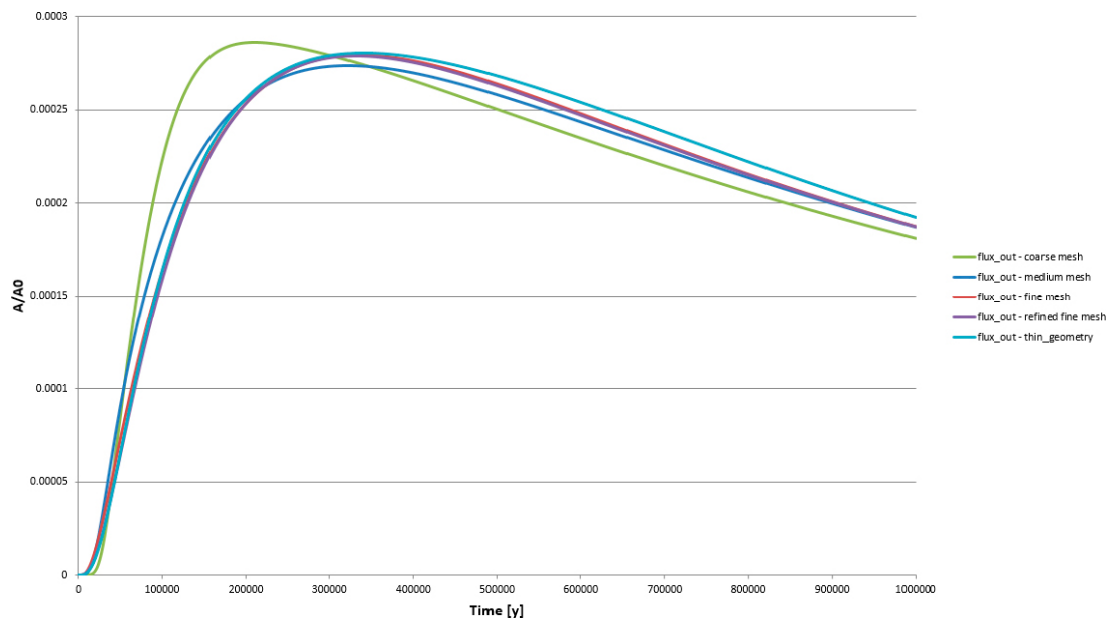
Figure 7-21. *Task9D – influence of spatial discretisation – tracer D.*

Influence of rock matrix thickness

The influence of the thickness of the rock matrix on the breakthrough curve (and the boundary conditions of zero mass flux over the outer boundary of the model) was tested. The simulation period was 10^6 years (10^7 for tracer D). Figure 7-22 shows the normalised breakthrough curves for each of the tracers, each for a rock matrix of thickness 1 m and 10 m. The "waviness" of the breakthrough curve for a thicker rock matrix is caused by the variable time step of the calculation over time. The figure shows that the influence of matrix thickness (near the BC) is more significant for conservative and low-sorbing tracers. The influence is expressed on the course of the descending part of the breakthrough curve.
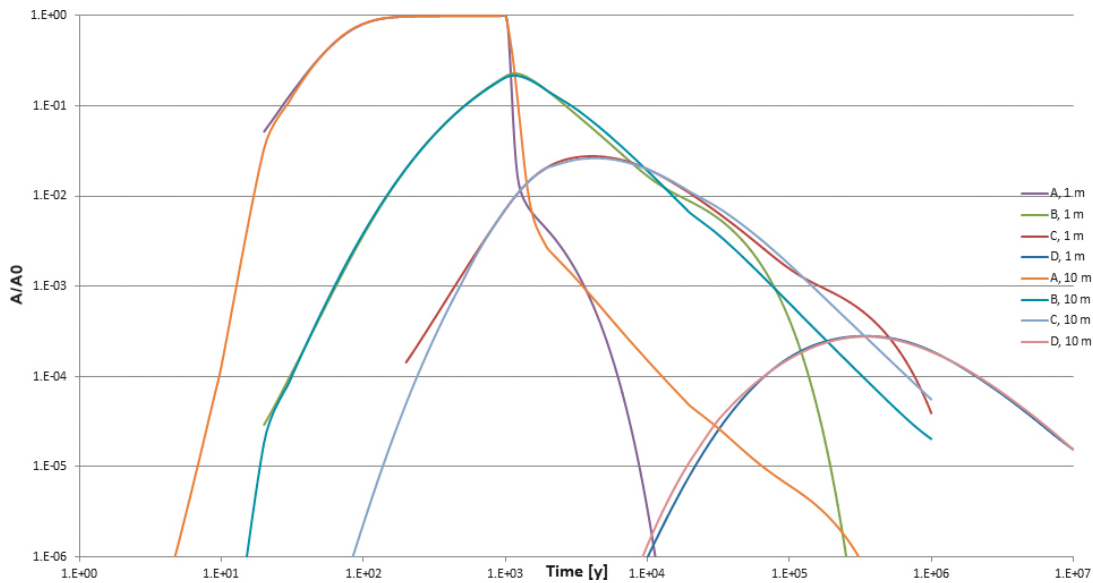
Figure 7-22. *Task9D-1a – influence of rock matrix thickness – normalised breakthrough curves.*

Influence of hydrodynamic dispersion in the fracture

The influence of the presence of hydrodynamic dispersion in the fracture on the results of normalised breakthrough curves was tested. The tests were performed on a computational mesh with a rock matrix thickness of 10 m. The simulation period was 10^6 years (10^7 for tracer D). Figure 7-23 shows normalised breakthrough curves for each of the tracers with and without hydrodynamic dispersion. It may be seen from the figure that the hydrodynamic dispersion has a great influence mainly on the shape of the leading edge of the breakthrough curve and also on the position of the maximum. The influence on the shape of the falling edge is negligible.
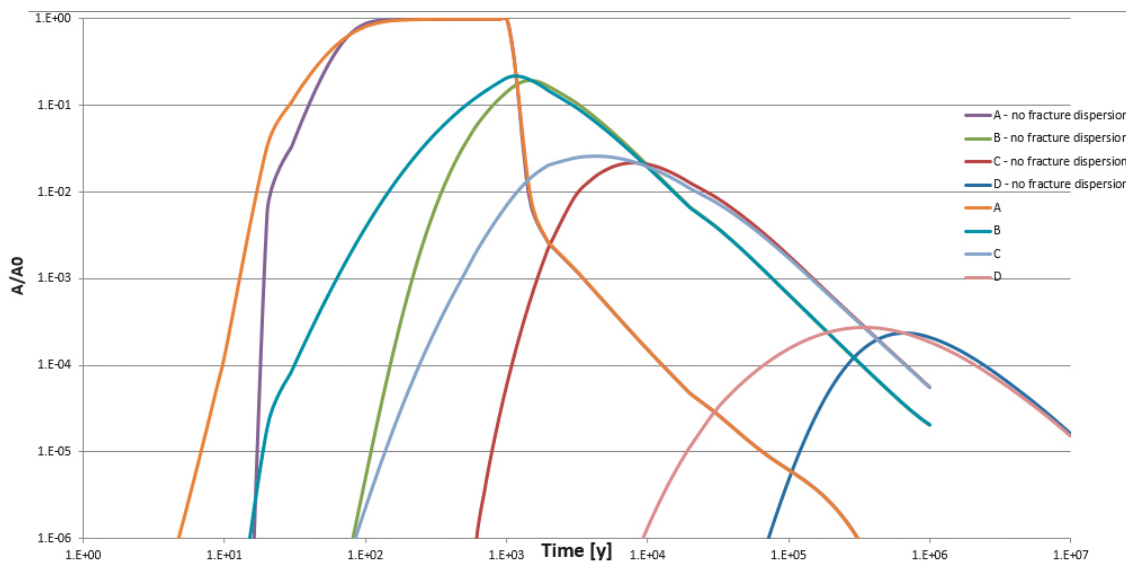
Figure 7-23. *Task9D-1a – influence of dispersion in the fracture – normalised breakthrough curves.*

8 Conclusion

The project solution has provided an understanding of the retention processes in many ways, especially concerning the origin of uncertainties in calculations whose analogue may be part of the safety assessment.

The following text summarises specific conclusions evaluating the applicability and limitations of various conceptual models and simulation algorithms, as well as findings from experimental data that have a general overlap, i.e. they relate in particular to the crystalline rock environment without being bound to a specific location.

International collaboration contributed both to the availability of large amounts of data and also to the evaluation of methodologies and results in a wider team, including direct comparison of the results of a larger number of models from different investigators. According to the requirements of the task description, verification of the simulation codes Flow123d and GoldSim used for the considered phenomenon of radionuclide transport in relatively diverse configurations was achieved, and critical situations requiring attention and a control of the solution were determined.

8.1 Evaluation of the models

The comparison of the results of the predictive calculations resulted primarily in the verification of the simulation codes, but also in the correct way of entering input data in various forms transformed from the supplied data. The models of the Czech investigators (co-investigators of the sub-project to which this report relates) were verified among themselves in all tasks 9A-9D. This report does not include the comparison and evaluation across the international teams. Comparison of model results from Task 9A is the subject of the published evaluation and modelling report (Soler et al. 2019). Reports for other tasks were not available at the time of writing this report for SÚRAO and are in final drafts when completing this publication under SKB (Soler et al. 2021a for 9B and Soler et al. 2021b for 9C). Models based on the same control equations and baseline assumptions gave consistent results, with any partial differences being clarified.

Although these were seemingly simple tasks (linear equations, regular geometry), it was determined that numerical algorithms may behave in a complicated and unpredictable way. Typical causes known in numerical mathematics may also be identified in the following tasks: large contrasts in the coefficients (manifested indirectly in the form of spatial mass balance in the case of sorption), spatial scale (extent of the breakthrough into the matrix) and temporal scale (decay rate versus transport rate).

The benefit of the calculation with the Pipe elements in GoldSim (or the algorithm based on the analytical solution of transverse diffusion into the matrix) is the elimination of the influence of discretisation, whereby providing the most accurate solution, at the expense of constraints in the geometry of the area and spatial inhomogeneity of the fractures. The procedure cannot be used other than for the transverse direction from the fracture and assuming a homogeneous matrix (without a BDZ, etc.). All of the models based on discretisation (GoldSim-CellNet, Flow123d and MT3D) suffer from inaccuracy due to the discretisation. In the case of a regular grid (GS-CellNet and MT3D), the sufficient refinement for the convergence of the solution was easier to achieve. On the other hand, the unstructured Flow123d mesh offers full flexibility in irregular geometries, as was the case with the TDE experiment with three boreholes, where various different conceptual simplifications had to be considered for GS-CellNet.

As with the original evaluation of the LTDE-SD experiments (Nilsson et al. 2010) and similar ones outside this project (Havlová et al. 2016), it was confirmed that the measured data characterising diffusion transport with sorption cannot be explained in many cases using standard equations and laboratory determined coefficients. Based on the previously designed concept of the BDZ (zone influenced by the drilling), the inverse models were implemented in the form of an inhomogeneous

matrix with various different coefficients depending on the distance from the borehole wall. Thereby, in most cases it was possible to obtain model results in agreement with the measurements, but with many limitations: often the determination is ambiguous, and the obtained coefficients and positions interfaces are not transferable to other cases.

The micro-DFN methodology is also able to successfully explain the measured data in a more "conceptual" way, where the origin of the inhomogeneity data is given by the actual data of the rock microstructure. On the contrary, a limitation is that such data are bound to a specific sample and, therefore, cannot be used for prediction in general with the current methods of obtaining and processing the input data. Furthermore, there is no tried-and-tested method for "upscaling" to a corresponding safety assessment. Therefore, the implementation of the project provides space for further research in this direction.

8.2   Benefits of the collaboration

Experimental data from underground laboratories in Sweden and Finland were provided in full to the whole international team of participants, which allowed a wide discussion about the interpretation of processes and the applicability of different types of models. For the further activities of SÚRAO, this brings a range of technical matters for the performance of experiments (which are not directly the subject of this "modelling" sub-project and result directly from materials available on the GWFTS portal) and suggestions for obtaining transport parameters of individual radionuclides for the needs of a safety assessment.

The discussions were largely aimed at distinguishing physical phenomena of interest and experimental artefacts. In particular, many discrepancies were found for the LTDE-SD experiment (Task 9B). At the same time, contradictory analogues were presented – cases where the "rapid" penetration of the tracer in a small concentration to a greater depth can be observed as a real phenomenon, versus a contamination of samples. The other investigators in Task 9 worked with the models under either of these assumptions.

For the use of the models, it is essential to ensure the conditions of laboratory and in-situ measurements, which will allow the connection between transport parameters at different scales, e.g. the effect of disturbance at the borehole wall and from the treated sample surface.

Furthermore, the necessity of simultaneous measurement of concentration (activity) both in the reservoir of the injection borehole (or fractures, etc.) and in the rock itself (at least during the disassembly phase) was confirmed. Models based on one type of data lead to ambiguous interpretations and do not allow to determine transport parameters that can be transferred to other conditions.

References

SKB's (Svensk Kärnbränslehantering AB) publications can be found at www.skb.com/publications.

Anderson J D, 1995. Computational fluid dynamics: the basics with applications. New York: McGraw Hill.

Andersson P, Nilsson K, Löfgren M, 2020. Task description of Task 9C – Modelling of REPRO experiment TDE. Task 9 of SKB Task Force GWFTS – Increasing the realism in solute transport modelling based on the field experiments REPRO and LTDE-SD. SKB P-17-31, Svensk Kärnbränslehantering AB.

Barten W, 1996. Linear response concept combining advection and limited rock matrix diffusion in a fracture network transport model. Water Resources Research 32, 3285–3296.

Bedekar V, Morway E D, Langevin C D, Tonkin M, 2016a. MT3D-USGS version 1: A U S. Geological Survey release of MT3DMS updated with new and expanded transport capabilities for use with MODFLOW. U. S. Geological Survey Techniques and Methods 6–A53.

Bedekar V, Morway E D, Langevin C D, Tonkin M, 2016b. MT3D-USGS: Groundwater solute transport simulator for MODFLOW: U S. Version 1.0.0 Geological Survey Software Release, 30 September 2016. Available at: http://dx.doi.org/10.5066/F75T3HKD

Box M J, 1965. A new method of constrained optimization and a comparison with other methods, The Computer Journal 8, 42–52.

Crawford J, Soler J M, Trinchero P, Hokr M, Havlová V, Vetešník A, Gvoždík L, Milický M, Polák M, Reimitz D, Říha J, Trpkošová D, Višňák J, Vopálka D, Meng S, Moreno L, Liu L, Svensson U, 2021. Evaluation and modelling report of Task 9D regarding safety assessment calculations based on gained knowledge within Task 9. Task 9 of SKB Task Force GWFTS – Increasing the realism in solute transport modelling based on the field experiments REPRO and LTDE-SD. SKB R-21-17, Svensk Kärnbränslehantering AB.

GoldSim, 2014. GoldSim contaminant transport module user's guide. Version 6.4. GoldSim Technology Group.

Hartley L J, 1998. NAPSAC Release 4.1, Technical summary document. AEA-R&R-0271, AEA Technology, UK.

Havlová V, Hofmanová E, Kolomá K, Trpkošová D, 2016. Realizace a vyhodnocení LTD etapa III. experiment v Grimsel Test Site. Průběžná zpráva projektu 2016. ÚJV Řež, A S. (In Czech.)

Havlová V, Zuna M, Večerník P, Brázda L, Kolomá K, Trpkošová D, Gvoždík L, Milický M, Sosna K, Svoboda J, Staš L, Souček K, 2017. Přenos hodnot migračních PArametrů granitických hornin z MIkroměřítka do REálného měřítka horninového masivu (PAMIRE) (Transfer of granitic rock migration parameters from microscale to real scale in the rock massive). Final Report, ÚJV Řež, ÚJV Z4932. (In Czech.)

Havlová V, Zuna M, Brázda L, Kolomá K, Galeková E, Rosendorf T, Jankovský F, 2019. Radionuclide migration processes in a crystalline rock environment and the migration parameters of rocks of the Bohemian Massif. Final report. SÚRAO TZ 333/2018/EN.

Hokr M, Havlová V, Vetešník A, Říha J, Trpkošová D,Vopálka D, 2015. Testování transportních modelů s využitím in-situ zahraničních experimentů. Zpráva SÚRAO, č. 33/2015. (In Czech.)

Hokr M, Havlová V, Vetešník A, Gvoždík L, Milický M, Polák M, Reimitz D, Říha J, Trpkošová D, Višňák J, Vopálka D, 2016. Testování transportních modelů s využitím in-situ zahraničních experimentů. Zpráva SÚRAO, č. 77/2016. (In Czech.)

Hokr M, Havlová V, Vetešník A, Gvoždík L, Milický M, Polák M, Reimitz D, Říha J, Trpkošová D, Višňák J, Vopálka D, 2017. Testování transportních modelů s využitím in-situ zahraničních experimentů. Zpráva SÚRAO, č. 172/2017. (In Czech.)

Hokr M, Havlová V, Vetešník A, Gvoždík L, Milický M, Polák M, Reimitz D, Říha J, Trpkošová D, Višňák J, Vopálka D, 2020. Testování transportních modelů s využitím in-situ zahraničních experimentů, SURAO Report TZ 481/2020. (In Czech.)

Huang I B, Yen S K, 2002. Diffusion in hollow cylinders for some boundary conditions: I. Mathematical treatment. Materials Chemistry and Physics 74, 289–299.

Kaukonen V, Hakanen M, Lindberg A, 1997. Diffusion and Sorption of HTO, Np, Na and Cl in rocks and minerals of Kivetty and Olkiluoto. Posiva 97-07, Posiva Oy, Finland.

Kryl J, Švagera O, Bukovská Z, Soejono I, Zelinková T, 2020. Výzkum puklinové konektivity v PVP Bukov (Research of fracture connectivity at PVP Bukov). Interim report SÚRAO, TZ 459/2020. (In Czech.)

Löfgren M, Nilsson K, 2019. Task description of Task 9A – Modelling of REPRO experiments WPDE-1 and WPDE-2. Task 9 of SKB Task Force GWFTS – Increasing the realism in solute transport modelling based on the field experiments REPRO and LTDE-SD. SKB P-17-18, Svensk Kärnbränslehantering AB.

Löfgren M, Nilsson K, 2020. Task description of Task 9B – Modelling of LTDE-SD performed at Äspö HRL. Task 9 of SKB Task Force GWFTS – Increasing the realism in solute transport modelling based on the field experiments REPRO and LTDE-SD. SKB P-17-30, Svensk Kärnbränslehantering AB.

Nilsson K, Byegård J, Selnert E, Widestrand H, Höglund S, Gustafsson E, 2010. Äspö Hard Rock Laboratory. Long Term Sorption Diffusion Experiment (LTDE-SD). Results from rock sample analyses and modelling. SKB R-10-68, Svensk Kärnbränslehantering AB.

Press W H, Teukolsky S A, Vetterling W T, Flannery B P, 2007. The art of scientific computing. 3rd ed. New York: Cambridge University Press.

Skagius K, Pettersson M, Wiborgh M, Albinsson Y, Holgersson S, 1999. Compilation of data for the analysis of radionuclide migration from SFL 3-5. SKB R-99-13, Svensk Kärnbränslehantering AB.

Soler J M, Neretnieks I, Moreno L, Liu L, Meng S, Svensson U, Trinchero P, Iraola A, Ebrahimi H, Molinero J, Vidstrand P, Deissmann D, Říha J, Hokr M, Vetešník A, Vopálka D, Gvoždík L, Polák M, Trpkošová D, Havlová V, Park D-K, Ji S-H, Tachi Y, Ito T, 2019. Evaluation and modelling report of Task 9A based on comparisons and analyses of predictive modelling results for the REPRO WPDE experiments. Task 9 of SKB Task Force GWFTS – Increasing the realism in solute transport modelling based on the field experiments REPRO and LTDE-SD. SKB R-17-10, Svensk Kärnbränslehantering AB.

Soler J M, Meng S, Moreno L, Neretnieks I, Liu L, Kekäläinen P, Hokr M, Říha J, Vetešník A, Reimitz D, Višňák J, Vopálka D, Kröhn K P, Tachi Y, Ito T, Svensson U, Iraola A, Trinchero P, Voutilainen M, Deissmann G, Bosbach D, Park D K, Ji S-H, Gvoždík L, Milický M, Polák M, Makedonska N, Kuluris S P, Karra S, Hari S V, Gylling B, Lanyon G W, 2021a. Evaluation report of Task 9B based on comparisons and analyses of modelling results for the Äspö HRL LTDE SD experiments. Task 9 of SKB Task Force GWFTS – Increasing the realism in solute transport modelling based on the field experiments REPRO and LTDE-SD. SKB TR-20-17, Svensk Kärnbränslehantering AB.

Soler J M, Kekäläinen P, Pulkkanen V M, Moreno L, Iraola A, Trinchero P, Hokr M, Říha J, Havlová V, Trpkošová D, Vetešník A, Reimitz D, Višňák J, Vopálka D, Gvoždík L, Milický M, Polák M, Fukatsu Y, Ito T, Tachi Y, Svensson U, Park D K, Ji S-H, Gylling B, Lanyon G W, 2021b. Evaluation report of Task 9C based on comparisons and analyses of modelling results for the ONKALO REPRO-TDE experiment. Task 9 of SKB Task Force GWFTS – Increasing the realism in solute transport modelling based on the field experiments REPRO and LTDE-SD. SKB TR-21-09, Svensk Kärnbränslehantering AB.

Sudicky E A, Frind E O, 1982. Contaminant transport in fractured porous media: Analytical solutions for a system of parallel fractures. Water Resources Research 18, 1634–1642.

TUL, 2015. FLOW123d, version 1.8.2. Documentation of file formats and brief user manual, NTI TUL. Available at: http://flow123d.github.io/

Vanýsek P, 2009. Ionic conductivity and diffusion at infinite dilution. In Lide D R (ed). CRC handbook of chemistry and physics: a ready-reference book of chemical and physical data. 90th ed. Cleveland, OH: CRC Press.

Vilks P, Miller N H, Stanchell F W, 2005. Laboratory program supporting SKB's Long Term Diffusion experiment. Report 06819-REP-01300-10111-R00, Atomic Energy of Canada Limited.

Widestrand H, Byegård J, Cvetkovic V, Tullborg E-L, Winberg A, Andersson P, Siitari-Kauppi M, 2007. Sorbing tracer experiments in a crystalline rock fracture at Äspö (Sweden): 1. Experimental setup and microscale characterization of retention properties. Water Resources Research 43. doi:10.1029/2006WR005277

Widestrand H, Byegård J, Nilsson K, Höglund S, Gustafsson E, Kronberg M, 2010. Long Term Sorption Diffusion Experiment (LTDE-SD). Performance of main in situ experiment and results from water phase measurements. SKB R-10-67, Svensk Kärnbränslehantering AB.

Wood, 2018. ConnectFlow Technical Summary. Release 12.0. Wood, UK.

Zheng C, 2010. MT3DMS v5.3 Supplemental user's guide. Technical Report to the U S. Army Engineer Research and Development Center, Department of Geological Sciences, University of Alabama.

Zheng C, Wang P P, 1999. MT3DMS: A modular three-dimensional multi-species transport model for simulation of advection, dispersion and chemical reactions of contaminants in groundwater systems; documentation and user guide. U S. Army Engineer Research and Development Center Contract Report SERDP-99-1, Vicksburg, MS.

Data deliveries of Task 9

Table 0-1. Distributed data within the GWFTS platform via the web portal SKB (https://www.skb. se/taskforce/).

Delivery number	Description	Note	File
1	Task 9A Description	Updated and delivered by the Technical Committee of Task 9, November 22, 2015	Download (pdf)
	Task 9B-1 Description	Delivered by the Technical Committee of Task 9, November 26, 2015	Download (word)
2	Data for Task Description 9A	Delivered by the Technical Committee of Task 9, May 12, 2015	Download (xls)
3	Description of the fluid inlet device in REPRO		Download (pdf)
	WPDE Photographs with higher resolution than earlier distributed	Delivered by the Technical Committee of Task 9, May 25, 2015	Download (Word)
4	Template for reporting of Task 9A		Download (word)
	Template for delivering results of Task 9A	Delivered by the Technical Committee of Task 9, June 15, 2015	Download (xls)
5	Task Description 9B-1 Appendix 1	November 25, 2015	Download (word)
6	Lab program supporting LTDE-SD, Vilks et al. 2005	Additional files for Task 9B-1	Download (pdf)
	Evolution of pH and Eh in LTDE-SD	Additional files for Task 9B-1	Download (xls)
	Template for delivering data Task 9B-1 15-11-23	Additional files for Task 9B-1	Download (xlsx)
7	Errata for Task Description 9B-1 of 2015-11-26	Delivered by Task 9 Technical Committee, April 21, 2016	Download (pdf)
8	Updated information (time line, core storage, and decay correction) on the Task Description 9B-1 of 2015-11-26.	Delivered by Task 9 Technical Committee, April 25, 2016	Download (pdf)
9	Draft Task Description for Task 9B-2.	Delivered by Task 9 Technical Committee, May 2, 2016	Download (word)
10	Experimental data of Repro WPDE 1 and 2, i.e. Task 9A.	Delivered by Task 9 Technical Committee, June 16, 2016	Download 1 (xlsx) Download 2 (xlsx) Download 3 (xlsx) Download 4 (xlsx)
11	Updated Task Description for Task 9B-2, and the associated data.	Data delivered by Task 9 TC, June 22, 2016	Download 1 (xlsx) Download 2 (xlsx) Download 3 (xlsx) Download 4 (word)
12	Appendices to Task Description for Task 9B-2: Pictures of A and D cores, and geological characterization.	Data delivered by Task 9 TC, September 30, 2016	Download 1 (word) Download 2 (word)
13	SKB General report template and instructions.	Delivered by TF GWFTS Secretariat, October 5 2016.	Download 1 (word) Download 2 (pdf)
14	Task 9B -Geological description of a piece of rock from the LTDE-SD site.	Report by Henrik Drake, Linnaeus University, Sweden. Delivered by Task 9 TC October 7 2016.	Download (pdf)

Delivery number	Description	Note	File
15	Task 9A Evaluation material for the Task 9A Evaluation report	Data delivered by the Task 9 Evaluator, December 2 2016	Download 1 (Evaluation draft, word), Download 2 (Figures, pdf), Download 3 (Compilation draft, pdf)
16	Task Description for Task 9B-3 including separate Appendix with high resolution pictures of A and D cores.	Data delivered by Task 9 TC, December 21, 2016	Download 1 (pdf, 1 Mb), Appendix pdf 9MB, Appendix Word 43MB
17	Clarification of data for Task 9A (REPRO) and Task 9B (LTDE-SD)	Data delivered by the Principal Investigators of Task 9, April 13 2017	Download 1 (word), Download 2 (word)
18	The data package includes the results from C-14-PMMA autoradiography and X-ray tomography on samples from REPRO and LTDE-SD. The total size of all of the files is about 11.5 GB, however when compressed they take only about 0.6 GB.		Download the data package from the ftp-server: Task 9/Additional Data Deliveries.
	Also, there is information included about conversion of gray values from C-14-PMMA image to porosities. There is also a program for opening the *.raw images and short instruction how to open the files.	Data delivered by University of Helsinki, March 29 2017	Download instructions for the ftp-server.
19	Supporting lab tests with dyes (Uranine and Potassium permanganate) in flowing water around a core from REPRO – WPDE in a tube of plexiglass. The control widgets of the videos may appear when hoovering over the individual pictures in slides 3, 4, 6 and 7.	Data delivered by HYRL, and presented at TF GWFTS meeting 35.	Download (pptx, 77 Mb)
20	An update on the tracer cocktail densities in Task 9A.		Download (pdf)
21	An update on various artefacts that have been discussed in Task 9B.		Download (pdf)
22	Task description of Task 9C		Download (pdf, 5 Mb)
	Template for result predictions of Task 9C	Delivered by the Principal Investigators of Task 9, November 14, 2017.	Download (xlsx)
23	Task 9C: Update on pressure gradients in REPRO TDE	Delivered by Task 9 PI May 25, 2018	Download (pdf)
24	Task 9B2: Accompanying data (revised PEEK data compared to DD11).	Delivered by Task 9 PI July 25, 2018	Download (pdf)
25	Task 9C: Additional updated pressure data of REPRO TDE, and clarifications.	First delivered July 31, updated September 7, 2018 by Task 9 TC.	Download (pdf)
26	Task description of Task 9D1 and 9D2	Delivered by the Principal Investigators of Task 9, September 12, 2018.	Download (pdf)
27	Final draft SKB P-16-12 – Long Term Sorption Diffusion Experiment (LTDE-SD) Over-core Drilling and Extraction of Core Samples	Delivered by Task 9 PIs September 27, 2018.	
28	LTDE-SD (Task 9B): Revised background tracer concentrations, preliminary memo	Delivered by Task 9 Principal Investigator Kersti Nilsson November 5, 2018	Download (Word)

Delivery number	Description	Note	File
29	LTDE-SD (Task 9B): Memo; Updated detection and reporting limits and risk of contamination for Co-57, Ba-133, Cs-137 and Ra-226, revised due to potential contamination during the sample preparation, Part 1.	Delivered by Kersti Nilsson and Johan Byegård, January 21, 2019.	Download (pdf)
30	Task 9C data: Updated caliper volumes.	Data delivered by Kersti Nilsson and Johan Byegård, February 13, 2019.	Download (pdf)
31	Task 9C data: Experimental activity and pressure values.	Data delivered by Kersti Nilsson and Johan Byegård, March 8, 2019	Download (xlsx)
32	Updated Task Description for Task 9D1-2. Updated text in the TD is marked with yellow.	The updated TD is delivered by James Crawford, May 6, 2019.	Download (pdf)
33	Task 9B data: Updated information on core concentrations in LTDE-SD.	Data delivered by Kersti Nilsson and Johan Byegård, June 13, 2019	Download (xlsx)
34	Task 9C data: Updated experimental values for REPRO TDE.	Data delivered by Kersti Nilsson and Johan Byegård, June 18, 2019	Download (xlsx)
35	Task 9B Memo Part 2 on potential contamination levels in LTDE-SD.	Delivered by Kersti Nilsson and Johan Byegård, July 11, 2019	Download (pdf)
36	Tentative Task Description for Task 9C Extension (migration of Rn and Ra).	The tentative TD is delivered by Johan Byegård and James Crawford, July 16, 2019.	Download (pdf)
37	Updated Task Description for Task 9C Extension (migration of Rn and Ra).	This data delivery is replacing Data Delivery 36. The updated TD is delivered by Johan Byegård and James Crawford, August 27, 2019.	Download (pdf)
38	Task 9C data: Updated experimental values for REPRO TDE, II	Data delivered by Kersti Nilsson, December 18, 2019	Download (pdf)
39	Template for reporting Task 9C contributions for the joint Modelling and Evaluation Task 9C report		Template for reporting Task 9C (word)
	Generic template for Task 9 report e.g. Task 9B modelling reports, Task 9C joint M & E report, Task 9C Extension report	Templates delivered by TF GWFTS Secretariat February 26, 2020	Task 9 Manuscript Public report – Template Generic (word)
40	Updated Rock Matrix Data Draft P-17-30 Task Description for Task 9B		Rock Matrix data (xls)
	Updated info of 9B	Delivered by Kersti Nilsson and Björn Gylling, March 10, 2020	Draft P-17-30 (word)
41	On-line gamma measurement values for the observation holes and pressure data		Data delivery TDE (xls)
	Draft P-17-31 – Task descriptions of Task 9C	Data delivered by Kersti Nilsson, Geosigma, March 26, 2020	Draft SKB P-17-31 Task desriptions Task 9C (word, 16 MB)
42	Template for reporting Task 9D contributions for the joint Modelling and Evaluation Task 9D report	Template delivered by TF GWFTS Secretariat May 15, 2020.	Template for reporting Task 9D (word)

SKB is responsible for managing spent nuclear fuel and radioactive waste produced by the Swedish nuclear power plants such that man and the environment are protected in the near and distant future.

skb.se